Degradation Mechanisms and Applications in Ion Intercalation Materials

by

Debbie Zhuang

B.S. in Chemical Engineering and Mathematics—Applied Science,
University of California, San Diego (2019)

Submitted to the Department of Chemical Engineering
in partial fulfillment of the requirements for the degree of

Doctor of Philosophy

at the

MASSACHUSETTS INSTITUTE OF TECHNOLOGY

September 2024

Author .....
Debbie Zhuang
Department of Chemical Engineering
23rd of July 2024

Certified by .....
Martin Z. Bazant
E. G. Roos Professor of Chemical Engineering
Professor of Mathematics
Thesis Supervisor

Accepted by .....
Hadley D. Sikes
Willard Henry Dow Professor of Chemical Engineering
Chairman, Department Committee on Graduate Theses

Degradation Mechanisms and Applications in Ion Intercalation Materials

by

Debbie Zhuang

Submitted to the Department of Chemical Engineering
on 23rd of July 2024, in partial fulfillment of the
requirements for the degree of
Doctor of Philosophy

Abstract

Lithium ion batteries (LiBs) are a pivotal energy storage technology that are widely adopted for their high energy density and safety. From a macroscopic level, LiBs operate at a micrometer lengthscale, but consist of many active material nanoparticles which participate in reversible electrochemical reactions that store and release energy. These particles control the crucial processes for energy storage in macroscopic devices, generating a process spanning multiple length and time scales in LiBs. However, despite the ubiquitous application of LiBs in many industries, degradation limits their lifespan, hindering their broader applicability in usages demanding high energy density and extended lifespans, such as electric vehicles (EVs). Dominant degradation occurs at the nanoparticle level involving various mechanisms, such as formation of resistive films on the particle surface or surface phase transformations in common LiB materials. The effects of degradation are observed at the macroscopic level from electrochemical responses such as voltage or current measurements. Bridging the gap between microscopic and macroscopic scales to extract particle level degradation mechanisms from electrode scale responses is essential for understanding LiB degradation. These methods can be used to quantify degradation in battery materials for second life use, designing degradation resistant materials, and more.

Here, I propose a comprehensive multiscale framework that initially models LiB degradation at a single particle scale, using nickel rich materials as an example, then projects single particle degradation into population scale for both solid solution and phase separating materials. Furthermore, I analyze and design improved pulse diagnostics using hybrid pulse power characterization (HPPC) methods to extract physical microscopic degradation mechanisms from electrode-level responses. Overall, I set up a consistent framework modeling degradation from single particle to population level and vice versa in LiBs.

Thesis Supervisor: Martin Z. Bazant
Title: E. G. Roos Professor of Chemical Engineering
Professor of Mathematics

Dedicated to my wonderful parents
and sister

Acknowledgments

Thank you so much to all those I have met in graduate school and before who have made this journey possible by allowi ng me to explore my scientific interests or piquing my interest in different subjects. First and foremost, to my advisor Martin, thank you for your constant support and optimism. Your passion for research, excitement, and insightful comments have been invaluable throughout this entire journey. I would also like to thank Richard for your support, enthusiasm, and humor throughout the years. It has truly been a pleasure to learn from you and be mentored by you, and I have learned so much about math and science from you. I would also like to thank Mehran for being a part of my thesis committee and being arguably the person I learned the most from in graduate school (from your courses). Your precision, methodical teaching, and your insightful questions when I come to you for help have really made an impact on me. I would also like to thank Will Chueh for frequently hosting me at Stanford for both official and unofficial visits. Your enthusiasm and support of our collaborations has made much of this interdisciplinary research possible.

I would like to praise God for all He has done for me in the last five years, and for bringing me through this journey. I would also like to thank my church, the Church in Cambridge, for their support and love over the past five years. I especially want to thank Carol, Henry, and Yu Song for their care throughout the years. MIT Christians on Campus has also been a crucial part of my spiritual journey here. Thank you so much Laura, for all your support and nourishing throughout the years, and to the members of all the various small groups I have been in. I would also like to thank my companions Cassia, Sophia, and Shulammite for constantly encouraging me, praying with me, and always being down for boba.

In addition, my collaborators that I have worked with have taught me so much about research and supported me throughout. Without them, I would not have enjoyed doing research half as much. I also would not have been able to do much of the work that I have done without our insightful conversations. Starting from my undergraduate years, thank you Marc Riera, Kelly, and Kartik for your staunch

support and friendship. Thank you for never letting me go a day without laughing in the Paesani lab. In my graduate years, I am grateful to my D3BATT collaborators from the Chueh and Braatz groups, who have made my time here enjoyable and made my research fruitful. Giacomo, Marc Berliner, and Jinwook, thank you for all your help with numerical methods and for teaching me about optimization and identifiability, as well as being such kind friends. I have learned so much and enjoyed our collaborations immensely, so much that I now have card access to your office from my constant visits. Without my labmates in the Bazant lab, I would not be able to do any of the research that I had done. Our fruitful research conversations as well as jokes throughout the day always keep me grounded and happy. I want to thank Huanhuan, Michael, Yash, Alex, Sam, Cristina, Nick, and Pedro for being awesome labmates who have made late nights in the Bazant lab much more bearable.

I am even more forever indebted to all who have mentored me in my undergraduate and graduate programs. My academic journey would not have been possible without the support of these ones, who have given me so much emotional as well as practical support. Francesco, thank you so much for teaching me everything and always supporting me through every process from undergraduate to graduate school. Your support during many of my hardest times in graduate school have been invaluable. I am so grateful for your mentorship and care. I admire your research integrity, passion, and drive, and hope that I make you proud. Dimitrios, thank you so much for your mentoring and constant emotional support. I appreciate your passion for research and your kindheartedness so much, and your humor never fails to make me laugh. Often chatting with you about research greatly enlightens me. Without you, my days in graduate school would have been immensely more difficult and much less fun. Dan Cogswell, I appreciate your mentoring during my graduate school period so much. I learned so much about systematically doing research and batteries from you, and appreciated learning from your knowledge and humor.

My friends at MIT have really been my home away from home in Boston, and there is not enough I can say in their praises. Thank you so much—Rohan, Chris, Rose, Akiva & Alison, and Dan Chu for supporting me through thick and thin. Our

game nights every week are always the highlight of my week, and gym times together are the highlight of my day. Rohan, thank you so much for always supportive and a shoulder that I can lean on. Your friendship and care is invaluable to me. Thanks for being my older brother when my sister is not around to take care of me. Chris, thank you for all the walks and chats—I value your constant companionship so much. Thank you for always being supportive and caring. Rose, I appreciate your kindness and support to me throughout the years, and for always loving and caring for me. Thank you for always letting me make fun of you.

Most importantly, I would like to thank my family for their unwavering support. Without them and all the sacrifices they've made for me, I would not be able to pursue my dreams. Thank you to my parents, Sheng and Zhiqing, for loving me and nurturing me and supporting my pursuit of my dreams even throughout any circumstances. Thank you for always encouraging me and caring for all my needs. Thank you to my favorite person and sister Ruby, for loving and supporting me throughout all that has happened in grad school. Thank you for being my staunchest supporter. I also immensely appreciate my best friend Wendy, who is not official family but as close as family, for your loyal friendship and support throughout the years.

Contents

List of Figures

Chapter 1

Introduction

Rechargeable battery demand is projected to grow exponentially in the next decade. Lithium ion batteries, ubiquitous in our society for renewable energy storage purposes [19], operate through various processes such as electrochemical reactions, solid diffusion, and electrolyte diffusion. However, these same processes also impose inherent performance limitations on batteries [19]. These limitations hinder applications of lithium ion batteries as energy storage devices in many industries. Understanding the constraints on kinetic and transport timescales is often key to conceptualizing and designing better lithium ion batteries. A lithium ion battery typically consists of two electrodes made of active material that store and release lithium-ion electron pairs through intercalation reactions on the particle surface, releasing electrochemical energy [20]. Lithium-ion rich electrolyte facilitates transport between the electrodes during charging and discharging. This multiscale structure enables efficient reversible energy storage but also introduces complex interactions between different timescales within the electrode.

1.1 Battery Degradation

A significant factor preventing more widespread application of lithium ion batteries is degradation, which leads to reduced performance over time. Various degradation mechanisms affect the active material. For instance, the graphite anode often develops

a solid electrolyte interphase layer which increases resistance and reduces usable capacity [21]. The anode can also undergo lithium plating and form dendrites [22], which can induce short circuits and remove usable lithium capacity from a cell. Significant experimental [23, 24] and theoretical [21, 25, 26] efforts have been directed towards investigating the degradation of graphite electrodes, resulting in substantial progress in recent years. Electrochemical measurements have revealed strong asymmetry in solid electrolyte interphase (SEI) growth between charge and discharge cycles [24]. Imaging techniques, including cryo-transmission electron microscopy, have been used to observe the formation of a two-layer SEI *in situ*, visually documenting SEI growth. On the modeling frontier, computational studies using atomistic techniques have extracted transport properties of lithium ions and electrons through an idealized SEI layer [26]. Additionally, continuum scale models have incorporated the effects of SEI on the electrode scale, highlighting the role of lithium ion diffusivity through the SEI in the long timescale dynamics of interphase growth [21]. Similar mesoscale models have found asymmetry between charge and discharge cycles of SEI growth, hypothesizing that the SEI acts as a mixed ion-electron conductor with conductivity varying as a function of lithium concentration [25].

Cathodes can undergo various types of degradation, particularly in nickel-rich materials, which can experience phase transformations and densification at the surface. These changes modify reaction kinetics and decrease surface diffusivity [27, 28]. Such phase transitions often accompany oxygen gas release in nickel rich materials [29]. Other common degradation mechanisms in nickel-rich materials include transition metal dissolution, where metals leach into the electrolyte [30]. Mechanical issues such as particle cracking and intercalation stress in polycrystalline particles also pose significant challenges [31]. Recent advances in experimental and computational techniques have enhanced our understanding of these degradation mechanisms. Atomistic simulations have provided thermodynamic insights into surface phase transformations [32] and the effects of nickel content [33]. Continuum electrochemical models [34], such as shrinking core-type models, have revealed the impacts of electrochemical cycling on single particles. To validate these, finite element and finite volume models have

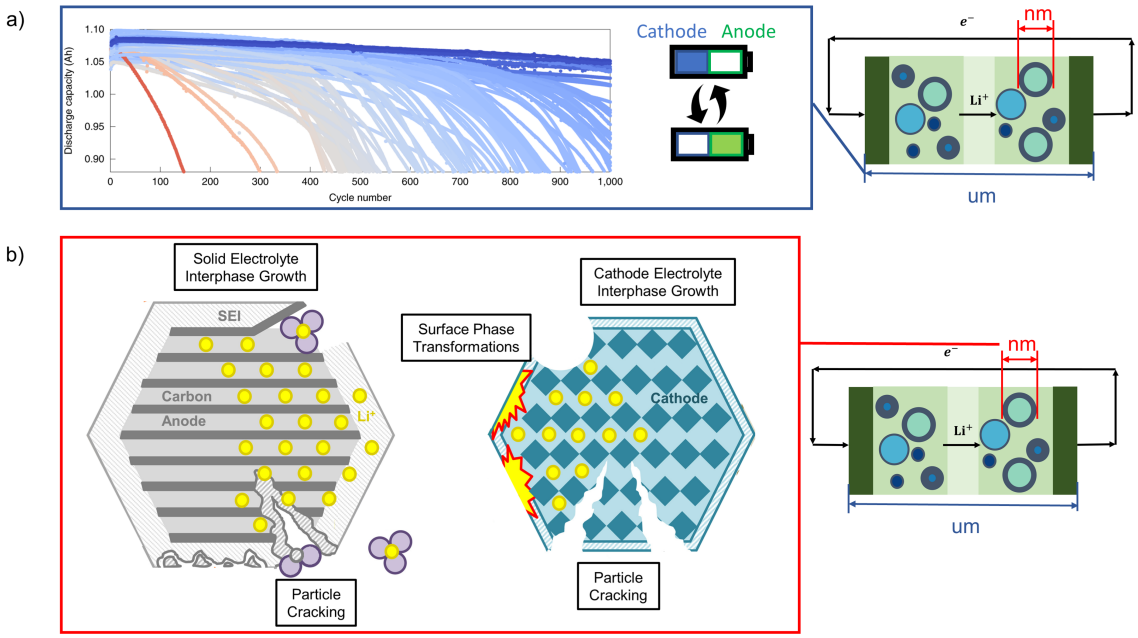

Figure 1: a) Using a figure from Ref. [1], the impact of degradation on the macroscopic level response of lithium ion batteries is seen through capacity loss with respect to cycle number, which varies based on manufacturing conditions. b) From Ref. [2], single particle level degradation mechanisms such as formation of resistive films, mechanical cracking, and surface phase transformations are shown to be the cause of device level capacity loss.

highlighted the role of high voltage cycling in mechanical fracture [35]. Experimental techniques like X-ray absorption spectroscopy, X-ray diffraction, and scanning transmission electron microscopy [28, 36, 27] have been instrumental in visualizing these degradation processes. These imaging methods have documented increased surface phase transformations, cation disordered intermediate phases, and varying phase compositions at the surface under high voltage cycling.

Degradation mechanisms manifest at the microscopic level but are observed macroscopically through electrochemical signals, as shown in Fig. 1a. It often appears as a loss in macroscopic capacity, typically illustrated through capacity loss relative to cycle number [1]. After degradation, voltage shifts as a function of capacity are indicative of battery deterioration. The criteria for degradation, such as the common benchmark of 80% of usable capacity [37], are arbitrarily chosen and do not neces-

sarily correlate with power output or other critical performance metrics for energy storage devices.

Increased degradation significantly affects the operation of a lithium ion battery. In battery management systems, optimized operation [38] can be applied to improve performance for second life applications [39], but without knowledge of degradation mechanisms, neither precise optimized operation nor choice of accurate recycling strategies are possible. While impedance measurements [40, 41] have been used to extract some degradation mechanisms, such as resistance growth or area specific impedance [42], the lack of a physics-based framework hinders a comprehensive understanding of degradation. Recent work [2] has separated degradation mechanisms successfully into phenomenological degradation behavior, such as loss of lithium inventory and loss of active material. These lumped parameters are difficult to connect directly with specific physical degradation mechanisms. Even when physical mechanisms are identified, designing experiments to extract such details can be challenging. Therefore, a complete overhaul of the degradation framework is necessary to extract information on microscopic mechanisms. This will enable more accurate comprehension and management of degradation processes, ultimately leading to better battery performance and longevity.

In this work, I aimed to analyze degradation from a microscopic to a macroscopic scale, and then overhaul the traditional methods of modeling degradation to apply physically driven degradation mechanisms instead of phenomenological ones. First, I investigated a major microscopic degradation mechanism in nickel rich materials—surface phase transformations, studied through cation disorder, an intermediate phase between layered and densified phases [12]. After this, I applied statistical mechanical methods to bridge multiple single particle degradation mechanisms to electrode scale. This involved formulating a fitness framework for extracting the degraded reaction rate for each particle, enabling the understanding of how individual particle degradation contributes to overall electrode performance [13]. Since many battery materials are phase separating, scaling analyses for phase separating battery particle populations were analyzed using eigendecompositions to extract timescales [14]. Following,

I investigated hybrid pulse power characterization (HPPC) techniques, which are a diagnostic technique applying intermittent rests and pulses [15]. Voltage pulse HPPC methods were designed, applying the fitness framework to extract physical degradation mechanisms. This step involved creating diagnostic protocols that could identify specific degradation mechanisms through controlled voltage pulses. Then, optimal design of these voltage pulse HPPC methods was performed with model-based design-of-experiment methods for accurate and fast estimation of degradation parameters, which is not expanded on in this thesis but can be found in Ref. [16]. A bidirectional strategy was applied in this thesis where microscopic degradation mechanisms were incorporated into a macroscopic model, and conversely, microscopic mechanisms were extracted from macroscopic electrode responses, making our approach practical for real-world applications. By integrating these steps, I created a comprehensive framework to accurately diagnose battery degradation from a fundamental physical perspective, leading to improved battery management and extended lifespan.

1.2 Multiscale Modeling of Batteries

Before delving into an in-depth analysis of the following work, it is crucial to establish physical understanding of the timescales associated with various processes in lithium ion batteries. During charging, intercalation reactions occur at the surface of active material particles at the anode and deintercalation at the cathode, whereas during discharge, the reverse processes occur. Solid diffusion from the surface to the bulk mediates the storage of lithium ions in the material. At the particle level, timescales of solid diffusion and reaction compete, such that mass conservation can be modeled by

$$\frac{\partial c}{\partial t} = -\nabla \cdot \mathbf{j}, \tag{1}$$

with a reactive boundary condition $-\mathbf{n} \cdot \mathbf{j} = R$, where $\mathbf{j}$ is the diffusion driven flux and R is the surface reaction rate. The competing timescales at the single particle level [3] are the solid diffusion timescale $\tau_{D,p} = L_p^2/D_p$, the process timescale $\tau_{I,p} = I^{-1}$, and the reaction timescale $\tau_{R,p} = L_p c_{max}/i_0$. Here, L_p is the particle length, D_p is the

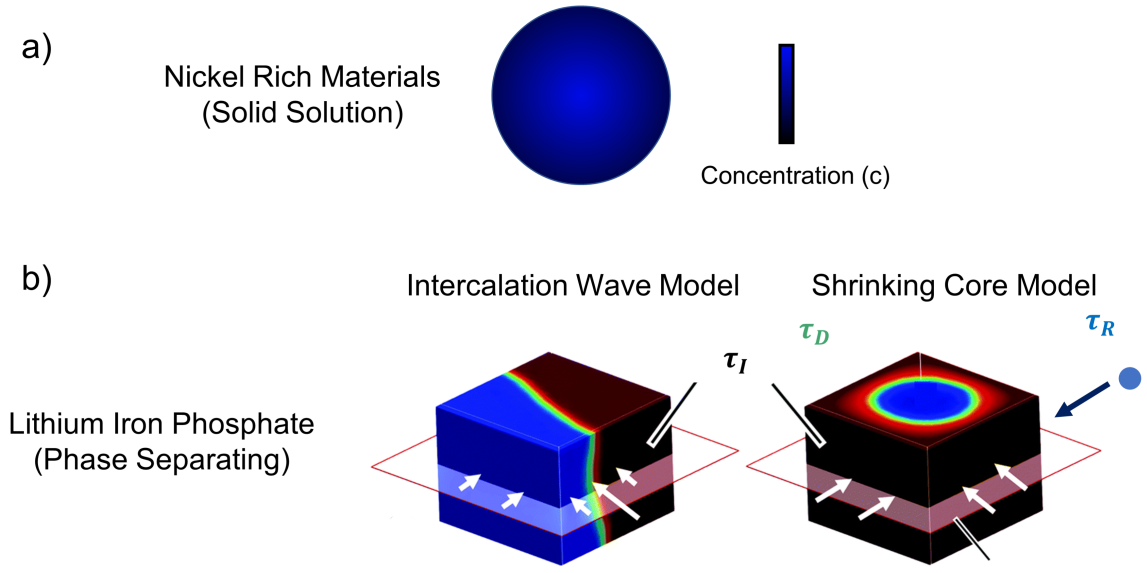

Figure 2: a) Example showing single particle reaction-diffusion behavior for a nickel rich material, which has solid solution thermodynamics, or for lithium iron phosphate, with phase separating thermodynamics. b) Competition between the process, reaction, and diffusion timescales trigger the appearance of different bulk phenomena in phase separating materials such as intercalation wave behavior or shrinking core behavior [3], with figures showing behavior of the different regimes taken from Ref. [3].

solid particle diffusivity, I is the applied C-rate, c_{max} is the maximum concentration per particle, and i_0 is the exchange current density of the material.

As analyzed in Ref. [3], competition between the reaction timescale, process timescale and diffusion timescale influences whether core-shell behavior or intercalation wave behavior in phase separating particles appears, as shown in Fig. 2. When $\tau_{I,p} \gg \tau_{D,p}$, the quasi-equilibrium (reaction limited) regime is attained, characterized by intercalation processes occurring at a much slower rate compared to diffusion processes. This is ideal for the application of the reaction-limited model in the current work. Most common battery electrode materials lie in the reaction limited regime [3]. Exceptions occur at high pulses, when the dimensionless current is large ($i/i_0 \geq 10^3$), or when particle size is large (as in graphite platelets), such that $L_p \geq 10^5$ nm. Here, i is the dimensionalized applied current. Thus, we can frequently assume that the system is reaction limited [3], allowing us to neglect solid state diffusion in the

particles.

At the electrode scale, similar timescale arguments apply. In the macroscopic design of an electrode, limitations stemming from electrolyte diffusion/conduction or solid conduction can significantly modify cell-level behavior [43]. However, due to the substantial amount of carbon additives in battery manufacturing, solid electronic conduction rarely is limiting. Consequently, limitations arising from electrolyte transport are often of primary interest in pulse processes. These limitations can be effectively understood through scaling analyses. From porous electrode style transport equations in Ref. [44], we observe that electrolyte scale transport is captured along the electrode with lithium ion mass conservation in the electrolyte

$$\frac{\partial(\varepsilon c_l)}{\partial t} = \frac{1}{\nu_+}\left(-\nabla \cdot \mathbf{F}_{l,+} + R_{V,+}\right), \tag{2}$$

where ε is the porosity, c_l is the lithium concentration in electrolyte, ν_+ is the number of ions per molecule of neutral salt, $\mathbf{F}_{l,+}$ is the flux of lithium ions, and $R_{V,+}$ is the volumetric reaction rate of the lithium ions. Charging occurs during the electrode process timescale as

$$\tau_{I,l} = \frac{\nu_+ \varepsilon c_l}{(1-\varepsilon) P_L I \rho_s}, \tag{3}$$

where P_L is the volumetric electrode loading, I is the C-rate of the electrode, and ρ_s is the lithium site density of the active material. For electrolyte diffusion limitation, we observe

$$\tau_{D,l} = \frac{\varepsilon^a L_l^2}{D_l}, \tag{4}$$

which is the timescale on which electrolyte diffusion occurs, where a is the Bruggeman scaling coefficient, L_l is the electrode length, and D_l is the effective electrolyte diffusivity. For electrolyte conduction, we observe that

$$\tau_{\sigma,l} = \frac{\varepsilon^a L_l^2 c_l z_+ e^2 \nu_+}{t_+^0 \sigma_l k_B T} \tag{5}$$

is the electrolyte transport timescale, where z_+ is the valence number of lithium ions, σ_l is the electrolyte conductivity, and t_+^0 is the transference number.

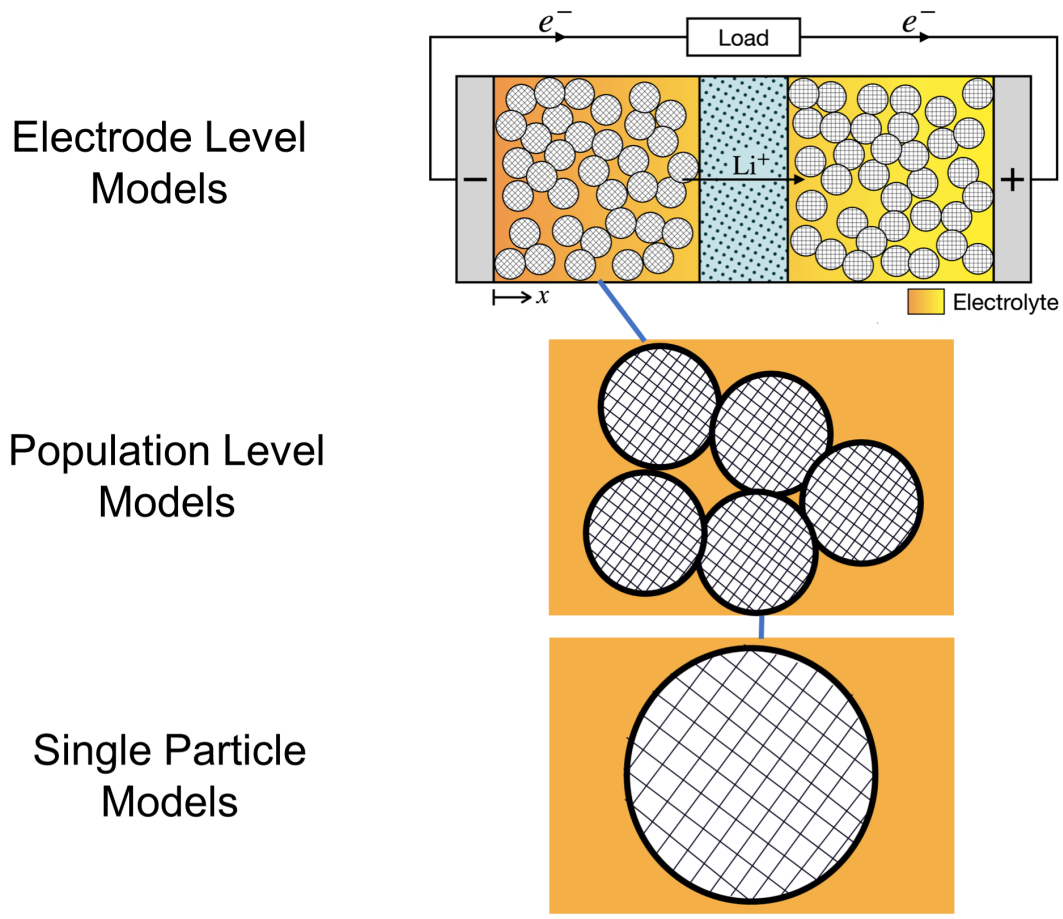

Figure 3: Figure displaying models appearing at different scales for a lithium ion battery, from single particle to population to electrode. Electrode scale figure is taken from Ref. [4].

When we compare the particle and electrode level timescales, the limiting timescales become apparent. Generally, in particle level mechanisms, solid diffusion timescales occur on the range of $\tau_{D,p} \sim 0.01 - 100\,\mathrm{s}$ [45, 46, 3], while reaction timescales occur on $\tau_{R,p} \sim 1 - 10\,\mathrm{s}$. At the electrode level, process timescales depend on applied C-rate and are in the range of $\tau_{I,p} \sim 1000\,\mathrm{s}$ for a 1 C charge process, and can be shorter for higher C-rates or longer for lower C-rates. Using electrolyte transport parameters from Ref. [47], we observe that $\tau_{D,l} \sim 10\,\mathrm{s}$ and $\tau_{\sigma,l} \sim 10\,\mathrm{s}$. In comparison, on the electrode scale, the process timescale for a 1 C charge is $\tau_{I,l} \sim 0.01\,\mathrm{s}$ for lithium iron phosphate, and is faster for higher C-rates. Particle-level reaction and diffusion

interact with electrode-scale transport limitations, resulting in a complex interplay of length and timescales that poses significant challenges for electrode modeling. A single-particle level model alone is insufficient to accurately capture the system-level behavior of a porous electrode, but allows us to gain insight into how to bridge scales to electrode level.

A hierarchical set of models can be used to capture these electrodes, shown in Fig. 3. Single particle models can capture the timescales of reaction and diffusion in a nanoparticle, using standard reaction-diffusion models. Because of the computational efficiency of single particle models, the incorporation of complicated physical models is usually performed with single particles [48]. However, single particle behavior does not capture that of a collection of particles under a current constraint for solid solution [49] or phase separating materials [50]. To capture population level behavior, population dynamics models, which capture many-particle interactions through the current constraint, can be applied. Initially, simple models capturing transformation and relaxation timescales were formulated, which eventually evolved to more rigorous models incorporating accurate reaction rates from chemical master equations [51, 11, 52]. These models can capture effects on particle activation fraction and distribution broadening [51, 13]. Despite being less efficient than single particle models, population models are more accurate.

However, electrolyte and electronic transport effects on the electrode scale are still not properly captured in population dynamics models, which can often be limiting factors at high currents [48]. Porous electrode theory couples the particle level and electrode level continuum modeling with a standard single particle model, neglecting many particle effects. Conservation equations on electrolyte and electronic conduction are postulated in the full cell. These standard porous electrode models [53, 54] have been developed to model the behavior of lithium ion batteries by Newman and coworkers. Standard porous electrode models are more computationally expensive than single particle or population dynamics models. However, porous electrode models do not incorporate the thermodynamics of phase separation or many-particle effects, which play a role from single particle behavior to active particle fraction.

To remedy this, multiphase porous electrode theory [55, 44] was formulated to include many particle as well as thermodynamic effects to properly capture behavior of phase separating electrodes. Through these models, the active particle fraction can be accurately captured, which can be computationally expensive because of the fine discretization needed at particle level to model phase boundaries, as well as at electrode level to capture transport limitations.

1.3 Particle Level Degradation

Starting our investigation at the particle level allows us to integrate reactions and solid diffusion processes while considering degradation at this scale. Nickel rich materials are an increasingly common class of cathode materials [56] valued for their high energy and power densities. Compared to lithium iron phosphate cathodes, nickel rich materials can offer up to 50% higher energy density. Typically synthesized in layered form, these materials generally have varying ratios of nickel, manganese, and cobalt ($LiNi_xMn_yCo_zO_2$), which respectively contribute to capacity, stability, and better kinetics of the materials [57]. The nickel content in recent years in these materials has increased to reduce cobalt usage. This shift is motivated by the high cost and negative environmental impact associated with cobalt [58], as well as the strong correlation between cobalt mining and human rights violations, such as child labor and unsafe worksites. Nickel-rich materials, with their high energy density and reduced environmental toxicity, offer a promising alternative, but come with their own set of challenges. The high energy density and reduced environmental toxicity of these materials come at the expense of increased degradation and electrochemical instability in higher nickel content materials [33]. Cycling-induced particle cracking commonly occurs in nickel-rich particles, especially after repeated charging and discharging cycles [59]. Especially at high voltages ($\geq 4.5\,\mathrm{V}$), surface phase transformations and oxygen release [27] can rapidly degrade the active material surface, leading to densification and transformation into various phases such as spinel, rock salt, and disordered rock salt [32]. Though specific surface phases vary based on cy-

cling conditions, a disordered layer always appears in between the surface and bulk phases.

Much work has been performed to investigate these mechanisms. Experimental cycling of nickel-rich cells has provided insights into cathode degradation at the surface [28, 60], revealing varying thicknesses of different surface phases. Investigations from atomic scale simulations with density functional theory of nickel rich degradation mechanisms [32, 61] have been performed to extract formation energies of various phases under different electrochemical conditions. However, there exists a discrepancy in the timescales between the predictions offered by the current atomistic models (nanoseconds) and the operating timescales of the battery (hours) [43]. To accurately capture degradation in a battery, modeling techniques must be computationally efficient enough to operate on timescales of at least hours. Additionally, these techniques do not capture the multiscale structure of lithium ion batteries. Thus, there is a pressing need for degradation modeling to accurately simulate degradation processes within the timescales relevant to battery degradation.

Hence, in Chapter 2, our aim is to develop a mesoscale model for the degradation of nickel-rich materials at the single particle level, focusing on cation disorder as a proxy for surface phase transformations. We leverage the periodic layered structures of these crystalline materials to formulate a thermodynamic model of defect formation, which is then incorporated into a single particle reaction-diffusion model. Our model successfully captures the degradation behavior of a single particle under the whole voltage operating window for these systems.

1.4 Particle Level to Electrode Level

Degradation mechanisms primarily occur at the single particle level, ultimately manifesting in observable effects at the electrode scale. Electrochemical methods, such as voltage measurements or capacity loss curves, are commonly used to quantify degradation in electrodes [1]. However, deconvoluting the different electrochemical signals is challenging due to the lack of physics-based models that connect microscopic degra-

dation processes to macroscopic behavior. Moreover, the criteria used to determine degradation, such as reaching 80% of the original capacity, lack physical relevance to the battery's performance requirements, particularly in terms of power output [62]. Therefore, there is a need to develop more physically meaningful degradation criteria related to power fade to better assess the degradation of lithium-ion cells in practical applications.

1.4.1 Solid Solution Materials

To develop a more physically meaningful macroscopic degradation criterion, we examine solid solution materials, which have a monotonically increasing/decreasing chemical potential with increased lithium concentration. As discussed in Sec. 1.2, the interplay between different timescales indicates that a single particle model for degradation is insufficient for scaling degradation to the electrode level. Consequently, we need statistical mechanical methods to map degradation from the particle level to the electrode scale. In biological systems, concerted behavior between individuals in a population is well documented [63, 64], particularly in the context of evolution. Analogously, in electrochemical systems, concerted population behavior has been observed through electrochemical oscillations in voltage measurements [65]. Population scale behavior is often simplified using a population balance (Fokker-Planck) model, where heterogeneity in driving force is accounted for via an effective diffusivity [66]. In genotype evolution, different "states of health" of genes can lead to modified effectiveness of reproductivity, which is frequently modeled using a fitness landscape. Analogously, in battery systems, the rate capability of each battery particle can be compared to the "fitness" of each gene. Here, the fitness indicates the effectiveness of a single particle in storing and releasing energy through an electrochemical reaction relative to the rest of the population. By applying similar methods to capture the rate capability of each particle, we can develop a framework for mapping single-particle degradation to the system level. This approach is investigated in detail in Chapter 3, where we explore these methods for deriving a macroscopic degradation criterion that better reflects the physical degradation mechanisms at play in lithium ion batteries.

1.4.2 Phase Separating Materials

Many common battery materials, such as lithium iron phosphate [67] and graphite [68], are all thermodynamically phase separating rather than solid solution materials. Here, phase separation implies that the chemical potentials of these materials change non-monotonically as lithium is inserted or extracted to reach different concentrations [69]. Consequently, varying fractions of (meta)stable phases in phase separating materials appear instead of the full spectrum of possible concentrations. At the single-particle scale, this behavior manifests as intercalation waves rather than bulk/surface quasi-equilibrium behavior [3]. At the population scale [8, 65], macroscopic voltage oscillations are observed. While portions of this behavior were explained through simulated models using multiphase porous electrode theory [8], these explanations have been predominantly phenomenological. The energy barrier of the chemical potential has been found to significantly influence the activation behavior of the particles. Due to the nonlinear kinetics and explicit concentration dependence of reaction rates, asymmetry in activation behavior between charge and discharge has also been observed, with a transition between low and high active particle fractions noted only during the discharge process. However, the mathematical theory behind these behaviors is still not yet developed.

From a theoretical perspective, simplified population models [11, 70] have also been studied to obtain equilibrium or near equilibrium behavior of populations, but do not capture dynamical transformation behavior in the spinodal gap. In a porous electrode, where the process timescale is controlled by the applied current or voltage, dynamical studies are more important than near-equilibrium studies. The applied voltages or currents often modify the free energy landscape, which is not accounted for in near-equilibrium studies. Here, we perform a nonequilibrium study capturing the timescales by mapping the reaction rates and thermodynamic potentials to an effective nonequilibrium free energy landscape. Using the eigenvalues of the Liouville operator, we extract timescales of the population transformation behavior using properties of the effective free energy landscape. When comparing these timescales with the total

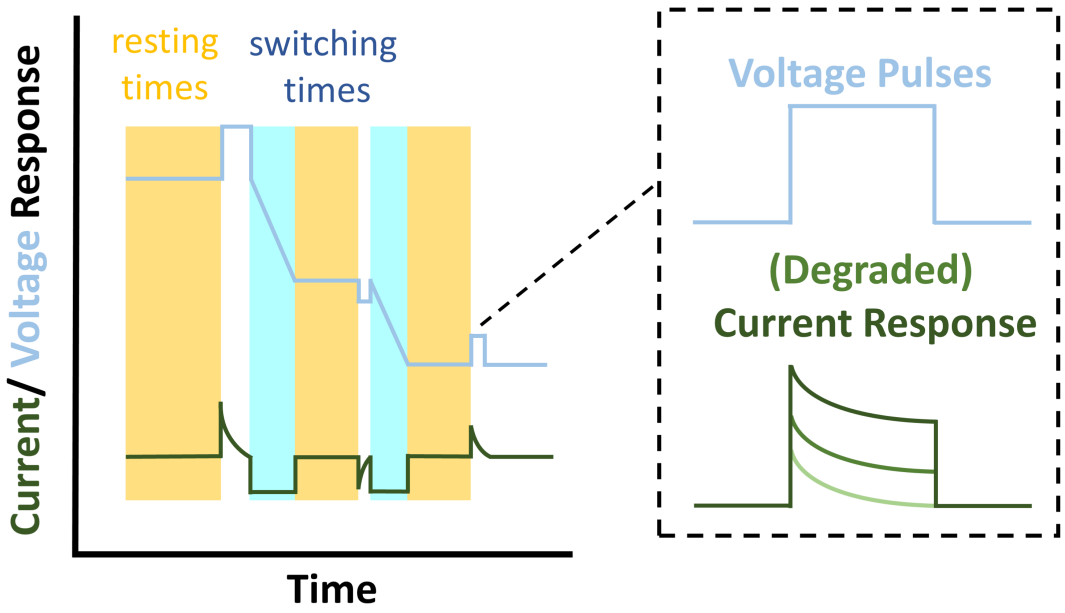

Figure 4: Example hybrid power pulse protocol, showing intermittent rests and pulses. Voltage pulses are applied and the (degraded) current responses are recorded for future diagnostics purposes.

process timescale, the physical mechanism behind the transitions between the low and high active particle fraction regimes becomes clear. This approach allows for direct prediction of active particle fraction and potential from a population with a defined C-rate. For future applications, these techniques can be particularly useful for predicting active particle fraction in pulses, specifically for diagnostics pulses. We investigate these points in Chapter 4.

1.5 Electrode Level to Particle Level

1.5.1 Pulse Diagnostics

To determine optimized operations for a battery pack or make second life decisions post recycling in a practical way, it is crucial to first estimate extent of microscopic degradation in lithium ion batteries. Much effort has been dedicated to estimating degradation in lithium ion cells. High-precision coulometry tests can accurately

estimate some degradation modes, but require equipment with high measurement precision [71, 72]. Techniques such as electrochemical impedance spectroscopy (EIS) measure the linear response of a cell to small perturbations, but only accurately capture near equilibrium behavior [73]. These low rate perturbations do not push the battery to its operational limits. Other pulse-type diagnostics, such as hybrid pulse power characterization (HPPC) [62, 74], use nonequilibrium measurements to extract information. These measurements alternate rest and pulse measurements, as shown in Fig. 4, to capture nonequilibrium cell behavior at high rates, which are the regimes lithium ion batteries commonly operate in.

Pulse measurements are also commonly used to extract information about diffusivities, employing techniques such as galvanotstatic/potentiostatic intermittent titration techniques (GITT/PITT) [75, 76]. Despite widespread use of pulse techniques in electrochemistry, their impact on cells is still poorly understood. Though attempts to analyze pulse protocols through porous electrode simulations [77, 78] have been made, selection and design of different pulse experiments is still fairly arbitrary. Unjustified choices in state of charge and pulse magnitude design of HPPC protocols were made in the initial design of protocols [62], which have not been modified in the last twenty years. In addition, the physical analysis of pulse dynamics, which operate in the reaction-limited regime due to the high pulse magnitudes [3], is still insufficient.

We desire to establish a physical interpretation of pulses that can extract degradation mechanisms. In view of bridging particle level and electrode level degradation from physically derived particle level degradation mechanisms, we attempt to incorporate these methods into the interpretation of pulses. We use the rate capability, or "fitness" derived in the previous chapter, as a new power fade metric to determine degradation of cells. These methods will be expounded in Chapter 5.

1.5.2 Optimal Design of Diagnostics

The analysis of pulse diagnostics in the previous chapter significantly enhances the application of diagnostics to battery systems. Current trends in battery manage-

ment systems include using rule or optimization based methods to manage energy systems, jointly optimizing cycle life and performance [79]. This optimization requires intimate knowledge of the current degradation state of the cells. However, in many battery management systems or recycling protocols, there is insufficient time to perform traditional slow pulse diagnostics on cells [38]. Fast and accurate pulse diagnostics on lithium ion battery cells are required for efficient diagnostics towards second life or battery management applications. These topics are further investigated in Ref. [16], an extension of the current work using optimal design-of-experiment for pulse diagnostics design.

1.6 Conclusion

Here, our analysis of degradation and its applications in lithium ion batteries begins at the single particle level, where nickel-rich degradation mechanisms are modeled. The single particle level degradation models are projected to population level through a Fokker-Planck model to understand population scale degradation for solid solution materials. Additionally, timescale analyses of population scale behavior for phase separating materials, which are common in lithium ion batteries, are performed to understand their nonequilibrium behavior. Following this, we extract specific degradation mechanisms from diagnostics through a physical analysis of pulses, connecting macroscopic pulses to specific particle level degradation mechanisms. Optimal design is applied to these protocols for non-phase separating materials, ensuring efficient and accurate diagnostics.

Chapter 2

Single Particle Layered-Oxide Cathode Degradation

Theory of layered-oxide cathode degradation in Li-ion batteries by oxidation-induced cation disorder [12]

2.1 Introduction

2.1.1 Motivation

As Li-ion batteries continue to revolutionize energy storage and power global electrification, it is increasingly important to understand the microscopic degradation mechanisms that limit their efficiency, rate capability, and lifetime at the particle scale. Degradation is exacerbated by efforts to increase energy density, while lowering material costs. This tradeoff is well illustrated by nickel-rich cathode materials, based on nickel-manganese-cobalt (NMC) layered oxides [33, 80]: as scarce and expensive cobalt is replaced by more plentiful and affordable nickel, the nickel-rich oxide cathode degrades more easily at the high voltages required for high energy density

The present chapter is based on my published work in the Journal of the Electrochemical Society [12].

batteries. The microscopic mechanisms are still poorly understood, so it is critical to develop a predictive theory of degradation at the particle level, in order to understand and optimize this tradeoff.

Nickel-rich materials degrade with cycling by a variety of possible mechanisms [81, 82, 83, 84], such as phase transformations, cation disorder, surface reconstruction [28, 27], particle cracking [31, 85, 59], and transition-metal dissolution [86, 87]. Notably, the various possible degradation mechanisms depend on the specific transition-metal chemical properties of different nickel-rich materials. Some nickel-rich degradation mechanisms, such as transition metal dissolution, can affect degradation at the anode through increasing the conductivity of the solid-electrolyte interphase on the graphite anode. This happens by the incorporation of transition metal ions dissolved in the solution from cathode degradation [30, 88]. An additional complexity is that nickel-rich layered oxides are currently being developed into many different compositions with added transition metals such as cobalt, manganese, and aluminum, which all have varying chemical properties. The degradation mechanisms of nickel-rich materials all are coupled, with cation disorder driving much of the bulk phase transitions and the surface phase transformations [89]. Here we seek to elucidate the physical mechanisms behind degradation of nickel-rich cathode materials to increase battery lifetime and reduce safety risks during operation from degradation-induced short circuits.

Although Li-ion battery capacity fade has been the focus of extensive research, most studies have focused on degradation mechanisms in the standard graphite anode, such as solid electrolyte interphase growth [21, 24, 25, 90] and lithium plating [91, 92]. However, recent experiments have shown that the amount of cathode and anode degradation in batteries is on par with each other, especially in nickel-rich materials [93]. Cycling experiments with microscopy techniques have been performed to visualize cathode degradation at the atomic scale [28, 94, 27, 60], providing necessary experimental support for modeling at the particle level. However, there have been few attempts to model cathode degradation beyond atomistic simulations or machine learning with limited physical insight [95]. Atomic scale studies using density

functional theory and other methods have been used to study cathode degradation [96, 32, 61] to calculate the formation energies of these phases and the relationship between diffusivity coefficients and defects, but because of the scale at which degradation happens in a battery, this is impossible to translate directly into a porous electrode scale battery model. The timescales of interest in atomic scale modeling are on the scale of nanoseconds at most, but the scale at which a battery operates is from hours to months, especially when degradation starts becoming of interest. There is a crucial need to develop cathode degradation models that can be applied at the porous electrode scale in battery simulations.

Phase transformations at the surface and bulk, one of the main degradation mechanisms in nickel rich materials, have been observed since the initial characterization of nickel rich materials [97, 32, 98, 99]. Phase transformations and surface reconstruction, shown in Fig. 1a, increase after cycling [60], and the phases formed are highly dependent on the material used [32, 61]. Based on the varying cycling protocols used during (de)intercalation, the amount of phase transformations and the thicknesses of the surface reconstruction layers change [60, 100]. Spinel, rock salt, and disordered rock salt phases, along with other phases such as γ phases have all been measured experimentally [32, 60, 28], but no agreements have been reached over the phases formed, except that the phases are denser than the original layered phases. These dense surface phases affect operation of a battery, modifying the kinetics and transport of these materials, causing batteries to become unusable after a certain point in their cycle life [101, 102, 103].

These phase transformations in the bulk and surface of cathode materials are a well-known degradation mechanism in nickel rich materials that have been studied with many experimental imaging techniques [28, 104, 105]. Computationally, density functional theory and Monte Carlo simulations have been used to study the effect of cation disorder on these phases [32, 106, 61, 107]. Limitations based on computational power create difficulties in modeling the entire disorder process using quantum mechanical first-principles methods. Understanding and reducing the degradation of batteries is an important barrier to the continued electrification of our current energy

storage systems [81, 97]. Thus, studying the amount of disorder, which drives the transitions to denser surface phases, is critical to studying the long-time operation of batteries and the continued expansion of decarbonized energy storage methods [108].

Here, we propose a physics-based mesoscale model that can be used to predict the long-term effects of cation disorder and phase transformations of nickel rich materials on degradation. The free energy is based on electrostatics in periodic layered crystal structures and does not require any empirical fitting of data. It is derived directly from measured material properties, such as electronegativities of the transition metals. In addition, this model can be applied to any form of layered nickel-rich battery material to study the effects of disordered regions. The thermodynamic model is then coupled to a simple model of the irreversible surface oxidation reaction (with a fitted rate constant and onset potential) and cation diffusion into the bulk, in order to predict the dynamics of degradation in layered oxides.

2.1.2 Background

It is important to note that the phase transformations associated with surface degradation are driven by defects, which can be created in the synthesis of these materials [109, 110] and also increase during battery operation [111]. We take advantage of this to aid our modeling of degradation in nickel-rich cathodes, as well as go through some of the history in physics of using lattice models and dipoles to model structures. Defects trigger phase transformations to denser phases, such as rock salt, spinel, or disordered rock salt structures usually found at the surface of NMC materials [27, 60, 61, 94, 112].

The main defect for nickel rich crystal structures is the antisite defect [96], which can be observed as a kind of Schottky defect in an ionic solid lattice [113, 114, 115]. The description of the "anion" defect in our case is not an ionic defect but a negatively charged electron, while the cation defect is a lithium ion in the analogue to Schottky disorder. The equilibrium concentration of Frenkel/Schottky defects is usually denoted by equilibrium constants using the law of mass action, $K_{eq} = e^{-G/k_B T}$, in terms of the free energy of formation G [115]. However, it is challenging to estimate

formation energies without atomic scale calculations. We instead turn to a method driven by topological defects in physics of studying this kind of disorder.

The theory behind our model was inspired by Kosterlitz and Thouless's groundbreaking work on 2D-topological defects [116, 117]. The defects in this model are described by "twisting" of ordered structures to form "vortices". The idea behind our lattice model, shown in Fig. 1a, is that for NMC defects the antisite defect is the most energetically favorable [96], which makes them the driving force for phase transitions in nickel rich materials. They can also be thought of as "flipping" structures that are normally topologically perfect, but through entropy and electrostatic changes from the configurational "flip" can have modified energies. Since the lattice changes in these materials are quite small between the fully lithiated and empty states [118], we do not account for lattice size changes in this material.

In Kosterlitz-Thouless (KT) transitions, the separation of the interaction energies into entropy, core interactions, and mean field interactions with the bulk is another key to the correct calculations of topological defect theory. This is analogous to ionic Born solvation modeling, but instead of ion-water systems, our current system is a solid state system where electrostatics dominate [119]. The energy required to create a cavity in the solution is analogous to the "core" interaction energy, while the integrated electrostatic interactions with the bulk is analogous to the "bulk" of the electrostatic energies.

The energetic barrier of transitions from a perfect NMC lattice to the disordered phase using statistical models of layered lattices was captured based on the fact that electrostatic interactions dominate in these ionic crystals [120] and the radii of nickel and lithium ions are similar in size. The phases formed in the densified states are still uncertain from experimental measurements, but we know the phase transformations are driven by cation disorder, so the amount of defects formed can be used as an indicator for the amount of surface reconstruction or phase transformations [121]. Highly disordered nickel in the lithium layer [61] indicates the occurrence of spinel or rock salt phase transitions.

In the traditional Butler-Volmer (BV) phenomenological model of intercalation

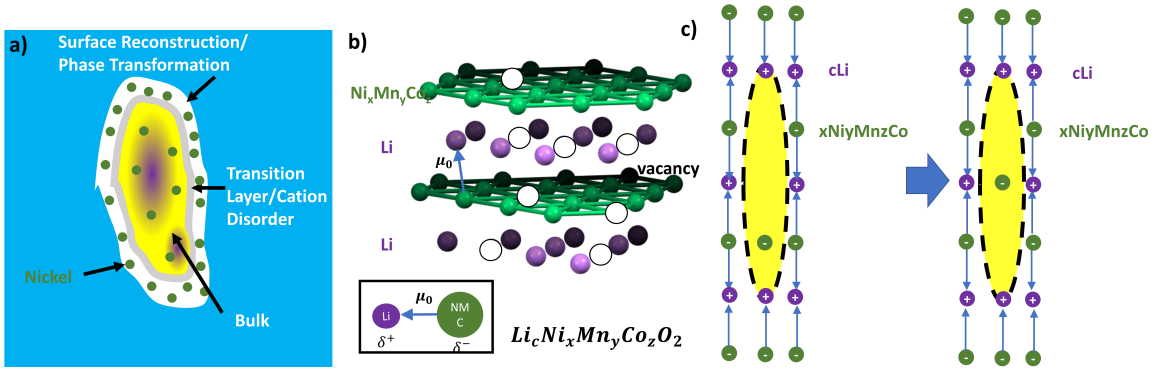

Figure 1: a) Schematic of surface reconstruction and phase transformations in a cathode particle, happening from the edge of the particle to the bulk. b) Microscopic schematic of cation disorder defined by the lithium and electrons at the transition metal sites, where a nickel migrates from a transition metal layer to an empty site in a lithium layer. The dipoles are defined as from the transition metal sites to the lithium sites. c) Schematic representation of disorder in our model from layer to layer. The yellow center are the "core" interactions while everything outside counts as the "bulk" interactions.

kinetics in battery materials, classical ion transfer is assumed to be the dominant reaction mechanism and the electronic degrees of freedom are not considered [53, 122]. In contrast, electron transfer is generally described using Marcus theory [123, 124] for localized (metallic) electron transfer, or Marcus-Hush-Chidsey theory for delocalized electron transfer [125, 126], in case of Faradaic reactions at liquid/solid electrode interfaces. Bai and Bazant first hypothesized that electron transfer to reduce the electrode host could be rate-limiting in Li-ion batteries, compared to the fast step of lithium ion insertion, and showed the MHC theory could predict curved Tafel plots for lithium iron phosphate electrodes [127]. Fraggedakis et al. then derived a general theory of coupled-ion electron transfer (CIET) applied to lithium intercalation reaction kinetics [128] with strong experimental support from nanoscale x-ray imaging of lithium concentration evolution [50] and from pulsed electrochemical measurements for a wide range of Li-ion battery materials [129]. In stark contrast to BV models, the CIET theory connects reaction rates to microscopic material properties and predicts curved Tafel plots with concentration-dependent limiting currents at high overpotentials.

The basic idea behind CIET is that lithium ion transfer into the lattice is accompanied by the formation of a neutral polaron quasi-particle by electron transfer to a weakly coupled reduced state of the solid host, typically involving a reduced transition metal cation. We theorize that ion-electron pairs are also key features of defects in intercalation materials, which may be modeled as dipoles in the dominant electrostatic free energy of the electrode. These dipoles can also be seen as "bound" defects [114], which can be important in intermetallics. The dipolar behavior of electrostatics [130] interacting with the change of charges at the core are shown in this study to qualitatively reproduce the large difference in amount of defects driven at different cutoff voltages [131, 57, 132].

Lattice models, commonly used in physics, can be used to study layered materials, where the energy calculations are further simplified by the layered effect. Such models of nickel-rich cathodes have been used to study the effect of cation disorder on voltage profiles [133, 134]. Nearest-neighbor lattice models have also been used to model the temperature dependent order-disorder transition of different lithium layered oxide materials [135, 97, 136]. However, in these models often only the nearest-neighbor or next nearest-model terms were used to study these effects, neglecting the electrostatic environment and ignoring convergence of the electrostatic interactions. These models were also not expanded to formulate chemical potential models for dynamic free energy models.

Here, we present a general microscopic theory of cation disorder in ionic crystals, specifically applied to nickel-rich oxide degradation. Using dipole-charge interactions assuming a mean field made up of alternating dipole layers from the ion-electron pairs placed at the Li-TM sites as shown in Fig. 1b, we verify the convergence of these electrostatic calculations (shown in Appendix B) and present a rigorous electrostatic mean field model. These dipole interactions have been theorized to play a role in the formation of these disordered materials [137, 138, 139]. Then, accounting for configurational entropy, a free energy model for the material is derived, which can be used to derive chemical potentials for dynamic simulations. This model is derived mainly for disorder and not for intercalation, but a verification of the chemical

potential reveals that the voltage range is on the same order as a battery intercalation material, as shown in Fig 4c, further validating our results.

We formulate this model as a first order approximation to be used as a theoretical model for any layered oxide cathode material disorder that one wishes to study. The model can also be extended to materials such as lithium iron phosphate [46] where analogous iron-antisite defects have found to be important in determining the particle-size-dependent effective diffusivity. The ideas based in electrostatics and statistical thermodynamics come together to formulate a model for studying degradation of lithium oxide materials.

2.2 Theory

2.2.1 Bulk

Chemical Potential

The model is formulated as follows. Based on the alternating locations of the nickel and lithium layers, dipoles of alternating directions are formed between the nickel and lithium layers in the mean field approximation, where "even" and "odd" layers have dipoles in alternating directions, as shown in Fig. 1c. However, in addition to the fact that the bulk dipole layers alternate directions when a nickel atom migrates to a lithium layer, the core part of the interaction is also modified when a defective configuration is formed. We account for this similarly to Kosterlitz and Thouless [116], where these energy calculations are separated into a "core" term and a "bulk" term, where the bulk term is accounted for from the alternating layers and the core term is from the charge interactions near the defective site.

To calculate the difference between energies of the defective and normal configurations $\Delta G = G_1 - G_2 = H - TS$, we find the difference between the two states–a defective configuration where a nickel atom has moved to a lithium site G_2, and a non-defective configuration where the nickel atom is in its original nickel site G_1, based on the crystal structure of $LiNiO_2$ from the Cambridge Structural

Database [140, 141]. The mean field dipoles can be defined at different concentrations of lithium c, defect concentrations of nickel v, and ratios of nickel manganese cobalt $x : y : z$. The variable names used in this paper are redefined in Appendix 2.9 for clarity. The dipoles in the structure are shown in Fig. 1b using electronegativity, defined from the positively charged lithium sites (from the lithium ion placed in the sites) to the negatively charged nickel-manganese-cobalt sites (from the electron localized on the transition metal), with the dipole written as $\boldsymbol{\mu}_0 = e\mathbf{r}_0\left((x-2v)\mathrm{EN}_{Ni} + y\mathrm{EN}_{Mn} + z\mathrm{EN}_{Co} - \mathrm{EN}_{Li}\right)$, where $\mathbf{r}_0$ is the vector distance between transition metal site and lithium site, and EN is the electronegativity of the atom or the "attractiveness" of an atom to electrons [142]. We see that there are alternating rows of dipoles pointing in opposite directions from the formulation of dipoles in this model. Only the dipoles added by intercalation are considered in this crystal structure and not the ions pre-existing in the non-intercalated structure, since when an energy difference is calculated between the original and defective state, the intercalation host crystal interactions cancel out. To avoid the fact that many electronegativity scales are based on formation energies, the Allred-Rochow scale was chosen. This scale is more simplistic than other electronegativity scales and generally uses the ideas of electrostatics based on effective nuclear charge, consistent with our theory [143].

In the lithium layers and transition metal layers, there are automatic constraints on the concentrations of lithium and defective nickel in the lithium layers, or nickel and vacancies in the transition metal layers. The definition of the material ratio gives us that $x + y + z = 1$, and from the site constraint of lithium atoms, we know that $c + v \leq 1$. By the mass constraint of nickel atoms, $v \leq x$ must always be true. These constraints are automatically satisfied by how the entropy equation was defined.

We consider the perfect configuration G_1 before a defect is formed in the core as well as a defective configuration G_2. Assuming that the neutral lattice contains a lithium-electron pair for notation purposes, the reaction that occurs can be written in Kroger-Vink notation as $\mathrm{V}'_{\mathrm{Li}} + \mathrm{Ni}^{\mathrm{x}}_{\mathrm{Ni}} \rightarrow \mathrm{Ni}^{\cdot}_{\mathrm{Li}} + \mathrm{V}''_{\mathrm{Ni}}$. For comparison, the lithium intercalation reaction written in Kroger-Vink notation is $\mathrm{e}' + \mathrm{V}'_{\mathrm{Li}} + \mathrm{Li}^{\cdot} + \mathrm{Ni}^{\mathrm{x}}_{\mathrm{Ni}} \rightarrow$

$Li^x_{Li} + Ni^x_{Ni}$. Since the oxygen lattice around lithium and nickel ions are identical and the radii of lithium and nickel are very similar, by symmetry the oxygen atoms can be neglected in the modeling of the crystal structure and only the lithium and nickel layers are considered. The crystal structure used was taken from the the Materials Project structure mp-632864 for $LiNiO_2$ [144, 145, 146, 147, 148].

In this structure, dipoles are formed from the intercalated lithium ion, which is positively charged, interacting with the localized electron on the transition metal ion. Thus, we have alternating layers of dipoles that form the bulk of the electrostatic free energies of the crystal structure. When an antisite defect is formed, one of the dipoles is broken and forms a broken "core," which is also called the defect core for future reference. When studying the energetic interactions of antisite defect formation, we can separate the interactions into the broken "core" term as well as the electrostatic bulk interaction terms, shown in Fig. 1c where the circled yellow site is the broken core and the outside is the mean field term.

We first start by studying the bulk interaction term, also known as the mean field (MF) term. It simplifies the problem to consider splitting the dipole layers between the ones pointing "up" and the ones pointing "down" by the symmetry between these layers. In the following notation, "even" indicates the layer that a core electron would belong to if it was moved half a layer up and the alternating layers pointed downward in the diagram, while "odd" indicates a layer that the core electron would belong to if it was moved half a layer down and the alternating layers pointed upward in the diagram. The definition of the dipole is thus always positive in "odd" layers and negative in "even" layers in the original configuration, while it is always negative in "odd" layers and positive in "even" layers in the defective configuration as shown in Fig. 1c [149]. The electrostatic interactions in the layers are thus opposite to each other. By the definition of charge-dipole interactions, the even and odd interactions

will be

$$
\begin{aligned}
H_{MF,even} &= -\frac{1}{2}\frac{cqe}{4\pi\varepsilon}\sum_{i\in even}\sum_{j\in i}\frac{-\boldsymbol{\mu}_0\cdot\boldsymbol{r}_{ij}}{r_{ij}^3} \\
H_{MF,odd} &= -\frac{1}{2}\frac{cqe}{4\pi\varepsilon}\sum_{i\in odd}\sum_{j\in i}\frac{\boldsymbol{\mu}_0\cdot\boldsymbol{r}_{ij}}{r_{ij}^3},
\end{aligned}
\tag{1}
$$

where the factor of $\frac{1}{2}$ accounts for the fact that the charges are split over a dipole in the layer above and the layer below, and the $-cqe$ prefactor accounts for the amount of dipoles at each site in a mean field description, since only the intercalated lithium sites c can have lithium-electron dipoles [150, 130, 151, 152]. Here, e is a unit charge and q is the magnitude of the charge. We sum over the layers in the crystal structure indexed by i, which are separated into even and odd layers, and then sum over the sites in the ith layer indexed by j. Since the dipole vector, $\boldsymbol{\mu}_0$, is defined as pointing from the transition metal layer to the lithium layer, assuming the centered atom is the red lithium site, the even layers are shown in the image are the orange dipole layers, while the odd layers are the blue dipole layers. Here, the distance $\boldsymbol{r}_{ij}$ is the distance between the center of the dipole $\boldsymbol{\mu}_0$ and the defect center, and the scalar r_{ij} is the magnitude of that vector.

Because ions in this problem are assumed to only move as a result of defects or intercalation and the induced dipoles from electronic movement are ignored, the dielectric constant applied is the static dielectric constant of this material. These approximations cause our simple theoretical model to neglect induced many-body interactions that are not captured by a mean-field model, but it is a good first approximation. The full mean-field theory is then written as

$$
\begin{aligned}
H_{1,MF} &= \left(H_{MV_{even}} + H_{MV_{odd}}\right) \\
H_{2,MF} &= -\left(H_{MV_{even}} + H_{MV_{odd}}\right),
\end{aligned}
\tag{2}
$$

split over the even and odd layers.

The broken "core" of the structure is studied next. It is known that the defective nickel is more likely to be in the reduced (+3) oxidation state. Since at the core, there

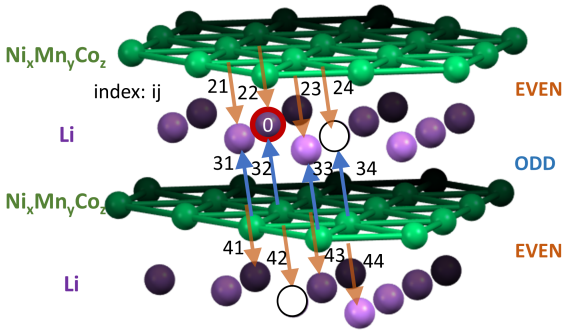

Figure 2: Detailed schematic of charge-dipole model, where in $\boldsymbol{\mu}_{ij}$, i is the layer index, which can be either "even" or "odd", and j is the atom number in the layer. "0" is the central site where the antisite defect occurs.

is only one negatively charged transition metal interacting with the mean field, this greatly simplifies our energy calculation to be interactions with the two lithium ions within the vicinity of the layer, shown in Fig. 1c. We use charge-charge interactions to model the core interactions. In the core, only half of the ions on the edges are considered (the other half is used to generate the dipoles in the mean field terms). Thus, at each end of the core, we have a nickel-lithium interaction from the nickel to the edge. The electrostatic core interactions in the two configurations are found to be

$$\begin{aligned} H_{1,core} &= -\frac{(1-v)}{2}\left(\frac{c(qe)^2}{4\pi\varepsilon r_0}+\frac{c(qe)^2}{4\pi\varepsilon(3r_0)}\right) \\ H_{2,core} &= -\frac{(1-v)}{2}\left(\frac{c(qe)^2}{4\pi\varepsilon(2r_0)}+\frac{c(qe)^2}{4\pi\varepsilon(2r_0)}\right). \end{aligned} \tag{3}$$

This gives us

$$\begin{aligned} H_{MF} &= H_{2,MF} - H_{1,MF} \\ H_{core} &= H_{2,core} - H_{1,core} \end{aligned} \tag{4}$$

as the final enthalpic interaction energy difference between the defective and bulk configurations.

By using the definition of dipole charge-interactions [130], the final mean field

energy difference between the two configurations is found to be

$$H_{MF} = -\frac{cqe}{4\pi\varepsilon}\left(\sum_{i\in\text{even}}\sum_{j\in i}\frac{\boldsymbol{\mu}_0\cdot\mathbf{r}_{ij}}{|r_{ij}|^3} - \sum_{i\in\text{odd}}\sum_{j\in i}\frac{\boldsymbol{\mu}_0\cdot\mathbf{r}_{ij}}{|r_{ij}|^3}\right), \tag{5}$$

is the vector between the center of dipole ij and the defect center and $\boldsymbol{\mu}_0$ is the dipole between lithium sites to transition metal sites defined in the previous solution, where $r_{ij} = |\mathbf{r}_{ij}|$.The defect core interaction difference is found to be

$$H_{core} = \frac{(qe)^2(1-v)c}{12\pi\varepsilon r_0}, \tag{6}$$

The final electrostatic energy is found to be

$$H = H_{MF} + H_{core}, \tag{7}$$

shown in Figs. 3b and 3e. The electrostatic energies in these materials were found to be lower at a state with more defects, indicating that a highly defective state is energetically favorable. This is expected as the formation of such a state reduces the magnitude of electrostatic interactions between layers.

In this electrostatics problem, the dielectric constant ε is estimated using the Clausius-Mosotti relation for a spherical inclusion in a homogeneous effective medium. Since the dielectric response of the material is based on the interactions induced by other atoms and the energies converge quickly in these structures (shown in Appendix B), in the core and near field interactions, a simple dielectric constant can be used in this model. The movement of the ionic lattice is considered in this problem, so the low frequency (static) dielectric constant needs to be applied. The dielectric constant can be found to change with the amount of intercalation or defects locally. When the crystal structure is nearly perfect, the dielectric constant for layered lithium oxide materials has been found to linearly decrease with the increase of defect concentration, specifically for lithium niobium oxide [153, 154, 155].

We seek an approximation rule to calculate the average dielectric constant of materials at different concentrations and to reproduce the behavior seen for lithium

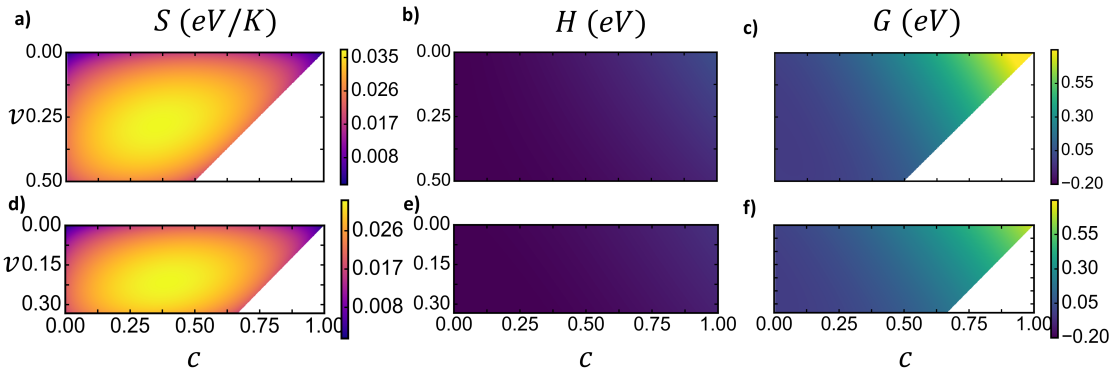

Figure 3: a), b), and c) are the entropy, enthalpy, and Gibbs free energy calculations for NMC532, while d), e), and f) are the entropy, enthalpy and Gibbs free energy calculations for NMC111. Because of the total site constraint in the lithium layer in the crystal structure, when the concentration in the lithium layer is above a certain level, there are not enough sites for nickel to have a high concentration of defects in the system, so there are white triangular regions of no solution for the entropy calculations. This also causes there to be regions of no solutions for the free energy calculations.

metal oxide materials. The dielectric constant of metal oxides is estimated following the additive rule in "well-behaved" metal oxides, based on Clausius-Mosotti dielectric theory [156, 157], which has been found to work extremely well for many kinds of oxide materials [158, 159]. The additive rule has been found to be a good predictor of the dielectric constant of oxide materials even before measurement, with the dielectric constant ε obtained from

$$\frac{\varepsilon - 1}{\varepsilon + 2} = \frac{4}{3}\pi \sum_i \alpha_i n_i, \tag{8}$$

where α_i is the polarizability of the atom i and n_i is the number density of atom i. For our material, we consider atom types Li, Ni, Mn, Co, and O. The dielectric constant decreases with respect to lithium concentration and defect concentration, as shown in Appendix C. This dielectric constant calculation is only valid for bulk dielectric constants since we do not consider image charge effects from the bulk/electrolyte interface.

The second part of the energy from the configurational entropy of the model can be split into two parts. First, in the lithium layers, the sites are either filled with

lithium, defective nickel, or empty, which can be written as

$$\Omega_{Li} = \frac{N!}{(Nc)!(Nv)!(N(1-c-v))!}, \tag{9}$$

where N is the total number of lithium sites considered. In addition, the nickel layers are either filled with nickel or empty, with the following number of combinations

$$\Omega_{Ni} = \frac{(Nx)!}{(Nv)!(N(x-v))!}. \tag{10}$$

The total configurational entropy change is described as

$$\begin{aligned} S =& k_B \ln\left(\Omega_{Li} * \Omega_{Ni}\right) \\ \approx& k_B N \left(x \ln x - c \ln c - (1-c-v)\ln(1-c-v)\right. \\ & \left. -2v \ln v - (x-v)\ln(x-v)\right), \end{aligned} \tag{11}$$

which is plotted in Figs. 3a and 3d for NMC532 and NMC111 separately. The configurational free energy prefers moderate values for v and c because of the higher number of possible states at at these concentrations. More importantly, the entropy of the configuration limits the accessible states at higher lithium concentrations, because it is physically impossibly for high concentrations of defects to be reached at high lithium concentration from lack of available sites, creating the inaccessible triangular regions in Fig. 3a and d.

The final free energy can be described as $G = H - TS$ from Eqs. 7 and 11, plotted in Figs. 3d and 3f. More information on these calculations can be seen in Appendix 2.8. This free energy is dominated by the electrostatics, but there is a strict cutoff from the possible available sites in the entropic component. The diffusional chemical potentials, which describe the dynamic behavior of the model, can be defined from the free energy. The diffusional chemical potentials are defined as $\mu_c = \frac{\delta G}{\delta c}$ for intercalation and $\mu_v = \frac{\delta G}{\delta v}$ for defects, shown in Fig. 4, and the analytical solutions for the chemical potentials can be found in Appendix A. From Figs. 4b and 4d, at lower concentration, there is a larger driving force towards a

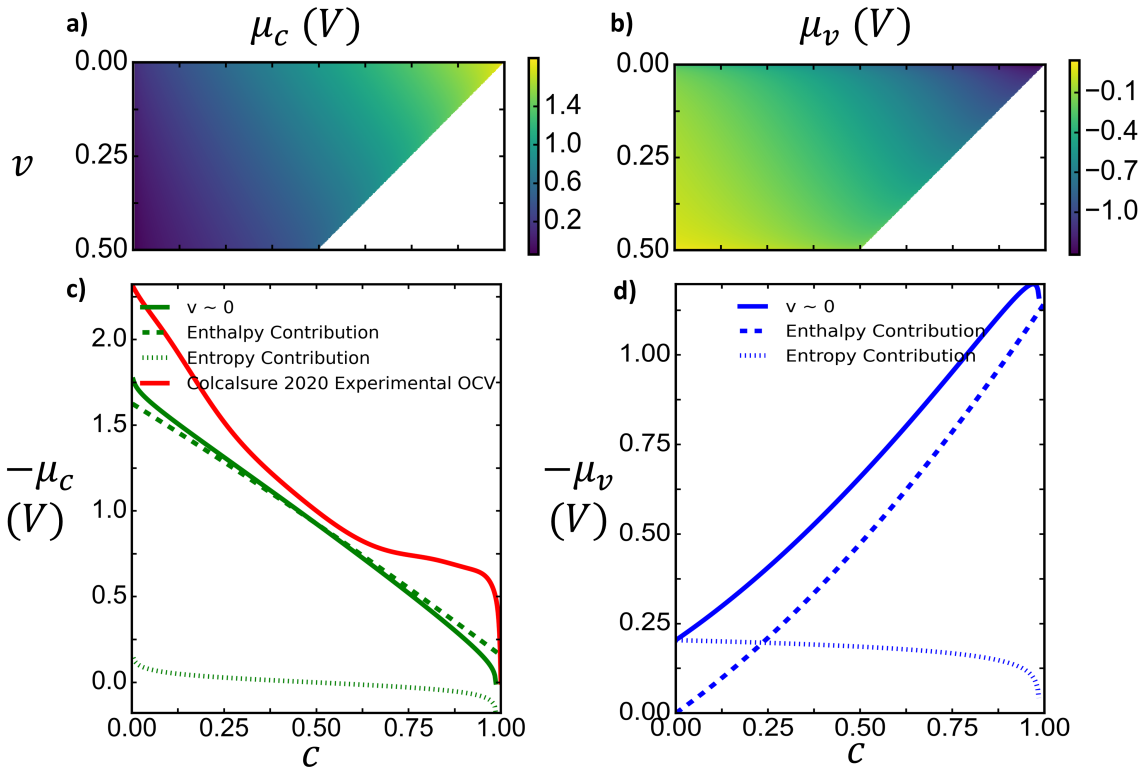

Figure 4: a) Intercalation chemical potential for a NMC532 material. b) Defect chemical potential for a NMC532 material. c) Intercalation chemical potential when defect amount is close to zero and the contributions from enthalpy and entropy. We also plot an open circuit voltage from experimental measurements [5] for comparison. d) Defect chemical potential when the defect concentration is close to 0 and the contributions from entropy and enthalpy. (Potentials are shifted in c) and d) by an arbitrary reference potential for ease of readability.)

more defective state, qualitatively matching experimental measurements where the high voltage/low concentration regions cause more cation disorder. Since the chemical potential is defined with an arbitrary reference value, for ease of comparison between the intercalation and the defect chemical potential we choose to shift the reference potentials to overlap. The chemical potential contribution from entropy is derived analytically in the appendix, while the contribution from enthalpic terms is calculated numerically in Appendix A, and the contributions are plotted in Figs. 4c and 4d. For both intercalation and defect formation, the enthalpic chemical potential dominates the trend in these materials.

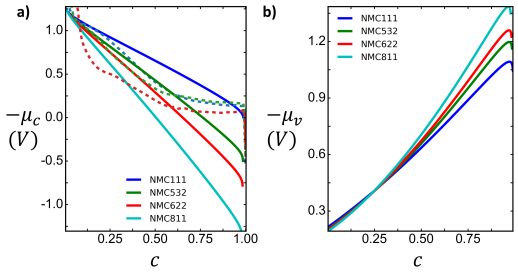

Figure 5: Nickel ratio effect on the a) intercalation and b) defect formation chemical potentials of the material. The solid lines are for the calculated values, while the dotted lines are from experimentally measured values from Ref. [6].

The advantage of these simplistic models is that they can be applied to nickel rich materials of any composition and provide a rough estimate of the energy of any of these new compositions of materials in Fig. 5. In the previous discussion, Figs. 3c and 3f provide an example of different ratios of nickel in the crystal structures for NMC532 and NMC111. Experimentally, higher nickel ratio materials were revealed to have larger voltage ranges [6] and degrade more quickly than lower nickel ratio materials [84], which is also shown in our theoretical predictions for chemical potential of these materials in Fig. 5. Our model follows the general trend of increasing nickel content causing a larger slope in the chemical potential for intercalation. The different electronegativity of the transition metal materials, which modifies the dipole magnitude, causes this change in slope. In addition, the nickel concentration plays an important role in the entropy cutoff by controlling the maximum amount of nickel in the material that can form defects. Though the enthalpic interactions dominate, the entropic interactions also become important in restricting the strict limits of amount of defects. At lower concentrations, the driving force towards defect formation is higher for larger nickel content materials, which has been observed experimentally as well [6]. We note that though the model for "intercalation" description was not as complex, we still capture the effect of the transition-metal concentration on the intercalation chemical potential of the material. The slope changes near delithiated and fully lithiated for lithium intercalation are expected to come from different ionization potentials of the lattice since the lithium-rich or poor regions exist in a highly charged state [160].

Dynamic Model

Using the free energy models formulated above, chemical potentials, which are the driving forces for dynamic models, can be derived for the material. We model the most simplistic version of a battery model–a single particle model. The dynamic model at the surface is described using a single particle reaction-diffusion model with a driving force from the diffusional chemical potential gradient. Both the lithium concentration c in the lithium layer and the defect concentration v in the lithium layer are modeled through nonequilibrium thermodynamic driving forces, the gradients of chemical potential [161, 162]. The boundary conditions applied for both models are applied through the intercalation reaction for lithium concentration and the oxygen degradation reaction at the surface, described in the following section.

A simple single particle model [48] was used in this system to model the cycling behavior, based on more complicated porous electrode models [122]. For intercalation, the simple form of mass conservation with a diffusive driving force can be described as

$$\frac{\partial c}{\partial t} = -\nabla \cdot \mathbf{F}_c, \ \mathbf{F}_c = -\frac{D_c c}{k_B T} \nabla \mu_c, \tag{12}$$

where $D_c \propto (1 - v)$ because of the effect of "blocked" sites on the diffusivity of the material [46, 163]. In addition, because of the change of the maximum number of required sites, during cycling, the chemical potential parameter actually varies with $\mu_c(c/(1 - v))$ to rescale to the proper number of total sites. The dynamic equation for conservation of defects is described as

$$\frac{\partial v}{\partial t} = -\nabla \cdot \mathbf{F}_v, \ \mathbf{F}_v = -\frac{D_v v}{k_B T} \nabla \mu_v, \tag{13}$$

if we assume a constant diffusivity coefficient for both models for the flux $\mathbf{F_{c/v}}$ in the bulk. For simplicity, we assume that the diffusion coefficients are constant. The boundary equations applied for the particle are

$$-\mathbf{n} \cdot \mathbf{F}_v = i_{int} \tag{14}$$

for surface reaction of intercalation i_{int}. [164, 69] For the defect concentration, a simple degradation mechanism explained in 2.2.2 is prescribed, which gives the boundary condition of

$$-\mathbf{n} \cdot \mathbf{F}_c = 2i_{oxy}. \tag{15}$$

2.2.2 Surface

Intercalation

Since blocked sites from defects play a central role in our theory, it is imperative to use an accurate reaction model that captures configurational entropy and polaron formation energies. For this purpose, the recent theory of coupled ion-electron transfer (CIET) for ion intercalation [128] is adopted as the boundary condition, where the concept of ion-electron polaron pairs complements the idea of dipole pairs to describe the electrostatic interactions among disordered cations. In CIET theory, the blocked sites play a much more dominant role than in classical Butler-Volmer models, because theory predicts a reaction-limited current i_{lim} which has a strong asymmetry dependence on all of the species concentrations: $i_{lim} = c_+(1-c-v)i_r^*$ for negative overpotentials and $i_{lim} = c(1-c-v)i_r^*$ for positive overpotentials [129].

These limits arise from the general form of the intercalation rate given by

$$i_{int} = i_r^* \int_{-\infty}^{\infty} (1-c-v)\left(c_+ n_e p_{red}(\varepsilon) - c(1-n_e)p_{ox}(\varepsilon)\right)\rho d\varepsilon, \tag{16}$$

where the conditional probability that an electron of energy ε relative to the Fermi level participates in reduction or oxidation is given by

$$p_{red/ox}(\varepsilon) = \frac{1}{\sqrt{4\pi\lambda/k_BT}} \exp\left(-\frac{(\lambda \pm \eta_f \mp \varepsilon)^2}{4\lambda k_BT}\right). \tag{17}$$

Here, c is the dimensionless lithium ion concentration (filling fraction) in the host crystal; v is the dimensionless defect concentration, or the nickel filling fraction in the lithium layers; c_+ is the lithium ion concentration at the reacting surface, related to the nearby electrolyte concentration by an adsorption isotherm, assuming fast surface

adsorption compared to CIET intercalation; $n_e(\varepsilon)$ is the Fermi-Dirac distribution, and η_f is the formal overpotential defined as $e\eta_f = e\eta + k_B T \ln \frac{c_+}{c}$ [129]. As the overpotential is $e\eta = \mu_R - (\mu_O + n\mu_e)$ [69] where n is the number of electrons, we see that the overpotential $e\eta = \mu_c - k_B T \ln c_+ + e\Delta\phi$, is related to the difference between the intercalation chemical potential μ_c and the potential difference $\Delta\phi = (\phi_e - \phi)$ between the solid ϕ_e and the electrolyte ϕ. The parameters in the model are λ, the Marcus reorganization energy for electron transfer; i_r^*, the prefactor for current related to electronic coupling and the ion-transfer energy; $\rho(\varepsilon)$, the energetic density of states (band structure).

Our reaction rate differs from the typical CIET model for lithium intercalation since the empty sites must also be reduced by the number of blocked sites in the material from defects, contributing to the factor by v. Under the assumption that the electron donor is metallic, we can assume a uniform density of state [165, 126] which allows us to use the simple and accurate approximation of the MHC formula by Zeng et al. [166] to derive a closed formula for the CIET reaction rate for lithium insertion:

$$i_{int} = i_r^*(1 - c - v)\left(\frac{c_+}{1 + \exp\left(\frac{\eta_f}{k_B T}\right)} - \frac{c}{1 + \exp\left(\frac{-\eta_f}{k_B T}\right)}\right) \operatorname{erfc}\left(\frac{\lambda - \sqrt{1 + \sqrt{\lambda} + \eta_f^2}}{2\sqrt{\lambda k_B T}}\right), \tag{18}$$

which reduces to the form given by Zhang et al. [129] in the limit of a defect-free host crystal, $v = 0$.

Defects

In the bulk, phase transformations and cation disorder are triggered by the oxidation of reactive oxygen ions at the solid surface, typically an edge plane of the layered oxide crystal. [167, 168]. At high voltages, degradation at the surface is much more pronounced, especially those triggered by oxygen vacancy formation and oxygen changes at the surface [36, 169, 170]; experimentally, oxygen vacancy formation at

high voltages has also been observed [171]. Since the dielectric "bulk" of the medium consists of oxygen ions, and the lithium and nickel ions only interact at close range for quick convergence of the free energies, we assume that the bulk dielectric constant is affected by the local oxygen, defect, and lithium concentrations, where the oxygen vacancies are assumed to not propagate into the bulk, as shown in Fig. 6a [61]. It is generally considered that oxygen evolution only happens at the surface of nickel rich electrodes because of the large migration barrier of the oxygen in the bulk [172, 173]. Recent experiments, however, have suggested that oxygen vacancies can propagate into the bulk [29, 167]. After the first couple cycles, bulk induced oxygen vacancy degradation can start influencing the degradation of overlithiated oxides [167, 29]. For simplicity, we can assume that oxygen vacancies propagate slowly into the bulk and account for them at the surface only. As such, we will have an oxygen boundary condition only occurring at the surface.

The loss of available oxygen at the interface can be explained by several possible mechanisms, sketched in Fig. 6a. In the simplest possible mechanism, oxygen ions are oxidized at the surface according to the half reaction, $O^{2-} \rightarrow 0.5O_2 + 2e^-$, and there is a loss of oxygen ions at the surface in the lattice [167] that can be released as gases [6], which has been experimentally observed. Another possible mechanism involves oxidation and dehydrogenation of the organic electrolyte solvent, which has been observed experimentally [7, 174]. We propose that this reaction could release electrons to the crystal that trigger cation disorder while creating a reactive hydroyxl group on the surface, again involving the reactive oxygen ion at the edge plane. The reaction can be modeled as EMC/EC $\rightarrow$ DeH EMC/EC$^+$ + H$^+$ + 2e$^-$, where the proton and dehydrogenated electrolyte product can bond with the oxygen at the surface. The products have been experimentally observed through FT-IR experiments for EMC and EC.

Experimentally, we know that the amount of oxygen degradation significantly affects the amount of cation disorder [175, 176]. For the oxygen release mechanism, we postulate that when oxygen is oxidized in a material, the loss of two oxygens in a bulk requires the solid to accept electrons to conserve charge neutrality, which occurs

through oxidation of transition metals. One electron is required for the electrochemical reaction, and one is required for the oxidation of the nickel ion to +3 state. The full reaction can be written in Kroger-Vink notation as $2\mathrm{Ni}^{\cdot}_{\mathrm{Ni}} + \mathrm{O}^{\mathrm{x}}_{\mathrm{O}} \rightarrow 2\mathrm{Ni}^{\mathrm{x}}_{\mathrm{Ni}} + \mathrm{V}^{\cdot\cdot}_{\mathrm{O}} + 0.5\mathrm{O}_2$. Thus, the amount of oxygen degradation increases the concentration of the reduced nickel (+3) in the material, which heightens the possibility of cation disorder. For the dehydrogenation mechanism, we propose that dehyrogenation releases two electrons, one which is required at the electrode and the other which oxidizes the nickel ion. Thus, the amount of reduced nickel in the material also decreases, causing a similar effect as the gas release mechanism to the cation disorder in the system.

For the simplest model, we assume the dependence of the reactant, the reduced nickel, in the defect formation reaction is linear. We know that i_v is proportional to the amount of oxygen loss, which is i_{oxy}. Thus we apply $i_v = i_{oxy}$ to the defect formation conservation equation boundary equation to obtain $-\mathbf{n} \cdot \mathbf{F}_c = i_v = i_{oxy}$. This simple boundary condition which includes the electrochemical surface reaction components of our degradation can be applied to the model, while keeping the focus on the bulk defects triggering phase transformations. The formation voltage for this reaction is roughly $E^\theta = 4.4\,\mathrm{V}$, which also depends on the ratios of transition metals as well as the electrolyte used [120, 175]. Therefore, the overpotential driving this reaction is $e\eta = E^\theta + e\Delta\phi$.

Based on the observation that oxygen formation reaction is irreversible, a simple Tafel reaction model was used for the oxidation current

$$i_{oxy} = k_{0,oxy} c_{oxy} \exp\left(\frac{\eta}{k_B T}\right), \tag{19}$$

with a reaction parameter of exchange current density $k_{0,oxy}$, shown in Fig. 6b, assuming that the increase of oxidation products (e.g. oxygen gas) is usually released to the environment [164]. c_{oxy} is the concentration of oxygen ions at the solid surface, which can be modeled by the conservation equation in Appdx. 2.8. The magnitude of reaction drops off as $\eta \leq 0$, and increases as $\eta > 0$, and the amount of reaction decreases linearly as the amount of oxygen vacancies increase.

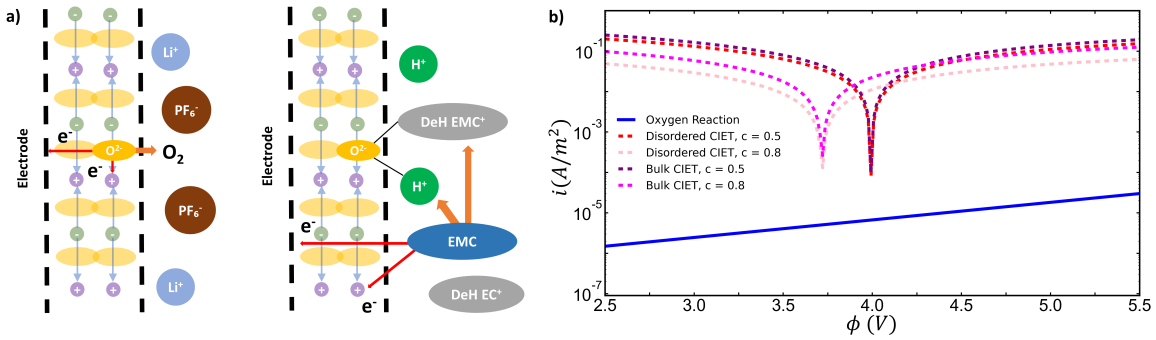

Figure 6: a) Schematic of oxygen reaction and change of dielectric constant at the surface of the particle, where the yellow circles are oxygen ions. Nickel is driven into the bulk crystal, and the oxygen reaction at the electrolyte interface forms oxygen vacant sites, free electrons, and releases oxygen gas or other oxidation products to the electrolyte. The mechanisms of oxygen release and dehydrogenation of EMC/EC are both proposed in this model [6, 7]. b) Evans diagram of the oxygen reaction model used and behavior relative to voltage applied. The coupled-ion electron transfer intercalation reactions are plotted as well at bulk ($v = 0$) and defective ($v = 0.1$) phases with different lithium concentrations. It can be seen that defective phases reduce the magnitude of the intercalation reaction through blockage of available sites.

2.3 Simulations

2.3.1 Cycling

Using a model of NMC532 for the defective system and a open circuit voltage profile of NMC532 from Colclasure et al. [5], we perform reaction-diffusion simulations with a single particle model as described in Section 2.2.1 to study the surface degradation of nickel-rich electrodes and are able to qualitatively reproduce the high voltage growth of the cation disordered phase at the surface using a single particle model to simulate cycling in an electrochemical cell. A single particle model is able to capture the electrochemical behavior without the complexity of electrolyte diffusion limitation or cell size limitations. In these simulations, we do not aim for a perfect fit of the model, but attempt to show that qualitatively correct behavior can be achieved using these ideas. Using a cutoff voltage of 4.4 V vs. Li/Li^+ for oxygen formation, we can reproduce the behavior observed at surfaces for nickel rich electrodes [36, 27] based on the fact that the overpotential at high voltages will be positive in some regions,

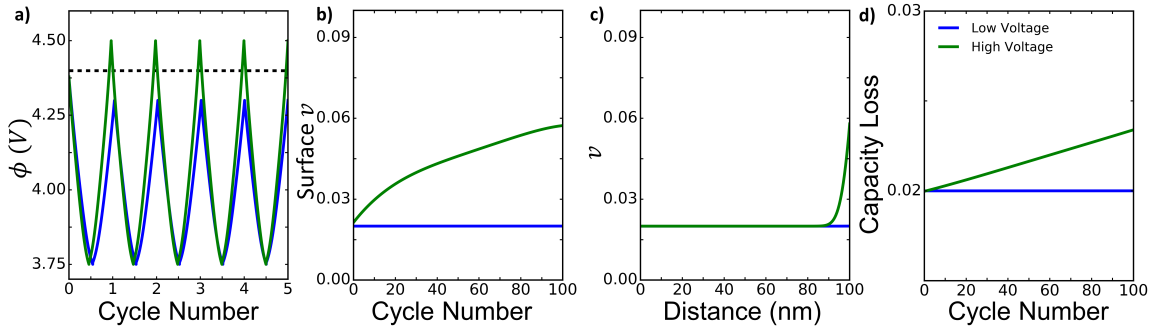

Figure 7: a) Voltage plots for the first five cycles between low and high voltage simulations for NMC532. Higher voltage cycling tends to exceed the potential for oxygen formation. b) Defect growth in the first 100 cycles at the surface of the particle. c) Defect growth at the end of the first 100 cycles throughout the length of the particle, where $R = 0$ is the center of the particle and $R = 100\,\text{nm}$ is the edge of the particle. d) Capacity loss during cycling with voltage limits of either 4.3 V or 4.5 V.

increasing the oxygen formation reaction amount as in Fig. 7a. The experimental results that were used for comparison were selected based on criteria described in Appendix 2.10.

For this set of simulations, the exchange current density for intercalation and reorganization energy are taken to be roughly $i_r^* = 8\,\text{A/m}^2$ for NMC532 and $\lambda = 3.78k_BT$ for NMC111 since data for NMC532 was not freely available [129]. In our simulations, roughly 20 nm of the cation disorder growth in the high voltage model was achieved using an oxygen reaction parameter of $k_{0,oxy} = 5 \times 10^{-6}\text{A/m}^2$. The diffusion coefficient for intercalation was assumed to be $D_c = 1 \times 10^{-12}(1 - v)\text{m}^2/\text{s}$ [177, 178] by the scale of diffusion measured experimentally, while for defects it was assumed to be $D_v = 5 \times 10^{-24}\text{m}^2/\text{s}$. A single spherical particle of radius $R = 100\,\text{nm}$ was used to model a NMC battery nanoparticle with a discretization of 200 finite difference volumes, where details are seen in Appendix 2.8. This particle defect concentration initialized at a homogeneously distributed distribution of the optimal defect concentration of 2% in the particle [179], so the initial concentration $v(t = 0) = 0.02$. The initial concentration of lithium in NMC532 $c(t = 0)$ was set to 0.4.

Single particles of NMC532 such that $x = 0.5$ are cycled at 1 C for 100 cycles, with a set of low voltage simulations with higher voltage cutoffs up to 4.3 V and a set

of high voltage simulations up to 4.5 V, modeling the experimental behavior in Yan et al. [60]. The lower voltage cutoff was permanently set to 3.75 V. More information on the numerical simulations can be seen in Appendix 2.8. The amount of cation disorder growth post cycling and the overpotentials in the simulations are shown in Figs. 7b and 7c. In these ranges, based on the asymmetry of the Butler-Volmer reaction, there is more oxygen formation at the surface of the particle, causing cation disorder to initiate at the surface and diffuse inward. At high voltages, the amount of cation disorder nears the amount measured in experiments to be roughly 20 nm, close to the experimental measurement of 25 nm of disorder [60]. The surface phase appears when the amount of defects is high and grows inward towards the center of the particle as the amount increases. Meanwhile, there is almost no growth for the low voltage phase, similarly to the experimental measurement of 2 nm of cation disorder [60]. From our simulated results, we see that there is a larger amount of capacity fade happening after 100 cycles at higher voltages than at lower, with most of it happening at the surface of the particle at higher voltages. We see our model is able to reproduce the experimental data observed qualitatively.

2.3.2 Voltage Hold

In addition to cycling results from a constant current perspective, the cutoff voltage with respect to the system is also an important parameter. Voltage hold tests are also often performed to understand the degradation of batteries [180, 170] at higher voltage. Three constant current cycles at C/20 were performed and constant voltage holds of 10 h were performed for the NMC532 single particle model described above in Fig. 8. The effect of the oxygen reaction potential, which is applied at 4.4 V in our system, was found to be quite significant. Large amounts of capacity growth are found at voltage holds past the oxygen reaction potential, while minimal amounts are found at lower voltages. The amount of time spent at higher potentials is critical to controlling the amount of degradation in the particle, which is also observed experimentally [6].

From the simulated data for constant current cycling and voltage holds at high

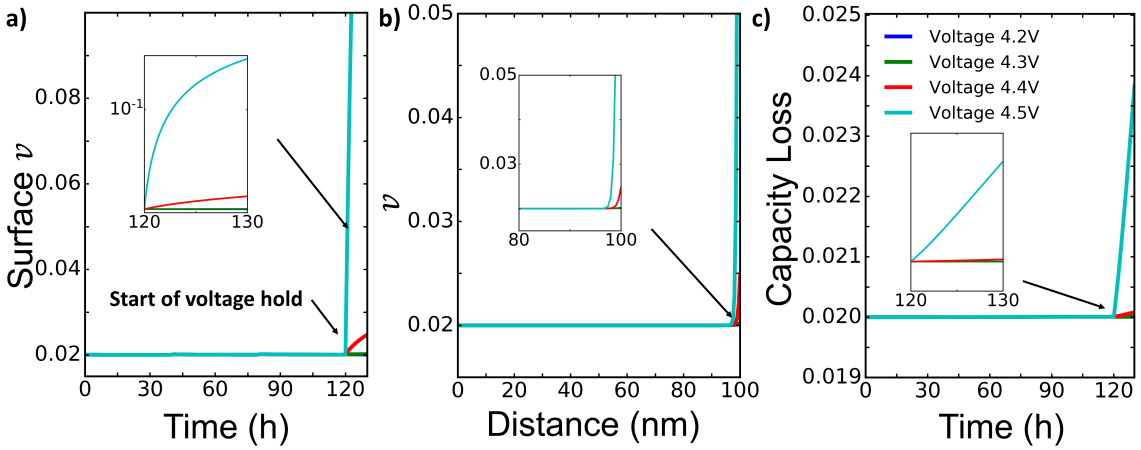

Figure 8: Three C/20 cycles are performed before a 10 h voltage hold is applied to particles at voltage of 4.2 V, 4.3 V, and 4.4 V for NMC532. a) The surface defect amount v is plotted as a function of the fraction of the total simulation time. The voltage hold occurs around 60 h in the simulation. b) The variation of the capacity loss within a battery, where the distance is from the center of the particle to the edge, is plotted. c) The total capacity loss in the battery is plotted as a function of the fraction of total simulation time.

potentials shown, we see that high voltage cycling in nickel rich electrodes causes irreversible effects on the degradation of the particle. The degradation behavior shows that the operation time at lower voltages contributes negligibly to degradation of the electrode. Thus, for cases where preventing degradation is extremely important, avoiding the higher voltage range is crucial. If higher voltage operation is necessary, higher voltage operation should be applied later in the operation of the battery, to push back the onset of irreversible degradation. Experimental data from voltage hold simulations can be used to "invert" kinetic parameters for the degradation models described in these papers to infer more accurate exchange current densities for degradation reactions as shown in Appendix 2.7. Data provided at different cutoff voltages provides very impactful information on the voltage cutoffs for when degradation occurs [29].

The application of different coatings or additives may help reduce the amount of oxygen reaction in the particle, helping control the amount of degradation [181]. Commercialized batteries, especially for nickel rich materials, have different types

of additives and coatings, such as aluminium oxides [182], carbon coatings [183], and others [184]. These can change the surface kinetics and dielectric properties of materials. Coating materials reduce the amount of degradation by reacting with the surface layers to form a more stable interface, changing the kinetic properties of degradation. Using such related models to understand how coatings change the kinetic properties of degradation, or the redox potential at the interface, may prove extremely useful in future material design.

2.4 Appendix: Diffusional Chemical Potentials

Simple formulae for the entropic contributions to the diffusional chemical potentials for intercalation and defects, respectively, are given by

$$-T\frac{\partial S}{\partial c} = k_B T \ln \frac{c}{1-c-v} \tag{20}$$

$$-T\frac{\partial S}{\partial v} = k_B T \left(\ln \frac{v}{x-v} + \ln \frac{v}{1-c-v} \right) \tag{21}$$

based on our ideal solid solution models for lithium ion intercalation between the nickel oxide layers and for vacancy-mediated defects within the layer. Expressions for the enthalpic contributions from dipole-dipole interactions, core energy, and dielectric decrement are more complicated and must be calculated numerically. Combining the enthalpic and entropic contributions, we obtain the total diffusional chemical potentials for lithium intercalation and vacancy-mediated defects, respectively:

$$\mu_c = \frac{\partial H}{\partial c} \tag{22}$$

$$= -\frac{qe}{4\pi\varepsilon}\left(\sum_{i\in\text{even}}\sum_{j\in i}\frac{\boldsymbol{\mu}_{ij}\cdot\mathbf{r}_{ij,0}}{|r_{ij,0}|^3} - \sum_{i\in\text{odd}}\sum_{j\in i}\frac{\boldsymbol{\mu}_{ij}\cdot\mathbf{r}_{ij,0}}{|r_{ij,0}|^3}\right) + \frac{(qe)^2(1-v)}{12\pi\varepsilon r_0} - \frac{\Delta H(c,v)}{\varepsilon}\frac{\partial\varepsilon}{\partial c}$$

$$+k_BT\ln\frac{c}{1-c-v} \tag{23}$$

$$\mu_v = \frac{\partial H}{\partial v} \tag{24}$$

$$= \frac{cqe^2\text{EN}_{Ni}}{2\pi\varepsilon}\left(\sum_{i\in\text{even}}\sum_{j\in i}\frac{\boldsymbol{\mu}_{ij}\cdot\mathbf{r}_{ij,0}}{\mu_{ij}|r_{ij,0}|^3} - \sum_{i\in\text{odd}}\sum_{j\in i}\frac{\boldsymbol{\mu}_{ij}\cdot\mathbf{r}_{ij,0}}{\mu_{ij}|r_{ij,0}|^3}\right) - \frac{(qe)^2c}{12\pi\varepsilon r_0} - \frac{\Delta H(c,v)}{\varepsilon}\frac{\partial\varepsilon}{\partial v}$$

$$+k_BT\left(\ln\frac{v}{x-v} + \ln\frac{v}{1-c-v}\right) \tag{25}$$

where $\mu_{ij} = |\boldsymbol{\mu}_{ij}|$.

2.5 Appendix: Convergence of Calculations

The convergence of electrostatic dipole-charge calculations is shown in Fig. 9. It is well known that charge-charge interactions in an electrostatic system will not converge above three dimensions [117]. However, based on the order of magnitude reduction from dipole-charge interactions, these interactions converge quite quickly.

2.6 Appendix: Dielectric Constant Calculations

The dielectric constant plotted with the Maxwell-Garnett equation for $\text{Li}_c\text{Ni}_x\text{Mn}_y\text{Co}_z\text{O}_2$ is shown as below as the additive rule. The additive rule is

$$\frac{\varepsilon-1}{\varepsilon+2} = \frac{4}{3}\pi\sum_i \alpha_i n_i, \tag{26}$$

where α_i is the polarizability of the atom i and n_i is the number density of atom i [156, 157]. There is an decrease the dielectric constant with the amount of decrease in lithium concentration in the material.

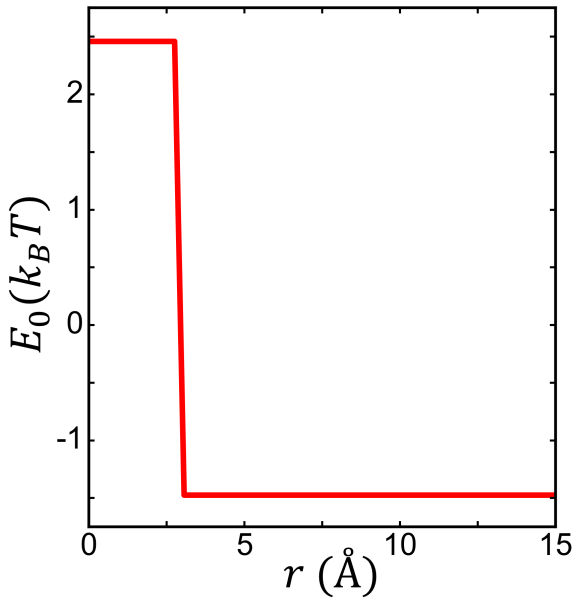

Figure 9: Convergence of electrostatic calculations with respect to the cutoff distance from the center of the defect.

2.7 Appendix: Analytical Solution

Assuming solid diffusion is not limiting, using a simplified single particle model, we can predict the scaling of the amount of degradation in the first few cycles with a voltage hold. Here, we first start with the reaction rate integrated over time

$$\begin{aligned} Q_{loss} &= \int_0^{\tau} j_{deg} A dt \\ &= \int_0^1 \tau k_{0,deg} \exp\left(\eta + \mu(c) - \mu_{deg}\right) dc \\ &\propto \tau \int_0^1 \exp\left(2\text{arcsinh}\left(\frac{Rc_{max}}{6\tau F k_0(c)}\right) + \mu(c) - \mu_{deg}\right) dc \\ &\propto \tau N \int_0^1 \exp\left(2\text{arcsinh}\left(\frac{Rc_{max}}{6\tau F k_0(c)}\right) + \mu(c) - \mu_{deg}\right) dc. \end{aligned} \tag{27}$$

Since the exponential term is quite small when the voltage is not above the cutoff voltage, the capacity loss scales with the amount of time spent in a higher voltage regime, which indicates a linear scaling with the number of cycles. For a voltage hold,

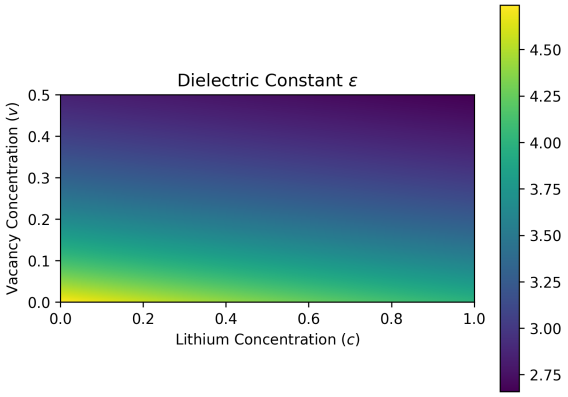

Figure 10: Dielectric Constant Measured with the Additive Rule.

this equation simplifies to

$$\begin{aligned} Q_{loss} &= \int_0^{\tau} k_{0,deg} \exp\left(V - \mu_{deg}\right) dt \\ &= k_{0,deg} \tau \exp\left(V - \mu_{deg}\right). \end{aligned} \tag{28}$$

This relation is linear with respect to time spent in the voltage hold, as shown in Fig. 8c, and depends exponentially on the value of the voltage hold. If we assume the degradation voltage is at μ_{deg}, then the exchange current density for voltage loss is generally

$$k_{0,deg} = \frac{Q_{loss}}{\tau \exp\left(V - \mu_{deg}\right)}. \tag{29}$$

2.8 Appendix: Numerical Implementation

The two separate numerical calculations were both implemented in MATLAB and can be found at `https://github.com/lightningclaw001/public_paper_scripts/tree/main/cation_disorder_defect`. The thermodynamic model was calculated using the unit cell of Materials Project structure mp-632864 for $LiNiO_2$ [144, 145, 146, 147, 148]. The unit cell was reproduced and based on the convergence calculations in Appendix 2.5, a cutoff of 20 Å. Atoms within the convergence criteria were summed with Eq. 7 to find the enthalpy, which combined with Eq. 11, gives the total free energy $G = H - TS$. The analytical solutions to the chemical potentials were

calculated as Appendix 2.4, or as $\mu_c = \frac{\delta G}{\delta c}$ or $\mu_v = \frac{\delta G}{\delta v}$.

A spherical single particle finite difference model [48] (reaction diffusion model) was implemented for Eqs. 12, 14 for concentration, and Eqs. 13, 15 for vacancies. The sphere was discretized into n sections, with Δx as the size of each section, where the boundary conditions Eqs. 14 and 15 were applied at the edges, and r_i is the radius at the center of each discretization. The fluxes $F_{i-0.5}$ were defined at the edges of the discretizations (at $r_{i-0.5}$). The bulk equations for concentration were then

$$\frac{dc_i}{dt} = -\frac{1}{r_i^2}\frac{(r_{i+0.5}^2 F_{c,i+0.5} - r_{i-0.5}^2 F_{c,i-0.5})}{\Delta x}, \tag{30}$$

where the fluxes are defined as

$$F_{c,i+0.5} = -\frac{(D_c c(1-v)\mu_c)\big|_{i+1} - (D_c c(1-v)\mu_c)\big|_i}{\Delta x}. \tag{31}$$

At the boundary, the flux $F_{c,n+0.5} = -i_{int}$ is related to the intercalation current.

For the vacancies in the system, we have similar discretizations such that

$$\frac{dv_i}{dt} = -\frac{1}{r_i^2}\frac{(r_{i+0.5}^2 F_{v,i+0.5} - r_{i-0.5}^2 F_{v,i-0.5})}{\Delta x}, \tag{32}$$

where the fluxes are defined as

$$F_{v,i+0.5} = -\frac{(D_v v\mu_v)\big|_{i+1} - (D_v v\mu_v)\big|_i}{\Delta x}. \tag{33}$$

At the boundary, the flux $F_{v,n+0.5} = -i_v = 2i_{oxy}$ is related to the oxygen degradation current, where the conservation equation is written as

$$\frac{\partial c_{oxy}}{\partial t} = 2\pi r_n \Delta x \; i_{oxy}. \tag{34}$$

An additional algebraic constraint for the current constraint was added so that

$$\sum_{i=1}^{n} v_i \frac{dc_i}{dt} = R_{constraint}, \tag{35}$$

where v_n is the volume fraction of each section, $v_i = \frac{r_{i+0.5}^3 - r_{i-0.5}^3}{r_n^3}$. The ode solver ode15s was used to solve this problem with relative and absolute tolerances of 1×10^{-8}.

2.9 Appendix: Symbols

Here, we have appended a table of the symbols used in this paper for ease of understanding:

Symbol	Meaning	Units
c	lithium concentration in the solid material	dimensionless
c_+	Li^+ concentration in the electrolyte	M
v	defect concentration	dimensionless
x	nickel concentration in NMC material	dimensionless
y	manganese concentration in NMC material	dimensionless
z	cobalt concentration in NMC material	dimensionless
$\boldsymbol{\mu}_0$	dipole pointing from transition metal layer to the lithium layer	C·m
$\mathbf{r}_{ij}$	distance vector between the defect center and site ij	m
r_{ij}	magnitude of distance vector between the defect center and site ij	m
ε	dielectric constant, see Appendix C	F/m
$\mathbf{r}_0$	distance vector between a transition metal-lithium dipole	m
r_0	magnitude of distance vector between a transition metal-lithium dipole	m
H	enthalpy	eV
S	entropy	eV/K
G	Gibbs free energy, $G = H - TS$	eV
μ_c	chemical potential for intercalation	k_BT
μ_v	chemical potential for defect formation	k_BT
D_c	diffusion coefficient for lithium concentration	m^2/s
$\mathbf{F}_c$	flux for lithium diffusion	m/s
D_v	diffusion coefficient for defect formation	m^2/s
$\mathbf{F}_v$	flux for defect formation	m/s
i_{int}	intercalation current	A/m^2 s
i_{oxy}	oxygen degradation current	A/m^2 s
i_r^*	exchange current density	A/m^2 s
λ	reorganization energy	k_BT
η	overpotential	k_BT/e
η_f	formal overpotential, $\eta_f = \eta + \ln \frac{c_+}{c}$	k_BT/e
ϕ	potential difference between electrolyte and solid	k_BT

2.10 Appendix: Experimental Data Selection

To obtain experimental data about disorder, recent microscopy experiments are very useful in discovering the amount of disorder in the system. Many experimentalists use gas formation or other mechanisms [6] to deduce the amount of phase transitions, but for our model specifically studying cation disorder, it is imperative to have a spatially defined set of experiments with clear experimental cutoffs for a specific material. In addition, many common experimental measurements for phase transitions also measure the oxidation state of different atoms, but this does not give the necessary information because it discusses more the specific phases that we see [28]. Since our paper is focused on cation disorder, which is the trigger for phase transformations, knowing the amount of densified phases such as rock salt or spinel phases does not provide the exact data we want. We have chosen experimental data with a good set of electrochemical range (voltage cutoffs) as well as spatial range, along with a material that we are interested in, which needs to be nickel rich and layered [60]. Similar material is also well-characterized for modeling purposes in terms of open circuit voltage and electrochemical parameters [5], which was also previously verified and tested by the authors, and compared with other experiments and simulations [49]. Coupled ion electron transfer kinetics parameters for nickel rich materials were also obtained with this set of materials [129]. Thus, we chose this set of experiments to model and compare because of a) rigor of experiments and well-planned and defined experiments b) availability of modeling infrastructure and kinetic and thermodynamic parameters.

Chapter 3

Degradation from Single Particle to Electrode Level (Solid Solution)

Population effects driving active material degradation in intercalation electrodes [13]

3.1 Introduction

Though an accurate model of single particle level degradation for nickel rich cathodes was formulated for surface reconstruction, the many different types of degradation indicate that more forms of degradation need to be accounted for in modeling. For example, cathode degradation is generally caused by particle level physical mechanisms such as electrochemical resistance growth from films at the electrode/electrolyte interface [24, 25], phase transformations and loss of kinetic abilities at the surface or bulk [27, 185], as well as electrolyte loss [186, 187]. The apparent capacity loss from the convolution of these mechanisms cannot be physically explained by a single degradation mechanism, since it is caused by many degradation mechanisms, and results in slightly different behavior in electrode-level phenomena. To understand this problem

The present chapter is based on my published work in the journal of Physical Review E [13].

through modeling, the multiscale nature of the porous electrode problem indicates that the models need to be coarse grained over many degradation mechanisms to extract macroscopic degradation behavior.

Electrode-level degradation phenomena is seen in capacity loss curves and in voltage-capacity curves [1]. This is seen through impedance experiments, where impedance growth has been found to be mainly from the cathode side [40, 188, 189, 101], while anode degradation is generally motivated by solid electrolyte interphase formation and lithium plating [91, 24]. Understanding the increase of cathode impedance is a critical step of deconvoluting electrode-level degradation. Previous work [40, 41] has identified resistance growth as a large component of this failure, but has not clarified the separation of all the different mechanisms. To deconvolute these particle level mechanisms, it is imperative to understand the different relationships between the particle level driving forces and electrode-level behavior of the degradation mechanisms, especially in relation to particle population dynamics. This reveals a more complete understanding of electrode degradation.

In many physical theories, single particle models are used, but can be inaccurate due to not accounting for interactions between particles. This concerted behavior between individuals in population dynamics has been observed in many systems, from biological systems such as fireflies [190, 63] to electrochemical oscillations in batteries [65]. In a battery, the effects of population dynamics can appear in solid solution materials [49] as well as in phase separating materials as each particle activates and phase transitions [55, 10, 8, 191]. Past biological modeling used population dynamics [192, 193, 194] studied with the Fokker-Planck equation [195] to understand the growth and eventual death of biological populations [196, 197]. The idea of a fitness landscape [197], where the fitness represents the reproductive rate of a genotype, or "effectiveness", was incorporated into these models to explain why populations evolve towards certain traits. We can similarly apply this idea to model particle population dynamics in lithium-ion batteries.

For a battery, the fitness can be envisioned for each particle as the effectiveness of carrying the current load, as shown in Fig. 1 for a population distribution affected

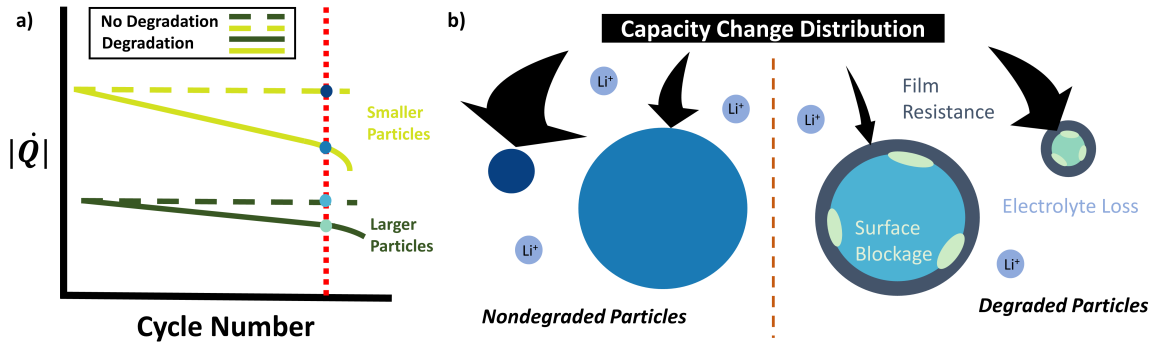

Figure 1: Schematic of particle size distribution effect on current distribution in a constant current charge or discharge simulation for a battery. a) The absolute value of the capacity change fraction of each particle is plotted with respect to the cycle number as the system is degraded. This accounts for effects of degraded charge transfer kinetics and particle size contributions by reducing the nondegraded current to the degraded current. b) A snapshot at a single time point for a sample of degraded or nondegraded particles of small or large particle sizes is shown, where the capacity change distribution splits the current between the different particles based on their size effects and degradation.

by degradation effects and particle size effects. Fig. 1a shows the fitness as a rate of change of the capacity fraction of each particle, which is the capability of carrying current. However, fitness landscapes can also evolve depending on the environment they are in [196, 64], which in turn affects the evolution of population dynamics, called coevolution [198]. In a system of battery particles, the fitness landscape of the particles changes [199] as the battery is cycled, similarly to how the fitness of different genotypes changes with evolution [200]. Thus, it is important to quantify the fitness landscape of battery particle systems as they evolve.

In this work, through methods of population dynamics coupled with electrochemical kinetics in a simple battery model, we gain an understanding of active material degradation at the particle scale and how it affects electrode-level degradation phenomena. We simulate an interacting population of particles in a single electrode volume in a porous electrode. Initially, particle size effects influence the current distribution in the population, while as the battery is cycled, degradation also influences the current distribution. Fitness and degradation are observed to have an autocat-

alytic relationship from the simulations. We use specific degradation mechanisms to understand the effect on the electrode-level behavior of each of these materials. Inversely, experimental information on the capacity loss profile and voltage-capacity curves may provide insight on the particle level degradation mechanisms present.

3.2 Theory

In porous electrode theories, single particle models are often used to described the active material interactions of the system [122], which can be inaccurate from not accounting for interparticle interactions. To remedy this, we formulate a theory in porous intercalation electrodes featuring the cumulative effect of population dynamics including degradation. We consider particles with a size distribution, each of which is treated homogeneously during (de)intercalation. The population $f(t, c; r)$ is the probability distribution of particles with radius r and concentration c at time t. The evolution of population $f(t, c; r)$ can be tracked by the modified Fokker-Planck equation. During evolution, the fitness function W is introduced to modify the intercalation rate of degradation. The analytic expressions of fitness functions for three degradation modes are derived.

3.2.1 Conservation Equation

A porous electrode is normally modeled using volume discretizations at the electrode scale, with single particle models in each volume to simulate the particle level intercalation and diffusion mechanisms of lithium ions [122, 53]. To account for interparticle interactions, many active material particles need to be modeled in the same volume, which are under the same voltage. The dynamics of a population can be driven by controlled parameters imposed on the system [201, 202], such as the applied current or voltage. Neglecting transport limitations at the electrode scale, these models can be simplified to a single volume.

We can use the Fokker-Planck equation, which is commonly used to simulate population dynamics of evolving probability distributions $f(t, c; r)$ of multiple fields

(such as concentration and particle size) under time evolution, to model this as

$$\frac{\partial f}{\partial t} = -\frac{\partial}{\partial c}\left(fR\right) + \frac{\partial}{\partial c}\left(D\frac{\partial}{\partial c}\left(fW\right)\right). \tag{1}$$

In this equation, the first term is from the mean of the reaction happening amongst the particles in the system, while the second term is from the variance of the reaction amongst the particles. The variables are defined as R, the volumetric reaction rate derived from the mean of the transition rates, and D, the thermal diffusivity related to the fluctuations of the transition rates [203], with the full definitions in Appendix 3.4. The full derivation of the modified Fokker-Planck equation accounting for the fitness value can be seen in Appendix 3.4 and reveals that the appearance of the fitness function W is from the change in the effective reaction rate from degraded charge transfer kinetics and particle size effects [51, 194, 193, 70]. For better understanding of interparticle effects, we write this in the form where the volumetric reaction is replaced by the nondegraded intercalation rate per area multiplied by the fitness of the battery W as

$$\frac{\partial f}{\partial t} = -\frac{\partial}{\partial c}\left(f\bar{i}W\right) + \frac{\partial}{\partial c}\left(D\frac{\partial}{\partial c}\left(fW\right)\right), \tag{2}$$

where $D = kk_BT/N_t$ is the thermal diffusivity parameter, $k = \bar{i}/\eta$ for a linear form of the reaction rate, and N_t is the maximum number of molecules in the system. Here $\bar{i}$ is the nondegraded intercalation current per area, i is the real intercalation current per area, R is the real volumetric reaction rate per volume, and $W = R/\bar{i}$ is the fitness function, which is defined and expounded in the following section.

3.2.2 Intercalation Kinetics

The intercalation kinetics control the mean of the time evolution of the system as defined in Eq. 2, and thus an accurate description of kinetics becomes imperative [51, 204, 205]. For electrochemical systems, well-known physical models exist for thermodynamically consistent reactions such as the Butler-Volmer reaction [206, 122, 53]. Increasingly complex models as coupled ion electron transfer (CIET) theory [128, 129]

have been further derived and verified experimentally from x-ray imaging of lithium iron phosphate materials to account for electron availability from the density of states of the intercalation material. These intercalation models can be used to quantify the heterogeneity and degradation growth in a population of battery particles.

The general form of the intercalation reaction takes the form of

$$i(\eta) = k_0(c)h(\eta); \quad h(\eta) = r_{\leftarrow} - r_{\rightarrow}, \tag{3}$$

where $k_0(c)$ is a transition state term describing the overall rate of reaction (incorporating exchange current density) and $h(\eta)$ is from the thermodynamic driving force composed of a forward $r_{\rightarrow}$ and backward reaction $r_{\leftarrow}$ driven by the overpotential

$$e\eta = (e\phi_s + \mu(c)) - (e\phi_+ + k_B T \ln a_+)\,, \tag{4}$$

where c is the concentration of the intercalated lithium, $\mu(c)$ is the chemical potential of the intercalated lithium, $\phi_{+/s}$ is the lithium ion electrical potential in electrolyte or solid, and a_+ is the activity of the lithium ions in electrolyte.

When there is no degradation accounted for in the system, the intercalation reaction can be similarly defined as

$$\bar{i}(\eta) = \bar{k}_0(c)\bar{h}(\eta), \tag{5}$$

where the overbar indicates a system without degradation. The Butler-Volmer reaction rate is modeled with transition state theory as

$$\bar{i}(\eta) = k_0(c)\left(\exp\left(-\alpha\eta\right) - \exp\left((1-\alpha)\eta\right)\right), \tag{6}$$

with the thermodynamically consistent prefactor $k_0(c) = k_0^* c^{\alpha}(1-c)^{1-\alpha}a_+^{1-\alpha}$, where k_0^* is the reaction current prefactor, α is the charge transfer coefficient, and a_+ is the activity coefficient for the electrolyte. The reaction rate from coupled ion electron transfer, which accounts for electron availability, is modeled using an approximation

as [128, 166]

$$\bar{i}(\eta) = k_0(c)\left(a_+ \text{helper}(-\eta_f, \lambda) - c\,\text{helper}(\eta_f, \lambda)\right), \tag{7}$$

with prefactor $k_0(c) = k_0^*(1-c)$, where the helper function is defined as [166]

$$\text{helper}(\eta_f, \lambda) = \frac{\sqrt{\lambda\pi}}{1+\exp\left(-\eta_f\right)} \text{erfc}\left(\frac{\lambda - \sqrt{1+\sqrt{\lambda}+\eta_f^2}}{2\sqrt{\lambda}}\right). \tag{8}$$

Here, the formal overpotential is defined as $e\eta_f = e\eta - k_B T \ln \frac{c}{a_+}$, which is the overpotential with the ionic concentration dependencies removed, and λ is the Marcus reorganization energy for electron transfer in the solid material. In this electrochemical reaction, the overall reaction is driven by the difference between the reduction and oxidation reactions, $\bar{i} = \bar{i}_{red} - \bar{i}_{ox}$, where $\bar{i}_{red} = k_0(c)a_+\text{helper}(-\eta_f, \lambda)$ and $\bar{i}_{ox} = k_0(c)c\text{helper}(\eta_f, \lambda)$. There is a limiting current reached with this model from the density of states of the material used with respect to overpotential, $i_{lim} = k_0^*(1-c)$, unlike the Butler-Volmer model, which grows exponentially with overpotential [129]. Kinetic behavior at high overpotentials is strongly affected by the correct choice of reaction kinetics.

An important term we will encounter is the idea of an inverse differential resistance, or differential conductance, $\frac{\partial \bar{i}}{\partial \eta}$, which is first mentioned in Refs. [164, 69] to explain the idea of autocatalytic reactions. Since degradation affects the overpotential, the differential conductance reveals the acceleration of the reaction with overpotential. Experimentally, this differential conductance also appears in the charge transfer resistance term in electrochemical impedance spectroscopy measurements [206]. A negative differential conductance means that the reaction is self-driving or autocatalytic, as opposed to a reaction that is self-limiting or autoinhibitory. This differential conductance incorporates an effect from the driving force term $h(\eta)$ as well as from the transition state term $k_0(c)$. For a solid solution material, the effect of the driving force term is generally autocatalytic, with the exception of Marcus-type electron transfer reactions, which may have inverted regions causing local values of autoinhibitory reactions [207, 126]. However, the effect of the transition state term is not

necessarily autocatalytic and can amplify nonheterogeneity in population dynamics, as explored in Ref. [51].

3.2.3 Fitness Function

As seen from the population evolution equation (Eq. 2), the fitness of particle population dynamics, especially in relation to resistance evolution as the battery is cycled, is important to quantify [21, 208, 25, 24]. The coupling of degradation evolution, kinetics, and particle size distributions in a porous electrode model is difficult to model because capturing multiscale effects [209] and calculating implicit solutions numerically at each step in the Fokker-Planck solution is computationally expensive. We aim to formulate in a simple manner the solution of the Fokker-Planck equation with the formulation of the fitness function W.

The fitness model captures a ratio between the real and ideal currents, which linearizes the kinetics of the system. The advantage of using a fitness function formulation is that from the definition of the fitness variable, we keep the original formulations of our reaction rates without having to self consistently solve implicit kinetic equations in the population balance. This becomes especially difficult for models with a film resistance contribution, as implicit solutions are necessary for these models. In addition, with the use of a fitness function model, there is a separation between the different contributions of particle size as well as modes of degradation on fitness, so there is a clear dominant mechanism from degradation.

The nondegraded intercalation current without degradation $\bar{i}$ is the reference that the current at a certain overpotential reaches with no degradation. In physical particles, there are often degradation effects, especially as the particles are cycled, so the real current magnitude $|i|$ is generally smaller than the nondegraded current magnitude $|\bar{i}|$. The general definition of the fitness, or "performance", is the ratio of the volumetric reaction rate accounting for particle size and degradation effects, or

$$W = \frac{R}{\bar{i}}, \tag{9}$$

where R is the volumetric reaction rate and $\bar{i}$ is the nondegraded intercalation current per area without any resistance. This is an important ratio that relates our known electrochemical reaction data $\bar{i}$, the nondegraded current, with the real volumetric current R. In physical terms, W can also be thought of as an effectiveness parameter that indicates the ability to accept current, representing the performance of a battery, since a higher effectiveness indicates a better performing particle. However, a better performing particle is also more sensitive to degradation effects, so infinitely small particles are not the most beneficial in electrode design.

Intercalation currents in battery particles are usually modeled as surface reactions [54, 44]. However, the total capacity in the system depends on the particle volume. Solid diffusion is often not limiting in intercalation materials, where reaction limitations tend to be more important in nanoscale systems [3]. Under this assumption, there is a simple scaling of the particle size (radius r) relating the reaction rate per volume R to the reaction rate per area i as $VR = Ai$, where V is the particle volume and A is the particle area. Using this, for spherical particles, the fitness can be simplified to

$$W = \frac{1}{r}\frac{i}{\bar{i}}, \tag{10}$$

which relates the particle filling rate to the current density as shown earlier. This introduces a separation between particle size effects $1/r$ and degraded charge transfer effects $i/\bar{i}$. The initial distribution of the "fitness" is determined by the size of the particle distribution as $W = 1/r$ since there is no degradation.

3.2.4 Degradation Models

From the degraded charge transfer effect of fitness $i/\bar{i}$, we see that the degradation buildup on each particle also plays a role in the fitness. Mechanically and electrochemically, there are many different modes of degradation in a lithium-ion battery [81]. For simplicity, we only consider the most important electrochemical degradation modes in lithium ion batteries. There are three possible modes of electrochemical active degradation in a battery material that we will consider. The first is formation

of a film resistance on the battery, based on some film-forming reaction, such as solid-electrolyte interphase formation [21, 210]. The result of this is an increased surface resistance that mainly plays a role in affecting the kinetics by reducing the overpotential.

The second mode of degradation is through the reduction of active material, from phase transformations into rock salt or spinel phases (such as in nickel rich materials), which cause changes in surface kinetics and active material capacity [211, 212]. This would result in the loss of active material, which plays a role through rescaling the available lithium concentration in the system. It mainly reduces the number of available sites in the transition state, which affects the reaction kinetics.

The last mode of degradation is a general contribution from degradation in the battery, either in the cathode or anode, as a loss of electrolyte in the system from degradation reactions. This can be modeled with a loss in electrolyte concentration [21, 186].

Since we use nickel-rich materials as an example, degradation reactions are modeled at higher voltages [83, 57] using a simple Tafel reaction to define the degradation current as

$$i_{deg} = k_{0,deg} \exp\left(\mu^0_{deg} - \mu_{res} + iR_f\right) \tag{11}$$

where μ^0_{deg} is the cutoff potential for degradation.

Resistive Film

A resistive film may form as a type of solid electrolyte interphase on the cathode [213, 94] or anode [214] and grow continuously. Experimental measurements of resistive interface growth have found that though the initial amount of growth is quite rapid, even past the initial stages, there is often continuous growth of resistive film on active material [23]. For any intercalation reaction, when a resistive film grows, it affects the current i through the reduction of the overpotential to $\eta + iR_f$ with film resistance R_f.

From the definition of the fitness of the reaction rate in Eq. 10, it is necessary to

obtain $i/\bar{i}$ when there is a resistive film. The simplest electrochemical reaction is a symmetric Butler-Volmer model, which can be solved with fewer simplifications than the generic Butler-Volmer model because of the symmetry of the model. If we do a Taylor expansion on this system and assume that the charge transfer coefficient is symmetric, we can obtain an analytic expression for the driving force term in Eq. 46. We obtain the fitness value any given time as

$$W = \frac{1}{r}\left[1 + \alpha i \coth\left(\alpha\eta\right) R_f\right] + \mathcal{O}(R_f^2). \tag{12}$$

A more general case can be found by linearizing the full kinetic model with respect to the overpotential. Using this, we can avoid the need to find an implicit solution of this problem. A natural dependence on the differential conductance occurs from how resistance affects overpotential. The ratio of the degraded to nondegraded current is found to be

$$\frac{i}{\bar{i}} = \frac{1}{1 - R_f \frac{\partial \bar{i}}{\partial \eta}} + \mathcal{O}(R_f^2) \tag{13}$$

from the linearizations in Appendix 3.81, where the second order solution can be seen in Appendix 3.6. Thus, the fitness value is found to be

$$W = \frac{1}{r}\left(1 - R_f \frac{\partial \bar{i}}{\partial \eta}\right)^{-1} + \mathcal{O}(R_f^2), \tag{14}$$

which is the general formula for any reaction rate. The specific analytical formulas for each reaction rate (Butler-Volmer and CIET) can be found in Appendix A.

For the resistive film model, with the electrochemical cycling of a battery, the resistance on a particle R_f $(\Omega \cdot m^2)$ changes as

$$\frac{dR_f(t,c,r)}{dt} = \beta i_{deg}, \tag{15}$$

with the value of the degradation current per area i_{deg} from Eq. 11. The resistivity per amount of reaction is $\beta = n\mathrm{MM}/(F\sigma\rho)$, which is the resistivity per amount of resistance reaction in units of $\Omega{\cdot}m^4/C$. This is a property of the material which makes

up the resistive film. It is related to the conductivity of the material σ, the density of the material ρ, the number of lithium atoms per chemical formula in the film material n, Faraday's constant F, as well as the molecular mass of the film material MM. For materials such as lithium carbonate which form inorganic films in batteries, we expect the resistivity parameter β to be on the range of $10^{-7} - 10^{-5}\ \Omega \cdot \mathrm{m}^4/\mathrm{C}$ [215]. Since we are only concerned with the dependence of the resistance with the particle size, we can take the mean value of Eq. 15 over the concentration distribution using Appendix 3.5.

Surface Blockage

The model of fitness in surface blockage is similarly defined to the approximate solution of the resistance formation model. The surface blockage model is a homogeneous version of a model for phase transitions from cation disorder-induced degradation, especially common in nickel rich materials, which involves a change in surface concentration as well as bulk availability [12, 28, 60]. The rescaled capacity is defined as $\tilde{c}$. Since there is a loss of active material in this model, in the chemical potential model of the active material, the real concentration needs to be rescaled by the amount of capacity loss as $\mu_c(c/\tilde{c})$ instead of $\mu_c(c)$. The value of degraded to nondegraded current is shifted as a result, as the reaction is affected by the rescaled chemical potential as well as the reduction in the number of available sites, which influences the reaction rate through transition state theory. We can calculate these two effects separately.

We first calculate the effects from the reaction rate without prefactor, which comes from the effect of overpotential on this mechanism. The ratio of the degraded to nondegraded reaction rate without the prefactor is found to be

$$\frac{h}{\bar{h}} \approx 1 + \frac{1}{\bar{h}} \frac{c(1-\tilde{c})}{\tilde{c}^2} \frac{\partial \mu_c}{\partial c} \frac{\partial \bar{h}}{\partial \eta} \tag{16}$$

from a Taylor expansion of h in Appendix 3.82, where we again see a form similar to the differential conductance. This change in maximum capacity plays a role by limiting the current in these coupled-ion electron transfer reactions. If we mainly

consider surface effects, we can neglect this term.

Following, we can calculate the effects of the prefactor ratios, which consist of the surface effects. For an nondegraded Butler-Volmer current, the ratios of the prefactors is $\left(\frac{\tilde{c}-c}{1-c}\right)^{1-\alpha}$ from the thermodynamically consistent Butler-Volmer equation [69]. For the coupled-ion electron transfer reaction, the ratios of the prefactors is $\frac{\tilde{c}-c}{1-c}$ when the transition state is assumed to occupy one site. Thus, the total fitness for the surface blockage model results in

$$W \approx \frac{1}{r}\left(\frac{\tilde{c}-c}{1-c}\right)^{n} + \mathcal{O}((\tilde{c}-1)^2), \tag{17}$$

where $n = 1-\alpha$ for the Butler-Volmer equation, and $n = 1$ for the coupled-ion electron transfer reaction rate.

For a model of surface blockage, the amount of degradation is classified by

$$\frac{d\tilde{c}(t,c,r)}{dt} = -\frac{i_{deg}C}{\rho_{s,max}r} \tag{18}$$

an equation that scales with the size of the battery particle and the total site density of the material. Here, C is the Coulomb number and $\rho_{s,max}$ is the maximum site density of the material in mol/m^3. This equation can again be integrated over all concentration values for an average value per particle size as in Appendix 3.5.

Electrolyte Loss

In a full battery cell, the amount of degradation should be affected by degradation on the other electrode (anode) as well. The formation of degradation on the anode will often lead to a loss of usable lithium capacity from the lithium consumed in the side reaction to form products [216]. These products consist of the solid electrolyte interphase, cathode electrolyte interphase, and others. Since we are modeling a perfect electrolyte bath, which does not use an opposing electrode, we cannot "consume" lithium ions on the other electrode and reduce the total usable lithium concentration. Thus, electrolyte loss needs to be prescribed in the system, which we choose to be

linear for simplicity [21]. We call this degradation mechanism electrolyte loss since it reduces the available electrolyte.

In the Butler-Volmer equation, the electrolyte concentration affects the transition state prefactor as $k_0(c) \propto c_+^{1-\alpha}$. In addition, there is a subtle effect on shifting the overpotential from the entropic component. From linearizing the reaction rate without prefactor h in Appendix 3.83 and applying the definition of the thermodynamic factor $\frac{\partial \ln a_+}{\partial \ln c_+}$ from Ref. [122], which relates the activity in a Stefan-Maxwell concentrated electrolyte with the lithium ion concentration, we can obtain the fitness value. We see that the fitness value in a Butler-Volmer equation is simply found to be

$$W = \frac{a_+^{1-\alpha}}{r}\left[1 + \frac{1}{\bar{h}}\frac{\partial \ln a_+}{\partial \ln c_+} k_B T \frac{\partial \bar{h}}{\partial \eta}(1 - c_+)\right] + \mathcal{O}((c_+ - 1)^2) \tag{19}$$

with our linear approximation for concentrated solutions. A dilute solution approximation can also be used, where the thermodynamic factor is unity.

For coupled ion electron transfer, the effect of electrolyte is more complicated [129]. In the reduction reaction, since the electrolyte is a reactant, there is a direct concentration dependence on the reduction reaction, but not on the oxidation reaction. In addition, in the formal overpotential, the electrolyte does not influence the amount of available sites in the overpotential except through the activity in a concentrated solution. Thus, it does not change the overpotential of the reaction for a dilute model [128]. As derived in Appendix 3.83, we see that

$$W = \frac{1}{r}\left[1 - \frac{\partial \ln a_+}{\partial \ln c_+}\frac{\bar{i}_{red}}{\bar{i}}(1 - c_+)\right] + \mathcal{O}((c_+ - 1)^2) \tag{20}$$

is the fitness value for the electrolyte loss model if a CIET reaction rate is used. For a CIET reaction rate, the reduction current ratio in the total reaction contributes strongly to scaling the value of the fitness function. This causes the fitness in intercalating systems to be lower than in deintercalating systems for this model.

Assuming that the initial electrolyte concentration is unity, the degradation rate

for a half-cell model with a electrolyte loss can be prescribed using the simple relation

$$c_+ = 1 - kt, \tag{21}$$

where $k > 0$ is a parameter that reduces the availability of electrolyte with time in units of M/hr if the initial concentration is 1 M and t is the amount of time spent cycling the battery in hours.

Combined Model

These three degradation models can be combined into an overall fitness value to account for multiple degradation effects to the first order approximation. Similarly, if other fitness values for different degradation mechanisms are also derived, they can be combined into such an overall fitness value. The value of the combined fitness function for the Butler-Volmer equation is

$$W \approx \frac{a_+^{1-\alpha}}{r}\left(\frac{\tilde{c}-c}{1-c}\right)^{1-\alpha}[1+\alpha i\coth(\alpha\eta)R_f]\left[1+\frac{1}{\bar{h}}\frac{\partial \ln a_+}{\partial \ln c_+}\frac{k_B T}{e}\frac{\partial \bar{h}}{\partial \eta}(1-c_+)\right]. \tag{22}$$

For the coupled-ion electron transfer system, the overall fitness function can be written as

$$W \approx \frac{1}{r}\left(\frac{\tilde{c}-c}{1-c}\right)\frac{1}{1-R_f\frac{\partial \bar{i}}{\partial \eta}}\left[1-\frac{\bar{i}_{red}}{\bar{i}}(1-c_+)\frac{\partial \ln a_+}{\partial \ln c_+}\right]. \tag{23}$$

From each of these equations, we can see the explicit contributions of particle size and the three different degradation modes we are modeling (resistive film, surface blockage, and electrolyte loss). The separate effects of each degradation mode contribute to the overall fitness, aiding understanding of which modes are the most detrimental and should be mitigated to preserve the current capability of the battery.

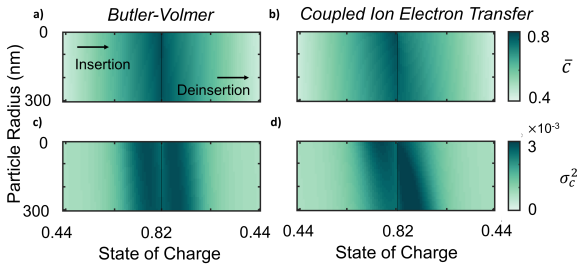

3.3 Simulations

3.3.1 Numerical Setup

Here, we attempt to model the degradation of a nickel manganese cobalt oxide blend electrode with a ratio of 5:3:2 (NMC532) under constant current cycling and capture the evolution of capacity changes and degradation with time evolution. Using the Fokker-Planck model in Eq. 2, we model a single electrode volume. We simulate each degradation mode separately to analyze their individual effects. Simulations were performed with MATLAB using autodifferentiation from CasADi [217] to increase speed of solving the DAE system. The Fokker-Planck numerical simulations were performed until end of life for each degradation and reaction model. Simulation parameters and details were reported in Appendix 3.9.

3.3.2 Analysis

We first focus on the particle level details of degradation, and then analyze how dynamics at the microscale affects electrode-level degradation. From the particle level details of kinetics and degradation, we observe the heterogeneity between particles in intercalation. To understand their contributions to degradation, the fitness values in the simulation are observed. The heterogeneity of degradation at the particle level scale and the autocatalytic relationship between fitness and degradation are discussed. Following this, microscale degradation is then used to explain electrode-level phenomena, with the voltage curves and the capacity loss data as an example. Heterogeneity at the particle level is then found to heavily influence electrode-level degradation effects, especially from the smaller particles.

Particle Level Heterogeneities

In a single cycle, the average concentration at each particle radius is plotted in Fig. 3.3.2a,b and the variance of the concentrations is plotted below in Fig. 3.3.2c,d. We observe that even the differences between these reaction rates can cause heterogeneity in the intercalation of particles. This is influenced by the "limiting current" for coupled-ion electron transfer type reactions from the electron availability, while the Butler-Volmer reaction grows exponentially with overpotential and is unbounded. This limiting current is bounded by the transition state value $\gamma^{\ddagger} = (1-c)^{-1}$, which shows up in both reaction rates, but because of the exponential form of the Butler-Volmer equation, it affects the coupled-ion electron transfer reactions more strongly. This causes an asymmetry between charge and discharge in the CIET reaction rate, stemming from the prefactor. The asymmetry in discharge is discussed further in Refs. [51, 49].

The heterogeneity at the particle level scale representing the effectiveness of each particle is described by the fitness. This describes each particle's inherent current-carrying capability. The initial value of performance is defined by the inverse particle size as shown in Fig. 2a. After cycling, the fitness function W is plotted in Fig. 2, where the analytical values can be found in Appendices 3.2.4, 3.2.4, and 3.2.4. The fitness becomes infinitely small from the unbounded behavior of Butler Volmer reactions for some values in Fig. 2b, where the reaction is infinitely large for intermediate concentrations. This causes asymptotic behavior in the Butler-Volmer solution for the resistive film and electrolyte loss models.

We observe that as the battery is cycled, the value of the fitness function is reduced from degradation accumulation. Overall, the reduction of the fitness values drives further increases in heterogeneity in degradation, which triggers more heterogeneous reduction in the fitness values. Thus, we observe an autocatalytic effect between fitness and degradation.

This autocatalytic relationship between fitness and degradation is further seen in Fig. 3. The relative degradation parameter with respect to the maximum parameter

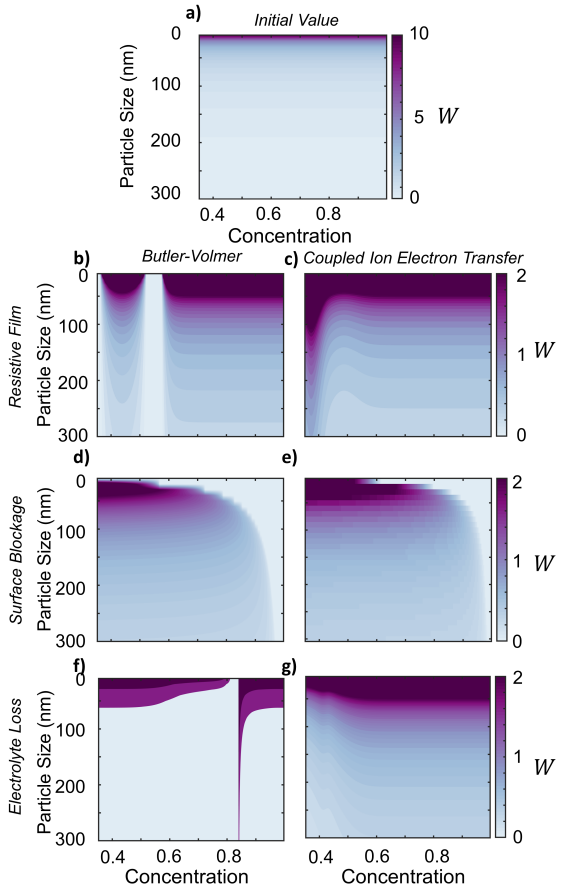

Figure 2: a) The initial fitness value $\bar{W} = 1/r$ is plotted in the first cycle with respect to each concentration and particle size at a single time point during the initial cycle. b,c,d,e,f,g) For each Butler-Volmer/coupled ion electron transfer reaction rate, the fitness values W from a set of simulations each with a single degradation mode towards the end of cycling are plotted with respect to concentration and particle size at a single time point during one of the last few cycles.

at each time is plotted for the Butler-Volmer or coupled ion electron transfer reactions with the degradation mechanisms from film resistance or surface blockage. Resistance growth asymmetry happens in the first couple cycles in Fig. 3a and b, where more resistance forms on the larger particles and reaches steady values after the first few cycles to attempt to homogenize the system. Initially, no autocatalytic behavior is observed as the initial resistance formation seen is part of the "formation cycling" in battery electrodes [218, 219] to stabilize the system and reduce the homogeneity between the particle sizes.

The second step of nonheterogeneity in resistance formation appears after forma-

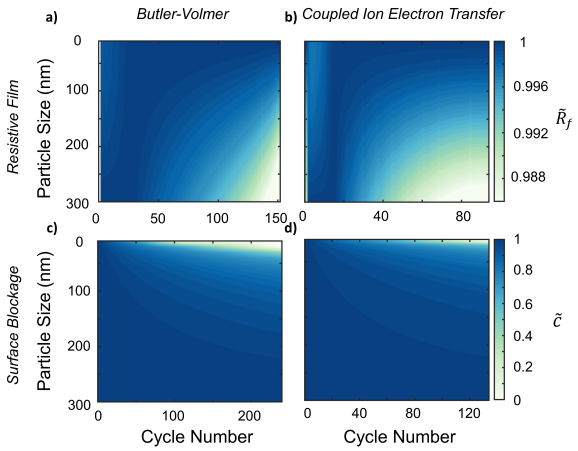

Figure 3: a,b) For a set of simulations with only resistive film growth, relative resistance at each cycle to the maximum resistance at each cycle is plotted with respect to cycle number and particle size, for the Butler-Volmer and coupled ion electron transfer reactions. c,d) For a set of simulations with only surface blockage increase, surface blockage at each cycle relative to the maximum surface blockage at each cycle is plotted with respect to cycle number and particle size, for the Butler-Volmer and coupled ion electron transfer reactions. (The degradation mechanism of electrolyte loss is prescribed so it has no heterogeneity). This plot displays the heterogeneity growth in degradation as we cycle the battery.

tion cycling in the battery lifetime and reduces the overall capacity of the battery as shown in Fig. 3. Because of the larger fitness values for small particles, there is a higher capacity change fraction distributed to them, causing more degradation from the higher amounts of degradation current. This degradation growth behavior becomes autocatalytic as more asymmetry in degradation growth is observed with cycling. This is seen in the later cycles in Fig. 3ab, where more resistance forms on the smaller particles towards the end of life. Similarly, for the surface blockage mechanism, there is an autocatalytic effect on degradation favoring smaller particles. This is coupled with the fitness values, which eventually lose all their available capacity towards end of life and leaves only larger particles operational. Thus, for both the surface blockage and resistance formation models, heterogeneity grows autocatalytically as we cycle the batteries, with degradation favoring the smaller particles and larger particles remaining more stable.

From the combined observations of particle level degradation at different particle sizes, we theorize that the terminating behavior of battery capacity is not caused

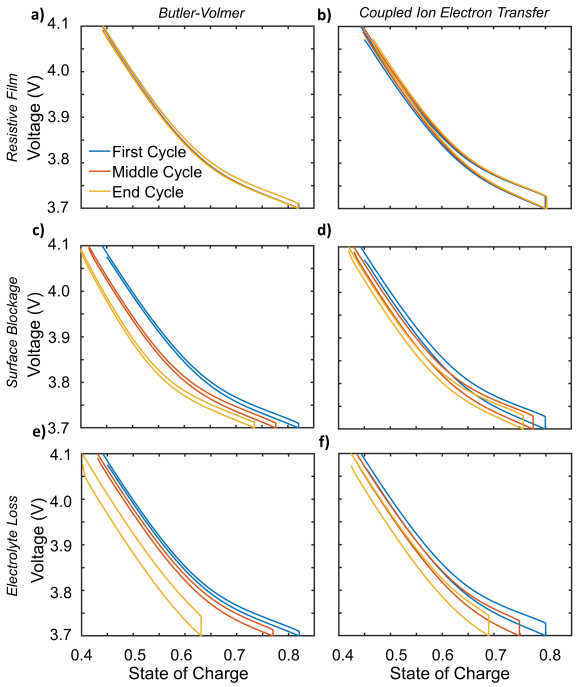

Figure 4: The voltage discharge and charge curves from simulations with a single degradation mechanism with respect to the state of charge of the cathode are plotted at the beginning, middle, and end cycle of each set of simulations with each reaction model (BV/CIET for a,c,e and b,d,f) and degradation mechanism (resistive film for a and b, capacity loss for c and d, and electrolyte loss for e and f).

by the average particle size, but rather the smaller particle sizes. As observed in Fig. 3, at later stages in cycling, degradation starts to accumulate on all particles, but especially quickly on smaller particles, which require larger amounts of potential to charge/discharge and thus causes a stronger drop in battery capacity. This autocatalytic behavior between fitness and degradation drives a strong heterogeneity in fitness values in Fig. 2 as the battery is cycled. This continually favors smaller particles as the system reaches end of life in Fig. 3.

Electrode-Level Measurements

The effects of heterogeneous degradation effects can be shown to influence the experimental measurements of electrode-level electrochemical phenomena. The shifting and hysteresis behavior of the voltage curve provides important pieces of electrode-level information from cycling the degraded cells. The capacity loss profile can also be

observed and information on the degradation mechanisms can be extracted from the shape of these curves.

Expansion of the voltage curves, or hysteresis, occurs from kinetic limitations in the system, which are often caused by degradation mechanisms that do not degrade the active material. For the electrolyte loss mechanism in Fig. 4, the formal overpotential for the coupled-ion electron transfer reaction does not contain any electrolyte effects. The main influence of degradation is on the kinetics in the reduction direction of the reaction. Thus, there is no shift in the open circuit voltage (OCV) curves and only an "expansion" of the charge/discharge curve around the original open circuit voltage, which occurs from the limitations on the kinetics. The apparent shift in the open circuit voltage comes from the need to apply higher electrolyte potentials to compensate for lower electrolyte concentrations. There is an asymmetry between insertion and deinsertion since the influence of electrolyte concentration appears solely in the reduction reaction.

Shifts in the voltage measurement, however, generally occur from either shifts in overpotentials required or active material ranges. The surface blockage mechanism observes a leftward shift compared to the potential of the original model, occurring from the reduction of available transition state sites and the shift in the OCV. This causes the change in active material range in the surface blockage mechanism, which generates a shift in the overpotential ranges, translating to the accessible voltage range. Similarly, because of the shifted overpotentials for the Butler-Volmer formulation for the electrolyte loss mechanism, there is a downward shift of the open circuit voltage curve. This is in contrast to the surface blockage mechanism, since there is not a change in range of active material voltage, but a shift in the electrolyte potential applied. This generates a downward movement on the voltage curve instead of leftward shift of charging range.

The electrode-level behavior of "expansion" and "shifting" of the discharge curves provides us with macroscopic information on the contributions of the degradation mechanisms from kinetic effects or changes in the overpotential (which can be caused by electrolyte concentration loss or active material degradation). Generally, a combi-

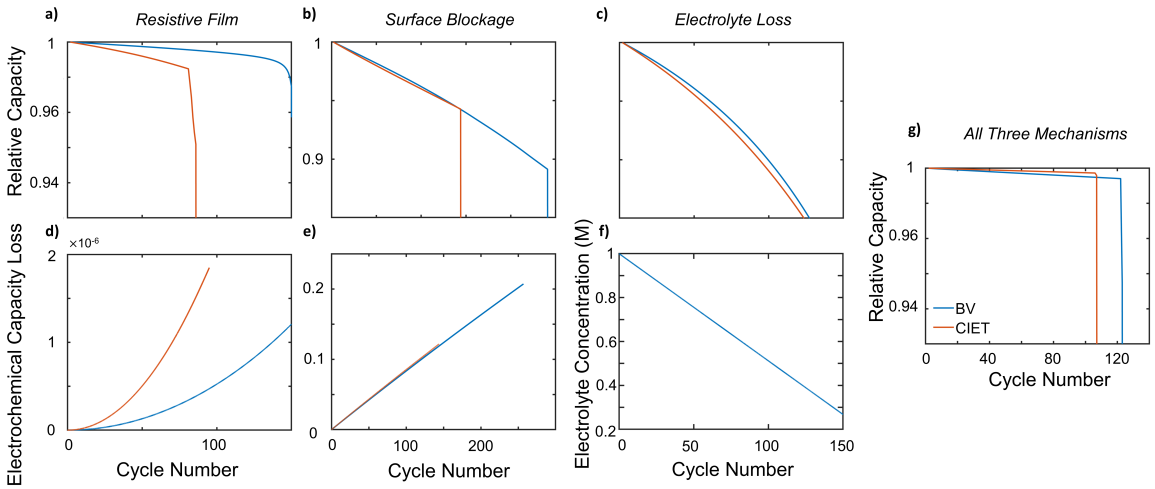

Figure 5: a,b,c) The capacity cutoff for each cycle with respect to the cycle number for BV/CIET is plotted for sets of simulations with the three separate degradation mechanisms in the first row, while the real relative electrochemical capacity loss from the integrated degradation current with respect to the cycle number is plotted in the second row in d) and e). For the electrolyte loss model, because the electrochemical capacity loss is from the anode, we instead plot the prescribed degradation of electrolyte concentration with respect to cycle number in f). g) We plot the capacity loss curve with respect to cycle number for a set of simulations with all three degradation mechanisms implemented for the two reaction models.

nation of these will contribute to the physical degradation of voltage curves. Through observing the expansions and shifts of the degraded charge/discharge curve, we can learn about whether degradation consists of active material degradation or electrochemical changes in kinetics at the surface.

In capacity loss curves, a linear drop in capacity is observed in Fig. 5, which later rolls over into a steeper capacity loss curve when more degradation has accumulated. Each degradation mechanism contributes differently to the terminal behavior of the capacity. The resistance formation mechanism and surface blockage mechanism both cause sharp terminating curves, but the resistive film mechanism is much smoother than that of the surface blockage mechanism. The electrolyte loss mechanism has a smooth and nonlinear drop off as the concentration of electrolyte drops, especially at lower electrolyte concentrations.

The different shapes of these drop offs may be able to give insight into the dom-

inance of different degradation mechanisms from the experimental observation of capacity loss plots. In addition, a set of simulations where all three models were combined was performed, where it can be seen that the dominant degradation mechanism tends to override the capacity loss curve (in, this case, the surface blockage mechanism) in Fig. 5g.

3.4 Appendix: Derivation of the Modified Fokker-Planck Equation

The derivation of Fokker-Planck with resistance evolution in these systems is similar to that of biological evolution with a fitness landscape. In fact, we expect to see the fitness effects more strongly as we apply current/voltage to a control system instead of letting the population evolve naturally as in genetics. Starting from the Langevin equation, we can derive the Fokker-Planck equations needed as follows. The Langevin equation for the filling of a battery particle, assuming no solid diffusion limitation, is

$$V_j \dot{c}_j = -A_j \left(i_j(\Delta\mu) + F_j(i_j) \right), \quad j = 1 \dots N, \tag{24}$$

where V is the total volume of the particle, A is the area of the particle, c is the concentration of the particle, which is the site density of the intercalation material scaled by the maximum site density, $c = \rho/\rho_{s,max}$, i is the reaction rate caused by the difference between the reservoir potential μ_{res} and the particle potential μ, which is related to the driving force $\Delta\mu = \mu_{res} - \mu$, and $F(i)$ is the random force for particle j, which depends on the reaction magnitude i by the fluctuation-dissipation theorem [220, 161]. In a battery particle, we know the volume of a particle scales with the particle size as $V_j \propto r_j^3$ and the surface area scales with the particle size as $A_j \propto r_j^2$, where r_j is the radius of a spherical particle. We can simplify the Langevin equation into

$$\dot{c}_j = -\frac{1}{r_j} \left(i_j + F_j(i_j) \right), \quad j = 1 \dots N. \tag{25}$$

In a reactive system, for $j = 1 \dots N$ particles, every particle obeys the Langevin equation under a total constraint. Reactions happening directly between the particles are assumed to be nonexistent [221] and reactions only happen between the active material particles and the environment.

This constraint is usually some form of constant current or voltage. For constant current, we expect that $\sum_j m_j \dot{c}_{eff,j} = \text{Rxn}_{constraint}$ for applying a current constraint from all particles, or for constant voltage that $\mu_{res} = \mu_{constraint}$ for all particles i.

If we assume that the probability density of particles in the system is at $f(c)$, we can convert this system of Langevin equations into a Fokker-Planck equation (acknowledging that the system is not deterministic from the noise term $F(i)$) [66, 203]. At each concentration variable, we need to take a small time increment such that we can sum the transition rates leaving and arriving at the current concentration as the chemical master equation

$$\begin{aligned} f(t + \Delta t, c; r) = f(t, c; r) + \Delta t \int_0^1 p(c - c', c') f(t, c'; r) W(t, c', r) dc' \\ - \Delta t \int_0^1 p(c', c) f(t, c; r) W(t, c, r) dc'. \end{aligned} \tag{26}$$

Here, $p(x, y)$ is the transition matrix from state y to x before dampening the transition probabilities with the fitness. It needs to be weighed by the changes in the transition state matrix because there is a modified amount of transitions happening from the changes in the fitness variable.

The derivation of Fokker-Planck with resistance evolution in these systems is similar to that of a fitness landscape in genetics. We can start with the chemical master equation, which comes from the continuum limit of the previous equation to derive the full Fokker-Planck equation

$$\frac{\partial f(t, c; r)}{\partial t} = \int^* dc' p(c - c', c') f(t, c'; r) W(t, c', r) - \int^* dc' p(c' - c, c) f(t, c; r) W(t, c, r), \tag{27}$$

and change the integration variable c or c' to the difference between these two variables $y = c - c'$.

We take a Taylor expansion of the system only around the change of concentration variable y. The Taylor expansion on the term in the integral returns

$$\begin{aligned} &p(y, c-y)f(c-y)W(c-y) = p(y,c)f(c)W(c) \\ &- y\frac{\partial}{\partial c}\left(p(y,c)f(c)W(c)\right)\frac{y^2}{2} + \frac{\partial^2}{\partial x^2}\left(p(y,c)f(c)W(c)\right) + ... \end{aligned} \tag{28}$$

We know that there is no flux when there is no concentration change, so then the zeroth order term from the expansion is zero. Thus, only including the first and the second order term of the expansion, we see that the chemical master equation now is converted to the Fokker-Planck equation, which after moving the integrals into the derivative terms is revealed as

$$\frac{\partial f(t,c;r)}{\partial t} = -\frac{\partial}{\partial c}\left[f(c)W(c)\left(\int dyyp(y,c)\right)\right] + \frac{1}{2}\frac{\partial^2}{\partial c^2}\left[f(c)W(c)\left(\int dyy^2p(y,c)\right)\right] \tag{29}$$

to obtain the Fokker-Planck equation we are familiar with. For simplicity in notation, we define the first order term as the reaction rate such that $i = \int_0^1 dc'c'p(c',c)$ to represent the driving velocity from the mean in concentration change from the transition probabilities. The second order term as $D = \int_0^1 dc'c'^2p(c',c)$ represents the fluctuations, or the variance from the concentration change for the transition probabilities. From the definition of the intercalation reaction rate and the definition of a diffusion coefficient explicitly defined above, we see that

$$\frac{\partial f}{\partial t} = -\frac{\partial}{\partial c}\left(fR\right) + \frac{\partial}{\partial c}\left(D\frac{\partial}{\partial c}\left(fW\right)\right). \tag{30}$$

where $D = kk_BT/N_t$ and $k = i/\eta$ for a linear form of the reaction rate mapping to previously electrochemical Fokker-Planck methods. This is the full Fokker-Planck equation with the resistance evolution terms [51, 164, 194, 70].

3.5 Appendix: General Properties of the Fokker-Planck Model

Some general properties need to be defined in these systems. Since we assume there cannot easily be particle size changes in the system, we see that

$$\int_0^1 f(t,c;r)dc = g(r), \tag{31}$$

which is constant with time as the size distribution $g(r)$ of the particles. The average over all the volumes for any property x can be defined as

$$\langle x \rangle = \frac{\int_0^\infty \int_0^1 xr^3 f(t,c;r)dcdr}{\int_0^\infty \int_0^1 r^3 f(t,c;r)dcdr} = \frac{\int_0^\infty \int_0^1 xr^3 f(t,c;r)dcdr}{\int_0^\infty r^3 g(r)dr}, \tag{32}$$

since the volume of each particle is of a different size, which scales with r^3.

3.6 Appendix: Second Order Solution to Resistive Film Model

The second order Taylor expansion to the resistive film model is as below:

$$i = \bar{i} + \left.\frac{\partial i}{\partial R_f}\right|_{R_f=0} R_f + \frac{1}{2}\left.\frac{\partial^2 i}{\partial R_f^2}\right|_{R_f=0} R_f^2 + \mathcal{O}(R_f^3) = \bar{i} + iR_f\frac{\partial \bar{i}}{\partial \eta} + R_f^2\frac{1}{2}\left(\left(\frac{\partial \bar{i}}{\partial \eta}\right)^2 + i\frac{\partial^2 \bar{i}}{\partial \eta^2}\right) + \mathcal{O}(R_f^3). \tag{33}$$

The ratio between the degraded and nondegraded currents in the second order is given by

$$\frac{i}{\bar{i}} = \left(1 - R_f\frac{\partial \bar{i}}{\partial \eta} - R_f^2\frac{1}{2}\left(\bar{i}^{-1}\left(\frac{\partial \bar{i}}{\partial \eta}\right)^2 + \frac{\partial^2 \bar{i}}{\partial \eta^2}\right)\right)^{-1} + \mathcal{O}(R_f^3). \tag{34}$$

The fitness value of the landscape is given by

$$W(t,c,r,R_f) \approx \frac{1}{r}\frac{1}{1-R_f\frac{\partial\bar{i}}{\partial\eta}-R_f^2\frac{1}{2}\left(\bar{i}^{-1}\left(\frac{\partial\bar{i}}{\partial\eta}\right)^2+\frac{\partial^2\bar{i}}{\partial\eta^2}\right)}. \tag{35}$$

The second order model is not used in the simulations, but is given as an example to show how higher order terms would be derived.

3.7 Appendix: Analytical Differential Conductance

The transition state prefactor for the thermodynamically consistent Butler-Volmer equation is

$$k_0(c) = k_0^* c^\alpha (a_+(1-c))^{1-\alpha}, \tag{36}$$

where α is the charge transfer coefficient, a_+ is the electrolyte activity coefficient, and k_0^* is the current rate prefactor. The analytical differential conductances are reported in the following sections where all values are reported in non-dimensionalized form. In these functions, the exchange current density is actually the fitted prefactor [3] that includes the lumped reaction rate prefactors. For coupled ion-electron transfer, the formal overpotential is $e\eta_f = e\eta + k_BT\ln\frac{a_+}{c}$ to satisfy the De Donder relation [129]. In future equations, it is assumed that the overpotential η is nondimensionalized with the dimensional group $\frac{e}{k_BT}$. In this series of equations, the helper function is found to be

$$\text{helper}(\eta_f,\lambda) = \frac{\sqrt{\lambda\pi}}{1+\exp(-\eta_f)}\text{erfc}\left(\frac{\lambda-\sqrt{1+\sqrt{\lambda}+\eta_f^2}}{2\sqrt{\lambda}}\right) \tag{37}$$

and the derivative of the helper function with respect to the formal overpotential is found to be

$$\frac{d\text{helper}}{d\eta_f}(\eta_f,\lambda) = \frac{\sqrt{\pi}\exp(-\eta_f)\sqrt{\lambda}\text{erfc}\left(\frac{\lambda-\sqrt{\eta_f^2+\sqrt{\lambda}+1}}{2\sqrt{\lambda}}\right)+\frac{\left(\exp(-\eta_f)+1\right)\eta_f\exp\left(-\frac{\left(\sqrt{\eta_f^2+\sqrt{\lambda}+1}-\lambda\right)^2}{4\lambda}\right)}{\sqrt{\eta_f^2+\sqrt{\lambda}+1}}}{\left(\exp(-\eta_f)+1\right)^2}. \tag{38}$$

In fact, though $\frac{d\text{helper}}{d\eta_f}(\eta_f, \lambda)$ is not strictly equal to $\frac{d\text{helper}}{d\eta}(\eta_f, \lambda)$, to the first order approximation of a Taylor expansion, if the perturbation to the electrolyte concentration and solid concentration at any given time is small, this solution is correct. The derivation is shown in the following equation

$$\begin{aligned}\frac{d\text{helper}}{d\eta} &= \frac{d\text{helper}}{d\eta_f - k_B T d\ln a_+ + k_B T d\ln c} \\ &= \frac{d\text{helper}}{d\eta_f}\left[1 + k_B T\frac{d\ln a_+}{d\eta_f} - k_B T\frac{d\ln c}{d\eta_f}\right] + \mathcal{O}(\Delta a_{(+)}^2) \\ &\approx \frac{d\text{helper}}{d\eta_f}.\end{aligned} \tag{39}$$

We thus use this approximation for most of our solutions, since perturbations to the electrolyte and solid lithium concentrations are not that large.

The second derivative of the helper function can also be found analytically to be

$$\begin{aligned}\frac{d^2\text{helper}}{d\eta_f^2}(\eta_f, \lambda) = -\frac{1}{2\left(e^{-\eta_f}+1\right)^3}\Bigg(&-4\sqrt{\pi}e^{-2\eta_f}\sqrt{\lambda}\,\text{erf}\left(\frac{\lambda - \sqrt{\eta_f^2+\sqrt{\lambda}+1}}{2\sqrt{\lambda}}\right) \\ &+ 2\sqrt{\pi}e^{-2\eta_f}\left(e^{\eta_f}+1\right)\sqrt{\lambda}\,\text{erf}\left(\frac{\lambda - \sqrt{\eta_f^2+\sqrt{\lambda}+1}}{2\sqrt{\lambda}}\right) \\ &+ \frac{\eta_f^2\left(e^{-\eta_f}+1\right)^2 e^{-\frac{\left(\sqrt{\eta_f^2+\sqrt{\lambda}+1}-\lambda\right)^2}{4\lambda}}\left(\lambda - \sqrt{\eta_f^2+\sqrt{\lambda}+1}\right)}{\lambda\left(\eta_f^2+\sqrt{\lambda}+1\right)} \\ &+ \frac{2\left(e^{-\eta_f}+1\right)^2 e^{-\frac{\left(\sqrt{\eta_f^2+\sqrt{\lambda}+1}-\lambda\right)^2}{4\lambda}}}{\sqrt{\eta_f^2+\sqrt{\lambda}+1}} - \frac{2\eta_f^2\left(e^{-\eta_f}+1\right)^2 e^{-\frac{\left(\sqrt{\eta_f^2+\sqrt{\lambda}+1}-\lambda\right)^2}{4\lambda}}}{\left(\eta_f^2+\sqrt{\lambda}+1\right)^{3/2}} \\ &+ \frac{4\left(e^{\eta_f}+1\right)\eta_f e^{-\frac{\left(\sqrt{\eta_f^2+\sqrt{\lambda}+1}-\lambda\right)^2}{4\lambda}-2\eta_f}}{\sqrt{\eta_f^2+\sqrt{\lambda}+1}}\Bigg).\end{aligned} \tag{40}$$

Model	Reaction Model $i(c)$	$\frac{\partial \bar{i}}{\partial \eta}$	$\frac{\partial^2 \bar{i}}{\partial \eta^2}$
Butler-Volmer	$k_0(c)\left(\exp\left(-\alpha\eta\right) - \exp\left((1-\alpha)\eta\right)\right)$	$-k_0(c)\left(\alpha\exp\left(-\alpha\eta\right) + (1-\alpha)\exp\left((1-\alpha)\eta\right)\right)$	$k_0(c)\left(\alpha^2\exp\left(-\alpha\eta\right) - (1-\alpha)^2\exp\left((1-\alpha)\eta\right)\right)$
Coupled Ion Electron Transfer	$k_0^*(1-c)\left(a_+\text{helper}(-\eta_f,\lambda) - c\text{helper}(\eta_f,\lambda)\right)$	$-k_0^*(1-c)\left(a_+\frac{d\text{helper}}{d\eta_f}(-\eta_f,\lambda) + c\frac{d\text{helper}}{d\eta_f}(\eta_f,\lambda)\right)$	$k_0^*(1-c)\left(a_+\frac{d^2\text{helper}}{d\eta_f^2}(-\eta_f,\lambda) - c\frac{d^2\text{helper}}{d\eta_f^2}(\eta_f,\lambda)\right)$

3.8 Appendix: Partial Derivatives

3.8.1 Film Resistance

For the film resistance model, the partial derivative with respect to the film resistance can be found as

$$\frac{\partial i}{\partial R_f} = \frac{\partial i}{\partial \eta}\frac{\partial \eta}{\partial R_f} = i\frac{\partial \bar{i}}{\partial \eta}, \tag{41}$$

which naturally evokes the value of the differential conductance. The Taylor expansion of the system with respect to R_f is

$$i = \bar{i} + \left.\frac{\partial i}{\partial R_f}\right|_{R_f=0} R_f + \mathcal{O}(R_f^2) = \bar{i} + iR_f\frac{\partial \bar{i}}{\partial \eta} + \mathcal{O}(R_f^2), \tag{42}$$

where all derivatives are evaluated at no degradation (we will neglect the evaluation terms for some future derivatives). By combining terms and dividing by $\bar{i}$, we see that

$$\frac{i}{\bar{i}} = \frac{1}{1 - R_f\frac{\partial \bar{i}}{\partial \eta}} + \mathcal{O}(R_f^2), \tag{43}$$

which gives

$$W = \frac{1}{r}\left(1 - R_f\frac{\partial \bar{i}}{\partial \eta}\right)^{-1} + \mathcal{O}(R_f^2). \tag{44}$$

For a symmetric Butler-Volmer model, it becomes more convenient to separate the prefactor effect and the driving force effect as $i = k_0(c)h(c,\eta)$. Thus, we can expand the system as

$$\frac{i}{\bar{i}} = \frac{k_0}{\bar{k}_0}\frac{h}{\bar{h}} = \frac{h}{\bar{h}}. \tag{45}$$

When linearizing a symmetric Butler-Volmer model, a Taylor expansion of the driving force term shows that

$$h(\eta, i, R_f) = \bar{h}(\eta)\left[\left(\sum_{k=2n,n\in\mathbb{N}} \frac{(\alpha i R_f)^k}{k!}\right) + \left(\sum_{k=2n+1,n\in\mathbb{N}} \frac{(\alpha i R_f)^k}{k!}\right)\coth\alpha\eta\right]. \tag{46}$$

We see that to the first order,

$$W = \frac{1}{r}\left[1 + \alpha i \coth\left(\alpha\eta\right) R_f\right] + \mathcal{O}(R_f^2) \tag{47}$$

3.8.2 Appendix: Surface Blockage

For the surface blockage model, we separate the reaction rate effects into the prefactor effects from $k_0(c)$ and the reaction effects from $h(\eta)$. Similarly to the approximation for resistance formation (but using h instead of i), a Taylor expansion can be performed on $h(\eta)$ with respect to $\tilde{c} - 1$ so that

$$h = \bar{h} + \left.\frac{\partial h}{\partial \tilde{c}}\right|_{\tilde{c}=1} (\tilde{c} - 1) + \mathcal{O}(\tilde{c}^2) \approx \bar{h} + \frac{c(1-\tilde{c})}{(\tilde{c}-1)^2}\frac{\partial \mu_c}{\partial c}\frac{\partial \bar{h}}{\partial \eta}. \tag{48}$$

Again, we see a form of differential conductance appear in this solution, since the differential conductance without the transition state prefactor can be obtained with the following relation

$$\frac{\partial h}{\partial \tilde{c}} = \frac{\partial h}{\partial \eta}\frac{\partial \eta}{\partial \tilde{c}} = -\frac{c}{\tilde{c}^2}\frac{\partial \mu_c}{\partial c}\frac{\partial \bar{h}}{\partial \eta}. \tag{49}$$

If we divide both sides of Eq. 48 by $\bar{h}$, we see that the ratio of the degraded to nondegraded reaction rate without the prefactor is found to be

$$\frac{h}{\bar{h}} \approx 1 + \frac{1}{\bar{h}}\frac{c(1-\tilde{c})}{\tilde{c}^2}\frac{\partial \mu_c}{\partial c}\frac{\partial \bar{h}}{\partial \eta}. \tag{50}$$

In addition, the effects from $k_0(c)$ are shown as

$$\frac{k_0(c)}{\bar{k}_0(c)} = \frac{\tilde{c} - c}{1 - c} \tag{51}$$

for CIET and

$$\frac{k_0(c)}{\bar{k}_0(c)} = \left(\frac{\tilde{c} - c}{1 - c}\right)^{1-\alpha} \tag{52}$$

for the BV reaction. Combining the two effects, we see that the fitness for the surface blockage model is

$$W \approx \frac{1}{r}\left(\frac{\tilde{c}-c}{1-c}\right)^n \left(1+\frac{1}{\bar{h}}\frac{c(1-\tilde{c})}{\tilde{c}^2}\frac{\partial \mu_c}{\partial c}\frac{\partial \bar{h}}{\partial \eta}\right), \tag{53}$$

where $n = 1-\alpha$ for BV and $n = 1$ for CIET. The effects of the latter term can be neglected if we focus on surface effects, so the approximation is

$$W = \frac{1}{r}\left(\frac{\tilde{c}-c}{1-c}\right)^n + \mathcal{O}\left((1-\tilde{c})^2\right). \tag{54}$$

3.8.3 Appendix: Electrolyte Loss

For the electrolyte loss model, we operate exactly as we did in the surface blockage model, separating the reaction into the prefactor and the driving force components $i = k_0 h$ for a Butler-Volmer system. We can separate the contributions from the transition state (performing a Taylor expansion on $c_+ - 1$) and the non-transition state effects

$$h = \bar{h} + \left.\frac{\partial h}{\partial c_+}\right|_{c_+=1}(c_+-1) + \mathcal{O}(\tilde{c}^2) \approx \bar{h} + \left.\frac{\partial h}{\partial \eta}\right|_{c_+=1}\left.\frac{\partial \eta}{\partial c_+}\right|_{c_+=1}(c_+-1) = \bar{h} + \frac{k_B T}{e}\frac{\partial \ln a_+}{\partial \ln c_+}\frac{\partial \bar{h}}{\partial \eta}(1-c_+). \tag{55}$$

For the overpotential for BV, $\frac{\partial \eta}{\partial c_+} = -\frac{k_B T}{e c_+}\frac{\partial \ln a_+}{\partial \ln c_+}$, while for a coupled-ion electron transfer kinetic system, there is no dependence on formal overpotential on the electrolyte concentration ($\frac{\partial \eta_f}{\partial c_+} = 0$). We also define the thermodynamic factor as $\frac{\partial \ln a_+}{\partial \ln c_+}$, which will be used in concentrated solution models [122]. We see that

$$\frac{h}{\bar{h}} = \left[1 + \frac{1}{\bar{h}}\frac{\partial \ln a_+}{\partial \ln c_+}\frac{k_B T}{e}\frac{\partial \bar{h}}{\partial \eta}(1-c_+)\right], \tag{56}$$

and since $\frac{k_0}{k_0} = a_+^{1-\alpha}$, easily

$$W = \frac{a_+^{1-\alpha}}{r}\left[1 + \frac{1}{\bar{h}}\frac{\partial \ln a_+}{\partial \ln c_+}\frac{k_B T}{e}\frac{\partial \bar{h}}{\partial \eta}(1-c_+)\right]. \tag{57}$$

For a coupled-ion electron transfer reaction, a Taylor expansion needs to be per-

formed directly on the electrolyte concentration on i since the effect of the electrolyte is convoluted throughout the reaction rate. We obtain

$$i = \bar{i} + \frac{di}{dc_+}(c_+ - 1) + \mathcal{O}\left((1 - c_+)^2\right) \tag{58}$$

where the full derivative of the current with respect to electrolyte concentration is

$$\frac{di}{dc_+} = \frac{\partial i}{\partial \eta_f}\frac{\partial \eta_f}{\partial c_+} + \frac{\partial i}{\partial c_+}, \tag{59}$$

with the differential conductance seen again. Since there is no dependence of the electrolyte concentration on the formal overpotential approximation ($\frac{\partial \eta_f}{\partial c_+} = 0$), the electrolyte concentration dependence purely affects the reduction reaction in the coupled-ion electron transfer formulation $\frac{\partial i}{\partial c_+} = \frac{i_{red}}{c_+}\frac{\partial \ln a_+}{\partial \ln c_+}$, where $i_{red} = k_0^*(1-c)a_+\text{helper}(-\eta_f, \lambda)$ is the reduction contribution to the driving force. For a Stefan-Maxwell formulation, we see that

$$\frac{di}{dc_+} = i_{red}c_+^{-1}\frac{\partial \ln a_+}{\partial \ln c_+}, \tag{60}$$

and thus, we see that

$$\frac{i}{\bar{i}} = \left[1 - \frac{\bar{i}_{red}}{\bar{i}}\left(1 - c_+\right)\frac{\partial \ln a_+}{\partial \ln c_+}\right], \tag{61}$$

which gives

$$W = \frac{1}{r}\left[1 - \frac{\bar{i}_{red}}{\bar{i}}\left(1 - c_+\right)\frac{\partial \ln a_+}{\partial \ln c_+}\right] + \mathcal{O}\left(((1 - c_+)^2\right). \tag{62}$$

3.9 Appendix: Simulation Parameters

An open circuit voltage model from Ref. [5] was used for the NMC532 solid active material. A constant exchange current density of $k_0^* = 10\,\text{A/m}^2$ for the intercalation reaction, while the reorganization energy in MHC/Marcus kinetics was found to be $3.78\,\text{k}_\text{B}\text{T}$ [129]. The thermal diffusivity parameter in the system D_0 was set to be $0.05\,\text{k}_\text{B}\text{T}$, and the degradation reaction formation voltage was set to $4.1\,\text{V}$ for all degradation mechanisms considered [83]. The generalized Butler-Volmer reaction rate [69] or coupled ion electron transfer reaction [128] were used to model

the electrochemical ion insertion reaction. A current control system with a C-rate of 1 C was used in each of the model systems starting at a concentration of 0.45, charging from 3.7 V to 4.1 V until the battery dies. Discretizations of 0.002 for the concentration and 10 nm were used for the radius, which was discretized from 10 nm to 300 nm. A normal distribution with an average of 100 nm and a variance of 100 nm was selected to perform this set of simulations, which is an abnormally large distribution used so that a wide variance of particle sizes could be sampled. For electrolyte, a dilute solution model of 1 M is used. The BV reaction rate as well as the localized and delocalized electron limits of CIET were used to study this system, which are displayed in Appendix A. The fitness values were used with the approximation from Eq. 14. The scripts used to run this set of simulations can be found in the public repository *lightningclaw001/public_paper_scripts* under the folder *fitness_distribution* (`https://github.com/lightningclaw001/public_paper_scripts/tree/main/fitness_distribution`) for the different models.

The degradation parameters are listed below. A resistivity of $1\,\Omega \cdot \mathrm{m}^4/\mathrm{C}$ was used in the resistive film simulations for the film material. The exchange current density of the degradation reaction for the BV reaction for resistive film formation was set to $0.04\,\mathrm{A/m^2}$, while for the CIET reaction it was set to $0.2\,\mathrm{A/m^2}$. The exchange current density of the degradation reaction $k_{0,deg}$ was set to $0.03\mathrm{A/m^2}$ for the surface blockage mechanism reactions. For the electrolyte loss reaction mechanism, the coefficient for electrolyte loss k was set to $0.003\,\mathrm{M/hr}$. The capacity loss and electrolyte loss models were chosen so that 90% of the original capacity is achieved roughly at the end of lifetime.

For all degradation models, the total intercalation current is then found to be

$$\langle \mathrm{Rxn}_{int} \rangle = \frac{d\langle c \rangle}{dt} = \frac{\int_0^\infty \int_0^1 c r^3 \frac{df}{dt} dc dr}{\int_0^\infty r^3 g(r) dr} \tag{63}$$

integrated over the total volume of the system, where $g(r) = \int_0^1 f(c, r) dc$ is the constant probability distribution of the particle sizes. The total degradation current

is then similarly found to be

$$\langle \mathrm{Rxn}_{deg} \rangle = \frac{\int_0^\infty \int_0^1 cr^2 i_{deg} dc dr}{\int_0^\infty r^3 g(r) dr} = \frac{\int_0^\infty r^2 \langle i_{deg} \rangle g(r) dr}{\int_0^\infty r^3 g(r) dr}, \tag{64}$$

since in the system, we only calculate the averaged amount of degradation over all particles of the same size $g(r)$. Thus, the total applied current in the system is system is found to be $\langle \mathrm{Rxn}_{constraint} \rangle = \langle \mathrm{Rxn}_{int} \rangle + \langle \mathrm{Rxn}_{deg} \rangle$.

Because the Butler-Volmer reaction grows exponentially as the overpotential in the system increases, the large values of the overpotential cause artificial numerical errors to be introduced because of the magnitude of reaction rates at high overpotentials. Thus, it becomes necessary to add a damping function multiplied to the reaction rates at the high overpotential terms to prevent this from happening, causing the Fokker-Planck equation to become

$$\frac{\partial f}{\partial t} = -\frac{\partial}{\partial c}\left(f i W \zeta\right) + \frac{\partial}{\partial c}\left(D \frac{\partial}{\partial c}\left(f W \zeta\right)\right) \tag{65}$$

Because the material is not thermodynamically phase separating, there is a very low density of the population at these high overpotential concentrations, so the damping function does not affect the solution of the system. We choose a damping function

$$\zeta(\eta, z) = \frac{1}{2}\left(\tanh\left(-(|\eta| - z)\right) + 1\right), \tag{66}$$

where z is the cutoff value for the overpotential, which we set to $z = 8\,\mathrm{k_B T}$. This damping function is symmetric with respect to $\eta = 0$ and dampens the overlarge values of reaction rate caused by the unphysically high overpotential from Butler-Volmer.

Because of the difficulty of numerically solving the reaction rate for many implicit solutions as would be required especially for a model with the resistive film buildup, we instead turn to our analytical approximations performed in Sec. 3.2.4 and use the $\mathcal{O}(3)$ approximation for the Butler-Volmer equation in Eq. 12, and the $\mathcal{O}(2)$ approximation for the coupled ion electron transfer solution in Eq. 14 for the Fokker-

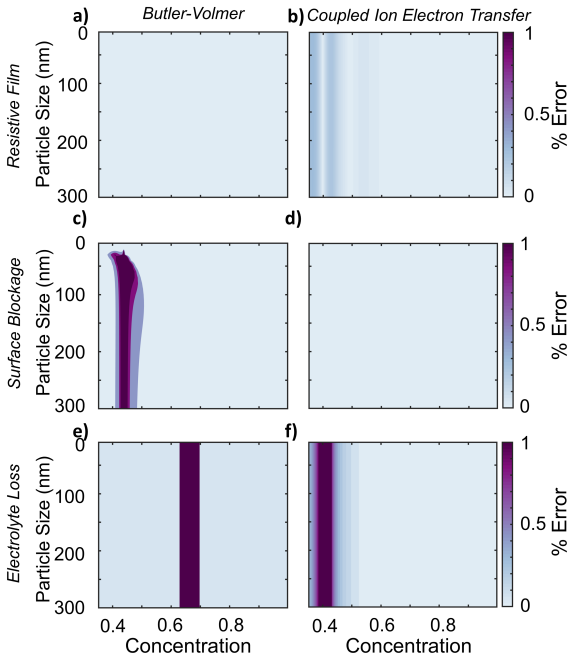

Figure 6: The percentage errors of the analytical solutions are plotted below for each reaction mechanism and degradation mechanism.

Planck Eq. 2. The errors to the numerical approximations are shown in Appendix 3.10. The other degradation mechanisms of surface blockage and electrolyte loss have simpler equations to solve and do not need implicit solutions for the intercalation rates, so their full solutions to Eq. 1 are used in the simulations. In the full model with all three degradation models, since it is necessary to solve the implicit reaction rate, we apply the approximations to the fitness function in Eqs. 22 and 23.

3.10 Appendix: Numerical Error

The $\mathcal{O}(4)$ error for the Butler-Volmer resistance reaction or the $\mathcal{O}(2)$ error for the other reaction rates and degradation mechanisms are shown in Fig. 6 for the approximate solutions to the analytical solutions. The exact degradation mechanisms are simulated for the surface blockage and the electrolyte loss solutions, but the error of the analytical solutions are provided for reference.

Chapter 4

Degradation from Single Particle to Electrode Level (Phase Separating)

Scaling analysis of mosaic phase separation in Li-ion batteries [14]

Methods of statistical physics [222, 223, 224, 225] enable the description of emergent macroscopic phenomena for interacting ensembles, as in liquids and glasses [226, 227] or population genetics [228]. Despite their importance, the understanding of these many-body systems remains incomplete, especially for open systems driven far from equilibrium [229, 164]. Lithium ion batteries and other engineered devices often belong to this class of systems, where macroscopic control can be exerted (e.g. current or voltage), but the non-equilibrium thermodynamics of particle-level heterogeneities (local compositions and phases) cannot be controlled.

These particle level heterogeneities in lithium ion batteries consist of electrochemically active particles ranging in size from nano to micrometers [230, 231], which participate in electrochemical reactions. Lithium ion-electron pairs intercalate into or out of active material particles, which enables reversible storage of electrochemical energy. Many of these materials phase separate into high and low lithium concen-

The present chapter is based on my submitted work [14].

tration phases during (de)intercalation, such as graphite [232, 233, 234, 91, 235, 10, 236, 237, 238], lithium iron phosphate (LFP) [239, 240, 8, 50, 241, 242], lithium titanate (LTO) [243, 244], lithium titania anatase [245] and lithium cobalt oxide (LCO) [246, 247], introducing intriguing coupled behavior such as voltage oscillations and history dependence [65, 13, 51, 49]. In these electrodes, total current or voltage control is applied on a macroscopic scale, reflecting that of a population of battery particles. Thus, the macroscopic feedback of such devices is dependent on the response of many microscopic particles.

Experimental observations in LFP [8] and graphite [238] porous electrodes have shown that the fraction of particles carrying the majority of the electrochemical current, deemed the active particle fraction, responds significantly to the magnitude and direction of the applied current. Such behavior includes a transition from particle-by-particle intercalation, which indicates a low active particle fraction, to concurrent intercalation [8], indicating high active particle fraction, where increased current results in the activation of a greater population of the electrode. The effect of the current on this transition suggests that nonequilibrium dynamics are responsible.

To investigate these dynamics, linear stability analysis of a single lithium iron phosphate particle [67, 164] reveals the suppression of phase separation at high discharge rates. Specifically at high rates, where nonequilibrium effects are introduced, suppression is caused by explicit concentration dependence (autocatalysis) [164, 51] in the reaction rates. This leads to kinetically-driven phase separation in the single particle stability factor from competition between solid diffusion and autocatalysis driven by reactions. Beyond single particle stability, macroscopic phase separation introduces non-uniform intercalation between particles [8], requiring population scale investigation in the nonlinear regime. Population balance models [51, 193] have been applied to investigate the (dis)charge behavior of phase separating particle populations. Thermodynamically, bimodal and unimodal regimes appear in the concentration distribution with increasing applied current as observed from simulations [193]. Thus, we aim to investigate the active particle fraction, which characterizes the behavior of phase separating populations [238, 8], whose physical interpretation remains

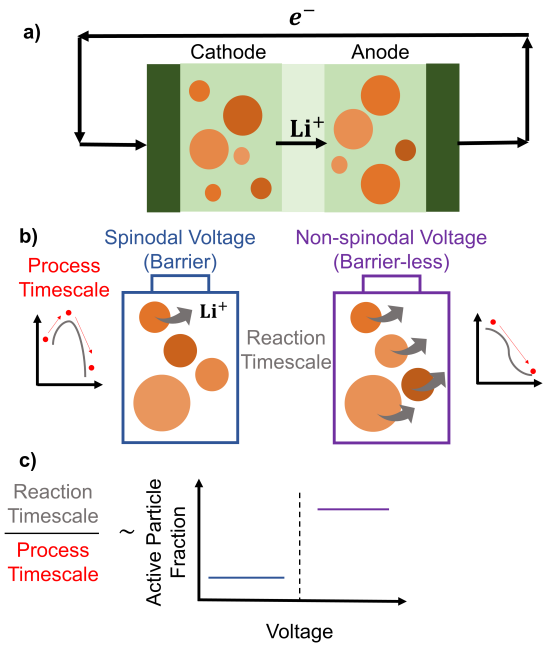

Figure 1: a) Example image of a lithium ion battery electrode, with many particles in both the cathode and anode that participate in electrochemical reactions. b) Different regimes of behavior are observed based on whether values in the spinodal voltage or larger voltages are applied, where particle-by-particle or concurrent [8] behavior can be observed. The particle-by-particle behavior is from the appearance of an nonequilibrium energy barrier in the region with an effective energy barrier, while the concurrent behavior is deterministic because there is no barrier. c) The active particle fraction, which relates the reaction timescales to the process timescales, can be low or high depending on the timescale interplay between the macroscopic and microscopic. The low active particle fraction region corresponds to the region with a barrier, while the high active particle fraction region corresponds to a barrier-less transition.

to be fully elucidated.

To investigate these problems, many particle simulations of phase separating electrodes [55, 10] have been performed using multiphase porous electrode theory [44], validating experimental observations of voltage oscillations [65] and asymmetry in active particle fraction [8] between charge and discharge. Specifically, activation behavior in simulations of these populations has been found to change with thermodynamic barrier height in the spinodal gap for the chemical potential [8]. While the phenomenology observing the transition has been established, the underlying mathematical theory driving these nonequilibrium transitions remains to be fully under-

stood. There is no simple theory to aid direct design of increased utilization through active particle fraction in electrodes.

Here, we aim to formulate a mathematical theory for predictive analysis of increased activation in electrodes. Scaling analyses are utilized to shed light on population timescale competition. In single particles of phase-separating electrode materials, such as LFP [50, 248] and graphite [91], the competition between the reaction, applied current (process), and diffusion timescales in a single particle for a phase separating material lead to various regimes of intercalation patterns, such as core-shell and intercalation wave behavior [3]. Additionally, coupled ion-electron transfer (CIET) reactions [249, 128] can directly control surface pattern formation by electro-autocatalysis [164]. However, since many-particle systems are nonlinear, single-particle scaling analyses are insufficient for determining the behavior of a multi-particle system. Scaling analyses derived from population balances predict timescale competition on a multi-particle scale through the active particle fraction, enabling direct prediction of a transition between stochastic and deterministic regimes.

The active particle fraction scales with the ratio between the single particle reaction timescale and the many particle process timescale, found to be asymmetric between charge/discharge. Our predicted analytical results are validated by comparison with multiphase porous electrode theory simulations [43], electrochemical measurements [9], and *operando* x-ray diffraction experiments [8], matching timescale trends and observed asymmetries between charge and discharge in the active particle fraction. This highlights the significant role played by nonequilibrium barriers and stochastic effects in determining population behavior, particularly within the spinodal gap.

4.1 Theory

4.1.1 Single Particle Model

Lithium ion batteries utilize active material particles ranging from nano to micrometer size at electrodes for energy storage and release with electrochemical reactions. Electrolyte solutions containing lithium ions facilitate current flow between the spatial distribution of the electrodes, which is incorporated into electrode-scale modeling [43]. However, even at the same electrolyte volume, population effects can be observed. We focus on a spatial volume where the bath is assumed to be homogeneous, and each particle is in contact with an electrolyte reservoir, whose potential can be controlled externally through μ_{res}, the reservoir potential in the electrolyte. For a system without transport effects, the reservoir potential essentially the applied voltage in a lithium ion battery. Electrochemical reactions on the surface and solid diffusion in the bulk drive the (de)intercalation process in the electrode. The intercalated lithium ion conservation equation in each particle n can be written as

$$\dot{c}_n = -\nabla \cdot \mathbf{j}_n, \tag{1}$$

describing the nondimensionalized concentration of lithium in the active material c with the flux $\mathbf{j}_n = -Dc/k_BT \ \nabla\mu$, driven by the chemical potential μ gradient and parameterized by the solid diffusivity D. We apply a reaction boundary condition of $-\mathbf{n} \cdot \mathbf{j}_n = i_n(c, \mu_{res})$ where $\mathbf{n}$ is the direction normal to the particle surface pointing outward and $i_n(c, \mu_{res})$ is the surface reaction rate dependent on intercalated lithium ion concentration and electrolyte bath potential [69].

Integrating Eq. 1 over the particle volume V and defining $\bar{c}_n = V^{-1} \int_V c_n dV$ as the average particle concentration, A as the surface, and $L \sim V/A$ as the characteristic length, we observe that the conservation equation can now be written as

$$\dot{\bar{c}}_n = V^{-1} \oint_A i(\bar{c}_n, \mu_{res}) dA + V^{-1} \oint_A \left(i(c_n, \mu_{res}) - i(\bar{c}_n, \mu_{res}) \right) dA. \tag{2}$$

Here, the differences from surface concentration to bulk introduce error in the bulk-averaged equation for concentration, found to be

$$\xi_n = V^{-1} \oint_A \left(i(c_n, \mu_{res}) - i(\bar{c}_n, \mu_{res})\right) dA, \tag{3}$$

which is highly history-dependent, changing based on diffusion limitations between the surface and bulk as well as between different regions on the surface. The appearance of this error is from the difference in surface concentration to average concentration in the particle, which can be driven by either spatial heterogeneities or diffusion limitations. For this model, the error, which we will further introduce as noise, is only induced by error in the model from neglecting diffusion limitations. Spatial heterogeneities can also induce noise, which is not explicitly included in the Langevin equation modeled.

Thus, for a 1D particle, assuming all future c_n refer to the average concentration, and applying the volume averaged reaction rate $R = V^{-1} \oint_A i dA$, the conservation equation for a battery particle is analogous to a Langevin equation where the white noise is driven by spatial heterogeneity of concentration

$$\dot{c}_n = R(c_n, \mu_{res}) + \xi_n. \tag{4}$$

This model is driven by the reaction rate R, which is dependent not only on the concentration c_n, but also on the reservoir chemical potential μ_{res}. The formula of the reaction rate is expounded in Sec. 4.1.4.

Using our general mass conservation equation in Eq. 2 by comparing the reaction rate to diffusivity, the maximum deviation of surface to bulk concentration is found to scale with the timescale ratio between single particle diffusion and reaction, $\Delta c \sim \tau_D/\tau_R$ [3]. If we perform a Taylor expansion on the magnitude of the noise from Eq. 3, the noise is thus bounded by the single particle reaction-diffusion timescale competition [3] such that $\xi \leq \left|\frac{dR}{dc}\frac{\tau_D}{\tau_R}\right|$. The time dependent solution from an analytical approximation to the reaction-diffusion equation can be found in Appendix 4.5, where a colored noise with a timescale of τ_R can be used as an approximation.

Using proper reaction models, the mass conservation in a reaction-limited phase separating single particle can be mapped to the problem of motion of a Brownian particle in a potential well [250]. Brownian motion is often modeled using the Langevin equation [251, 252], where motion is driven by a potential gradient and includes a white noise process as in Eq. 1.4 in Ref. [250]. The spatial potential gradient is the main driving force for movement in the particle.

The equilibrium thermodynamics of a single phase separating particle is well characterized [241]. However, the nonequilibrium energy barrier is distinct from the equilibrium miscibility gap, where both barriers are plotted in Fig. 2a for a linear reaction rate. Comparing Eqs. 4 and the Langevin equation for Brownian motion, the nonequilibrium barrier from integrated reaction rates is found to be the potential $R \sim -\nabla\Phi$, assuming that the integrated reaction rates are path-independent and the noise is near memory-less [251]. For simple linear reaction rates, the potential can be found analytically (shown in Fig. 2a later in the manuscript), while for nonlinear reaction rates, the direct potential cannot be integrated. However, potential differences and their derivatives are found through the integrated reaction rate such that

$$\Phi(c_f) - \Phi(c_0) = -\int_{c_0}^{c_f} R(c, \mu_{res}) dc \tag{5}$$

from the final concentration c_f to the initial concentration c_0. This provides an estimation of the nonequilibrium transformation barrier at any applied voltage for a single particle, similarly to Ref. [164]. The shapes of the potential well and the barrier heights control the timescales of the transformation process.

4.1.2 Many Particle Model

An averaged conservation equation (Eq. 4) for each of the particles can be constructed. However, when dealing with a large number of particles, the number of variables increases quickly and makes calculations intractable, necessitating various forms of averaging. By eliminating fast variables [253], the number of variables can be significantly reduced to a set of "slow" macroscopic descriptors, aligning with ther-

modynamic observations [254]. Integration can be performed by elimination of fast variables through projection operations [255, 252, 254, 224]. These methods are applicable only if the autocorrelation time of the Langevin noise is much smaller than the timescales of large variation [253]. For stochastic differential equations [256], this implies that the timescale of the noise term must be substantially shorter than that of the driving force.

In a reacting particle which is reaction limited, this assumption indicates that the difference in reaction rate from the exact surface concentration to the averaged bulk concentration is small. This condition ensures that no additional timescales, such as solid diffusion, convolute the integration of the reaction timescale, which is true for most battery materials and particle lengthscales except graphite platelets [3]. If this condition is satisfied, we can map this system to a Fokker-Planck equation to describe a reaction limited system of particles [13], shown in the projection operation in Appendix 4.6. Assuming white noise, this equation can be described with the operator $\mathcal{L}_D$, describing the evolution of the population given an initial distribution as

$$\frac{\partial f}{\partial t} = \mathcal{L}_D f = \frac{\partial (fR)}{\partial c} + \frac{\partial}{\partial c}\left(D_c \frac{\partial f}{\partial c} \right), \tag{6}$$

where the diffusivity D_c is analogous to the thermal diffusivity [51], which is related to the Langevin noise magnitude through the fluctuation dissipation theorem [252], $2D_c\delta(t-t') = \langle \xi(t)\xi(t') \rangle$, if the noise is assumed to be white. (The exact solution finds that the noise is colored, indicated in Appendix 4.5, but the magnitudes are quite small).

Error bounds on the Langevin equation inform the noise magnitude in the Fokker-Planck equation. From the bounds of the Langevin equation, we see that the magnitude of the noise in the Fokker-Planck equation is bounded by the values in the Langevin equation as $D_c \leq \frac{1}{2}\left(\frac{dR}{dc}\frac{\tau_D}{\tau_R}\right)^2$. From Ref. [3] and the expected magnitude of the stability function, the magnitude of the diffusivity is expected to be $\mathcal{O}(10^{-1}) \sim \mathcal{O}(10^{-15})$ s^{-1} depending on intercalation material and applied C-rate.

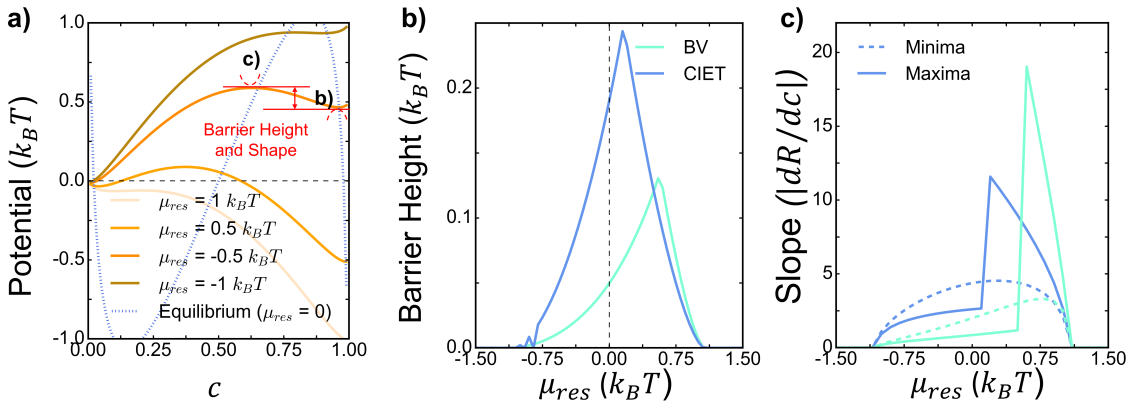

Figure 2: a) Potential barrier for a linear reaction rate as an example displaying the energy barriers at different applied voltages. The equilibrium thermodynamic barrier is plotted in dotted blue for reference. b) Different barrier heights are shown for the Butler-Volmer and coupled ion-electron transfer reaction rates at different applied voltages. c) The absolute value of the single particle stability criterion of the maxima and non-global minima are plotted for different potentials for the BV and CIET models. A clear asymmetry is seen in the evaluation of the slopes between charge and discharge.

4.1.3 Extraction of Process Timescales

The equilibrium solution to the Fokker-Planck equation can be found from properties of the operator $\mathcal{L}_D$ governing of the evolution of population dynamics [250, 257]. The solution can be expanded around its eigenfunctions, where the equilibrium solution corresponds to the eigenvalue with value zero [258]. Importantly, the timescale in which the equilibrium limit is reached is determined by the first nonzero eigenvalue of the operator. The timescale is proportional to the inverse of the first nonzero eigenvalue, $\tau = -1/\lambda_1$, suggesting that for each applied voltage, a process timescale representing a C-rate can be extracted.

We observe that the effective nonequilibrium potentials as derived in Eq. 5 for our particle exist in two possible regimes. The first arises when there are two local minima and an energy barrier separating them. This region occurs when the applied voltage is within the miscibility gap and is caused by a metastable concentration solution for zero reaction. This metastable concentration introduces a local maxima in the nonequilibrium barrier, differing from the equilibrium barrier, as in Fig. 2a. In this regime, results are stochastic, as noise is required to initiate barrier hopping for

individual particles. This regime corresponds to particle-by-particle intercalation [8]. In the other limit, at voltages that are outside the miscibility gap, there is no energy barrier. This regime is deterministic as no barrier crossing is required. Thus, two different timescales are extracted from these regimes.

In the stochastic regime, methods analogous to those for solving the Brownian particle problem can be applied to the intercalation process, where the transformation timescales depend on potential differences. For lithium iron phosphate, based on a boundary layer expansion [250], the first nonzero eigenvalue is found to be

$$\lambda_s \sim -\frac{\sqrt{dR/dc(c_{\max})|dR/dc(c_{\min})|}}{2\pi} \exp\left(-D_c^{-1}\int_{c_{\min}}^{c_{\max}} R(c)dc\right), \tag{7}$$

where s indicates the stochastic regime. Here, $c_{\min}$ and $c_{\max}$ are the non-global minima or maxima of the potential, both found when the reaction rate is zero ($R(c_{\min,\max}, \mu_{res}) = 0$). This is analogous to Kramer's problem of barrier crossing [259]. From the eigenvalues, the timescale in the stochastic region appears as

$$\tau_s \sim \frac{2\pi}{\sqrt{dR/dc(c_{\max})|dR/dc(c_{\min})|}} \exp\left(D_c^{-1}\int_{c_{\min}}^{c_{\max}} R(c)dc\right). \tag{8}$$

The barrier height of the potential as well as the curvature of the maxima and minima control the passage time from the local to the global minima [260] in transition state theory.

The barrier height can be obtained from the integrated reaction rate between the local minima and maxima, plotted in Fig. 2a for the Butler-Volmer and coupled ion electron transfer reaction rates, where the reaction rates are described in Section 4.1.1. The different barrier magnitudes in the stochastic regime are shown in Fig. 2b at varying applied voltages. While the magnitude of the barrier is expected to affect behavior within the spinodal gap, the stability criterion of the reaction [164] (the slope of the kinetics) also influences observed macroscopic asymmetries between charge and discharge. The curvature of the maxima and minima are found from the slope of the reaction kinetics when the rate is zero. The curvature of the potential happens to

be the single particle stability criteria [164], used in Ref. [67] to indicate whether a single particle will phase separate. Suppression of phase separation at discharge is predicted from a single particle model of lithium iron phosphate.

Similarly, the population scale model predicts significantly shorter timescales for relaxation during the discharge process as observed in Fig. 3c from larger magnitudes of the single particle stability criterion at the local maxima. In a broader sense, in the stochastic region, this suggests that the discharge process is more stable relative to charge at a population scale due to the longer timescales required to achieve equilibrium, driven by single particle stability at the local maxima.

In the deterministic regime, when no nonequilibrium energy barrier exists, similar approximations can be applied to find that the eigenvalues are deterministic [261, 262]. The deterministic timescale is directly found to be

$$\tau_d \sim -0.5 D_c^{-1} \left(\int_{c_0}^{c_f} R(c) dc \right)^{-1}, \tag{9}$$

where d indicates deterministic, outside the voltage range corresponding to the spinodal gap. This timescale coincides with the concurrent intercalation mechanism [8].

An equality boundary condition between the deterministic and stochastic timescales when there is no nonequilibrium potential barrier can be applied. This is denoted by the critical applied voltage $\mu_{res,crit}$ such that

$$\tau_d(\mu_{res,crit}) = \tau_s(\mu_{res,crit}). \tag{10}$$

The combination of these two timescales indicate the introduction of a piecewise process timescale, where the stochastic timescale is observed if the applied voltage corresponds to the spinodal gap, while the deterministic one is observed if not,

$$\tau_p = \begin{cases} \tau_s & |\mu_{res}| \leq \mu_{res,crit} \\ \tau_d & |\mu_{res}| > \mu_{res,crit} \end{cases}. \tag{11}$$

The selection of which timescale should be calculated depends on whether the voltage

is in the spinodal gap. This transition correlates with the passage between particle-by-particle to concurrent intercalation.

4.1.4 Reaction Models

The correct choice of reaction models is important to accurate model the intercalation process, as it impacts energy barriers, prefactors, and other stability criteria. Reactions are driven by the overpotential from the electrochemical potential differences between the electrolyte and intercalation solid, indicated as $e\eta = (e\phi_\mathrm{s} + \mu(c)) - (e\phi_+ + k_\mathrm{B}T \ln a_+) + iR_\mathrm{f}$, where $\mu(c)$ is the chemical potential of the intercalated lithium, ϕ_+/ϕ_s are electrical potentials of lithium ions in the electrolyte and solid, and c is the intercalated lithium concentration. The traditional volumetric Butler-Volmer (BV) reaction rate is modeled with transition state theory as

$$R = k_0(c) \left(\exp\left(-\alpha\eta\right) - \exp\left((1-\alpha)\eta\right)\right), \tag{12}$$

with the prefactor $k_0(c) = k_0^* a_O^{1-\alpha} a_R^\alpha$, where k_0^* is the reaction current prefactor, α is the charge transfer coefficient, and a_R or a_O are the activity of the oxidation or reduction agent. We assume $k_0^* = 1\,\mathrm{s}^{-1}$ for the Butler-Volmer reaction rate [241].

However, the standard Butler-Volmer model does not account for electron availability in the intercalation solid, which can become limiting at higher overpotentials [128, 249]. We account for this with the coupled-ion electron transfer (CIET) model, applying an analytic approximation for a simplified expression [166] given by

$$R = \frac{k_0^*(1-c)}{\sqrt{4\pi\lambda}} \left(\mathcal{H}(-\eta_f, \lambda) - c\mathcal{H}(\eta_f, \lambda)\right), \tag{13}$$

where the formal overpotential is η_f and the reorganization energy in the intercalation solid is λ. The formal overpotential $e\eta_f = e\eta - k_B T \ln c$ separates ion concentration

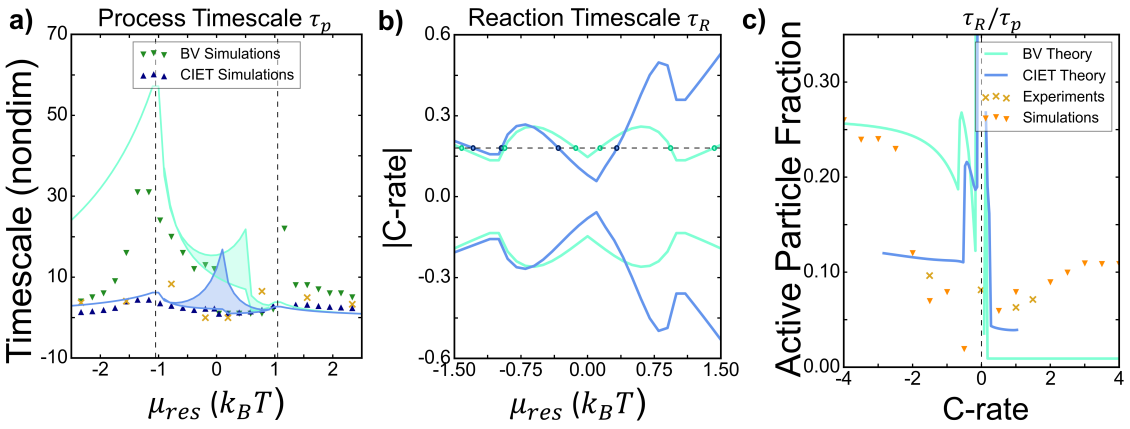

Figure 3: a) The transformation timescales of the intercalation process inside and outside the spinodal gap (indicated with the vertial dashed lines) are shown, with green or blue triangles indicating simulation data for the BV or CIET reaction models. Aquamarine and blue lines display the range of the theoretical model for the BV or CIET reaction models, where the bottom line shows the limit when the barrier influence is zero, while the top line displays the limit for a large impact from the barrier. Orange crosses show predicted timescales from Ref. [9] of voltage hold experiments for an LFP electrode. Inside the spinodal gap the process is stochastic, while outside the gap the process is deterministic, leading to the appearance of two regimes. b) The C-rate response from timescale analyses at different voltages are shown. The duplicate C-rate solutions at different voltages are indicated with a horizontal black line at |C-rate| = 0.18. c) The predicted active particle fraction at different C-rates is shown from the required particle fraction active necessary from the minimum voltage required in a) in aquamarine or dark blue for BV/CIET reactions. Orange crosses indicate experimental data from Ref. [8], while dark orange triangles indicate porous electrode simulation data from the same paper.

from the standard overpotential $e\eta$. The helper function $\mathcal{H}(\eta_f, \lambda)$ is defined as

$$\mathcal{H}(\eta_f, \lambda) = \frac{\sqrt{\lambda\pi}}{1 + \exp(-\eta_f)} \operatorname{erfc}\left(\frac{\lambda - \sqrt{1 + \sqrt{\lambda} + \eta_f^2}}{2\sqrt{\lambda}}\right). \tag{14}$$

We assume that the exchange current prefactor $k_0^* = 10\,\mathrm{s}^{-1}$ for the coupled ion electron transfer rate [129].

4.2 Analysis

We perform the above analytical timescale analyses for lithium iron phosphate, a common phase separating cathode material [67]. Single particle reaction rates [128] coupled with equilibrium thermodynamics can be integrated to extract nonequilibrium barriers and timescales. For lithium iron phosphate, a transition between the regimes with and without a barrier is observed based on applied potential in Fig. 2a. This indicates the appearance of the transition between the stochastic and deterministic timescales. We validate these timescale analyses with multiphase porous electrode theory simulations [44, 241, 242] with voltage control to extract timescales of phase transformations from a population. (Parameters and the model for the voltage control simulations were described in Appendix 4.3.) Experimental measurements from Refs. [9] and [8] were used for validation.

4.2.1 Process Timescale

A clear two phase regime is observed between the stochastic and deterministic regions as in Fig. 3c for both theory and simulations. By extracting process timescales from the intercalation process in Eq. 11, specific timescales from the two phase transition can be observed. For current control, the process timescale is directly found to be the inverse C-rate, $\tau_p \sim \text{C-rate}^{-1}$ [3].

For voltage control, the process timescale can be predicted from the applied voltage in Eq. 11, observed in Fig. 3a. In the spinodal gap, the process timescales are driven by the energy barrier and the curvature of the barrier (which contributes to the prefactor in Eq. 7). The barrier height and the single particle stability criterion (dR/dc), which affects the prefactor, are shown respectively in Fig. 2b/c. The magnitude of the concentration induced noise influences the contribution of the barrier height to the timescale. If the white noise magnitude is large (D_c), the effects of the potential barrier are diminished and the single particle stability criteria dominates the timescale measurement, as shown in the lower limit of the theoretical prediction in the spinodal gap for Fig. 3a. The upper limit indicates when the barrier effects are more

pronounced, shown in the upper limit of the theoretical prediction in the spinodal gap. Strong asymmetry with fast reactions for discharge is observed in porous electrode simulations when barrier effects are diminished, suggesting that barrier effects are minimal and single particle stability controls timescales.

Additionally, theoretical predictions show local maxima in the transformation timescales are observed at the critical voltages that eliminate the energy barrier. The appearance of local maxima matches experimental observations in Ref. [9] for lithium iron phosphate (dis)charge timescales under voltage holds, shown with orange crosses, as well as porous electrode simulation results shown with triangles, both in Fig. 3a. The appearance of the maxima arises from the decrease in timescale in both the deterministic region and the spinodal region when voltages further from the critical voltage are applied.

4.2.2 Reaction Timescale

The single particle reaction timescale under voltage control is directly found to be $\tau_R \sim R^{-1}$. However, the selection of the single particle reaction timescale under current control is subtle, as multiple chemical potential solutions can generate the same C-rate at varying active particle fractions, as shown in Fig. 3. However, when specific C-rates are applied, reproducible voltages, which give rise to repeatable active particle fractions, are selected for each C-rate, despite the multiplicity of solutions. This repeatability is caused by the principle of energy minimization, where the system chooses the minimum voltage needed to extract the same current [263]. The minimum voltage principle also gives rise to a nonequilibrium zero current voltage gap discussed in Appendix 4.4. From the selection of the minimum applied voltage, a single particle reaction timescale for voltage control can be found. Thus, the reaction timescale is directly related to the minimum voltage required for a certain current, found through the reciprocal of the single particle reaction rate calculated at that voltage.

4.2.3 Timescale Competition

The single-particle reaction timescale τ_R, which indicates the activation of all particles concurrently, competes with the process timescale τ_p. This competition is observed through changes in the active particle fraction (APF), described by the fraction of particles carrying the majority of the current [8]. Experimentally, the active particle fraction is found by setting a specific current cutoff and defining the active particle fraction as the fraction of particles whose current is above a certain value. However, in practice it has been found that the trend relating active particle fraction is uncorrelated with the specific current cutoff value [8].

Thus, since the active particle fraction is roughly uncorrelated with the cutoff value, the low rate particles do not contribute much to the total current and can be neglected in the total current calculation. The approximation can be made that C-rate = APF $\times$ R, indicating that the total C-rate is carried by the reaction rate of the activated particles. The active particle fraction can then determined from the fraction of single particles needed to extract the macroscopic current,

$$\text{APF} \sim \frac{\tau_R}{\tau_p}, \tag{15}$$

as illustrated in Fig. 3c. The active particle fraction is essentially a nondimensionalized factor proportional to the ratio between the reaction and the process timescales. Competition between the reaction timescale and the process timescale alters the active particle fraction, indicating that the timescale ratios relate single particle to population properties. When the reaction timescale selected by the minimum voltage is large relative to the process timescale, more particles are needed to carry the current, resulting in a higher active particle fraction. Conversely, if the reaction timescale is smaller, fewer particles are required and the active particle fraction is smaller. From a physical perspective, the predicted active particle fraction represents a nondimensionalized measure that assesses the utility of the electrode particles at the applied voltage.

This observation facilitates the transition between the low vs. high particle ac-

tivation fraction regimes between small and large C-rates, leading to the observed asymmetry between charge and discharge. Analytical approximations of the active particle fraction indicate that the active particle fraction appears physically as competition between the single particle reaction and population process timescale. The asymmetry is validated with constant current porous electrode theory simulations shown by triangles, as well as *operando* x-ray diffraction experiments [8] under constant current shown by crosses. When a low C-rate is applied, low voltage values in the miscibility gap satisfy the current constraint, causing the intercalation process to be in the stochastic regime. At higher C-rates, larger voltage values outside the miscibility gap are required to extract more current. When a high C-rate is applied, asymmetry between charge and discharge appears because of the shorter timescales predicted in the discharge process, as seen in Fig. 3b. This is caused by differences in nonequilibrium barrier heights in the (dis)charge process in Fig. 2b, generating asymmetry in process timescales observed in Fig. 3c.

4.3 Simulation and Theory Parameters

A free energy model includes the homogeneous term

$$g_h(c) = \Omega c(1-c) + k_B T \left(c \ln c + (1-c) \ln (1-c)\right) \tag{16}$$

in the total free energy

$$G(c, \nabla c) = \int_V \left(g_h(c) + \frac{1}{2}\kappa |\nabla c|^2 \right) dV, \tag{17}$$

where Ω is the regular solution parameter and κ is the gradient penalty term based on the Cahn-Hilliard free energy. The chemical potential is found to be the variational derivative of the free energy $\mu = \frac{\delta G}{\delta c}$. An Allen-Cahn [69] reaction model, found to be suitably appropriate for modeling reaction limited nanoparticles, was used as

$$\dot{c} = -\nabla \cdot \mathbf{j} + R \tag{18}$$

to model our equation with the Butler-Volmer reaction rate. The Butler-Volmer reaction is modeled as in Ref. [69] as

$$R = k_0 a_l^{1-\alpha} a_R^{\alpha} / \gamma^{\ddagger} \left(e^{-\alpha\eta} - e^{(1-\alpha)\eta} \right). \tag{19}$$

Here, the activity of the reduction agent $a_R = \frac{c}{1-c}$, while the transition state is related to the number of blocked sites $\gamma^{\ddagger} = (1-c)^{-1}$. The electrolyte activity a_l is set to 1 when there is no change in electrolyte concentration.

In our simulations, we perform a voltage hold of 3 hours for each set of simulations, using 100 particles in each simulation for many particle effects. The simulations were conducted in a single volume with the Allen-Cahn reaction model [69]. The absolute and relative tolerance were both set to 1×10^{-6} with an average particle size of 100 nm and a standard deviation of 0.1 nm and an initial concentration of 0.02 or 0.98, depending on whether a higher or lower voltage is applied. An electrolyte concentration of 1000 $\mathrm{mol/m^3}$ using an electrolyte model from Ref. [77] was used as the bath. In the electrode materials, a solid diffusivity of $5.3 \times 10^{-19} \mathrm{m^2/s}$ was applied. The gradient penalty term κ was assigned to be $5.0148 \times 10^{-10} \mathrm{J/m}$, while the regular solution parameter was $\Omega = 1.8560 \times 10^{-20} \mathrm{J/atom}$.

The cutoff for active particle fraction was set to be $5 \times 10^{-4} \mathrm{s^{-1}}$ arbitrarily, but we note that as long as the cutoff is consistent, the exact value is not important.

4.4 Appendix: Zero Current Voltage Gap

The nonequilibrium barrier modifies the magnitude of the zero current voltage barrier, as observed in Fig. 4. The zero current voltage barrier is generated by the difference between the minimum voltage needed to extract the low C-rate values. Unlike the equilibrium barrier derived from thermodynamic properties, this barrier is triggered by the minimum voltage needed to access a certain timescale. Experimentally measured zero current voltage barriers, such as $0.8\,\mathrm{k_B T}$ predicted in Ref. [11] and $1.4\,\mathrm{k_B T}$ in Ref. [10], are much smaller than the $4\,\mathrm{k_B T}$ equilibrium barrier predicted in Ref. [8],

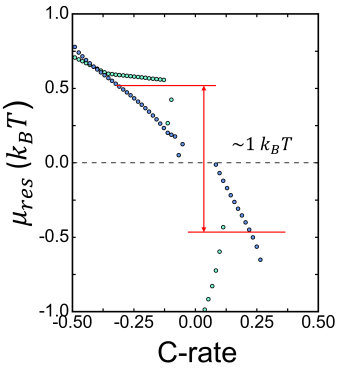

Figure 4: The zero current voltage gap [10, 11] for a lithium iron phosphate material plotted by showing the minimum voltage required to access certain C-rates, with the scale of experimental measurements ($1\,k_BT$) for reference.

which does not account for the nonequilibrium reactions in the barriers. In contrast, our observations indicate that the predicted zero current voltage barrier is approximately $\sim 1\,k_BT$ for both reaction rates, aligning much more closely with experimental measurements. This suggests that it is necessary to capture the nonequilibrium barrier to accurately model the spinodal gap.

4.5 Appendix: Solution to Time Correlation Function

The time dependent value of the noise can be predicted by the analytical solution of the spherical reaction diffusion equation, found in Ref. [48]. Based on the definition of the noise and its dependence on the difference between surface and bulk values, we observe that

$$\xi(t) \approx 3\frac{dR}{dc}\int_0^1 \left(c(\tilde{L}) - c(1)\right)\tilde{L}^2 d\tilde{L}, \tag{20}$$

where $\tilde{L}$ is the nondimensionalized radius based on the particle size L. This analysis is based on scaling of the conservation equation. Using the Fourier expansion in Refs. [48, 264] as well as a Taylor series at the boundary, expanding the concentrations

such that $c(\tilde{L}) = c(1) + \frac{dc}{d\tilde{L}}(\tilde{L}-1)$, the noise is approximated as

$$\xi(t) \approx 3\frac{dR}{dc}\int_0^1 \frac{dc}{d\delta}\frac{d\delta(m)}{dm}\frac{d\left(m(\tilde{L})-m(1)\right)}{d\tilde{L}}(\tilde{L}-1)\tilde{L}^2 d\tilde{L}, \tag{21}$$

which indicates that the noise is approximated as

$$\xi(t) \approx 3\frac{JL\text{C-rate}}{c_{s,max}D(c)^2}\frac{dD}{dc}(c)\int_0^1 \left(\tilde{L} - \sum_{k=1}^{\infty}\frac{2}{\lambda_k}\exp\left(-\frac{\lambda_k^2 D}{L^2}t\right)\cos\left(\lambda_k\tilde{L}\right)\csc\left(\lambda_k\right)\right)\left(\tilde{L}-1\right)\tilde{L}^2 d\tilde{L}, \tag{22}$$

where we assume that the state of charge is approximately $c = t\text{C-rate}$. The eigenvalues are found with $\sin\lambda_k - \lambda_k\cos\lambda_k = 0$. Since the Fourier terms are much smaller in magnitude than $\tilde{L}$, we observe that the correlation function is observed to be nearly exponential with a time constant of τ_R. Through numerical solutions to the correlation function, it is found that a near exponential approximation can be used such that the correlation function can be approximated as

$$\langle \xi(t)\xi(t+\tau)\rangle \approx \Gamma e^{-t/\tau_R}, \tag{23}$$

where $\Gamma = \mathcal{O}(10^{-29})$ for lithium iron phosphate. Thus, we assume that the noise generated from diffusion limitations can be approximated as colored noise with a time constant of τ_R. If the colored noise satisfying Eq. 23 is applied, we observe that a new Langevin equation can be modeled as

$$\dot{c} = R + \sqrt{\Gamma}\xi(t). \tag{24}$$

To linear order, the solution for the single particle equation can be approximated to be

$$c = \sqrt{\Gamma}\int_0^t \xi(\tau)e^{-\tau_R^{-1}(t-\tau)}d\tau, \tag{25}$$

where τ_R^{-1} is an averaged timescale representing the driven reaction rate such that $\tau_R = \left(\int_0^1 R(c)dc\right)^{-1}$, which is the exchange current density for a linear reaction rate. By multiplying Eq. 24 by $2c$ and averaging, we find that the variance evolution is

shown as

$$\begin{aligned}\frac{d\left\langle c^2\right\rangle}{dt} &= -2\left\langle Rc^2\right\rangle + 2\sqrt{\Gamma}\left\langle c(t)\xi(t)\right\rangle \\ &\approx -2\left\langle Rc^2\right\rangle + 2\sqrt{\Gamma}\left\langle \xi(t)\xi(t)\right\rangle \\ &= -2\left\langle Rc^2\right\rangle + \Gamma\tau_R\left(1-e^{-2\tau_R^{-1}t}\right).\end{aligned} \tag{26}$$

Similarly, applying the integral over c^2 to the marginal over the noise in the Fokker-Planck equation as in Eq. 6 indicates that

$$\frac{\partial\left\langle c^2\right\rangle}{\partial t} = -2\left\langle Rc^2\right\rangle + 2B(t), \tag{27}$$

where $B(t)$ is the noise in the Fokker-Planck equation. The solution of the noise is mapped to

$$B(t) = \frac{1}{2}\Gamma\tau_R\left(1-e^{-2\tau_R^{-1}t}\right). \tag{28}$$

A modified Fokker-Planck equation to the linear order accounting for the effects of colored noise can be observed as

$$\frac{\partial\bar{f}}{\partial t} = \mathcal{L}_D\bar{f} = \frac{\partial(\bar{f}R)}{\partial c} + \Gamma\frac{\partial}{\partial c}\left(\frac{1}{2}\tau_R\left(1-e^{-2\tau_R^{-1}t}\right)\frac{\partial\bar{f}}{\partial c}\right). \tag{29}$$

However, the magnitude of this noise is small enough that a white noise approximation is sufficient, which is applied in the manuscript.

4.6 Appendix: Projection Operation

We assume that the white noise can be expanded in powers of the correlation time [265], assumed to be a Markov process with a stationary distribution of $e(\xi)$. Thus, we can separate a linear operator on the ξ dependence such that

$$\mathcal{W}(\xi|\xi') = W(\xi|\xi') - \delta(\xi-\xi')\int W(\xi''|\xi)d\xi'', \tag{30}$$

with a transition probability of $W(\xi|\xi')$ describing the transition between states ξ' and ξ. The projection $P(c,\xi|c',\xi') = e(\xi)\delta(c-c')$ can be applied to eliminate the fast variables on each conservation equation (Eq. 4), indicating that $P\rho(c,\xi) = e(\xi)\langle f\rangle$ using $\langle a\rangle = \int_\xi e(\xi)a(\xi)d\xi$ to indicate the average over the noise. We note that $P\mathcal{W} = 0$ is satisfied, since $\mathcal{W}$ operates independently of c. The joint probability distribution $f(c,\xi,t)$ [253] follows

$$\frac{\partial f(c,\xi,t)}{\partial t} = -\sum_i \frac{\partial}{\partial c_i}\left(R_i + \xi_i\right) f + \mathcal{W}f. \tag{31}$$

We apply the projection $Pf = e(\xi)\langle f\rangle$ [253], where we integrate over the noise to eliminate fast variables, observing that

$$\frac{\partial \bar{f}}{\partial t} = -\frac{\partial}{\partial c_i}\left(\langle R\rangle + \langle \Delta\xi_i \mathcal{W}^{-1}\Delta\xi_j\rangle\right)\bar{f}. \tag{32}$$

Chapter 5

Extracting Particle Degradation From Electrodes with Pulses

Physics-informed design of hybrid pulse power characterization tests for rechargeable batteries [15]

5.1 Introduction

Post degradation, degradation metrics are required for determining the remaining utility of the cell. A key metric in the design of Li-ion battery materials is rate capability for discharge [266, 267, 268], but there is a complex, material-dependent trade-off between increased cycling rates and reduced battery lifetime. Capacity fade and internal degradation resulting from long-term use of Li-ion batteries must be rapidly and accurately quantified in order to improve their performance, reliability, and safety [81, 269, 270, 271] and inform second-use and end-of-life decisions [39]. Degradation of Li-ion batteries stems from a plethora of physical mechanisms, such as solid electrolyte interphase (SEI) formation [272, 21, 24, 21, 25] and lithium metal plating [92, 91, 273, 236] at the anode and structural changes at the cathode, such

The present chapter is based on my published work in the Journal of the Electrochemical Society [15].

as oxidation-induced cation disorder [12], rock-salt phase-transitions and densification [27, 185], anti-site defects [46], and secondary particle cracking [85, 274]. These degradation mechanisms lead to losses in rate capability by lowering accessible capacity at the same current or power within the operating voltage range. When this measure of state of health (SoH) reaches a given threshold, such as 80% of the nominal capacity under slow discharge, the battery is considered to have reached the end of its useful life, but the internal state of degradation is unknown and difficult to assess.

During the course of battery operation, assessing the performance and health of a cell is a challenging task, normally addressed by intermittent diagnostic tests. Various types of diagnostic tests are performed non-destructively to evaluate the ability of a battery to store and release energy, typically after a battery has undergone significant electrochemical cycling [2, 275]. High-precision coulometry tests can infer different degradation modes from measurements [72, 71, 276], but require equipment with extreme measurement precision. Reference performance tests (RPT) measure the ability of a battery to charge and discharge a specific current [277, 278, 279]. Electrochemical impedance spectroscopy (EIS) quantifies the frequency-dependent response to small AC perturbations [280, 281]. Hybrid pulse power characterization (HPPC) tests utilize large intermittent current pulses and rest periods to capture the behavior of a cell under high currents far from equilibrium [74, 282, 62, 283]. All of these tests can be leveraged for interpretable machine learning of battery degradation, based on cell-level SoH and performance, such as internal resistance and accessible capacity [284, 285, 286, 287, 288], but connections to microscopic kinetic parameters could lead to more robust feature engineering and insights into the internal state of degradation.

To comprehensively understand the operational limits of a battery in diagnostics, it is essential to subject it to high-rate perturbations. It is advantageous to initiate experiments from an equilibrium state, as it facilitates better calibration and supplies a more controlled starting point for assessing behavior, which most diagnostic tests do not provide. For example, RPT tests impose a current constraint for a full (dis)charge, so the battery is continuously residing in a nonequilibrium state. Conversely, EIS is

generally performed near equilibrium in batteries, since applying a DC bias (as is often done in fuel cells) results in drifting spectra associated with dynamical heterogeneities and varying state of charge. Among the various diagnostic tests available, HPPC tests stand out, as they offer an abundance of kinetic information far from equilibrium yet are calibrated against equilibrium conditions.

State-of-the-art experimental design of diagnostics using pulses lacks a systematic basis to distinguish and quantify different degradation mechanisms. Information is typically extracted by fitting lumped parameters that are only qualitatively connected with degradation mechanisms, such as the loss of active material, loss of lithium inventory, or increasing area-specific impedance [289, 42]. While such results from diagnostic tests provide valuable insights, they are difficult to connect unambiguously with root causes of degradation [290, 1, 37, 291]. These observed "symptoms" do not offer a direct mapping to specific mechanisms that can be rigorously captured in physical models, such as film resistance and electrolyte concentration loss [12, 13].

The introduction of pulse measurements in electrochemistry is not a recent development, as they are frequently used to extract information on diffusive dynamics [20] with Galvanostatic and Potentiostatic Intermittent Titration Techniques (GITT, PITT) [292, 75, 76]. Pulse measurements are sometimes interpreted by porous electrode theory (PET) simulations [77, 78, 293, 128, 129, 294]. Despite their widespread utilization [295, 296], however, there is still inadequate understanding of how pulses affect cells. For HPPC tests in particular, the theoretical understanding of pulse dynamics in the short-time reaction-limited regime is incomplete, and no clear rationale for selecting specific states of charge and currents for the applied pulses is available. While some progress has been made with porous-electrode type modeling to simulate HPPC, as shown in Fig. 1b with pulses from measurements similar to industry-standard HPPC [74, 297, 62, 298, 299], these protocols have not yet been optimized to extract maximum information.

Current methods approaching experimental design with PET simulations present significant computational challenges due to the extensive search space and the significant computational time required [300]. Although efficient numerical solver backends

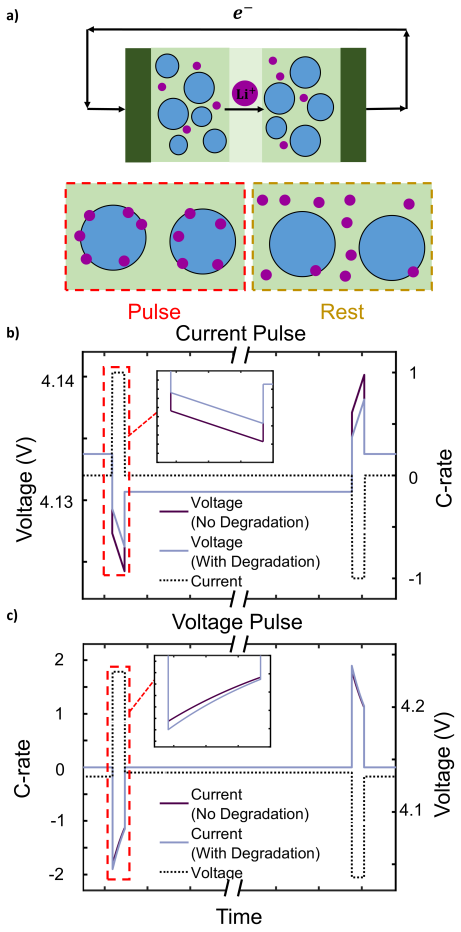

Figure 1: a) A comparison of the physical description of pulsing and resting in a battery cell, where lithium ions in the electrolyte are purple and battery particles are blue. b) Voltage response to a current pulse and c) current response to a voltage pulse and the effects of degradation on a pulse measurement in an industry-standard HPPC measurement are shown, with the pulse and rest sections displayed.

such as SUNDIALS [301] can help overcome these challenges [4], such problems are still rate limiting. As battery management systems move towards health monitoring and applying optimized protocols during operation, simple optimization problems to extract degradation from diagnostics become more attractive [38]. Previous work [74] analyzing HPPC modeling with porous electrode theories applied sensitivity studies for cell-specific models without providing general analysis of information content extracted from pulses. Furthermore, PET-type simulations often suffer from poor identifiability of parameters inferred from experimental data [300, 302, 303], which complicates attempts to predict improved experimental design. These problems have

hindered progress in the search for optimal protocols [304, 305], especially for battery management systems. Thus, simpler models of pulse diagnostics for a generalized design framework are necessary.

In view of these challenges, we choose to tackle this problem by establishing a physical interpretation of certain simulated cell behavior subject to pulsed conditions, and attempt to find a comprehensive method to understand pulse experiments. Because degradation mechanisms are convoluted between the two electrodes, distinguishing physical degradation mechanisms for a full cell is not a simple task. To address this challenge, we develop a theoretical framework to separate mechanisms for a half-cell material using the fitness framework for voltage pulses, and then expand the framework to a full cell. Our investigations have led to the development of an explicit representation that separates degradation mechanisms for full cells and can be used as a direct function for optimization problems. We demonstrate that voltage pulses using the fitness framework reliably extract dominant degradation mechanisms using multivariable optimization, and validate these results with porous electrode simulations. Overall, our analysis has also led us to propose voltage pulses, a novel method of measuring battery degradation, using a "fitness" framework [13]. The key advantage of the voltage pulse method is the explicit physical separability of degradation mechanisms from the fitness framework, shown in Eq. 13, which indicates that loss in fitness can be directly attributed to each degradation mechanism. This contrasts with implicit formulations in current pulses, simplifying numerical calculations. Asymmetric effects of the cathode/anode on the full cell system based on kinetic parameters are predicted from our explicit model, which increase numerical efficiency in optimization problems. Voltage pulses also provide other physical advantages, such as mitigating electrode heterogeneity that results from phase separation [8] and electroautocatalysis [49], which increases diagnostics accuracy. Current response is also closely linked to rate capability, which holds higher importance in high-rate battery operation relative to conventional degradation metrics, such as practical capacity and lifetime [306, 307].

This implementation of physics-informed HPPC significantly enhances the qual-

ity of information gathered compared to industry-standard HPPC experiments. The method demonstrates an asymmetric sensitivity of information to degradation parameters between charge and discharge from differing scales of cell kinetics. It enables us to discern the physical roots behind degradation symptoms more accurately and efficiently. The impact of different states of charge and voltages on probing distinct degradation mechanisms is also explored [42]. Our investigations also shed light on the limitations of HPPC experiments, specifically the fact that degradation mechanisms at the overpotential dominant electrode (the electrode where the overpotentials are larger than that at the opposing electrode) are extracted more easily than those at the non overpotential dominant electrode.

5.2 Theory

5.2.1 Degradation Mechanisms and Models

During a pulse, lithium ion-electron pairs (de)intercalate into the solid active material or electrolyte, driven by a current or voltage hold. This large perturbation over short timescales offers signifcant insight into the electrochemical dynamics [3]. Since ion diffusion timescales in the electrolyte and solid are much longer than the reaction timescales, the latter are most discernable immediately after the pulse is applied. Even at shorter timescales, double layer relaxation tends to dominate [308, 309, 310], so the experimental choice of measurement times must be tailored to avoid this effect. Timescale analysis is performed in the cell modeling sections.

In this context, we begin with a theoretical examination of the behavior within the battery during a pulse, providing guidance on how diagnostic experiments should be structured. We consider three common physical types of degradation related to power fade: film resistance R_f, which introduces an additional resistance to the overpotential applied to the (de)intercalation reaction, typically arising from solid electrolyte interphase formation [24]; surface blockage $\tilde{c}$ of kinetics, which reduces the number of available sites at the surface for intercalation, arising from phase transformations

at the surface [13, 12]; and electrolyte loss from parasitic reactions, which changes the availability of the reactant, the concentration of lithium ions in the electrolyte solution c_+ [311]. Many common degradation mechanisms can be lumped into these three categories, such as cathode electrolyte interphase (CEI) [210] or graphite solid electrolyte interphase (SEI) [21, 24, 25, 312] growth for the film resistance mechanism, structural disordering/phase transitions in nickel-rich materials for the surface blockage [12], and electrolyte decomposition for the electrolyte loss mechanism [81]. Other types of degradation mechanisms could be integrated as well. By systematically studying the impact of these degradation mechanisms within pulse experiments, we elucidate their individual contributions, facilitating design of diagnostic experiments tailored to distinguish degradation factors.

In order to assess the impact of cell degradation on rate capability, we employ multiphase porous electrode theory (MPET) simulations [44, 55] based on nonequilibrium thermodynamics [69] to compare the pulse response of a degraded cell and the response prior to degradation. Importantly, MPET captures the rate-dependent populations of active particles sustaining the applied current [10, 8, 234, 51], which control internal resistance and parasitic side reactions [49, 273, 91, 12, 13]. Degradation manifests itself by gradually altering the current or potential response from cycle to cycle, and the model attributes these changes to a number of physical mechanisms.

The response to large pulses is initially dominated by reaction kinetics [3]. Both cathode and anode kinetics contribute to cell performance during this period, and degradation from both electrodes collectively impacts current capacity. The net Faradaic reduction current at an electrode is the difference between the reduction and oxidation currents [20],

$$i = i_{\mathrm{red}} - i_{\mathrm{ox}} \tag{1}$$

which depend on the overpotential η, expressed as the change in free energy of the intercalation reaction per electron charge transferred [69],

$$e\eta = (e\phi_s + \mu(c)) - (e\phi_+ + k_B T \ln a_+) + iR_f, \tag{2}$$

where c is the concentration of the intercalated lithium in the solid, $\mu(c)$ is the chemical potential of the intercalated lithium, $\phi_{+/s}$ represents the lithium-ion electrical potential in electrolyte or solid, a_+ is the activity of the lithium ions in electrolyte depending on its concentration c_+, i denotes the intercalation current density, and R_f is the film resistance from degradation.

As an alternative to the traditional approach of modeling electrochemical reaction rates with the Butler-Volmer equation [20], we adopt the general quantum-mechanical framework for intercalation reaction kinetics provided by coupled ion-electron transfer (CIET) theory [249, 128] based on equilibrium thermodynamics [69]. The theory has two simple limits [249]: 1) For fast electron transfer with slow ion transfer ("ion-coupled electron transfer", ICET), the theory predicts Butler-Volmer kinetics with a new form of the exchange current that captures the microscopic physics more accurately; 2) in the opposite limit of rate-limiting electron transfer ("electron-coupled ion transfer", ECIT), the theory combines Marcus kinetics of electron transfer [313, 314] with corrections for nonequilibrium thermodynamics of ion transfer [69]. The latter was first proposed as a mechanism for lithium intercalation in lithium iron phosphate [127, 128], and recently validated by inverse learning from x-ray images [50, 249]. Given this rigorous validation for one important Li-ion battery material, we assume ECIT kinetics in our study, but we do not expect major changes to our results with other limits of CIET theory. The differences between ECIT and ICET are most pronounced at large overpotentials, while both limits of CIET theory predict a similar concentration-dependent exchange current at small overpotentials, which vanishes linearly at high filling fractions [249]. This universal concentration dependence of CIET kinetics has the strongest effect on degradation and capacity loss, as the reaction rate vanishes as the theoretical capacity is approached. Changes to the specific reaction model would only change the sensitivity to the underlying degradation parameters at large overpotentials relative to the reorganization energy (typically several 100 meV).

It is convenient that an accurate analytical approximation of the ECIT rate is

available [166, 249, 128], given by

$$i = \frac{k_0^*(\tilde{c} - c)}{\sqrt{4\pi\lambda}} \left(a_+ \mathcal{H}(-\eta_f, \lambda) - c\mathcal{H}(\eta_f, \lambda)\right), \tag{3}$$

in terms of the exchange current prefactor k_0^*, the rescaled capacity after degradation $\tilde{c}$, and the formal overpotential η_f and Marcus reorganization energy λ, each scaled to the thermal energy $(k_B T/e)$, where the function $\mathcal{H}(\eta_f, \lambda)$ is defined as

$$\mathcal{H}(\eta_f, \lambda) = \frac{\sqrt{\lambda\pi}}{1 + \exp(-\eta_f)} \operatorname{erfc}\left(\frac{\lambda - \sqrt{1 + \sqrt{\lambda} + \eta_f^2}}{2\sqrt{\lambda}}\right). \tag{4}$$

The dimensionless formal overpotential is defined as $e\eta_f = e\eta - k_B T \ln \frac{c}{a_+}$, where the ionic concentration dependencies are removed since ionic concentration is considered separately as a reactant. As with other reaction models, the reduction current $i_{\text{red}} = k_0^*(\tilde{c} - c)a_+ \mathcal{H}(-\eta_f, \lambda)/\sqrt{4\pi\lambda}$ dominates during intercalation, while the oxidation current is $i_{\text{ox}} = k_0^*(\tilde{c} - c)c\mathcal{H}(\eta_f, \lambda)/\sqrt{4\pi\lambda}$, which is dominant during de-intercalation. An important prediction of CIET theory is the linear decay of the reaction rate in the approach to complete filling of the (degraded) lattice, $i \sim (\tilde{c} - c)$, which requires a vacancy for the transition state [249, 128]. This leads to a strong effect of electro-autocatalysis [164], which leads to more homogeneous concentration profiles with higher resistance during intercalation and more unstable heterogeneous profiles with lower resistance during de-intercalation, as observed in recent experiments on both phase-separating [50] and solid-solution [49] cathode active materials.

5.2.2 Cell Models

Single Particle Model

A single particle model serves as the simplest representation emphasizing active material intercalation of the electrode. This model captures interplay between active material reaction and diffusion processes [43] using the particle lengthscale to estimate reaction area in a full electrode. During a pulse, the interplay between

timescales for reaction, diffusion and applied current determine the concentration profiles that arise within single particles [3], which can develop either bulk-surface quasi-equilibrium or diffusion-limited core-shell patterns. For phase separating materials, the former regime involves intercalation waves sweeping across the surface of the particle [315, 69], but as we consider here, for non-phase separating materials, the bulk-surface quasi-equilibrium structure corresponds to nearly uniform solid concentration, which is ideal for degradation estimation. In this case, it is only necessary to avoid solid diffusion limitation leading to non-uniform core-shell concentration profiles. In order to estimate the conditions for quasi-equilibrium, we perform a scaling analysis of the reaction-diffusion equation for a particle,

$$\frac{\partial c}{\partial t} = -\nabla \cdot \mathbf{F} + R, \tag{5}$$

such that $\tau_{D,p} = L_p^2/D_p$ and $\tau_{I,p} = I^{-1}$ are the solid diffusion and process timescales, respectively. Here, L_p is the particle length, D_p is the solid particle diffusivity, and I is the applied C-rate. When $\tau_{I,p} \gg \tau_{D,p}$, the quasi-equilibrium/reaction limited regime is reached, the ideal region for the application of the reaction-limited model in the current work. Conveniently, as observed in Fig. 4ab of Ref. [3], most common battery electrode materials lie in the reaction-limited regime. Exceptions occur at large pulses, when the dimensionless current is large ($i/i_0 \geq 10^3$), or when particle size is large (as in graphite platelets), such that $L_p \geq 10^5$ nm. Here, i_0 is the related to the exchange current density of the material, and i is the dimensionalized applied current. Thus, for our pulse measurements, we assume that the system is reaction limited [3], allowing us to neglect solid state diffusion in the particles.

The system consists of a single active material particle in an idealized electrolyte bath, corresponding to a half cell electrode only. We define $\phi = \phi_s - \phi_+$ as the difference between the solid and electrolyte potential, which is the electrical potential difference applied to the kinetic interface. Within this single-particle model, the electrolyte potential applied to the single particle is denoted as ϕ, while the current is i, representing the rate of lithium-electron pairs intercalating or deintercalating into

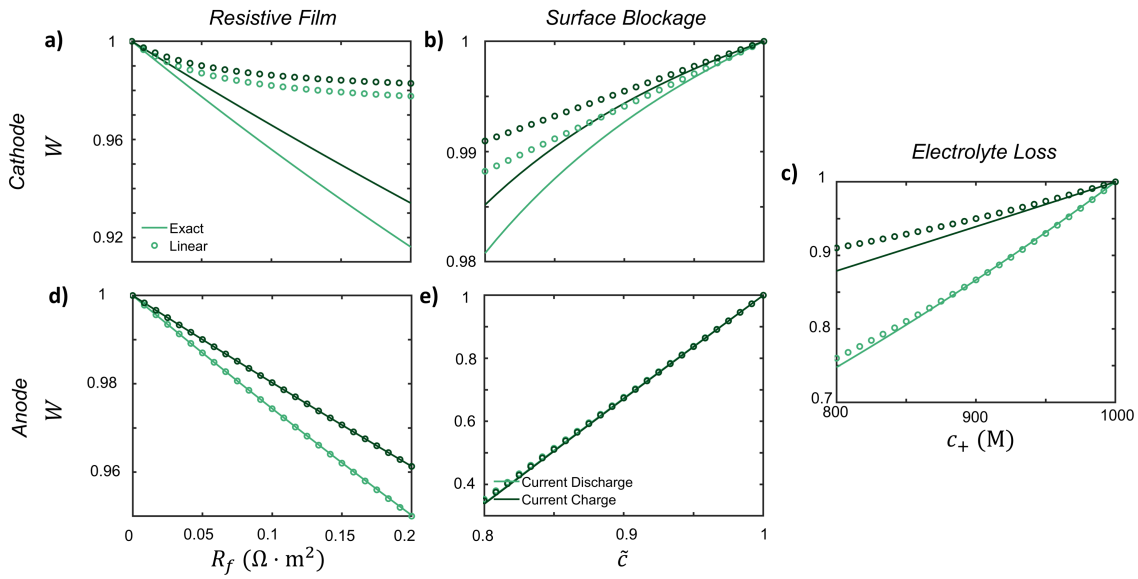

Figure 2: Goodness-of-fit results for the linear approximation and the exact calculation of the fitness W for each degradation mechanism in a full cell NMC532-graphite cell for a 100 mV (dis)charge pulse are shown at various states of degradation, from least to most degraded at a cathode state of charge of 0.8 and anode state of charge of 0.4. The effects of film resistance on the (a) cathode and (d) anode, the surface blockage of the (b) cathode and (e) anode, and the electrolyte concentration loss are plotted for this cell at values close to the initial nondegraded state.

the active material. The relationship between the current and potential is dictated by the reaction kinetics, modeled by the coupled-ion electron transfer kinetics. To account for the complexities of a full cell, further extensions to the model are required as discussed below.

Full Cell Model

In a realistic electrode, the single-particle model falls short at accurately capturing the cell-level transport limitations. To represent these interactions more realistically, electrode-scale models are employed, which more accurately capture the interplay between electrolyte transport and kinetics within the electrode. Since our primary focus is capturing the kinetics of the cell with a specific emphasis on degradation, we aim to incorporate the effects of the interacting cathode and anode in a full cell. From the macroscopic design of an electrode, limitations from electrolyte diffusion/conduction or solid conduction can aid the proper selection of timescales for pulse selection [43].

However, because of the large amount of carbon additives added in battery manufacturing, solid electronic conduction rarely is limiting. Thus, the limitations from electrolyte transport are often found to be of the most interest in a pulse process. These limitations can be understood using a scaling analysis.

From porous electrode style transport equations in Ref. [44], we observe that electrolyte-scale transport is captured along the electrode with lithium-ion mass conservation in the electrolyte,

$$\frac{\partial(\varepsilon c_l)}{\partial t} = \frac{1}{\nu_+}\left(-\nabla \cdot \mathbf{F}_{l,+} + R_{V,+}\right), \tag{6}$$

where ε is the porosity, c_l is the lithium concentration in electrolyte, ν_+ is the number of ions per molecule of neutral salt, $\mathbf{F}_{l,+}$ is the flux of lithium ions, and $R_{V,+}$ is the volumetric reaction rate of the lithium ions. Charging occurs during the electrode process timescale as

$$\tau_{I,l} = \frac{\nu_+ \varepsilon c_l}{(1-\varepsilon) P_L I \rho_s}, \tag{7}$$

where P_L is the volumetric electrode loading, I is the C-rate of the electrode, and ρ_s is the lithium site density of the active material. If measurements occur after this timescale, we can properly capture the pulse reaction dynamics. Analogously, the measurement timescale is the experimental timescale at which measurements are extracted, $\tau_{m,l} = t_{\text{pulse}}$. For electrolyte diffusion limitation, we observe that

$$\tau_{D,l} = \frac{\varepsilon^a L_l^2}{D_l}, \tag{8}$$

which is the timescale on which electrolyte diffusion occurs, where a is the Bruggeman scaling coefficient, L_l is the electrode length, and D_l is the effective electrolyte diffusivity. For electrolyte conduction, we observe that

$$\tau_{\sigma,l} = \frac{\varepsilon^a L_l^2 c_l z_+ e^2 \nu_+}{t_+^0 \sigma_l k_B T} \tag{9}$$

is the electrolyte transport timescale, where z_+ is the valence of lithium ions, σ_i is

the electrolyte conductivity, and t_+^0 is the transference number.

When the process timescale, electrolyte diffusion timescale, and electrolyte conduction timescales are compared, the timescales at which measurements should be applied become apparent. Using electrolyte transport parameters from Ref. [47], we observe that $\tau_{D,l} \sim 10\,\text{s}$ and $\tau_{\sigma,l} \sim 10\,\text{s}$. This indicates that electrolyte transport limitation occurs after the pulse is taken if measured around $\tau_{m,l} \sim 1\,\text{s}$. We avoid transport limitation when the measurement timescale $\tau_{m,l}$ is selected properly, and can use these approximations then. Thus, in the context of a full cell, when a voltage hold is applied, only the voltage difference $\phi_{\text{applied}} = \phi_{s,c} - \phi_{s,a}$ between the cathode and the anode is controlled. (In this full cell, we use the subscript a to refer to the anode, and the subscript c to refer to the cathode.) From the full cell constraint on the system, the total amount of cathode reaction must equal the anode reaction. The solid electrical potentials, $\phi_{s,c}$ and $\phi_{s,a}$, can be determined through a porous electrode theory model using current or voltage constraints.

Overall, our simple full cell electrode model has the governing equations

$$\begin{aligned} f_a i_a(\phi_a, R_{f,a}, \tilde{c}_a, c_+) &= -f_c i_c(\phi_c, R_{f,c}, \tilde{c}_c, c_+) \\ f_a i_a(\phi_a, R_{f,a}, \tilde{c}_a, c_+) &= i_{\text{cell}}, \end{aligned} \tag{10}$$

from the equality of the total anode and cathode reaction, where the reaction rates are defined with Eq. 3. In this equation, f represents the dimensionless factor $L(1-\varepsilon)P_L\langle\frac{A_p}{V_p}\rangle$, which relates the particle-scale current to the electrode-scale current densities for each electrode, where L is the length of the electrode, P_L is the volume loading of the solid material at the electrode, ε is the porosity of the electrode material, A_p is the particle area, V_p is the particle volume, and $\langle\rangle$ indicates the averaged parameter over the entire electrode. For the current density descriptions, i_a and i_c are the average particle level intercalation currents densities at the cathode and anode, while i_{cell} is the total cell-level intercalation current density. From the two constraints in Eq. 10, in a current control system, the cell current is fixed and the two voltage variables ϕ_a and ϕ_c are determined through the constraints. In contrast,

for a voltage control system, the difference between the cathode and anode voltages, $\phi_c - \phi_a$, is fixed and thus the cell-level current and absolute voltage values are variable.

5.2.3 Cycling Conditions

Current Pulses

When subjecting two cells to an identical current pulse, one in a nondegraded condition and the other in a degraded condition, differences emerge in voltage behavior. In contrast, the full cell current values are the same for both the nondegraded and degraded cells because of the current constraint. From the current constraint in a nondegraded cell, Eq. 10 holds. In a degraded cell, an analogous current constraint holds as

$$f_a i_a(\phi_{s,a} + \Delta\phi_{s,a}) = -f_c i_c(\phi_{s,c} + \Delta\phi_{s,c}) = i_{\text{cell}}, \tag{11}$$

but the voltage response is different. The voltage difference in the nondegraded cell is $\phi_{s,c} - \phi_{s,a}$. For the degraded cell, it contains an additional term from the voltage shift for degradation, resulting in $\Delta\phi_{s,c} - \Delta\phi_{s,a} + (\phi_{s,c} - \phi_{s,a})$. The two current hold equations (Eqs. 10, 11) can be solved for the exact solution of the voltage difference. Though an approximate linear solution of this model can be derived for the half cell, there is no absolute fitness for the full cell since the reference potentials between electrodes are arbitrary (the half cell linearizations are shown in Appendix 5.8). The only viable solution is an implicit solution for the current pulses.

Voltage Pulses

Analogously to the current pulses, we target an exact solution for the potential shift by resolving the current constraints. Voltage pulses have an advantage over current pulses in phase-separating materials, since most voltages chosen are outside the voltage corresponding to the miscibility gap in phase separating materials. In addition, the non-coupled behavior of voltage control avoids particle-by-particle and other population effects seen in current pulses [8], since all particles are connected to the bath. To streamline our analysis, new notation (such as the fitness variable W) is

introduced.

When a cell is subject to a voltage pulse before degradation occurs, the resulting current response is denoted as $\bar{i}$; upon degradation, the degraded response is i. We establish a relationship between the responses with the fitness $W = i/\bar{i}$, which is the ratio between the degraded and nondegraded current. This describes the change in rate capability of the battery [13] by linking it to physical degradation parameters. The exact solution of the current ratios for one electrode is the fitness

$$W = \frac{i(\phi, R_f, \tilde{c}, c_+)}{\bar{i}(\phi, R_f = 0, \tilde{c} = 1, c_+ = 1)}. \tag{12}$$

Since the same voltage is applied before and after degradation, it can be seen from Ref. [13] that a linear approximation can be applied to the degradation parameters since the degradation amount is small. The fitness is found for a coupled ion-electron transfer reaction to be

$$W = \frac{i}{\bar{i}} = \frac{\tilde{c} - c}{1 - c} \frac{1}{1 - R_f \frac{\partial \bar{i}}{\partial \eta}} \left[1 - \frac{\bar{i}_{\text{red}}}{\bar{i}} (1 - c_+) \frac{\partial \ln a_+}{\partial \ln c_+} \right]. \tag{13}$$

This equation provides direct physical insight into the factors influencing each degradation mechanism, and indicates that the contribution of each degradation mechanism is separable.

There are many advantages to applying the fitness framework relative to the analysis of raw electrochemical measurements, expounded in Ref. [13]. The linearized fitness framework is shown to be accurate at small amounts of degradation, which is true for any operational battery. In addition, each degradation mechanism is separable using this framework, simplifying the attribution of rate capability loss to specific degradation mechanisms. The explicit relationship between the rate capability and each degradation mechanism also eases numerical computation, in contrast to implicit solutions. Finally, the rate capability loss of each of the mechanisms is also physically correlated with kinetic parameters, introducing physical interpretability to the framework.

The physical interpretability is introduced by kinetic parameters that modulate the influence of degradation on fitness reduction. Specifically, the film resistance mechanism correlates with the differential conductance, denoted as $\frac{\partial \bar{i}}{\partial \eta}$ [164], which characterizes the rate of current acceleration in response to an increase in potential. For a coupled ion-electron transfer reaction, the differential conductance reaches a maximum from the limiting current (observed in Fig. 6b for a nickel manganese cobalt oxide electrode material). In comparison, using a Butler-Volmer reaction model will cause the differential conductance to grow exponentially. Both calculations are shown in Appendix D of Ref. [13]. Thus, the Butler-Volmer reaction model would indicate a higher impact of film resistance on the rate capability of a particle. Similarly, the electrolyte concentration mechanism is primarily related to the reduction current fraction in the total current, $\bar{i}_{\text{red}}/\bar{i}$ for the coupled ion electron transfer model. This arises because electrolyte concentration only participates as a reactant in the reduction reaction. In contrast, when using the standard Butler-Volmer reaction model, the differential conductance replaces the reduction current fraction as the kinetic prefactor modulating degradation effects on rate capability, shown in Eq. 22 in Ref. [13]. This indicates a larger sensitivity of the fitness loss with the Butler-Volmer model with respect to the electrolyte concentration. Overall, using a less physical Butler-Volmer type expression indicates a stronger impact of degradation parameters on fitness loss than the more physical coupled-ion electron transfer model.

As we extend the half cell model to a full cell, the presence of degradation, characterized by kinetic changes in the electrodes, introduces a shift in the behavior of the system. When the system is degraded, due to the current constraint requirement and the altered kinetics, the same absolute potentials $\phi_{s,c,a}$ cannot be applied to the cathode and the anode. This discrepancy arises because the equality in current is no longer maintained. To ensure the current constraint is still satisfied on the full cell, there is a necessity for a potential shift $\Delta\phi$ to be applied to both the solid potential at the anode and cathode. Consequently, the voltage in this degraded full cell is calculated as $(\phi_{s,c} + \Delta\phi) - (\phi_{s,a} + \Delta\phi) = \phi_{s,c} - \phi_{s,a}$, resulting in the same experimental voltage as previously measured. In short, this shift in potentials at both electrodes is

essential to maintain the current constraint in the presence of degradation.

We use specific notation to distinguish between fitness values with (W) and without ($\hat{W}$) the voltage shift. Analogously to Eq. 10, with the inclusion of the voltage shift, the modified current constraint $f_a i_a(\phi_{s,a} + \Delta\phi) = -f_c i_c(\phi_{s,c} + \Delta\phi)$ holds. This equation is solved implicitly to determine the value of the voltage shift. Once the voltage shift is determined, the fitness W can then be found by ensuring equality of the fitness values between the cathode and anode in the full cell as

$$W = \frac{i(\phi_{s,c} + \Delta\phi, R_{f,c}, \tilde{c}_c, c_+)}{\bar{i}(\phi_{s,c}, R_{f,c} = 0, \tilde{c}_c = 1, c_+ = 1)} = \frac{i(\phi_{s,a} + \Delta\phi, R_{f,a}, \tilde{c}_a, c_+)}{\bar{i}(\phi_{s,a}, R_{f,a} = 0, \tilde{c}_a = 1, c_+ = 1)}. \tag{14}$$

Linear Approximation for Degradation Though we have found an exact implicit solution for this problem, implicit solutions can be computationally inefficient, particularly for optimization processes. Obtaining an explicit solution for complex problems can significantly reduce optimization time and provide valuable physical insights. We take advantage of the explicit linearized fitness framework and perform a first-order linearized approximation for the voltage shift to simplify the calculations. After linearization for the voltage shift, we apply the fitness approximation of the half cell described in Eq. 13, generating an explicit expression for effects of degradation on the response. This approach combines computational efficiency with a high degree of accuracy.

Eq. 14 holds true in the exact solution of a voltage pulse problem. However, the full cell fitness is not only defined by the effects of degradation as the half cell fitness is, but also by a voltage shift from ensuring current equality between the two electrodes. We attempt a simple linear approximation to capture these effects. Initially, using the linear approximation in each electrode for the rate capability, the fitness without the voltage shift is found to be the current ratio $\hat{W}_{a,c} = i_{a,c}/\bar{i}_{a,c}$. To include the effects of the voltage shift, we introduce χ, which denotes the fractional change in the current with potential shift relative to that without

$$\chi_{a,c} = i_{a,c}(\phi_{s,a,c} + \Delta\phi)/i_{a,c}(\phi_{s,a,c}) - 1. \tag{15}$$

The overall fitness is obtained through the ratio of degraded Eq. 10 with the nondegraded version, resulting in

$$W = \hat{W}_a(\chi_a + 1) = \hat{W}_c(\chi_c + 1). \tag{16}$$

This expression captures the overall change in current in the full cell, incorporating both degradation and voltage shift effects when there is less degradation. The full cell fitness thus captures the half cell fitnesses with the inclusion of a voltage shift term.

To the first order, the voltage shift term can be approximated using a Taylor expansion on χ based on the voltage shift:

$$\chi = \frac{\partial \chi}{\partial \phi}\Delta\phi + \mathcal{O}((\Delta\phi)^2) \approx \hat{W}^{-1}\bar{i}^{-1}\frac{\partial \bar{i}}{\partial \eta}\Delta\phi. \tag{17}$$

Applying this approximation to Eq. 16, the voltage shift is approximated as

$$\Delta\phi = \frac{\hat{W}_c - \hat{W}_a}{f_a\frac{\partial \bar{i}}{\partial \eta}_a + f_c\frac{\partial \bar{i}}{\partial \eta}_c}\bar{i}_{\text{cell}} \tag{18}$$

with Eq. 10 constraining the full cell current equality. Thus, using Eqs. 17 and 18, the overall fitness is a weighted sum over the cathode and anode fitnesses

$$W = \frac{\hat{W}_c + \hat{W}_a\frac{f_c\frac{\partial \bar{i}}{\partial \eta}_c}{f_a\frac{\partial \bar{i}}{\partial \eta}_a}}{1 + \frac{f_c\frac{\partial \bar{i}}{\partial \eta}_c}{f_a\frac{\partial \bar{i}}{\partial \eta}_a}}, \tag{19}$$

which approximates the shifted fitness by considering the voltage change. This expression is a reweighted sum of the ratio between the electrode scale and kinetic capabilities of the electrodes, where f represents the rescaling to the electrode area from the particle area and $\frac{\partial i}{\partial \eta}$ is the differential conductance, reflecting the kinetic capability of the electrode material.

The explicit representation of the fitness term in a full cell offers a direct physical understanding of asymmetric effects from each electrode in a full cell model. The

conductance ratio $\left(f_c \frac{\partial \bar{i}}{\partial \eta_c}\right) / \left(f_a \frac{\partial \bar{i}}{\partial \eta_a}\right)$ represents a ratio of the conductances of the cathode relative to the anode for the entire electrode. This ratio is influenced by both material properties and electrode design, particularly the reactive surface area. From the limiting values of the formulae, the results of the full cell indicate that when the anode differential conductance is larger than that of the cathode, the fitness of the cathode dominates the full cell. Conversely, if the cathode differential conductance is larger than that of the anode, the fitness of the anode dominates. The conductance ratio thus aids distinguishing between electrodes by the different scales modulating the half-cell fitness influences on the full cell.

In most balanced full cells, $f_a \sim f_c$ to minimize total mass of the cell, causing f_a/f_c to be constant and electrode design dependent (neglecting small changes from degradation). The main variable affecting the conductance ratio is the differential conductance of the cathode and the anode. These are dependent on the kinetic properties of the intercalation reaction occurring in the electrode, as well as the state of charge and applied voltage. An electrode is referred to as "overpotential dominant" when the overpotential at one electrode is significantly larger than that at the opposing electrode, which often occurs when the exchange current densities of the electrodes differ by orders of magnitude. This concept relates to the dominance of the performance of one electrode to overall cell behavior. Special cases with respect to half cell electrodes or switching between dominant electrodes are considered in Appendix 5.10.

The explicit calculations from the linear approximation accelerate the optimization process compared to the implicit exact solution. The linearized model almost exactly matches the implicit solution in the feasible range of degradation for the dominant electrode. For instance, consider a NMC532-graphite cell in which the anode is potential dominant. The linear and exact approximate values from voltage pulses are plotted in Fig. 2, where differential conductance is derived in Appendix D in Ref. [13]. A good match is seen at the overpotential dominant electrode (anode), whereas at the non overpotential dominant electrode (cathode), the fitness values are smaller and the accuracy is reduced.

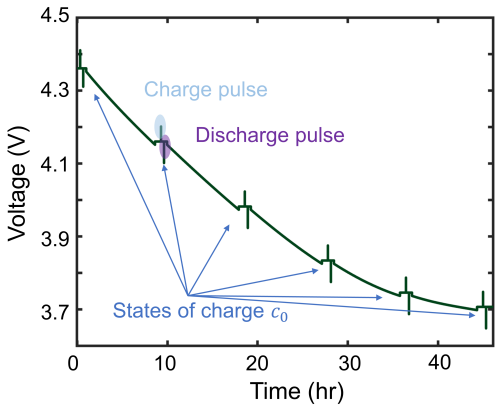

Figure 3: HPPC simulation shown for a single pulse size, with six different values of state of charge c_0 where the pulses are performed, with slow charges between the different state of charge values. The pulse experiments are repeated for each pulse value. The pulses are performed using the protocol in Algorithm 1.

5.3 Simulated Diagnostics

5.3.1 Virtual Experimental Design

Our primary goal of understanding pulses is to employ them in full cell diagnostics to quantitatively assess the extent of degradation in a cell. Determining the absolute degradation level in a specific cell is challenging due to significant variability between cells during manufacturing [316, 317]. Instead, we aim to establish a relative measure of degradation for each cell compared to its initial state, enabling more meaningful evaluation of battery degradation across different cells.

Based on our theory of voltage pulse measurements, Eq. 13 illustrates that degradation parameters influence half-cell kinetics jointly with kinetic-related parameters such as the differential conductance or the reduction current fraction. Figs. 4bc present the kinetically related differential conductance values and reduction current fractions at different states of charge and overpotentials, while Fig. 4d displays the effect of the surface blockage on the current at different states of charge. Applying high overpotentials generates a wide range of differential conductance values, which influences the calculation of the film resistance. The reduction current fraction is subject to a singularity when there is no current. This is seen in the denominator of

the reduction current fraction for the CIET reaction model,

$$\frac{\bar{i}_{\text{red}}}{\bar{i}} = \frac{\mathcal{H}(-\eta_f, \lambda)}{\mathcal{H}(-\eta_f, \lambda) - c\mathcal{H}(\eta_f, \lambda)}. \tag{20}$$

This indicates that in the linearized approximation, higher voltage pulse values have more numerical accuracy for estimating electrolyte loss. On the contrary, overpotential does not influence the fitness calculation for the surface blockage mechanism, and instead variations in states of charge are needed to observe changes in the current response. In summary, a wide spectrum of states of charge and large voltage pulse sizes are necessary to differentiate between the various degradation mechanism values. These considerations are valuable for designing industrial HPPC tests, where previously the choice of pulse size is arbitrary [62].

To account for the needs of varied pulse sizes and states of charge, we design a set of HPPC experiments, shown in Algorithm 1, that perform voltage/current pulses relative to the open circuit voltage at various states of charge for a single pulse size. This method is able to capture physical degradation mechanisms, and more importantly, quantify and separate each physical degradation mechanism, especially the dominant mechanism.

5.3.2 Virtual Experimental Procedure

The procedure is to perform current or voltage pulses of size i_{cell} or ΔV in our HPPC analysis with alternating pulses and rest states (Algorithm 1). Knowledge of the open circuit voltage curve $\text{OCV}(c_0)$ is necessary for this design structure, which may be difficult to validate once degradation occurs in a full cell. To ensure closeness to the true open circuit voltage curve, we perform voltage holds in between states of charge to ensure minimal influence of kinetics [164]. The rest and pulse times can vary with different battery material and design.

for c_0 *in all states of charge tested* **do**

`/* move the battery to the next state of charge */`

do a 0.05 C current hold until the voltage is at OCV(c_0);

`/* rest the battery */`

do a zero current hold for τ_{rest};

`/* equilibrate the battery to reduce the kinetic effects from moving to the next state of charge */`

do a voltage hold at OCV(c_0) until the current magnitude is less than 0.001 C;

`/* rest the battery */`

do a zero current hold for τ_{rest};

`/* perform a charge pulse */`

do a voltage or current hold for τ_{pulse} at OCV(c_0) + ΔV or i_{cell} current;

`/* rest the battery */`

do a zero current hold for τ_{rest};

`/* perform a discharge pulse */`

do a voltage or current hold for τ_{pulse} at OCV(c_0) − ΔV or $-i_{\text{cell}}$ current;

end

Algorithm 1: HPPC protocol.

5.4 Simulation Results

For each system, the HPPC protocol denoted in Algorithm 1 is executed using multiphase porous electrode theory simulations [53, 54, 43] implemented in the open-source MPET software package [44], which captures the electrode-scale transport and particle-scale kinetics in a full cell battery electrode. Porous electrode simulations capture the transport and kinetics of an electrode at two scales, with transport at the electrode scale covering electrolyte diffusion/conduction and solid conduction, and reactions/solid diffusion occurring at particle level. Simple one-dimensional Cahn-Hilliard [69] (similar to reaction-diffusion) models are used to capture particle

dynamics, modified to include fluxes from phase separating thermodynamics. Conservation equations for lithium ion mass and charge are applied at the electrode scale, capturing macroscopic transport between the cathode, separator, and anode. The current responses from voltage pulses, and voltage responses from current pulses, are used to optimize for the state of degradation and compared with the reference solution. The fitted solutions are extracted from pulse responses for the HPPC protocol at both the degraded and nondegraded states.

The objective function was assessed at the initial time measurement of the pulse from simulations, chosen for its accuracy in capturing kinetic information. We formulate the objective functions for minimization to ensure that each state of charge carries equal weight. For voltage pulses, the objective function is

$$f_{\min} = \min_{\text{deg}} \sum_{c_0} \left(W - \frac{i}{\bar{i}} \right)^2, \tag{21}$$

while for current pulses, the objective function is

$$f_{\min} = \min_{\text{deg}} \sum_{c_0} \left(\frac{\Delta V_{\text{predicted}}}{\Delta V_{\text{measured}}} - 1 \right)^2, \tag{22}$$

where deg $= \{R_{f,c/a}, \tilde{c}_{c/a}, c_+\}$ are the degradation parameters under consideration. The *fmincon* function in MATLAB was used to execute the optimization procedure. The code for the procedure is provided in *lightningclaw001/public_paper_scripts* under the folder *smart_HPPC* (`https://github.com/lightningclaw001/public_paper_scripts/tree/main/smart_HPPC`).

The optimization tests are conducted on a NMC532-graphite full cell. Kinetic parameters are obtained from Ref. [129], while electrode-scale parameters are obtained from Ref. [300]. Specific details regarding the porous electrode scale and kinetic parameters used are reported in Appendixes 5.5 and 5.6. A range of degradation parameters are assessed across various degradation states, spanning nine points from least to most degraded. Timescales of $\tau_{\text{rest}} = 20\,\text{min}$ and $\tau_{\text{pulse}} = 0.6\,\text{s}$ for resting and pulsing are employed, which was sufficient for relaxation in the simulations. For the

cathode, the filling fraction values of c_0 are set from 0.3 to 0.8 with a spacing of 0.1, which encompassed a total of six state of charge values for the cathode. The anode filling fraction values correspondingly varied from 0.9 to 0.4. The filling fraction values are derived from the parametrized ranges of the active material. Voltage pulses of 100 mV or current pulses of 0.1 C are applied, corresponding to the typical magnitude of common HPPC experiments [62, 3].

As seen in Fig. 4, the use of high voltage pulses allows for a broader range of information to be extracted due to wider variation in differential conductance values. This leads to more precise results for the film resistance values. Moreover, the utilization of higher filling fractions assesses a wide variance of surface blockage prefactors, as seen in Fig. 4d. This accounts for the increased sensitivity of surface blockage effects at lower filling fractions for the cathode, corresponding to higher filling fractions for the anode.

The optimization solutions for the exact method and linear approximation are shown in Fig. 6 for the voltage and current pulses respectively. With the large number of possible degradation mechanisms, only the dominant degradation mechanisms can be captured feasibly because of the insensitivity of degradation at the non-dominant electrode. This is mainly because of the differing electrode sensitivities, as observed in Fig. 5. Hence, multiple simulations are performed where the dominant degradation mechanism is different for each, plotted in Fig. 6. Some optimization error can be attributed to the averaging of porous electrode-scale effects.

For the current pulse results, only optimization results from the exact solution can be obtained. In contrast, for the voltage pulse results, both the exact solution and linearized result are calculated. The linear approximation exhibited a significant advantage in terms of computational efficiency. From the optimization speed, the linear approximation averaged roughly 1 s for each degradation state, relative to roughly 100 s per degradation state for the exact solution. For the current pulses, the computational demands are more substantial. A single current pulse took 200 s to solve, since separate cathode and anode potentials are extracted, increasing the number of variables in the system. In summary, optimizing from voltage pulses was

more efficient than current pulses. Specifically, the linearized approximation for voltage pulses had a tenfold speed-up relative to the exact solution, which only required a small trade-off in accuracy.

Due to the large number of degradation parameters, a sensitivity analysis was performed on the full cell to understand the dominance of different degradation mechanisms (Fig. 5). Voltage and current pulses using the implicit solutions are used for this analysis. Current pulses appeared extremely insensitive relative to voltage pulses in extracting degradation mechanisms, highlighting a benefit of using voltage pulses. The higher sensitivity of anode degradation parameters can be attributed to the lower exchange current density of graphite, which is approximately two orders of magnitudes lower than that of the nickel-rich material in the model. This causes overpotential dominance at the graphite anode.

In the sensitivity calculations for voltage pulses, we observe asymmetry between the charge and discharge directions for almost all degradation mechanisms. For the overpotential dominant electrode, sensitivity of degradation parameters depends on the fitness of the overpotential dominant electrode since $W \approx \hat{W}_\mathrm{d}$ from Eq. 19, where $\hat{W}_\mathrm{d}$ is the fitness of the overpotential dominant electrode. The directionality of intercalation at the overpotential dominant electrode during charge or discharge controls the sensitivity of the cell fitness. In the current cell setup, the overpotential dominant graphite anode deintercalates during discharge and intercalates during charge. Specifically as seen in Fig. 4bc, the magnitudes of differential conductance and reduction current fraction during deintercalation are both larger than the intercalation values. Since these parameters relate the fitness to the degradation parameters, the fitness is more sensitive during discharge, when the anode is deintercalating, compared to charge, as seen in Fig. 5cd for these two degradation mechanisms. In contrast, since the surface blockage mechanism is not potential dependent, no asymmetry appears between the charge and discharge directions for the anode as seen in Fig. 5e. Overall, when degradation parameters are at the overpotential dominant electrode or affect both electrodes, the sensitivity of cell fitness is dominated by the fitness of the overpotential dominant electrode.

For the degradation parameters at the non overpotential dominant electrode, simplifications lead to

$$W \approx \left(1 + \frac{f_{\mathrm{nd}} \frac{\partial \bar{i}}{\partial \eta_{\mathrm{nd}}}}{f_{\mathrm{d}} \frac{\partial \bar{i}}{\partial \eta_{\mathrm{d}}}}\right)^{-1} \hat{W}_{\mathrm{nd}}, \tag{23}$$

where d indicates overpotential dominant, nd is non overpotential dominant, and $\hat{W}$ is the fitness at the non overpotential dominant electrode. From the definition of a overpotential dominant electrode, this indicates that the conductance ratio between electrodes is large, meaning that the prefactor $\left(1 + \frac{f_{\mathrm{nd}} \frac{\partial \bar{i}}{\partial \eta_{\mathrm{nd}}}}{f_{\mathrm{d}} \frac{\partial \bar{i}}{\partial \eta_{\mathrm{d}}}}\right)^{-1}$ is necessarily large. Thus, the conductance ratio is more significant on the full cell fitness relative to the fitness of the non overpotential dominant electrode $\hat{W}_{\mathrm{nd}}$. The larger differential conductances during intercalation in the cathode, as seen in Fig. 5a, result in higher sensitivity in the cell fitness when discharging, where the non overpotential dominant cathode is intercalating, relative to charge. Unlike the overpotential dominant electrode, when degradation parameters are at the non overpotential dominant electrode, the cell fitness is dominated by the conductance ratios in the cell and not the fitness of the non overpotential dominant electrode. This elucidates the difficulty in resolving degradation mechanisms at non dominant electrodes.

Overall, a clear distinction between the information gain between charge and discharge pulses is observed. The information gain is asymmetric and depends on both the battery state of charge and overpotential dominance of electrodes. In degradation at both electrodes, the direction where the overpotential dominant electrode deintercalates is more sensitive. This is caused by asymmetry in kinetic factors correlating degradation to fitness for the overpotential dominant electrode, or dominance of the conductance ratio from the non overpotential dominant electrode. When the anode is overpotential dominant, discharge pulses contain more information about degradation, while the opposite is true when the cathode is overpotential dominant.

The results from these optimization procedures highlight the advantages of utilizing voltage pulses in this context. When it comes to learning degradation mechanisms, the necessity for optimization is evident, and mathematically simplifying the optimization problem becomes important. Voltage pulses offer several distinct

advantages. Firstly, they are able to quickly and explicitly approximate extent of degradation with the explicit expression, resulting in a significant reduction in fitting time, often by two orders of magnitude. This efficiency can be highly beneficial in practical applications. In addition, the sensitivity of current pulses is much weaker as compared to voltage pulses, as seen in Fig. 5. The stronger sensitivity of voltage pulses makes them a more effective diagnostic tool for capturing degradation behavior. Importantly, compared to current pulses, which introduce much nonlinear behavior from the coupled current control equation, fewer population effects are revealed from voltage control systems. Furthermore, voltage pulses are more physically tied to rate capability and directly related to degradation mechanisms as seen in the explicit approximation. The ability to gain deeper insights into the underlying physical mechanisms makes voltage pulses a superior choice in diagnostics.

5.5 Appendix: Variable Definitions

For ease of readability, variable definitions are placed in the following table. The subscript a depicts the anode, and the subscript c depicts the cathode. Bars above variables are used to define the value of the variable without any degradation or potential shift (e.g, $\bar{i} = R(\dots, R_f = 0, \tilde{c} = 1, c_+ = 1, \phi_s, \dots)$). Hats are used to define the variables without any voltage shift (e.g. $\hat{i} = R(\dots, R_f = 0.01, \tilde{c} = 0.99, c_+ = 0.99, \phi_s, \dots)$). The real solution is given without any hats or bars (e.g. $i = R(\dots, R_f = 0.01, \tilde{c} = 0.99, c_+ = 0.99, \phi_s + \Delta\phi, \dots)$).

Variable Name	Definition	NMC532 Cathode	Graphite Anode	Units
c	lithium concentration in solid	–	–	nondimensional
i	current density	–	–	$\mathrm{A/m^2}$
i_{red}	reduction current contribution to total density	–	–	$\mathrm{A/m^2}$
η	overpotential (driving force of reaction)	–	–	k_BT
k_0^*	exchange current density	10 [129]	0.2 [129]	$\mathrm{A/m^2}$
λ	reorganization energy of intercalation solid	3.78 [129]	5 [129]	k_BT
ε	porosity	0.4	0.4	nondimensional
P_L	volumetric loading of active material	0.69	0.69	nondimensional
L	length of electrode	5e-5	8.7e-5	m
A_p	area of particle p	–	–	$\mathrm{m^2}$
V_p	volume of particle p	–	–	$\mathrm{m^3}$
$\langle r_p \rangle$	mean particle p radius	1e-7	1e-7	m
ThermFac	thermodynamic factor $\frac{\partial \ln a_+}{\partial \ln c_+}$ [43]	–	–	nondimensional
R_f	film resistance	–	–	$\Omega \cdot \mathrm{m^2}$
$\tilde{c}$	rescaled capacity	– [12]	–	nondimensional
c_+	electrolyte concentration	–	–	M
W	fitness value $i/\bar{i}$ [13]	–	–	nondimensional
f	porous electrode rescaling ratio, $L(1-\varepsilon)P_L\langle\frac{A_p}{V_p}\rangle$	626.8	1100.6	nondimensional
χ	current ratio before and after potential shift $i(\phi_s + \Delta\phi)/i(\phi_s)$	–	–	nondimensional

5.6 Appendix: Full Cell Simulation Parameters

In the full cell, 10 volumes were used to discretize the cathode and the anode, while 5 volumes were used to discretize the separator. Both the relative and absolute tolerance were set to 1×10^{-6}. The temperature in the simulations was set to 298 K. It was assumed that there was enough carbon additives in the cell to cause the solid conductivity to have minimal effects. The Bruggeman exponents for the tortuosity were set to 1.5 for the cathode, the anode, and the separator [318]. A Stefan-Maxwell concentrated electrolyte model where the thermodynamic factor, diffusivity, and transference number were from Ref. [47] and the conductivity was from Ref. [77] was used in our parametrization. In the particle-scale models, a Cahn-Hilliard reaction-diffusion model [69] was used to describe the solid particles, with spherical shaped particles for both the graphite and the NMC532. The explicit activity contribution for the electrolyte is

$$a_+ = c_+^{601/620} \exp\Big(-1299/5000 - (24c_+^{1/2})/31 + (100164c_+^{3/2})/96875\Big), \tag{24}$$

analytically integrated from Ref. [47].

5.7 Appendix: Reference Electrode Fitness

Following the protocols in Ref. [13], we see that for a reference electrode, if the foil reaction is defined with a simple Butler-Volmer reaction as

$$i_a = 2k_0\sqrt{a_+}\sinh\Big(\frac{\eta}{2}\Big), \tag{25}$$

then the differential conductance is found to be

$$\frac{\partial i_a}{\partial \eta} = k_0\sqrt{a_+}\cosh\Big(\frac{\eta}{2}\Big), \tag{26}$$

and

$$\frac{Di_a}{Dc_+} = \frac{\partial i_a}{\partial c_+} + \frac{\partial i_a}{\partial \eta}\frac{\partial \eta}{\partial c_+} = \frac{i_a}{2c_+}\frac{\partial \ln a_+}{\partial \ln c_+}\left(1 - \frac{k_B T}{e}\coth\left(\frac{\eta}{2}\right)\right). \tag{27}$$

Because material-scale degradation does not generally happen at the reference electrode, the linearized fitness for a half-cell electrode is described as

$$\hat{W}_a = 1 - \frac{1}{2}\left(1 - \frac{k_B T}{e}\coth\left(\frac{\eta}{2}\right)\right)\frac{\partial \ln a_+}{\partial \ln c_+}(1 - c_+) \tag{28}$$

without any dependencies on film resistance or surface blockage from the cathode.

5.8 Appendix: Current Pulse Linear Approximation

For a model single particle, a current pulse will lead to a voltage response. The voltage response can be expressed in terms of the overpotential fitness variable U, which is defined as the ratio of the measured overpotential in the degraded state and overpotential in the non-degraded state for a half cell. For a half cell, where the direct measurement of the electrode potential is possible, we can write the fitness variable exactly as

$$\hat{U} = \frac{\phi - \phi(c)}{\bar{\phi} - \bar{\phi}(c)} = \frac{\eta}{\bar{\eta}} = \frac{\eta(i, R_f, \tilde{c}, c_+)}{\eta(i, R_f = 0, \tilde{c} = 1, c_+ = 1)}. \tag{29}$$

Analogous to the linear approximation of current fitness variable in (13), we also derive a linear approximation of U in the limit of small degradation variables. We perturb the non-degraded state by the degradation variables independently, and multiply each correction to the fitness variable, such that $\hat{U} \approx \hat{U}_{R_f}\hat{U}_{\tilde{c}}\hat{U}_{c_+}$:

$$\begin{aligned}\hat{U} = &\left(1 + \frac{iR_f}{\bar{\eta}}\right)\left(1 + \left(\frac{\partial i}{\partial \eta}\right)^{-1}\bar{\eta}^{-1}k_0 h(\bar{\eta})(\tilde{c} - 1)\right) \\ &\times \left(1 + \left(\frac{\partial i}{\partial \eta_f}\right)^{-1}\bar{\eta}^{-1}k_0^*(1 - c)g(-\bar{\eta}_f, \lambda)(c_+ - 1)\right).\end{aligned} \tag{30}$$

Importantly, this equality constraint in the linear approximation highlights one drawback of doing current pulses, primarily being the extra computational effort

needed to get a linear estimate of the degradation parameters from current pulses. In the following, we provide derivations of the individual components of $\hat{U}$.

A useful derivative for the full derivative which is used in later derivations is

$$\frac{D\eta}{DR_f} = \frac{\partial \eta}{\partial Y} + \frac{\partial \eta}{\partial i}\frac{\partial i}{\partial Y}, \tag{31}$$

where Y can be any degradation variable of R_f, $\tilde{c}$, or c_+.

5.8.1 Film Resistance

To determine $\hat{U}_{R_f}$, we can write the Taylor expansion of η with respect to R_f. In this expression, we can directly evaluate $D\eta/DR_f = \partial\eta/\partial R_f$ since $\partial i/\partial R_f = 0$.

$$\eta = \bar{\eta} + \left.\frac{\partial \eta}{\partial R_f}\right|_{R_f=0} R_f + \mathcal{O}(R_f^2). \tag{32}$$

By the definition of the overpotential, it is clear that the fitness variable is defined as

$$\hat{U}_{R_f} = 1 + \frac{iR_f}{\bar{\eta}} + \mathcal{O}(R_f^2). \tag{33}$$

5.8.2 Rescaled Capacity

To determine $\hat{U}_{\tilde{c}}$, we can write the Taylor expansion of η with respect to $\tilde{c}$. Since

$$\frac{D\eta}{D\tilde{c}} = \frac{\partial \eta}{\partial i}\frac{\partial i}{\partial \tilde{c}} = \left(\frac{\partial i}{\partial \eta}\right)^{-1}\frac{\partial i}{\partial c}, \tag{34}$$

we see that

$$\eta = \bar{\eta} + \left.\frac{D\eta}{D\tilde{c}}\right|_{\tilde{c}=1}(\tilde{c}-1) + \mathcal{O}(\tilde{c}^2) = \bar{\eta} + \left(\frac{\partial i}{\partial \eta}\right)^{-1}\frac{\partial i}{\partial c}_{\tilde{c}=1}(\tilde{c}-1) + \mathcal{O}(\tilde{c}^2). \tag{35}$$

Plugging in the values for the differential conductance gives that

$$\hat{U}_{\tilde{c}} = 1 + \left(\frac{\partial i}{\partial \eta}\right)^{-1}\bar{\eta}^{-1}k_0 h(\bar{\eta})(\tilde{c}-1) + \mathcal{O}(\tilde{c}^2), \tag{36}$$

where $h(\eta)$ is the overpotential-dependent part of the reaction as $i = k_0^*(1-c)h(\eta)$.

5.8.3 Electrolyte Loss

To simplify calculations, we use the formal overpotential, since this preemptively removes the electrolyte loss dependence from the model. Since

$$\frac{D\eta_f}{Dc_+} = \frac{\partial \eta_f}{\partial i}\frac{\partial i}{c_+} = \left(\frac{\partial i}{\partial \eta_f}\right)^{-1}\frac{\partial i}{\partial c_+} = \left(\frac{\partial i}{\partial \eta_f}\right)^{-1} k_0^*(1-c)g(-\eta_f,\lambda). \tag{37}$$

Since $\frac{\partial i}{\partial \eta_f} = \frac{\partial i}{\partial \eta}$, we can directly use this derived relationship in the Taylor expansion of the overpotential. To determine $\hat{U}_{c_+}$, write the Taylor expansion of η with respect to c_+,

$$\eta = \bar{\eta} + \left.\frac{D\eta}{Dc_+}\right|_{c_+=1}(c_+ - 1) + \mathcal{O}(c_+^2). \tag{38}$$

Upon combining these equations, we can determine the fitness variable as an implicit formula to the equation

$$\hat{U}_{c_+} = 1 + \left(\frac{\partial i}{\partial \eta_f}\right)^{-1}\bar{\eta}^{-1}k_0^*(1-c)g(-\bar{\eta}_f,\lambda)(c_+ - 1) + \mathcal{O}(c_+^2). \tag{39}$$

Though these analyses can be done directly for a half cell, they do not provide any inherent information on degradation of the full cell. The full cell fitness is

$$\begin{aligned} U &= \frac{\hat{U}_c\bar{\phi}_c - \hat{U}_a\bar{\phi}_a}{\bar{\phi}_c - \bar{\phi}_a} \\ &\approx \frac{\hat{U}_c(\bar{\eta}_c - \mu_c(c_c)) - \hat{U}_a(\bar{\eta}_a - \mu_a(c_a))}{(\bar{\eta}_c - \bar{\eta}_a) - (\mu_c(c_c) - \mu_a(c_a)))}. \end{aligned} \tag{40}$$

Because the intercalation potentials for the solid depend on the reference potential, there is no absolute U value that can be calculated for a full cell. Thus, the linearization only works at at the half cell level and cannot be brought to the full cell level.

5.9 Appendix: Multiple Degradation Mechanisms

A set of full cell simulations of NMC532-graphite with all degradation mechanisms present is shown in Fig. 7. The function does well at separating the dominant mechanism (the surface blockage mechanism for the anode, and then the electrolyte concentration loss mechanism) and quantitatively performs well in separating each of the degradation mechanisms, but does not perform as well qualitatively. The linear model drifts especially at the non kinetically limiting electrode because, as seen in Fig. 2, the cathode values especially do not capture the implicit contribution and drift at larger degradation amounts.

5.10 Appendix: Special Cases of Linearized Fitness

To preferably measure one electrode over the other, special care can be taken to consider the state of charge that the pulse is performed at. Based on the conductance ratio between the electrodes, we can approximate the state of charge dependence on the ratios as $\frac{f_c k_{0,c}(1-c_c)}{f_a k_{0,a}(1-c_a)}$, where the cathode and anode state of charges are related through mass conservation. The approximate weights between the cathode and the anode fitnesses can be tuned by the state of charges used to measure the materials.

A special case is the half cell with a lithium counter electrode. In this scenario, $f_a = 1$ since the lithium counter electrode is a foil. We also assume there is no degradation at the reference electrode $\hat{W}_a = 1$. As a result, the overall fitness value can be expressed as

$$W = \frac{\hat{W}_c + f_c \frac{\partial \bar{i}}{\partial \eta}_{c/a}}{1 + f_c \frac{\partial \bar{i}}{\partial \eta}_{c/a}}. \tag{41}$$

In a half cell with a lithium reference electrode, the reference electrode is primarily affected by electrolyte loss and no other degradation mechanisms, as detailed in Appendix 5.7. Due to the fact that the foil only has active area on the surface and not within the electrode, $f_c/f_a \gg 1$, the cathode is always potential dominant. This dominance at the cathode arises from the limited surface area available at the anode,

making it difficult to separate the degradation mechanisms at the cathode material. Given this dominance at the cathode, it is not desirable to conduct HPPC pulses on half cells.

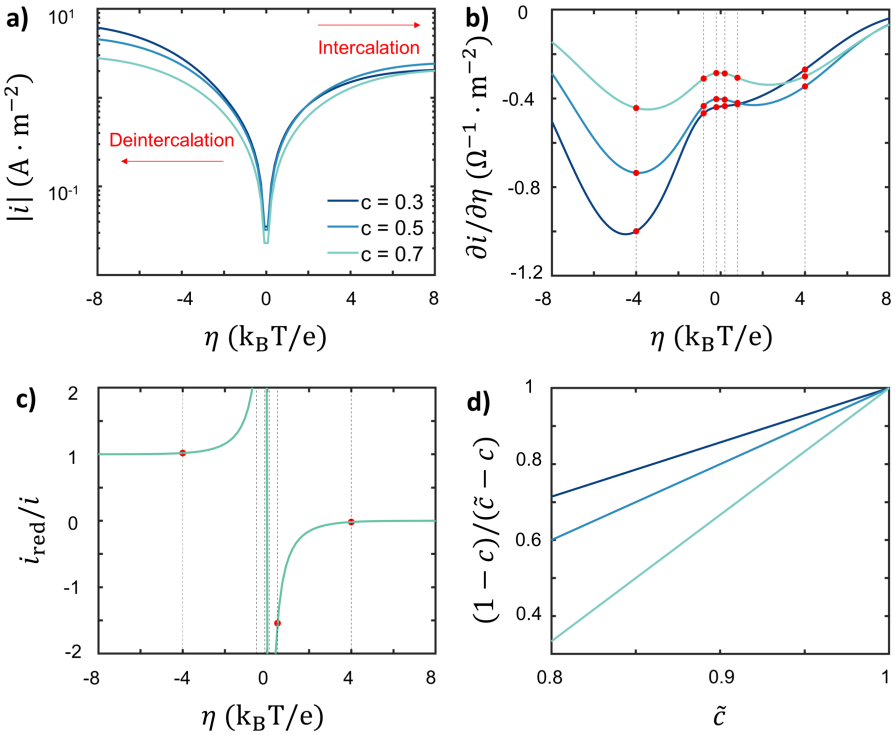

Figure 4: a) Tafel plot for a coupled-ion electron transfer reaction relative to the overpotential for a NMC532 model at different states of charge, which gives rise to different differential conductance behavior as well as reduction current fraction in the next two plots. b) Differential resistance values for a NMC532 model captured at different overpotentials for various states of charge are plotted. Specifically, pulses at 5, 20, and 100 mV overpotentials are plotted at the red points. c) Reduction current fraction is plotted with respect to different overpotentials. State of charge variation plays a minimal role in the reduction current fraction, causing reduction current fractions at different SOC values to overlap. The reduction current fraction values for pulse experiments at 5, 20, and 100 mV overpotentials are shown as red points. d) Kinetic fraction of surface blockage is plotted at different state of charge values for varying overpotentials.

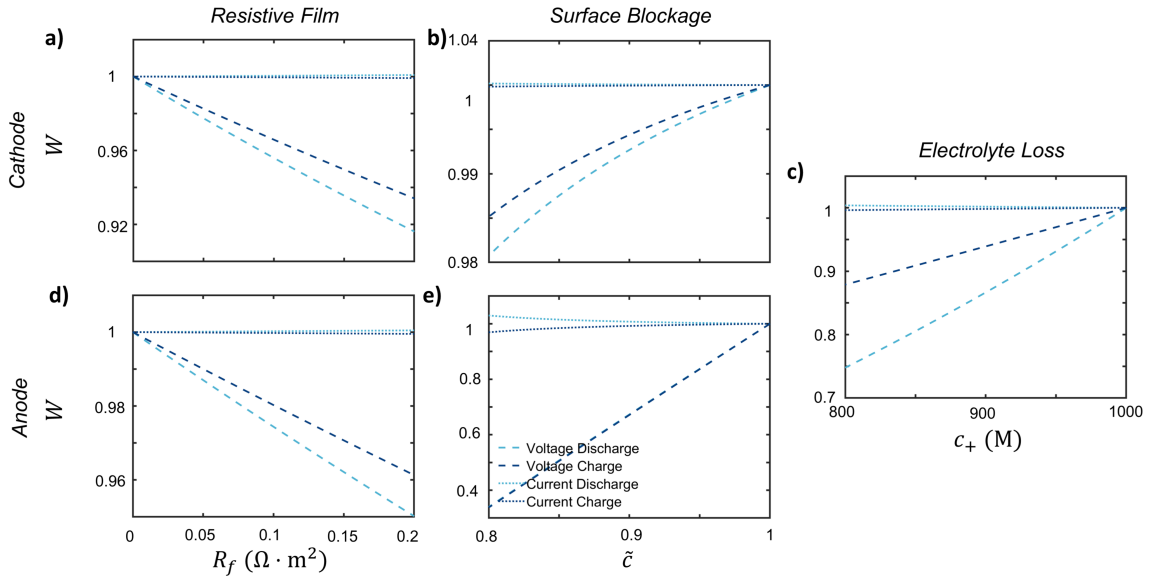

Figure 5: Sensitivity analysis of each degradation mechanisms on the fitness W for a NMC532-graphite cell for a 100 mV (dis)charge voltage pulse or for a 1 C (dis)charge current pulse at a cathode state of charge of 0.8 and anode state of charge of 0.4. The effects of film resistance for (a) the cathode, (b) the surface blockage for the cathode, (c) the electrolyte concentration, (d) the film resistance for the anode, and (e) the surface blockage of the anode are plotted for this cell for values close to the initial degradation state.

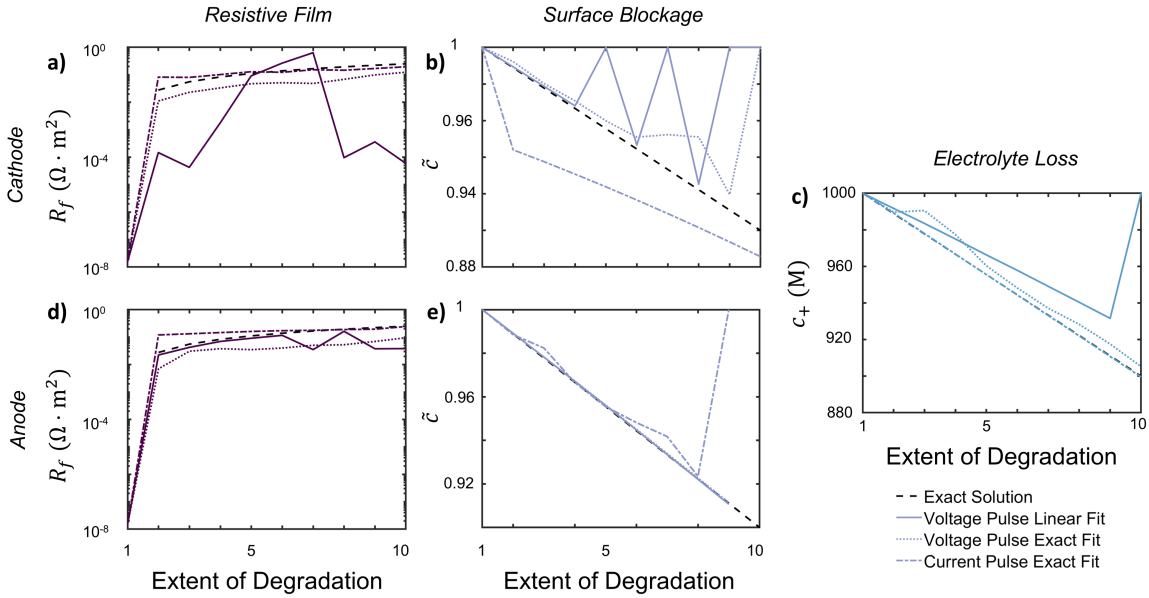

Figure 6: Comparison of fitting linearized or exact objective functions to simulated results for full cell simulation for NMC532-graphite at ten different degradation points for each degradation mechanism for voltage/current pulse HPPC is shown. (a,d) are the film resistance mechanisms for the cathode and anode; (b,e) are the surface blockage mechanisms for the cathode and anode, and (c) is the electrolyte loss mechanism.

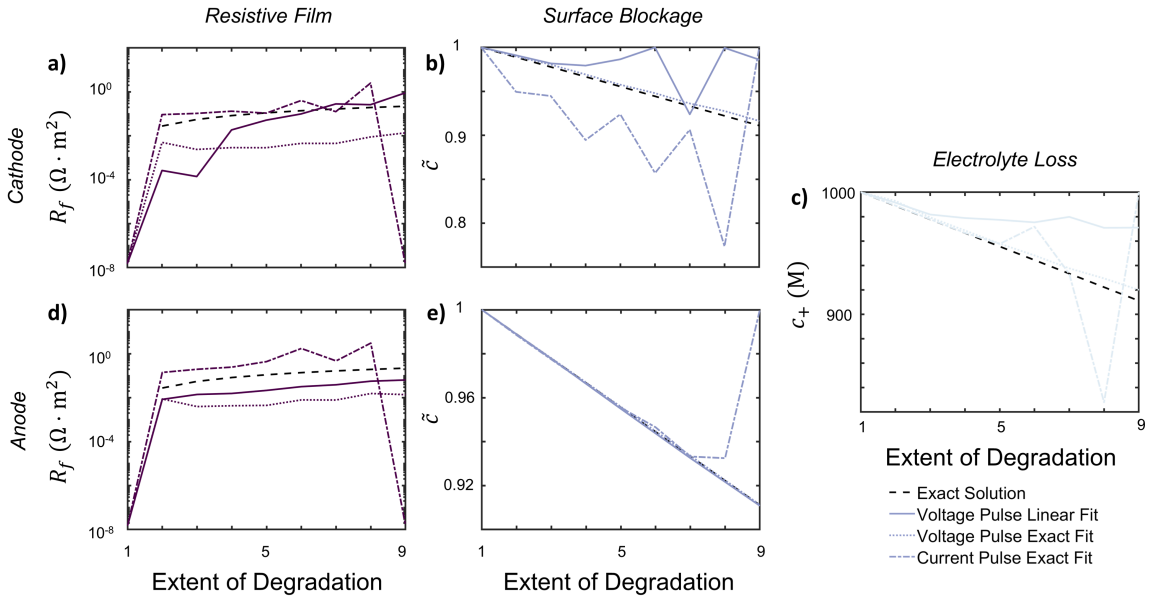

Figure 7: Comparison of fitting linearized objective function to exact results for full cell NMC532-graphite simulation at nine different degradation points for a combined set of simulations with all degradation mechanisms present. (a,d) are the film resistance mechanisms for the cathode and anode, (b,e) are the surface blockage mechanisms for the cathode and anode, and (c) is the electrolyte loss mechanism.

Chapter 6

Conclusions

Our multiscale model for understanding degradation can capture the effects of degradation from a single particle scale to a population scale, and then eventually to a porous electrode scale, as shown in Fig. 1. Microscopic degradation mechanisms were investigated at a particle level, using surface phase transformations of nickel rich materials as an example, and incorporated into population scale effects for solid solution or phase separating populations. Population balances with nickel rich materials were developed as an example for solid solution materials, while simple linearized models were applied and validated to represent the influence of degradation on kinetics. Scaling analyses using timescale competition for phase separating materials were developed to observe the competition between population and single particle timescales, using lithium iron phosphate as an example. The extraction of microscopic degradation mechanisms from macroscopic electrochemical responses using pulse diagnostics was also explored. Physical interpretations of pulses were formulated for a full cell electrode and proven to extract microscopic degradation mechanisms from particle level. These protocols were eventually optimized with model based design-of-experiment to extract particle level degradation efficiently and optimally from macroscopic signals.

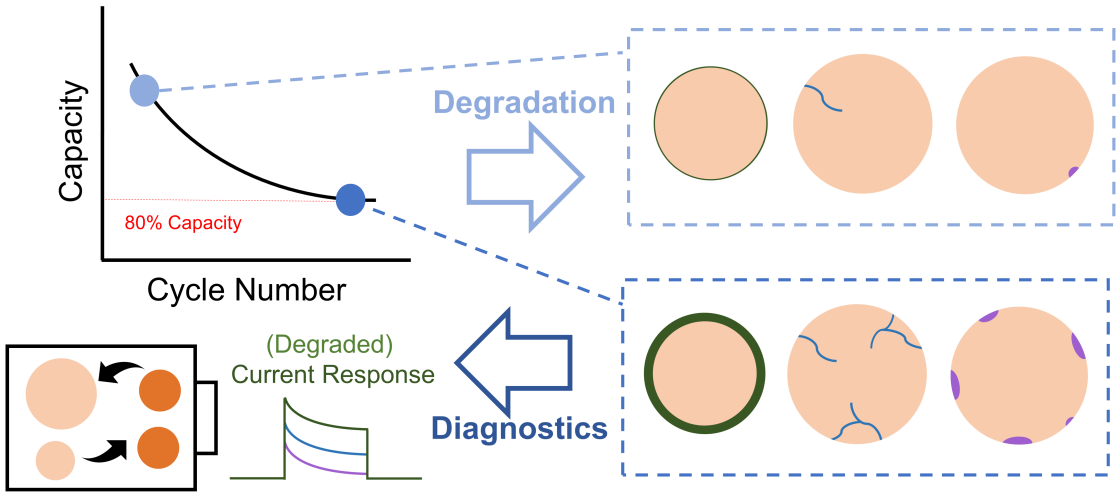

Figure 1: Figure displaying the scope of this thesis, from modeling particle level degradation [12] to projecting particle level to population scale degradation [13, 14], and finally applying electrode level understanding of diagnostics to particle level [15, 16].

6.1 Particle Level Degradation Mechanisms

In this study, we demonstrate the formulation of a degradation model that accounts for cation disorder coupled with oxygen formation at the surface of nickel-rich layered materials. Due to the high commercial availability of nickel, these materials are increasingly recognized as the next generation of battery cathode materials. These free energy models, combined with an oxygen vacancy boundary condition, qualitatively explain why high voltage cycling causes more phase transformations and disorder [60] in battery materials. To the authors' knowledge, this is the first model of free energy for cation degradation that can be easily derived from first principles which is applicable to continuum-scale battery simulations. It merges the detailed understanding of crystal structures from first principles with the computational tractability required for continuum-level battery modeling. This approach eliminates the need for experimental data to characterize the chemical potential functions or free energy models for degradation, requiring experimental data only to determine the kinetic parameters of degradation. This significantly enhances the practical applicability of the models.

These degradation models can be applied to porous electrode models to study the effects of various macroscopic battery parameters, such as particle size and charging rate, on cation disorder growth in the active materials [54, 53]. Cycling simulations at different operating conditions, such as constant current and constant voltage, can model their effects on inducing cation disorder and thus phase transformations in a battery, a crucial step to the study of long term maintenance of battery operation. Insight from single particle cycling simulations of these particles reveal that the degradation caused by higher voltage operation in these materials is irreversible and that if avoiding degradation is imperative, higher voltage ranges should be applied later in the operation of a battery. From a materials design perspective, maintaining a balanced Ni-Co-Mn ratio is thermodynamically preferable. Although Ni-rich materials have more attractive techno-economics, they are predicted to be less stable as the Ni concentration increases, promoting the blocking of lithium sites by nickel disorder [84].

6.2 Particle Level to Electrode Level

6.2.1 Solid Solution Materials

Degradation on populations of solid solution materials was mapped from a single particle level to an electrode level using a population balance equation. By employing the concept of fitness functions from biological populations, this idea was adapted to model the degradation of battery particles of varying sizes in a lithium-ion battery. The coevolution of fitness with reaction and degradation on these battery particles is simulated as the battery is cycled with the Fokker-Planck equation, using different intercalation reaction models. For all reaction models, the fitness function values are found to grow heterogeneously as the battery is cycled, starting with the initial formation cycles. This heterogeneous growth reflects the varying degradation rates among individual particles within the battery, which accumulate differently over successive charge-discharge cycles. After the formation cycles, degradation accumulates

while preferring smaller particles. The degradation growth on the smaller particles from the autocatalytic behavior between fitness and degradation contributes to the eventual death of the battery [188]. This overall trend causes the smaller particles to lose their usable capacity faster and contribute to the failure of the battery before the larger particles do.

From our simulations, we also learn that particle level degradation mechanisms drive electrode-level behavior of the system, and the shape of the behavior of electrode-level current-voltage relations gives insight into which of the degradation mechanisms is most dominant. "Expansion" of voltage curves can be attributed to changes in reaction kinetics, while "shifts" of the voltage curves are attributed to active material degradation or changes in overpotential. Asymmetric effects between intercalation and deintercalation in the voltage curve can be attributed to electrolyte loss effects from their stronger contribution to the reduction reaction. In addition, the shape of the capacity loss curve gives insight into the mode of degradation that is most dominant. Electrolyte loss has smoother terminal behavior, while resistive film and surface blockage all have sharper capacity loss drops.

Such a model of fitness evolution for driven electrochemical reactions can be expanded to systems beyond a simple Fokker-Planck model. These simple degradation mechanisms can be applied to porous electrode models [53, 54, 122] to study the effect of degradation at macroscopic scale. The development of simple, physically driven degradation models which can be applied to porous electrode scale simulations provide support for data-driven modeling of degradation, aiding solutions to the major challenges in developing and designing better Li-ion batteries [319].

6.2.2 Phase Separating Materials

Beginning with single-particle conservation equations, we derive a population balance model to describe the behavior of active material particles in a lithium-ion battery during a (dis)charge process. Different timescales in the problem are revealed through the process. Through the eigendecomposition of this population scale model, we identify two regimes of stochastic and deterministic intercalation in the process

timescale, depending on whether the applied voltage lies within the miscibility gap or not. Asymmetry driven by the single particle stability criterion on timescales in the stochastic regime is observed in the process. Predictions on the voltage values under different applied currents are made through minimizing applied voltage, which then reveals the single particle reaction timescales. The observation of particle activation fraction as a nondimensional factor integrating competition between reaction and process timescales is revealed.

Such timescale analyses provide simple analytic estimations to phenomena such as active particle fraction and population timescales for intercalation. These simple predictions allow for unprecedented direct analysis of phase separating particle populations, aiding the design and analysis of common phase separating materials such as lithium iron phosphate or graphite. This work can predict and control optimized operation of phase separating materials to improve utility through increased particle activation fraction.

6.3 Electrode Level to Particle Level

6.3.1 Pulse Diagnostics

An analysis of the physics behind pulse diagnostics was performed to extract degradation behavior from macroscopic measurements to particle level, focusing on hybrid pulse power characterization techniques (HPPC). The goal of this work has been to enhance the physical understanding of HPPC protocols as a means to diagnose battery degradation behavior. Such detailed physical information transcends the conventional lumped degradation modes, which merely offer insights into the "symptoms" of battery degradation. In this work, models for both current and voltage response during the pulse were formulated, generating expressions that directly relate physical degradation parameters to the observed response. Furthermore, we have demonstrated the benefits of using voltage pulses instead of current pulses, including stronger sensitivity with respect to degradation, explicit linear extraction of degradation mechanisms,

faster optimization, and mitigated population effects relative to current pulses for phase separating materials. Discharge pulses are found to contain more information in cases of anode overpotential dominance, while charge pulses are better for cathode overpotential dominance. We have shown that it is possible to extract the dominant degradation mechanisms from each electrode with a physics-based optimized HPPC protocol. This is key to tying together physics-based modeling [53, 54] with diagnostics obtained from battery experiments without the need for lumped degradation modes commonly used in battery degradation [320, 37]. With these physical degradation parameters, we can diagnose the physical-driven reasons for battery failure and, in turn, design future batteries to mitigate capacity loss.

Our derivations provide some generic useful physical insights. The overpotential-dominant electrode with slower kinetics dominates full cell electrochemical responses, which makes it difficult to probe the properties of the opposing electrode. For pulse schemes, the corresponding fitness variables are directly proportional to the ratio of instantaneous power. This relationship is crucial for assessing instantaneous power output, which is challenging without conducting experiments. These straightforward and explicit linear approximations provide a direct link between physically meaningful degradation parameters and power, offering a simplified pathway for evaluating the state of health of a battery system. Even without experimental validation, the increased physical understanding behind sensitivity and information gain in pulses, as well as pulse design methods in a full cell and the limitations of these techniques, are useful for optimal design. This deeper understanding of pulse diagnostics can lead to more accurate and faster degradation assessments, enabling better management and longer life for lithium-ion batteries.

Overall, a simple model that provides tractable analytical methods of extracting degradation mechanisms from single particle level was developed in this work, using approximations in Ref. [13]. Some drawbacks of our approach include a necessary physical understanding of the impact of degradation on the kinetics of the electrode material to be included in the model. In addition, mathematical models of the reaction kinetics must be selected before the optimization can be performed, although one can

imagine automating this process with inverse learning from data. Chemo-mechanics, microstructural effects [236], and phase separating dynamics have also been neglected in this model. Some degradation mechanisms, such as lithium plating and surface degradation in nickel-rich materials, can have similar electrochemical signatures, posing challenges in their differentiation. In addition, though the theoretical analysis of these experiments has revealed much about the practicality and also limitations of HPPC diagnostics, experimental validation is a crucial step. Experimental validation of our framework is imperative for our desire to apply diagnostics to real life battery systems. Forthcoming works will be focused on improved design-of-experiments for optimal HPPC and rigorously verifying these methods through experiments, using test pulses to validate the accuracy of our model for capturing degradation. By addressing these challenges and validating our models experimentally, we can enhance the reliability and applicability of our diagnostics framework. This will ultimately contribute to better battery management, longer battery lifespans, and more effective second-life applications, significantly advancing the field of lithium-ion battery technology.

6.3.2 Optimal Design of Pulses

An extension to this study, performed in Ref. [16], proposes a novel framework for optimizing HPPC protocols to extract degradation information related to the kinetics of lithium-ion batteries by considering properties specific to the reaction model and electrode materials. A two-objective optimization was defined by formulating the parametric uncertainty for reaction-limited degradation [15] and the diagnostic time using scaling analysis [3]. Model-based design-of-experiment was used to minimize the parametric uncertainty while the diagnostic time was used as a constraint to construct the Pareto front. While the degradation state is not known *a priori* (which is necessary for designing the optimal HPPC protocol), a *generalized* optimal HPPC protocol was designed by applying the mean-field average approach over an expected feasible region. The robustness of the designed HPPC protocols was evaluated by performing Markov Chain Monte Carlo simulations for various degradation states.

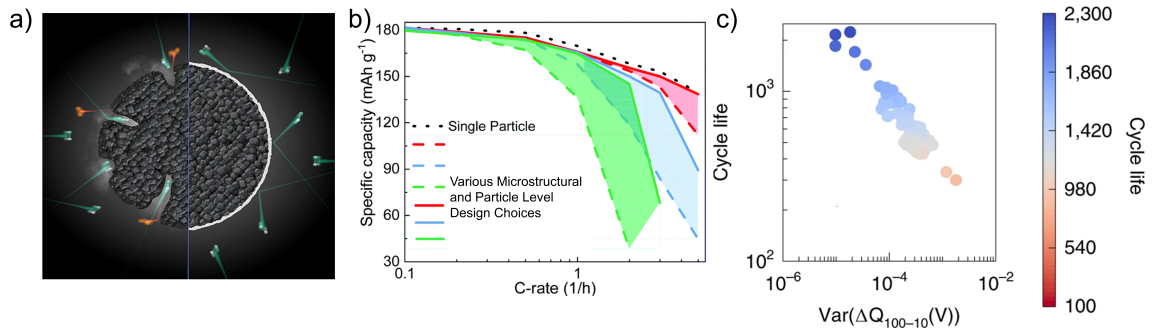

Figure 2: a) Example of improved surface coatings for transition metal oxide cathode materials [17]. b) Example of improved electrode utility from microstructural and particle level design choices [18]. c) Example of the impact of improved diagnostics on cycle life prediction [1].

These optimally designed pulses can be used to reduce required diagnostics time in high-power applications such as electric vehicles [62].

6.4 Outlook

Our multiscale model can be used in many directions for future applications, as shown in Fig. 2. Firstly, at the single particle level, improved operation can be designed from reaction-diffusion behavior. Our theory of degradation may help guide the development of surface modifications to stabilize transition metal oxides, where an example is shown in Fig. 2a. From a kinetic perspective, for a given NMC composition, the surface treatment must limit oxidation reactions that trigger cation disorder by passivating the reactive oxygen ions at the edge plane and blocking electron transfer to the electrolyte. Well known ceramic coatings, such as alumina (Al_2O_3), zirconia (ZrO_2), magnesium oxide (MgO), and other oxide materials, are able to perform these functions and can extend the cycle life of of nickel-rich oxides [321, 182, 7]. Some coatings, such as niobium oxides (NbO), not only passivate oxygen and block electron transfer, but also introduce more stable ions, such as Nb^{5+}, into the crystal structure near the surface at transition metal or lithium sites [322]. Our theory would suggest that such inserted ions from the coating may exchange with the more unstable

nickel ions and reduce the likelihood of cation reduction and disorder at the surface. Overall, guidance on synthesis of nickel rich materials or coatings be performed with future extensions of this model, providing overall predictions of optimal synthesis temperatures related to equilibrium thermodynamics.

Using our population scale models, improved electrode scale utility can also be designed and achieved from synthesis parameters such as particle size distribution, or operating conditions such as current or voltage, as indicated in Fig. 2b. Differences in particle size distributions are influenced by synthesis conditions such as temperature, precursor particle size, and timescales [323]. Our work can help with selection of the desired particle size distribution, guiding specific operation conditions of synthesis. This work also allows for design of electrode utility at different voltages or current, calculated from the varying amounts of power that can be extracted from the system. For phase separating materials, the active particle fraction can significantly impact the utility [8] at a population level. Even for solid solution materials, the appearance of fictitious phase separation [49] also indicates that higher utility distributed between particles can be achieved at a population scale. We expect that improved electrode scale utility can be impactful for both solid solution and phase separating devices.

We envision that in the future, these methods could help detect changes in degradation that are difficult to discern using conventional techniques. Our method allows for the determination of dominant degradation mechanisms for each electrode in operando, which allows for a pivotal method of detection and prevention of battery failure. Some factors, such as coupling between transition metal cathode degradation with resistive film growth on the graphite electrode, may need to be added to these models for more accurate modeling [324]. Moreover, the determination of the failure mechanism can also guide the selection of second life application for the degraded battery [325, 326, 327]. For instance, batteries retired from electric vehicles might still have sufficient capacity and power output for less demanding applications, such as stationary energy storage. Understanding the specific degradation mechanisms can help with repurposing, ensuring that the second life application maximizes the remaining useful life of the battery. The integration of advanced degradation diag-

nostics into battery management systems can significantly enhance the reliability, longevity, and economic value of lithium-ion batteries across their lifetime.

Additionally, the combination of these simpler population models and faster HPPC diagnostics can allow for improved diagnostics in the future, as indicated in Fig. 2c. These methods could even be incorporated for better model-based diagnostics, or data-driven diagnostics to determine better features representing degraded states. Enhanced diagnostics for batteries in use cases such as electric vehicles can improve range estimation, ensure safety, and extend battery life. Additionally, advanced diagnostics can facilitate more efficient recycling and reuse of battery materials, thereby reducing environmental impact. Overall, this work will pave the way for more physically grounded methods of understanding and measuring degradation in lithium ion batteries, from the particle to electrode scale.

Appendix A

Nonisothermal Open Driven Systems

A.1 Introduction

The coupling of reactions and transport has been found to affect the stability of phase separation of a system [328]. Specifically, thermodynamic stability of electrochemical systems has been found to affect the operation of lithium ion batteries and control macroscopic phase separation of these systems [164, 165]. Reactions often end up controlling the operational stability of these systems, as seen in the suppression of phase separation in lithium iron phosphate at high charging rates [67, 3, 329]. Spontaneous phase separation in these systems sometimes lead to undesired behavior, like phase separation in battery intercalation, which causes immense strain on the intercalation material and can lead to particle cracking and intergranular strain [330]. In operation, it can lead to localized degradation such as lithium plating and be potentially hazardous to battery users [92].

Nonisothermal effects can also play a role in the coupling of transport processes and reactions in a system. Temperature effects on the phase stability of systems have been noted in systems such as drug-polymer dispersion, block copolymer melts, and even biological transcription [331, 332, 333, 334]. Heat transfer and temperature effects influence stability of open driven systems, especially since temperature also affects reaction rates of the system, the transport coefficients, as well as the magnitude of driving forces of the system [161]. Thermal driven fluxes can appear in gaseous sys-

tems which can directly affect the transport processes in a system [161]. In this study we will isothermal thermodynamic stability to consider the thermodynamic stability of open driven systems, but in a nonisothermal fashion, with emphasis placed on the role of temperature and heat transfer related material properties on the stability of the system. We formulate a generalized theory for all open systems, but apply it to a battery intercalation system for specific applications.

Battery intercalation systems, considered open driven systems, are highly dependent on temperature effects because of reaction heat generation and sensitivity of material properties to temperature. As fast charging becomes preeminent in electric vehicles, temperature variation in batteries significantly increases. Thus, it becomes even more important to understand the effects of temperature on these systems, especially its effects on phase separation, which plays a large role in degradation in these systems [335, 336]. In addition, higher and lower temperature operation of battery systems also become more common, as electric vehicles expand to regions with colder winters and warmer summers, and as global warming starts to affect our entire ecosystem. Temperature effects play strong role in degradation and dendrite formation in a battery [337, 338, 339]. Since the temperature of a battery systems not only influences properties of the active material electrodes themselves [340, 341] but also the conductivity and diffusivity of the electrolyte, which often play critical roles in the lifetime of a battery [342, 47], porous electrode battery models often include correlations of temperature effects on the open circuit voltage and electrolyte properties, as well as energy balances on the general battery system, such as the porous electrode model softwares LIONSIMBA and dualfoil to remedy this [45, 343, 344, 345, 346]. It remains to be seen how temperature effects on phase stability carry over into battery operation, especially in a multiphase material [44], since these effects have not been included before.

The reaction rate model introduced also has a large effect on the current of the system. Since Butler-Volmer (BV) is a phenomenological reaction rate which is unphysical at high overpotentials because it does not account for electron transfer limitation [347], the artificial inflation of the current often causes the misunderstanding that

electrode reactions can contribute greatly to temperature gradients inside lithium-ion batteries [348]. Thus, many current battery models mistakenly attribute much heat generation to the electrode reactions, since electron transfer limitation is not accounted for in BV models. To account for this temperature dependent multiphase porous electrode model, a study of temperature stability and battery material properties on battery intercalation is necessary and will be performed in this paper.

Though temperature dependent models of catalysis and battery intercalation exist, to our knowledge, nonisothermal thermodynamic stability has not been studied before in a manner suitable for phase separation. A thermodynamically consistent theory on transport in nonisothermal open driven systems is derived in a rigorous fashion and applied to our problem of choice for intercalation in lithium-ion batteries. Though this problem has been worked on considering surface reactions in lithium-ion batteries [349], the general system of heterogeneous/homogeneous reactions has not been considered. Temperature dependent models for ion intercalation and for photocatalysis generally involve an energy balance as well as temperature dependent properties like electrolyte diffusivity, but no model that takes into account the effect of temperature on phase separation has ever been studied with thermodynamically consistent reaction rates, though more general models have been developed before [350, 351].

Our goal is to create a temperature dependent and thermodynamically consistent multiphase porous electrode model using the more physical quantum ion-electron transfer reaction rates, which requires understanding of how temperature stability affects open driven systems to understand phenomena in these temperature dependent models such as intercalation and photocatalysis, where stability of a system is extremely important for operation. To do this, first we build upon general nonisothermal nonequilibrium thermodynamics from transport laws including diffusion, reaction, and coupling interactions between the energy and mass balances and show these equations below, which can be applied to many other systems. Upon this, we try to perform a full analysis of the nonisothermal effects in battery intercalation materials, and analyze the effects of the contributions of each type of heat generation

on the system, incorporated into a porous electrode model software. We find that the effects of reaction heat generation are often over-accounted for because of the physically incorrect Butler-Volmer model at high overpotentials.

A.2 Theory

A.2.1 Balance Laws

We aspire to set up a thermodynamically consistent framework for transport theory in open system thermodynamics. We consider an open system of a battery particle with a certain reaction R happening at the particle surface, which depends on the system it is applied for. To understand the phase stability in our system, which may have contributions from mechanics and mass and energy transfer, we need to proceed with the balance laws in our system.

Mass Conservation

For a multicomponent system, we can use the mass averaged definitions of the material properties. The concentration of each component i can be defined as c_i, where $\sum c_i = 1$. The mass density in our system can be described as $\rho = \sum_i \rho_i c_i$ and the mass averaged velocity as $\mathbf{v} = (\sum_i \rho_i \mathbf{v}_i)/\rho$, which are the reference frame for velocity chosen in this problem. The mass averaged flux is $\mathbf{J} = (\sum_i \rho_i \mathbf{J}_i)/\rho$ averaged over all the particle species, where ρ is the average density, and all terms beyond first order nonlinear terms are dropped.

The overall mass balance is [352, 162, 353].

$$\frac{d}{dt}\int_V \sum_i \rho_i dV = -\int_A \sum_i \mathbf{n}\cdot\mathbf{J}_i dA. \tag{1}$$

Summing these two equations, the divergence theorem and Reynold's Transport Theorem can be applied to find that [352]

$$\int_V \dot{\rho} + \nabla\cdot(\rho\mathbf{v})\, dV = \int_V -\nabla\cdot\mathbf{J} dV, \tag{2}$$

where the sum of the divergence of the fluxes sums to zero when the system is closed for the bulk system. This term is extremely important in differentiating between open and closed systems in energy and momentum balances, as we will see later. The mass conservation equation is equivalent to the concentration conservation equation since we work with intercalation materials in this problem.

The mass boundary condition over the reactive area applies as the surface transport theorem to be [354]

$$\frac{d}{dt}\int_S \rho dS = \int_S \dot{\rho} + \nabla \cdot (\rho \mathbf{v})\, dS, \tag{3}$$

for any surface point with density ρ.

Momentum Conservation

We start with the general momentum balance of the system, applying the divergence theorem to the system.

$$\frac{d}{dt}\int_V \left(\sum_i \rho_i \mathbf{v}_i\right) dV = \int_A \mathbf{t}\cdot\mathbf{n} dA + \int_v \sum_i \rho_i \mathbf{b_i} dV, \tag{4}$$

with the traction $\mathbf{t}$ defined on the boundary A [352]. Since the momentum is a linear function of the density, we expect that the average value of the total momentum balances should hold, in terms of average momentum $\sum_i \rho_i \mathbf{v}_i = \rho \mathbf{v}$ and average body force $\mathbf{b}_0 = (\sum_i \rho_i \mathbf{b}_i)/\rho$. This equation is valid for any system, open or closed.

Differences between open and closed systems appear when the time dependent term is separated, since mass is no longer conserved in an open system. The mass balance can be applied to the momentum conservation equation through Reynold's

transport theorem as

$$\begin{aligned}\frac{d}{dt}\int_V \rho\mathbf{v}dV &= \int_V \frac{\partial(\rho\mathbf{v})}{\partial t} + \nabla\cdot(\rho\mathbf{v}\otimes\mathbf{v})\,dV \\ &= \int_V \rho\dot{\mathbf{v}} + \mathbf{v}\left(\dot{\rho} + \nabla\cdot(\rho\mathbf{v}) + \rho\nabla\cdot\mathbf{v}\right)dV \\ &= \int_V \rho\dot{\mathbf{v}} + \mathbf{v}\left(-\nabla\cdot\mathbf{J} + \rho\nabla\cdot\mathbf{v}\right)dV\end{aligned} \tag{5}$$

after applying the mass balance derived for the open system in the first step. Thus, for our open system, the mass fluxes in this system affect the momentum balance as well. Compared to that of a closed system, where the spatial movement of fluxes would have been nonexistent over the entire interval, the spatial divergence of the fluxes do not disappear in open systems. Thus, our system simplifies to

$$\rho\left(\dot{\mathbf{v}} + \mathbf{v}\nabla\cdot\mathbf{v}\right) - \mathbf{v}\nabla\cdot\mathbf{J} = \nabla\cdot\mathbf{T} + \rho\mathbf{b}_0 \tag{6}$$

using the localization theorem. For a closed system, the divergence of fluxes would disappear.

Energy Conservation

We notice that this generation of internal energy in an open system does not just include generation terms observed in a closed system—it accounts for the effect of the open system mass flux terms on the entropy of the system. This is not simply the chemical potential that is generated, but a combination of chemical potential and entropy. In addition, the amount of stress that is generated also needs to include the open system generation of stress, which is in the last term of the heat generation equation. The inclusion of the extra generation terms from an open system provides a framework to study the energy balance of the system for the time dependent terms. The energy balance, where the specific energy is defined per mole as $e_i = u_i + \frac{1}{2}|\mathbf{v}_i|^2$ is defined as

$$\frac{d}{dt}\int_V \sum_i \rho_i e_i dV = -\int_A \sum_i \mathbf{n}\cdot\mathbf{J}_{e,i}dA + W_0, \tag{7}$$

where W_0 is the conventional external power [352] defined as

$$W_0 = \int_S \sum_i \rho_i \mathbf{t}_i \cdot \mathbf{v}_i dA + \int_V \rho_i \mathbf{b}_i \cdot \mathbf{v}_i dV \tag{8}$$

applying the divergence theorem and $\mathbf{J}_{e,i}$ is the heat flux for species i, and the symmetry and definition of the stress tensor [355, 356]. The conventional external power comes from the effect of the surface traction term and the body forces. Here, we see that the energy flow is from all of the mass and heat fluxes in the system. Because there are external fields in our system, the flux is a combination of the Fourier heat flux as well as internal energy transported by the external fields applied. Thus, the flux can be defined using linear irreversible thermodynamics [161] as

$$\mathbf{J}_e = \mathbf{Q} + \sum_i \left(u_k + F z_i \phi\right) \mathbf{J}_i \tag{9}$$

from the electric field, where F is the Faraday constant, z_k is the ion number, and ϕ is the electric potential. Again, defining the average energy as $\rho e = \sum_i \rho_i e_i$ and average flux as $\rho \mathbf{J}_e = \sum_i \rho_i \mathbf{J}_{e,i}$, we can apply these averages and the divergence theorem as

$$\int_V \frac{\partial}{\partial t}\left(\rho e\right) + \nabla \cdot (\rho e \mathbf{v}) dV = \int_V -\nabla \cdot \mathbf{J}_e dV + W_0. \tag{10}$$

Applying the same principle as in the momentum balance, by a first order expansion of the first derivative, we see that

$$\begin{aligned} &\int_V \frac{\partial}{\partial t}\left(\rho e\right) + \nabla \cdot (\rho e \mathbf{v}) dV \\ =& \int_V \rho(\dot{e})_\rho + e\left(\dot{\rho} + \nabla \cdot (\rho \mathbf{v})\right) + \rho e \nabla \cdot \mathbf{v} dV \\ =& \int_V \rho(\dot{e})_\rho + e\left(-\nabla \cdot \mathbf{J}\right) + \rho e \nabla \cdot \mathbf{v} dV. \end{aligned} \tag{11}$$

We transform the conventional external power by the divergence theorem as

$$W_0 = \int_V \sum_i \rho_i \left(\mathbf{v}_i \cdot \left(\nabla \cdot \tilde{\mathbf{T}} + \mathbf{b}_i\right) + \nabla \mathbf{v}_i : \mathbf{T}\right) dV. \tag{12}$$

We notice that even the conventional external power changes for an open system—the mass flux terms—affect the amount of kinetic energy in the system. Applying the conservation equation for momentum, we obtain that

$$W_0 = \int_V \frac{1}{2}\rho(|\dot{\mathbf{v}}|^2) + |\mathbf{v}|^2 \left(\rho\nabla\cdot\mathbf{v} - \nabla\cdot\mathbf{j}\right) + \mathbf{T}\colon\mathbf{D}\; dV, \tag{13}$$

where the stretching $\mathbf{D}$ is the conjugate variable to the Cauchy stress $\mathbf{T}$. The power expended by the Cauchy stress, the internal power, is elastic. Neglecting the second order terms and keeping only the first order ones, the total energy balance can be written using the localization theorem as

$$\rho\left((\dot{e})_\rho + \left(e - |\mathbf{v}|^2\right)\nabla\cdot\mathbf{v}\right) - \left(e - |\mathbf{v}|^2\right)\nabla\cdot\mathbf{j} = -\nabla\cdot\mathbf{J}_e + \mathbf{T}:\mathbf{D} + \frac{1}{2}\rho(|\dot{\mathbf{v}}|^2) \tag{14}$$

where the density is held constant in the first term.

Finally, we need to supply the boundary conditions of the system for mass, energy, and momentum. Using the divergence theorem terms that appear at the interface, we let the subscript s depict surface in all the following interface balances, which apply as boundary conditions for our problems. This applies for the energy balance as

$$\rho_s\dot{u}_s = \nabla\cdot\mathbf{T}\cdot\mathbf{v}_s + \rho_s\mathbf{b}_{s,0}\cdot\mathbf{v}_s + [\rho(u-u_s)(\mathbf{v}-\mathbf{v}_s) - \mathbf{v}\cdot\mathbf{T} + \mathbf{q}]\cdot\mathbf{n}. \tag{15}$$

The momentum balance at the interface is

$$\rho_s\left(\dot{\mathbf{v}}_s + \mathbf{v}_s\nabla\cdot\mathbf{v}_s\right) - \mathbf{v}_s\nabla\cdot\mathbf{J}_s + [\rho(\mathbf{v}-\mathbf{v}_s)(\mathbf{v}-\mathbf{v}_s) - \mathbf{t}]\cdot\mathbf{n} = \nabla\cdot\mathbf{T}_s + \rho_s\mathbf{b}_{s,0}, \tag{16}$$

analogously derived from the balance at the bulk. For nondeforming surfaces, the energy and mass boundary conditions are simply applied as constant flux conditions $-\mathbf{n}\cdot\mathbf{j} = R$.

Temperature Balance

The temperature balance of the system needs to be defined from a combination of the energy balance as well as local equilibrium laws. The energy balance for an open system was derived in a previous section. We can apply the definition of the energy $\rho e = \sum_i \rho_i u_i + \frac{1}{2}\sum_i \rho_i |\mathbf{v}_i|^2$ and $\rho u = \sum_i \rho_i u_i$, to the energy balance of the system to obtain

$$\rho\left((\dot{u})_\rho + u\nabla\cdot\mathbf{v}\right) - u\nabla\cdot\mathbf{J} = -\nabla\cdot\mathbf{J}_u + \mathbf{T}:\mathbf{D}. \tag{17}$$

We can apply the identities defined above relating the internal energy to chemical potential and heat and mass transfer and write $\sum_i \rho_i c_{v,i} = \rho c_v$ and $\sum_i \rho_i h_i = \rho_{LiM,ref} c h_{LiM} + \rho_{M,ref}(1-c)h_M$ for the heat capacity and enthalpy per mass. However, to obtain the relation of the temperature change to the heat generation as well as mass transfer and momentum transfer in the system, we apply our previous derivation of internal energy change in the system. The energy change is found to be $\rho\dot{u} = \rho c_v \dot{T} + \rho h\dot{c} + \left(\mathbf{T}^e + \rho T\left(-\frac{\alpha}{\kappa_T}\mathbf{I} + \frac{\partial s}{\partial \boldsymbol{\varepsilon}_{kj}}\big|_{k\neq j}\right)\right):\mathbf{D}$ as derived in the appendix section.

Substituting this relation into the internal energy balance and removing the second order correcting terms, we obtain

$$\rho c_v\dot{T} + \rho h\dot{c} + \rho u\nabla\cdot\mathbf{v} = -\nabla\cdot\mathbf{Q} - \mathbf{J}\cdot\nabla u + \rho T\left(\mathbf{T}^p + \frac{\alpha}{\kappa_T}\mathbf{I} - \frac{\partial s}{\partial \boldsymbol{\varepsilon}_{kj}}\bigg|_{k\neq j}\right):\mathbf{D} + \mathbf{I}_e\cdot\mathbf{E}. \tag{18}$$

We do not have an enthalpy generation term in the first term since the internal energy is kept constant, which constitutes our energy balance of the system. The ohmic heat generation term comes from the fact that $\mathbf{E} = -\nabla\phi$ is the electric field and $\mathbf{I}_e = \sum_k F z_k \mathbf{J}_k$ is the current. Because our system is elastic, only the dissipative (plastic) stresses on the momentum balance affect the temperature balance of the system and not the elastic Cauchy strain. We see that our system is an open system, so the chemical potential and entropy changes from the mass balance also affect the energy balance of the system. For a closed system, the effect of mass change would disappear on the system.

Dimension Reduction

Here, we will perform dimensional reduction on our mass conservation, energy conservation, and momentum conservation equations, integrated over the normal direction to the reactive area, to achieve the Allen-Cahn reaction models derived in previous work [69, 164]. This section provides a derivation from the full transport models to the simplified electrochemical models often used in literature.

Here, we first start by combining the bulk and surface mass balances. The infinitesimal surface within the boundary S where the reaction happens can be called W. We call the combined total volume $U = V \cup W$, which has the boundary S. We define L as the length normal to the boundary area term S, which is the direction we will be dimensionally reducing our system in. The generalized transport theorem requires that for our bulk with a dividing surface that [354]

$$\frac{d}{dt}\int_V \rho dV = \int_V \dot{\rho} dV + \int_S \rho \mathbf{v} \cdot \mathbf{n} dS - \int_W [\rho \mathbf{v}_s \cdot \mathbf{n}] dW. \tag{19}$$

from summing over transport in all phases, where $[\rho \mathbf{n}] = (\rho_{in} - \rho_{out}) \cdot \mathbf{n}$ is the change of ρ at the boundary when there is flux both entering and leaving the boundary. By the divergence theorem, we can separate the contributions of convection into the bulk term as well as the surface term

$$\int_S \rho \mathbf{v} \cdot \mathbf{n} dS = \int_V \nabla \cdot (\rho \mathbf{v}) dV + \int_W [\rho \mathbf{v} \cdot \mathbf{n}] \, dW. \tag{20}$$

We see that our transport theory with the bulk next to a dividing surface becomes

$$\frac{d}{dt}\int_V \rho dV = \int_V \dot{\rho} + \nabla \cdot (\rho \mathbf{v}) dV + \int_W [\rho(\mathbf{v} - \mathbf{v}_s) \cdot \mathbf{n}] dW. \tag{21}$$

Thus, if we sum with the transport theorem of mass conservation at the surface, the total mass balance is

$$\frac{d}{dt}\left(\int_V \rho dV + \int_W \rho dW\right) = \int_S \left(\dot{\rho} + \nabla \cdot (\rho \mathbf{v})\right) dV + \int_W \left(\dot{\rho} + \nabla \cdot (\rho \mathbf{v}) + [\rho(\mathbf{v} - \mathbf{v}_s) \cdot \mathbf{n}]\right) dW. \tag{22}$$

To obtain the boundary condition, if we apply the divergence theorem to the left hand side of the equation, we see that

$$\frac{d}{dt}\left(\int_{U=V\cup W}\rho dV\right)=\int_{S}-\mathbf{n}\cdot\mathbf{J}dS, \tag{23}$$

or that the volumetric integral can be converted into the flux through the two-dimensional boundary. Generally, in systems where the reaction happens at the boundary, this term is generated from the reaction. The general transport equation becomes

$$\int_{S}-\mathbf{n}\cdot\left(\mathbf{J}+\left[\rho(\mathbf{v}-\mathbf{v}_{s})\right]\right)dS=\int_{U}\left(\dot{\rho}+\nabla\cdot(\rho\mathbf{v})\right)dU, \tag{24}$$

where U is the total volume containing both the bulk and the boundary. Since the definition of the reaction rate is the flux into the boundary at a certain time, defined as

$$\pm R=\mathbf{n}\cdot\left(\mathbf{J}+\left[\rho(\mathbf{v}-\mathbf{v}_{s})\right]\right) \tag{25}$$

where $+$ is for reactants and - is for products [69] is applied as the boundary condition in this system. Thus, we see that

$$\int_{S}-RdS=\int_{U}\dot{\rho}+\nabla\cdot(\rho\mathbf{v})\,dU \tag{26}$$

is the general solution.

We aim to integrate over the normal direction L to the reaction area to dimensionally reduce the system, and then apply the localization theorem. Thus, we see that

$$\dot{\rho}+\nabla\cdot(\rho\mathbf{v})=-\frac{R}{L}, \tag{27}$$

recovers the Allen-Cahn equation commonly used for intercalation materials such as lithium iron phosphate [69, 164].

A.2.2 Open System Thermodynamics

The thermodynamics in our particle can be defined now that the balance laws of the system have been well-defined. We defined some necessary properties for a 3D particle. Here, $\mathbf{K}$ is a tensor that represents energy penalties in different directions from the phase boundaries, $\mathbb{C}$ as the elastic tensor at constant temperature, and $\mathbf{M}$ is the stress-temperature modulus at constant strain [352]. Later we will attempt to formulate the Helmholtz free energy of a particle from the homogeneous, interfacial and mechanical free energies, which resembles the one formulated for an isothermal system, where $c = c_{\mathrm{LiM}}/c_{max}$ in the entire system [315, 69].

We first define the mechanics equations laid out in this problem. Based on the linear theory of elasticity [352], it can be assumed that the strain tensor is defined as $\boldsymbol{\varepsilon} = \frac{1}{2}\left(\nabla\mathbf{u} + (\nabla\mathbf{u})^T\right)$, where $\mathbf{u}$ is the displacement field based on material coordinates $\mathbf{u} = \mathbf{x} - \mathbf{X}$, where $\mathbf{X}$ is the undeformed configuration and $\mathbf{x}$ is the deformed configuration [352]. The elastic strain $\boldsymbol{\varepsilon^e} = \boldsymbol{\varepsilon} - \boldsymbol{\varepsilon^c}$ is one of the field variables in the system, where the chemical or stress free strain is $\boldsymbol{\varepsilon^c} = \boldsymbol{\varepsilon^0} c$ by Vergard's law [357]. The deformation gradient $\mathbf{F}$ is defined as $\mathbf{F} = \nabla\mathbf{x} \approx \mathbf{I} + \nabla\mathbf{u}$ in linear elasticity theory [352]. Since the volume change of the system dv is based on the deformation of the system for the fiber $dX_{ij} = F_{ij}dx_{ij}$, we see that the real volume formed by the deformed tetrahedron is known to be $dv = Jdv_0$ [358, 352], where $J = \det(\mathbf{F})$.

The free energy of an intercalation material should be defined not by the volume, but by the amount of lithiation host sites that exist in the material, regardless of density changes that may occur from mechanical volume changes. It becomes apparent from volume changes in our system that the number of intercalation sites is the most important criteria which determines the amount of free energy, which can change with elastic volume expansion. Thus, we define most quantities in the system per mole of intercalation site instead of per volume. Concentration related units are per maximum site density of the intercalation material $\rho_s c_{0,max}$. Since we realized that the total amount of the M site material does not change in the system, but only switches between the LiM and M states, before and after volume deformation,

the total amount changes are equivalent [352]. The reference amount of material is thus found to be $c_{max} = Jc_{0,max}$. Thus, the most accurate description of specific free energy for this system in units of energy per moles of intercalation species is $\tilde{f}_h = f_h/c_{0,max}$, and after volume deformation $\tilde{f}_h/J$, where $\tilde{f}_h$ is the molar form and f_h is the volumetric form of specific free energy. By similar arguments, the gradient energy term $\mathbf{K}$ and the elasticity tensor $\mathbb{C}$ both need to be reformulated to be per molar of maximum intercalation sites to be $\tilde{\mathbf{K}} = \mathbf{K}/J$ and $\tilde{\mathbb{C}} = \mathbb{C}/J$.

Thus, the specific free energy of intercalation materials can be defined by the density of the M species. The free energy for a simple thermoelastic material is

$$F = \int_V J\left(\tilde{f}_h + \frac{1}{2}\nabla c \cdot \tilde{\mathbf{K}}\nabla c + \frac{1}{2}\boldsymbol{\varepsilon^e} : \tilde{\mathbb{C}} : \boldsymbol{\varepsilon^e} + (T - T_0)\tilde{\mathbf{M}} : \boldsymbol{\varepsilon^e}\right) dV_0, \tag{28}$$

where the last term is from the mechanical strain of the system, with $\boldsymbol{\varepsilon}$ as is the strain, $\boldsymbol{\varepsilon_0}$ as the lattice expansion from chemical effects with Vergard's law so that $\boldsymbol{\varepsilon^c} = \boldsymbol{\varepsilon_0} c$ [359, 360, 352, 330, 357]. In this equation, the strain terms can also be combined into the Piola stress $\mathbf{T_{RR}} = 2\frac{\delta F}{\delta \boldsymbol{\varepsilon^e}}$, where the stress-temperature modulus and the elasticity tensor can both be seen as chain rule components of the second Piola stress, $\mathbb{C} = 2\frac{\partial \mathbf{T_{RR}}}{\partial \boldsymbol{\varepsilon^e}}$ and $\mathbf{M} = \frac{\partial \mathbf{T_{RR}}}{\partial T}$. By the free energy simplifications above, the free energy can be written more simply as

$$F = \int_V \left(f_h + \frac{1}{2}\nabla c \cdot \mathbf{K}\nabla c + \frac{1}{2}\boldsymbol{\varepsilon^e} : \mathbb{C} : \boldsymbol{\varepsilon^e} + (T - T_0)\mathbf{M} : \boldsymbol{\varepsilon^e}\right) dV_0, \tag{29}$$

Often, for small deformations, the Jacobian of the deformation gradient can be neglected since its value is close to unity. The formulation of the Helmholtz free energy initiates our thermodynamically consistent theory of open system thermodynamics, but does not represent either the rate controlled or chemical potential controlled systems that we are interested in.

We can fully define our open system through the combination of the interior of the particle, the boundary of our particle, and the environment (electrolyte) surrounding the particle. Each of the mass, energy, and momentum balances in these cases will be carefully defined, with different fluxes depending on whether voltage or current

control is needed. The boundary conditions of this system must also be carefully formulated to account for deformation of the surface [354]. We choose the dividing surface to be the interface between the solid and electrolyte phase in our system. When there is a dividing surface in our system, the application of the divergence theorem becomes slightly different from what is normally expected. In the following equation, V is the entire control volume, made up of the bulk of the particles V_b, the interface S, and the bulk of the electrolyte environment V_e.

$$\int_V P\mathbf{v}\cdot\mathbf{n}dV = \int_b \nabla\cdot(P\mathbf{v})dV_b + \int_S [P\mathbf{v}\cdot\mathbf{n}]dA + \int_e \nabla\cdot(P\mathbf{v})\,dV_e, \tag{30}$$

where $[P\mathbf{v}\cdot\mathbf{n}] = (P^i - P^j)\,\mathbf{n}^{i,j}$ is difference between the different phases.

Phase field equations have long been used to model phase transition mechanics in continuum systems, with applications from Cahn and Hilliard in materials science and Ginzburg and Landau in superconductivity [357, 361, 362]. The appearance of external fields, such as electric fields, in these phase field equations has also been coupled with these phase field equations for critical phenomena [363]. However, these derivations from free energy models implicitly indicate that entropy is the extensive variable from the choice of the free energy functional, rather than temperature, which is not an issue for systems with small variations in temperature. The appropriate thermodynamic potential in a nonisothermal system would be entropy, instead of free energy [364]. The nonisothermal thermodynamics of an open driven system in nonequilbrium needs to be formulated based on an entropy functional, based on the fact that naive treatment of nonisothermal models can violate the second law of entropy generation [365, 366]. Different systems require different equilibrium potentials.

Based on the isothermal nonequilibrium thermodynamics in Ref. [69] for reactive systems and general work from Cahn and Hilliard, we formulate the nonisothermal functionals as below in an open system with a simple single particle model using mass and energy balances [365, 361, 357]. Because we have an open system, based on the different types of control that are applied to the system, different equilibrium thermodynamic ensembles must be chosen [367]. The system is no longer isothermal,

which also requires a change in equilibrium potentials from nonisothermal systems. For isothermal rate control, since the number of particles is the extensive variable, the Helmholtz free energy $F = U - TS$ should be chosen to define the equilibrium of the system. For isothermal chemical potential control, since the chemical potential is the extensive variable, the potential should be Legendre transformed into the grand potential $\Omega = F - \mu N$ to define equilibrium and driving forces in the system. Similarly, for a nonisothermal rate controlled system, the Helmholtz free energy should be Legendre transformed to the entropy potential S to add temperature variations as the extensive variable. For a nonisothermal chemical potential controlled system, a Massieu free energy functional can be applied for a system with temperature variations such that $\Psi = \frac{U}{T} - \frac{\Omega}{T}$. The above equilibrium potentials and their corresponding flux equations and conservation equations for each system will be discussed. We will use the following system to show that in an Allen-Cahn/Cahn-Hilliard reaction model, although the extensive variables are different, the same mass conservation equation is reached using both of these systems. The only difference between these two models is the diffusive driving force, which requires the chemical potential to be monotonic to be able to derive a consistent thermodynamic model [368, 369].

Rate Control

Different potentials need to be applied for different types of control on the system. For a system under rate control, since in a nonisothermal system, temperature is also an extensive variable, we transform the potential to an entropy potential S, which indicates that

$$S = \int_V \left(s_h - \frac{1}{2}\frac{1}{T}\nabla c \cdot \mathbf{K}\nabla c - \frac{1}{2}\frac{1}{T}\boldsymbol{\sigma} \colon \boldsymbol{\varepsilon}^{\boldsymbol{e}} - \frac{1}{T}\left(T - T_0\right)\mathbf{M} \colon \boldsymbol{\varepsilon}^{\boldsymbol{e}} \right) dV_0 \tag{31}$$

if $\mathbf{K}$ is constant with temperature, with $s_h = \frac{u}{T} - \frac{f_h}{T}$, assuming that the equations including the order parameter are still valid when the temperature is not a constant, and $\boldsymbol{\sigma} = \frac{\delta F}{\delta \boldsymbol{\varepsilon}} = \mathbb{C} \colon \boldsymbol{\varepsilon}^{\boldsymbol{e}}$ is the elastic stress field. Thus, S is the equilibrium potential of a nonisothermal reaction control system.

The chemical potential of the active material is defined as

$$\mu = \frac{\delta F}{\delta c} = \frac{\partial f_h}{\partial c} - \nabla \cdot \mathbf{K} \nabla c - \boldsymbol{\sigma} : \boldsymbol{\epsilon_0} = \mu^{\Theta} + k_B T \ln a. \tag{32}$$

Since $\boldsymbol{\varepsilon} = \frac{1}{2}\left(\nabla \mathbf{u} + (\nabla \mathbf{u})^T\right)$ and $\boldsymbol{\sigma}$ is a symmetric matrix, we know that $\nabla \mathbf{u} : \boldsymbol{\sigma} = \boldsymbol{\varepsilon} : \boldsymbol{\sigma}$. In addition to these arguments, we obtain by their definitions the functional derivatives

$$\begin{aligned} \frac{\delta S}{\delta u} &= \frac{1}{T} \\ \frac{\delta S}{\delta c} &= \left(\frac{\partial s_h}{\partial c} + \frac{1}{T}\nabla \cdot \mathbf{K} \nabla c + \frac{1}{T}\boldsymbol{\sigma} : \boldsymbol{\varepsilon_0}\right) = -\frac{\mu}{T} \\ \frac{\delta S}{\delta \boldsymbol{\varepsilon}} &= -\frac{\boldsymbol{\sigma}}{T} - \frac{\mathbf{M}}{T}(T - T_0) = -\frac{\mathbf{T_{RR}}}{T}, \end{aligned} \tag{33}$$

since within a small error, for linear elasticity, the Cauchy ($\mathbf{T}$) and Piola stresses are the same and will be used interchangeably in the future analysis. In the stress field, the first term represents the stress from the change in volume of the system from elastic stress, while the second term is a stress tensor. The remaining terms come from the nonlocal effects of concentration on the microstructure, assuming a first order response theory [370, 371, 372]. These are the forces found in linear irreversible thermodynamics if we assume that the elasticity tensor is nonisothermal, with the last set of equations written in tensor form.

By the volume change and the fact that this system is open, we realize that the conservation equations for this system are nontrivial and should be written in a thermodynamically consistent manner to ensure that the correct quantities. First of all, the amount of the intercalation site material changes only with volume deformation, but the total amount over the entire volume does not change with reaction or stress/strain. We define the volume of the intercalated system to be V, which is defined as the JV_0 from the elastic deformation of the system. We call this density of intercalation site material per volume by n, and see that the total intercalation site amount is constant no matter the amount of deformation. With the different concentrations of lithium intercalated in the sites in the system, the density, energy, and

momentum are are affected by these concentration changes. Since the system is an intercalation system, only two types of material are considered—the empty intercalation site, M, which contains an empty lithium site, and LiM, the intercalated site. We can simplify a set of two mass balances into one concentration balance using the fact that $c_{LiM} + c_M = 1$, letting $c_{LiM} = c$ for future notation. As mentioned earlier, applying the constraint that the two concentrations sum to one, the two concentrations can simplify to one equation using the barycentric velocity defined by concentration $\mathbf{v} = \mathbf{v}_{LiM}c + \mathbf{v}_M(1-c)$.

Since reaction happens at the boundary, a simple reaction boundary condition is $-\mathbf{n} \cdot \mathbf{J} = R$ can describe the system, where by the definition of the reaction $\mathrm{Li}^+ + \mathrm{M} + \mathrm{e}^- \longrightarrow \mathrm{LiM}$, we see that $R = R_{LiM} = -R_M$ is the molar reaction rate. For consistent notation, $\mathbf{J}_{i,m}$ will refer to mass flux of component i, while $\mathbf{j}_i = \frac{\mathbf{J}_{i,m}}{MW_i}$ will refer to molar flux of component i, where $\mathbf{j}_{LiM} = \mathbf{j}$. Since $\frac{\delta F}{\delta S} = T$ to convert the flux definitions to that of an isothermal system [369], for nonisothermal conditions, the molar flux is

$$\mathbf{J}_b = \sum_{k \in \{c,u\}} M_{b,k} T \nabla \left(\frac{\delta S}{\delta k} \right) \tag{34}$$

where $M_{i,j}$ the nonisothermal Onsager flux coefficients, which will be derived below [162]. The molar flux terms are equivalent to the ones defined above in nonequilibrium thermodynamics per intercalation site, meaning that the mass fluxes can be defined as

$$\mathbf{j}_b = \sum_{k \in \{c,u\}} M_{b,k} n \mathrm{MW}_{Li} T \nabla \left(\frac{\delta S}{\delta k} \right). \tag{35}$$

Chemical Potential Control

For a chemical potential controlled system, we need to switch the equilibrium potential to the grand potential. The arguments of Plapp [369], by the definition of the grand potential, are usually applied when the chemical potential is monotonous or when the free energy is convex. Since the definitions of the susceptibilities are used, this method cannot be fully mapped to a phase separating system because the susceptibilities diverge at critical points. However, the same principles can be applied to understand

the dynamics of the system. The grand potential which will be used for a system under voltage control can be formulated as

$$\Omega = \int_V \left(\omega_h + \frac{1}{2}\nabla c \cdot \mathbf{K}\nabla c + \frac{1}{2}\boldsymbol{\sigma} : \boldsymbol{\varepsilon}^{\boldsymbol{e}} + (T - T_0)\mathbf{M} : \boldsymbol{\varepsilon}^{\boldsymbol{e}} \right) dV, \tag{36}$$

where $\omega_h = f_h - \mu c$, the commonly used grand potential such that $\Omega = F - \mu N$. The susceptibilities, $\chi_c = \frac{\partial c}{\partial \mu}$ can be used to derive the conservation equations in the system which is the form derived by Plapp. Plapp's derivation does not account for variation of temperature in energy and mass conservation. We apply the same methods as above to obtain a Massieu function [373] [367]

$$\Psi = S + \frac{\mu}{T}N \rightarrow \Psi = \frac{U}{T} - \frac{\Omega}{T}, \tag{37}$$

where the concentration is replaced by $-\frac{\mu}{T}$ as the independent variable. Similarly to the Legendre transform to entropy performed in the previous section based on Penrose and Fife [365, 366], this acknowledges the temperature variations of the system. Here, since $\psi_h = \frac{u}{T} - \frac{\omega_h}{T}$, we obtain the Massieu free entropy as

$$\Psi = \int_V \left(\psi_h - \frac{1}{2}\frac{1}{T}\nabla c \cdot \mathbf{K}\nabla c - \frac{1}{2}\frac{1}{T}\boldsymbol{\sigma} : \boldsymbol{\varepsilon}^{\boldsymbol{e}} - \frac{1}{T}\left(T - T_0\right)\mathbf{M} : \boldsymbol{\varepsilon}^{\boldsymbol{e}} \right) dV. \tag{38}$$

For the Massieu free entropy, the elasticity tensor and the stress-temperature modulus are identical to the one from entropy, so we will continue using the notation in the previous section to define those parts. The functional derivatives are

$$\begin{aligned} &\frac{\delta\Psi}{\delta u} = \frac{1}{T}\ ; \quad \frac{\delta\Psi}{\delta\left(-\frac{\mu}{T}\right)} = c\ ; \\ &\frac{\delta\Psi}{\delta\boldsymbol{\varepsilon}} = -\frac{\boldsymbol{\sigma}}{T} - \frac{\mathbf{M}}{T}(T - T_0) = -\frac{\mathbf{T_{RR}}}{T}, \end{aligned} \tag{39}$$

similarly to the approach taken to derive Eq. 33. Here, the flux terms need to be defined from deviation from Massieu free entropy, which can be defined as

$$\tilde{\mathbf{j}}_{\mathbf{b}} = \sum_{k \in \{-\frac{\mu}{T}, u\}} \tilde{M}_{b,k} T \nabla \left(\frac{\delta\Psi}{\delta k} \right) \tag{40}$$

for mass and energy and momentum separately. Though not explicitly written under the theory of thermoelasticity, we see that our equations are consistent with thermoelasticity [352].

A.2.3 Linear Stability Analysis

A general linear stability analysis can be applied to the system to understand the effect of perturbations on the stable states of the system. As an example, we perform a linear stability analysis on the rate control system. Assuming that $\mathbf{u} = (c, T, \mathbf{v})^{\mathrm{T}}$ and $\bar{\mathbf{u}} = \left(\bar{c}, \bar{T}, \bar{\mathbf{v}}\right)^{\mathrm{T}}$ is the steady state solution, we perform concentration and temperature perturbations with $\mathbf{u}(\mathbf{x}, \tau) = \bar{\mathbf{u}} + \boldsymbol{\delta}$, where $\boldsymbol{\delta} = (\delta c, \delta T, \delta \mathbf{v})^{T} = \boldsymbol{\epsilon} e^{\sigma t + i\mathbf{kx}}$ where σ is the growth rate, $\mathbf{k}$ is the perturbation wave vector, and $\boldsymbol{\delta}$ is the perturbation amplitude vector. The growth rate and the perturbation wave vector are the same for both terms, and only the perturbation amplitudes vary. However, we realize that the time constant for temperature changes is much smaller than that of concentration (which will be proved later in the discussion), indicating that we can assume that the energy balance is nearly at equilibrium. Considering only a first order perturbation in ε, we get a set of linear equations where the growth factor σ can be found by solving the secular equation $\det|\mathbf{J} - \sigma \mathbf{e}_1| = 0$ for $\mathbf{J}$ is the first order perturbation terms for (c, T) from the spatial side of the partial differential equation. For the rate controlled systems

$$\begin{aligned} \dot{\rho} + \nabla \cdot (\rho \mathbf{v}) &= -\nabla \cdot \mathbf{J} + \rho R \\ \rho c_v \dot{T} + \rho h \dot{c} + \rho u \nabla \cdot \mathbf{v} &= -\nabla \cdot \mathbf{Q} - \mathbf{J} \cdot \nabla u + T \frac{\alpha}{\kappa_T} \mathbf{I} \colon \mathbf{D} + \mathbf{I}_e \cdot \mathbf{E} \\ \rho \dot{\mathbf{v}} + \rho \mathbf{v} \nabla \cdot \mathbf{v} &= \mathbf{v} \nabla \cdot \mathbf{J} + \nabla \cdot \hat{\mathbf{T}} + \rho \mathbf{b}_0. \end{aligned} \tag{41}$$

All the Onsager coefficients $L_{ij}(c, T)$ are functions of concentration and temperature, and the equilibrium solutions of the problem are all indicated with bars. If we convert the balance equations into a concentration dependent format based by total number

of intercalation sites by dividing all equations by $\rho c_{0,max}$, we see that

$$\begin{aligned} \dot{c} + \nabla \cdot (c\mathbf{v}) &= -\nabla \cdot \mathbf{j} + R, \\ c_v \dot{T} + h\dot{c} + u\nabla \cdot \mathbf{v} &= -\nabla \cdot \mathbf{q} - \mathbf{j} \cdot \nabla u + T\frac{\alpha}{\kappa_T}\mathbf{I} \colon \mathbf{d} + \mathbf{i}_e \cdot \mathbf{E} \\ \dot{\mathbf{v}} + \mathbf{v}\nabla \cdot \mathbf{v} &= \mathbf{v}\nabla \cdot \mathbf{j} + \nabla \cdot \mathbf{T} + \mathbf{b}_0. \end{aligned} \tag{42}$$

We assume that the heat capacity c_v, the reaction rate R, the enthalpy h, and the internal energy u are defined per unit of intercalation material. In addition, $\mathbf{i}_e = \sum_k F z_k \mathbf{j}_k / \rho$ is the current per density per unit intercalation material, and $\mathbf{d} = \mathbf{D}/\rho$ is the stretching per unit intercalation material. We let $\frac{dR}{dc} = \frac{\partial R}{\partial c} + \frac{\partial R}{\partial \mu}\left(\frac{\partial \mu_h}{\partial c} + \kappa|\mathbf{k}|^2\right)$ and $\frac{dR}{dT} = \frac{\partial R}{\partial T} + \frac{\partial R}{\partial \mu}\frac{\partial \mu_h}{\partial T}$ in the following calculations, terms representing temperature and concentration dependence respectively without the gradient terms for simplicity in notation.

Performing a linear stability analysis on this system, we obtain that, keeping only the positive values, and recalling that the perturbation to the internal energy can be defined as $\delta u = c_v \delta T + h\delta c + \left(\mathbf{T} - T\frac{\alpha}{\kappa_T}\mathbf{I}\right) : \delta\mathbf{v}$, the real parts of the linear stability analysis are defined as

$$\begin{bmatrix} \sigma + \nabla \cdot \bar{\mathbf{v}} & 0 & \nabla \bar{c} \\ \bar{h}\sigma + c_v \nabla \cdot \bar{\mathbf{v}} & c_p \sigma + \bar{h}\nabla \cdot \bar{\mathbf{v}} & \left(\mathbf{T} - \bar{T}\frac{\alpha}{\kappa_T}\mathbf{I}\right)\nabla \cdot \bar{\mathbf{v}} \\ 0 & 0 & \sigma + \nabla \bar{\mathbf{v}} \end{bmatrix} \boldsymbol{\delta} = \begin{bmatrix} \bar{D}|\mathbf{k}|^2 \frac{\partial \mu}{\partial c} + \frac{dR}{dc} & \bar{D}|\mathbf{k}|^2 \frac{\partial \mu}{\partial T} + \frac{DR}{DT} & 0 \\ 0 & \bar{k}|\mathbf{k}|^2 & -\sigma \bar{T}\frac{\alpha}{\kappa_T}\mathbf{I} \colon \\ -\bar{\mathbf{v}}\bar{D}|\mathbf{k}|^2 \frac{\partial \mu}{\partial c} + b_0 & -\bar{\mathbf{v}}\bar{D}|\mathbf{k}|^2 \frac{\partial \mu}{\partial T} & 0 \end{bmatrix} \boldsymbol{\delta} \tag{43}$$

where the reaction rate is per volume instead of per mass. We assume that the heat capacity c_v and the internal energy u are defined per unit of intercalation material.

A.3 Applications

A.3.1 Ion Intercalation System

Reactions in systems can generally be separated into two types, heterogeneous reactions and homogeneous reactions [69]. For the application of an ion intercalation system, this is no different. We look at ion intercalation in LFP as an example to study our model. Accordingly, these transport equations over a certain volume have been split into two models—the first, the Cahn-Hilliard model, where the reaction only happens at the surface and diffusion within the particle drives the internal differences, such that a reactive boundary condition is applied. In the second, the Allen-Cahn model, reactions are assumed to happen homogeneously through the system, which can be modeled by averaging over the entire particle volume. Physical intercalation materials require by the Cahn-Hilliard model because reactions can only occur at the surface, where both electrolyte and intercalation solid exist, but lithium iron phosphate as an intercalation material has been successfully modeled using the Allen-Cahn reaction model [241] because it is reaction limited [3].

For the Allen-Cahn reaction model, based on the large diffusion values in the ion channels, diffusion in other directions was neglected for LFP. In general, it can be understood that depth-averaging in a system can be performed in a model where the phase boundary and diffusion can be neglected in other directions [315]. For simplicity, mechanical effects will be ignored in these models. Following Ref. [164], we implement a spherical particle with mass and energy balances to solve for the steady state solution. Temperature and concentration are assumed to be homogeneous in the particles, and the particle only exchanges mass with its environment.

We set up a particle in which an intercalation reaction happens on the solid/electrolyte boundary, with an electrolyte reservoir bath surrounding the particle. The reaction is described as $\mathrm{Li}^+ + \mathrm{e}^- + \mathrm{M} \longrightarrow \mathrm{LiM}$, where Li^+ is the intercalation species, e^- is the electron, M are the empty intercalation sites, and LiM is the intercalated species. We observe the conservation equations in the interior of the particle. These are identical to those in the environment bulk, since both of these systems are open systems next

to a boundary. Since our system is an open system in terms of mass, we do not expect conservation laws for closed systems to hold for such a system. For consistency in defining our averages, we use mass averages in our definitions. We have two species in our system, the fully lithiated LiM and the nonintercalated M component in the system, where M depends on the cathode material. The mass density in our system can be described as $\rho = c\rho_{LiM} + (1-c)\rho_M = \rho_M + c\rho_{Li}$ with $\rho_{LiM} = c\rho_{LiM,ref}$ and $\rho_M = (1-c)\rho_{M,ref}$, and the mass averaged velocity in this system is described as $\mathbf{v} = \rho_{LiM}\mathbf{v}_{LiM} + \rho_M\mathbf{v}_M$, which is the reference frame for velocity chosen in this problem.

To have a full understanding of the full 3D model of coupled fluxes in these systems, from the previous solution of the fluxes defined for the chemical potential control system, the Onsager fluxes are then found to be

$$\begin{aligned} \mathbf{j} &= \mathbf{L_{c,c}}\nabla\left(\frac{\delta S}{\delta c}\right) + \mathbf{L_{c,u}}\nabla\left(\frac{\delta S}{\delta u}\right) \\ \mathbf{q} &= \mathbf{L_{u,c}}\nabla\left(\frac{\delta S}{\delta c}\right) + \mathbf{L_{u,u}}\nabla\left(\frac{\delta S}{\delta u}\right) \end{aligned} \tag{44}$$

for this system, with $\mathbf{L_{c,c}} = \frac{\mathbf{D(c,T)}c}{k_B}$ and $\mathbf{L_{u,u}} = \boldsymbol{k}T^2$ with the diffusivity and conductivity tensors, with a Fourier approximation of heat conductivity, as quantified by Onsager [374, 375, 376, 377]. The Curie principle then requires $\mathbf{L_{c,u}} = \mathbf{L_{u,c}}$, which based on the Soret/Dufour coefficients, gives $\mathbf{L_{u,c}} = \mathbf{D_T}(\mathbf{c},\mathbf{T})c(1-c)T^2$ where $\mathbf{S_T} = \frac{\mathbf{D_T}}{\mathbf{D}}$ is the Soret coefficient [378, 161, 162]. Here, the $c(1-c)$ should be scaled by the total concentration, which we neglect in the notation. For each field, this simplifies to [162]

$$\begin{aligned} \mathbf{j} &= \frac{\mathbf{D}(\mathbf{c},\mathbf{T})c}{k_B}\nabla\left(-\frac{\mu}{T}\right) + \mathbf{D_T}(\mathbf{c},\mathbf{T})c(1-c)T^2\nabla\left(\frac{1}{T}\right) \\ \mathbf{q} &= \mathbf{D_T}(\mathbf{c},\mathbf{T})T^2\nabla\left(-\frac{\mu}{T}\right) + \boldsymbol{k}T^2\nabla\left(\frac{1}{T}\right). \end{aligned} \tag{45}$$

However, for most systems, we can neglect the co-diffusion terms. Next, we discuss the conservation equations for a heterogeneous reaction case and for a homogeneous reaction case.

Heterogeneous Reaction

For the case of a heterogeneous reaction, at the interface, the boundary conditions can be described by

$$-\mathbf{n} \cdot \mathbf{j} = R \tag{46}$$

where R indicates the boundary reaction term if there are no momentum changes in the system. The mass balance can be described by the heterogeneous Cahn-Hilliard equation, which is

$$\frac{\partial c}{\partial t} = -\nabla \cdot \mathbf{j}. \tag{47}$$

For LFP-like phase separating systems with an anisotropic interfacial thickness or slow currents, fast diffusion in the y axis can be observed, which indicates that a depth-averaged model can be used to gain physical insight into the system [330, 241, 67, 379]. As mentioned earlier, diffusivity of LFP in the y direction, however, is many orders of magnitude higher than in the other directions, thus indicating that we can neglect diffusion in the x and z directions, only considering diffusion in the y direction [380]. We simplify and leave a flux divergence that only depends on the y component. In our general depth-averaged equation for any converved quantity b, we see that

$$\frac{\partial}{\partial t} \int_y b dy = -\int_y \nabla \cdot \mathbf{j_b} dy + \int_y B_V dy. \tag{48}$$

Applying the result of the depth-averaged model, assuming that L_y is the depth of the particle, we apply the divergence theorem where R indicates a surface reaction for a Cahn-Hilliard model. Diffusion can often be neglected in these models. If we nondimensionalize the set of equations above using $\tilde{c} = \frac{c}{c_{max}}$, $\tilde{T} = \frac{T}{T_b}$, $\tilde{R} = \frac{R}{k_0 \exp(-E_A/k_B T_b)}$, $\tilde{t} = \frac{k_0 \exp(-E_A/k_B T_b) t}{L_y c_{max}}$, $\tilde{h} = \frac{h}{k_B T_b}$, and $\tilde{h}_{res} = \frac{h_{res}}{k_B T_b}$ where c_{max} is the maximum species concentration, and drop all of the tildes and bars in future notation, we obtain

$$\frac{\partial c}{\partial t} = R(c, \nabla c, \mu_{res}, T). \tag{49}$$

Most electrochemical reactions can be characterized with a heterogeneous reaction

using a Cahn-Hilliard model. The depth-averaged model in 1D can sometimes be used to model reaction limited particles, but is not accurate for all systems, as there are systems where internal phase separation happens in waves and diffusion in the ion channels drives the phase separation throughout the depth of the particle [330]. For these systems, a full (not depth-averaged) model is required.

For a Allen-Cahn model with homogeneous reaction, since the Biot numbers are assumed to be large, for a depth averaged model, we integrate both the simplified mass and energy conservation equations over the length of the y direction of the particle, where we assume that both concentration and energy are homogeneous within the y direction of particle. Because of the large Biot number, diffusive fluxes and Soret diffusion, which is much smaller than diffusion in a solid system, can be neglected. The Allen-Cahn equation can be written as

$$\frac{\partial c}{\partial t} = R(c, \nabla c, \mu_{res}, T), \tag{50}$$

where the reaction term is assumed to be homogeneous. Ultimately, if we ignore diffusion as in a nanoparticle, the Cahn-Hilliard reaction and the Allen-Cahn reaction converge to the same form with the difference of surface reaction or bulk reaction.

For an energy balance, the dependence of the ratio of heat transfer driven by the mass flux into the system to the diffusive heat flux indicates the importance of the inclusion of separate terms. The Biot number for heat transfer, Bi_T, gives a good indication of which one is the better model. Since heat conduction is extremely fast in a particle, causing the Bi_T to be extremely small (10^{-4}), it is necessary to include the conduction term in the system. The heat flux boundary condition for a Cahn-Hilliard model is described as Eq. 46 where the volume averaged energy balance results in [352] by the divergence theorem

$$c_v \frac{\partial \bar{T}}{\partial t} + \mathrm{Bi}_T h R = -h_T(\bar{T} - T_l), \tag{51}$$

where T_l is the electrolyte temperature. Nondimensionalizing this equation leads to

$$c_v \frac{\partial T}{\partial t} = \frac{1}{\zeta}\left(-(T - T_l) - \mathrm{Bi}_T hR\right) \tag{52}$$

where $\zeta = \frac{c_{max} h_T}{k_0 \exp(-E_A/k_B T_b)\rho c_v}$ scales between the mass and energy balance and $\mathrm{Bi}_T = \frac{k_B k_0 \exp(-E_A/k_B T_b)}{h_T}$ is the Biot number for heat transfer.

Homogeneous Reaction

For an Allen-Cahn model where reaction can be assumed to happen homogeneously in the system, similarly to the Cahn-Hilliard model, because of the small Biot heat transfer numbers, diffusion through the system cannot be ignored. This can be written as

$$\int_V c_v \frac{\partial T}{\partial t} dV = \int_V -\nabla \cdot \mathbf{q} dV - hRV, \tag{53}$$

Neglecting the non-Fourier terms which are small, we recover $h_T = \frac{k}{\Delta x}$, giving

$$c_v \frac{\partial T}{\partial t} = -\frac{h_T}{L_p}(T - T_l) - hR, \tag{54}$$

where h_T is the heat transfer coefficient, A is the area, and T_l is the temperature of the bath, assuming a homogeneous system. Conversion to temperature per volume gives

$$c_v \frac{\partial T}{\partial t} = -hR - \frac{h_T}{L_p}(T - T_l), \tag{55}$$

where L_p is the characteristic lengthscale of a particle and c_v is the heat capacity of the active material. Nondimensionalizing this equation leads to a slightly different form from the Cahn-Hilliard reaction

$$c_v \frac{\partial T}{\partial t} = \frac{1}{\zeta}\left(-(T - T_l) - \mathrm{Bi}_T hR\right), \tag{56}$$

where $\zeta = \frac{c_{max} h_T}{k_0 \exp(-E_A/k_B T_b) L_p \rho c_v}$ scales between the mass and energy balance and $\mathrm{Bi}_T = \frac{k_B k_0 \exp(-E_A/k_B T_b) L_y}{h_T}$ is the Biot number for heat transfer for an Allen-Cahn reaction.

A.3.2 General Porous Electrode Theory

The general heat generation equation used in most battery models, derived from the Gibbs Helmholtz relation, is only valid for solid solution materials, or when open circuit voltage relations are used to model batteries [343, 381],

$$\frac{dH}{dt} = T^2 \frac{d}{dT}\left(\frac{U^0}{T}\right) = T\frac{dU}{dT} - U, \tag{57}$$

where U is the open circuit voltage, which appears as a free energy term. As the Gibbs Helmholtz relation relies on thermodynamic partial derivatives that are correct only in closed, single component systems, this equation is not always correct. Our entire system, though it is closed by mass, is not a single component system. Changes in the amount of intercalated species change the entropy increase of the different species, which in turn changes the temperature of the system.

Now that we have defined the system, coupled with the open system is the electrolyte (reservoir), which needs to be fully defined with our open system relations. We assume that the reservoir chemical potential is set by the control value of the system, the reaction rate. Based on the intercalation reaction, the system is only affected through the reaction based on the ACR/CHR mass balances through the reservoir potential. However, the enthalpy effects of the system are not "controlled," and the energy of the open system is affected by the temperature and the potential of both the system and the reservoir, where the temperature of the reservoir is also changing since it is not controlled like the reservoir potential. Thus, the energy balance of the reservoir also needs to be defined since the temperature is not controlled. We realize that we have to define the energy balances of the particle and electrolyte jointly because of the shared reference chemical potential between the two.

A similar energy and mass balance must be applied to the reservoir systems, with the same nonisothermal flux terms as indicated above, in a control volume that contains the electrolyte surrounding a certain number of active material particles. We can construct a simplified electrolyte model to prove that in a single particle model, with only moderate changes in chemical potential, that the change of electrolyte

temperature is minimal with respect to the bulk environment. The addition of a charge balance, from ion transport in the electrolyte and intercalation reactions, can be added to the system, where $\rho_e = \sum_i z_i e c_{l,i}$, the charge density of the system. Here, we can apply charge neutrality at the scale we are studying. The current density in the electrolyte can be defined as the sum of ionic fluxes $\mathbf{i_l} = \sum_i z_i e \mathbf{j_{l,i}}$ from the cations and anions in a current controlled system to be

$$\begin{aligned} \frac{\partial c_{l,i}}{\partial t} &= -\nabla \cdot \mathbf{j_{l,i}} + R_{l,i} \\ c_v \frac{\partial T}{\partial t} &= -\nabla \cdot \mathbf{q} + Q_{l,i} + \sigma_l (\nabla \phi_l)^2 + \sigma_s (\nabla \phi_s)^2 \\ \frac{\partial \rho_{e,l}}{\partial t} &= -\nabla \cdot \mathbf{i_l} + \sum_i z_i e R_l \end{aligned} \tag{58}$$

with reactions and heat generation happening throughout the particles

$$\begin{aligned} R_{l,i} &= \sum_{particles} V_p \left(-\frac{\partial c}{\partial t} \right) \\ Q_l &= \sum_i \left(\sum_{particles} \left(h_{l,i} - h_{res} \right) V_p \left(-\frac{\partial c}{\partial t} \right) - \boldsymbol{\sigma} : \frac{\partial \boldsymbol{\varepsilon^e}}{\partial t} \right), \end{aligned} \tag{59}$$

neglecting mechanical effects. Q_l can be defined as the energy generated in the entire volume (including particles and electrolyte) [352]. Since electrolyte fluxes are similarly nonisothermal, the Onsager flux relations are the same as used above, excepting the Seebeck and Peltier effects. From the assumption of a binary electrolyte, the current density can be calculated from the fluxes of the cations and anions.

Here, to justify our previous assumption that the bulk electrolyte temperature is constant at the prescribed temperature, we perform scaling. For simplicity, in a single particle current control system, we assume that the reservoir system is homogeneous and diffusive effects are small. We apply an integral over the electrolyte volume to obtain

$$\frac{\partial c_l}{\partial t} = \sum_{particles} \frac{V_p}{V_l} \left(-\frac{\partial c}{\partial t} \right) - \frac{1}{V_l} \nabla \cdot \mathbf{j_l}. \tag{60}$$

For the energy balance, we apply the mass balance and then convert the energy bal-

ance to a volumetric form for particle per electrolyte volume for scaling comparisons, different from the usual definition of "volumetric." Applying the mass balance, we get that

$$c_{v,l}\frac{\partial T_l}{\partial t} = \sum_{particles}\frac{V_p}{V_l}(-h_{res})\left(-\frac{\partial c}{\partial t}\right) + \sum_{particles}\frac{h_T}{L_p}\frac{V_p}{V_l}(T - T_l) - \frac{1}{V_l}\nabla\cdot\mathbf{q_l} + \frac{\sigma_s}{V_l}(\nabla\phi_s)^2 \tag{61}$$

while making the same assumptions about reversible work as earlier, where σ_l is the conductivity of the electrolyte, since the current can be found from the current to be $\mathbf{i}_l = -\sigma_l\nabla\phi_\mathbf{l}$ from the definition of the electric field. This is the energy balance for the electrolyte in the system.

To justify our assumption that the electrolyte temperature is assumed to be constant with regard to the particle, if we assume that 1) the electrolyte is well mixed and can be locally modeled with a single volume, 2) heat transfer with the environment can be modeled with a flux term, 3) resistive heating is small, and 4) assuming that each of the particles are indistinguishable with a total of M particles, we obtain

$$c_{v,l}\frac{\partial T_l}{\partial t} = M\frac{V_p}{V_l}h_{res}R + M\frac{h_p}{L_p}\frac{V_p}{V_l}(T - T_l) - \frac{h_l}{L_l}(T_l - T_b) + \frac{\sigma_s(\nabla\phi_s)^2}{V_l}, \tag{62}$$

where $A_{p/l}$ is the particle or electrolyte area, $L_{p/l}$ is the particle or electrolyte length-scale, $V_{p/l}$ is is the volume of the particle or electrolyte, and $h_{p/l}$ is the heat transfer coefficient for the particle or electrolyte. Since the time constant for the energy balance is much smaller than that of the mass balance, we can assume our system is psuedo-steady in the energy balance, with

$$T_l \approx \frac{M\frac{A_p}{A_l}\left(\frac{L_p}{h}h_{res}R + T\right) + T_b}{M\frac{A_p}{A_l} + 1}. \tag{63}$$

Under the assumption that $MA_p/A_l \ll 1$, then the steady temperature of electrolyte can be assumed to be roughly the bulk electrolyte temperature. This requires the active area of the particles to be much smaller than that of the electrolyte in the system. In a single particle system, $A_p/A_l \ll 1$ is true, indicating that this is a

valid assumption. (Macroscopically, this type of parameter can be related to $M\frac{V_p}{V_l} = (1-\epsilon)P_L$, the fraction of active material of the system.) Our assumptions are correct for a single particle system, but in a battery, since the fraction of active material in the entire cathode/anode area is roughly 40% and the electrolyte volume lengths tend to be much larger than the particle scale, the electrolyte temperature is $T_l \approx \frac{L_p}{h_T} h_{res} R + T$, indicating that this assumption is not physically indicative of a real battery.

As an added check, the sum of the energy balances of these two systems in a single particle model brings us to the form of

$$\sum_{particles} V_p \frac{du}{dt} + V_l \frac{du_l}{dt} = \sum_{particles} (h - h_{res})R - \nabla \cdot \mathbf{q_l} + \sigma_s (\nabla \phi_s)^2 + \sigma_l (\nabla \phi_l)^2, \quad (64)$$

where we recover the $(h - h_{res})R$ term expected from simple closed system reaction kinetics terms. We note that the reaction rate is defined as lithium ions generated per electrolyte volume. Each term in these formulations matches the energy balances derived in previous models [122, 45].

A.3.3 Reaction Rate

Two different reaction rates–the Butler-Volmer (BV) reaction, and coupled ion electron transfer [347] are applied to this system.

Butler-Volmer

The thermodynamically reversible BV reaction is commonly used for electrochemical reactions because of its simplicity [349], but does not take into account electron availability in the system. It assumes that ion transfer is the limiting step in the reaction. For Butler-Volmer, which is a thermodynamically consistent transition state theory, we assume a general thermodynamically consistent Butler-Volmer reaction rate of the form where $k_0 = k_{0,0} e^{-E_A/k_B T_b}$ is the exchange current at the reference temperature T_b, μ is the chemical potential of species M, and μ_{res} is the reservoir chemical potential. The Butler-Volmer equation is a transition state theory equation. The transition state chemical potential $\mu_{\ddagger}^{ex}$, is defined as $\mu_{\ddagger}^{ex} = k_B T ln \gamma_{\ddagger} + (1-\alpha)\mu_{res} +$

$\alpha\mu$. We assume the transition state chemical potential excludes a single surface site and gives $\gamma_\ddagger = (1-c)^{-1}$. This simplifies to

$$R = k_{0,0} e^{-(E_A/k_BT - E_A/k_BT_b)} \frac{\gamma_{res}^{1-\alpha}\gamma^{\alpha}}{\gamma_\ddagger} \left(e^{-\alpha e\eta/k_BT} - e^{(1-\alpha)e\eta/k_BT}\right). \tag{65}$$

where $e\eta = \mu - \mu_{res}$ is the overpotential, which drives the reaction kinetics in the system. In an electrochemical system, the reaction rate R is related to the current as $I = neR$.

Coupled-Ion Electron Transfer

A realistic electrochemical reaction is neither fully limited by the ions, nor by the electrons, but accounts for the availability of both of these materials. The coupled ion electron transfer reaction model is a first principles reaction model that takes into account the effect of electron availability, specifically with the density of state, of the system [347]. Electron transfer reactions were first modeled by Marcus and coworkers, then extended to electrochemical reactions [124, 313]. Hush then extended Marcus theory to account for delocalized electronic states [126, 125]. In recent years, Fraggedakis et al. [347] formulated the full theory of coupled ion electron transfer based on careful experiments which were further verified with different intercalation materials [129]. In coupled ion electron transfer (CIET), the density of states of the electron donor $\rho(\varepsilon)$ is taken into account in the reaction rate, defined as

$$R = \int \rho(\varepsilon) \left(R_{\rightarrow}(\varepsilon) - R_{\leftarrow}(\varepsilon)\right) d\varepsilon \tag{66}$$

If there is a localized electron state, we recover Marcus theory, with $\rho(\varepsilon) = \delta(\varepsilon - \varepsilon_i)$, while if we consider a metallic donor, we recover the Marcus-Hush-Chidsey (MHC) model, with $\rho(\varepsilon) = 1$, where ε is the energy level. Zeng et al. [166] formulated a simple analytical equation to simplify the reaction rate of the system.

For ion intercalation with nondimensionalized values, we use the modified over-

potential $\eta_f = \mu - \mu_{res} - T \ln \frac{c}{1-c}$. The reaction should be described by

$$R = \int_{-\infty}^{\infty} \rho(\varepsilon) \frac{k_{0,0}}{\sqrt{T}} e^{-(E_A/k_B T - E_A/k_B T_b)} \left(n(\varepsilon)(1-c) e^{-\frac{(\lambda+\eta_f-\varepsilon)^2}{4\lambda T}} - (1-n(\varepsilon)) c e^{-\frac{(\lambda-\eta_f-\varepsilon)^2}{4\lambda T}} \right) d\varepsilon, \tag{67}$$

with either the MHC or Marcus DOS functions. Here, $n(\varepsilon)$ is the Fermi-Dirac distribution and λ is the reorganization energy.

A.3.4 Simplified Linear Stability Analysis

A simplified form of the linear stability analysis performed in Sec. A.2.3 can be applied to our ion intercalation system. We place our particle in a reservoir of chemical potential μ_{res} and temperature T_b, and choose the system to be the particle. By the analysis in Sec. A.3.1, we know that the temperature of the electrolyte in a single particle system can be assumed to be the bulk temperature, which is assumed to be constant at T_b in our model. Since the reaction rate is much larger than diffusion in this system, the diffusion term in the mass balance is neglected to simplify the system. In the following linear stability analysis, we include the modification of the use of the heat transfer coefficient instead of the heat conductivity. Assuming that the system is homogeneous in concentration and temperature, and the heat transfer coefficient has no temperature or concentration dependence, our mass and energy balances can be written as below:

$$\frac{\partial c}{\partial t} = R \tag{68}$$

$$c_v \frac{\partial T}{\partial t} = -\frac{h_T}{L}(T - T_b) - hR. \tag{69}$$

If we nondimensionalize the set of equations above using $\tilde{c} = \frac{c}{c_{max}}$, $\tilde{T} = \frac{T}{T_b}$, $\tilde{R} = \frac{R}{k_0}$, $\tau = \frac{k_0 t}{c_{max}}$, $\tilde{h} = \frac{h}{k_B T_b}$, $\tilde{h}_{res} = \frac{h_{res}}{k_B T_b}$, and $\tilde{h}_T = \frac{h_T}{h_{T,r}}$ where c_{max} is the maximum species concentration and $k_0 = k_{0,0} \exp\left(-\frac{E_A}{k_B T_b}\right)$, we obtain

$$\frac{\partial \tilde{c}}{\partial \tau} = \tilde{R} \tag{70}$$

$$\frac{\partial \tilde{T}}{\partial \tau} = \zeta \left(-(\tilde{T}-1)\tilde{h}_T - \tilde{h}\mathrm{Bi}_{\mathrm{heat}}\tilde{R} \right), \tag{71}$$

where $\mathrm{Bi}_{\mathrm{heat}} = \frac{k_B k_0}{h_{T,r}}$, the Biot heat transfer number, represents heat from the chemical potential to external heat transfer. For simplicity, we also neglect the tildes on the nondimensionalized equations. In this equation, $\zeta = \frac{c_{max} h_{T,r}}{k_0 L c_v}$ is the scale of heat transfer to reaction. The heat transfer coefficient in these systems is quite large, often causing the ζ value to be orders of magnitude larger than unity.

The full linear stability analysis for this system is found by solving

$$\sigma \mathbf{I}\boldsymbol{\delta} = \mathbf{J}\boldsymbol{\delta}, \tag{72}$$

where

$$\mathbf{J} = \begin{bmatrix} \frac{\partial R}{\partial c} + \frac{\partial R}{\partial \mu}\left(\frac{\partial \mu_h}{\partial c} + \kappa|\mathbf{k}|^2\right) & \frac{\partial R}{\partial T} + \frac{\partial R}{\partial \mu}\frac{\partial \mu_h}{\partial T} \\ -\mathrm{Bi}_T \xi \left(\bar{h}\left(\frac{\partial R}{\partial c} + \frac{\partial R}{\partial \mu}\left(\frac{\partial \mu_h}{\partial c} + \kappa|\mathbf{k}|^2\right)\right) + \bar{R}\frac{\partial h}{\partial c}\right) & -\xi\left(\left(\bar{h}_T + \frac{\partial h_T}{\partial T}(\bar{T}-1)\right) + \mathrm{Bi}_T \bar{h}\left(\frac{\partial R}{\partial T} + \frac{\partial R}{\partial \mu}\frac{\partial \mu_h}{\partial T}\right)\right) \end{bmatrix}. \tag{73}$$

The solution of the equation $\det|\sigma \mathbf{I}\boldsymbol{\sigma} - \mathbf{J}\boldsymbol{\delta}| = 0$, if we assume that the heat transfer coefficient h_T is not dependent on temperature or concentration, gives the full solution of

$$\begin{aligned} \sigma = \frac{1}{2}\Bigg(& \frac{dR}{dc} - \xi\left(1 + \mathrm{Bi}_T \frac{dR}{dT}\bar{h}\right) \\ & \pm \sqrt{\left(\frac{dR}{dc} - \xi\left(1 + \mathrm{Bi}_T \frac{dR}{dT}\bar{h}\right)\right)^2 + 4\xi\left(\frac{dR}{dc} - \mathrm{Bi}_T \bar{R}\frac{\partial h}{\partial c}\frac{dR}{dT}\right)}\Bigg), \end{aligned} \tag{74}$$

where the real parts of the critical solution are the solution to the problem. Assuming that $\sigma \ll 0$, and neglecting the second order term, we solve a linear problem,

$$\sigma = \frac{\xi\left(\frac{dR}{dc} - \mathrm{Bi}_T \frac{dR}{dT}\frac{\partial h}{\partial c}\right)}{\xi\left(1 + \mathrm{Bi}_T \frac{dR}{dc}\bar{h}\right) - \frac{dR}{dc}}. \tag{75}$$

Under the assumption of large ξ, we will see that the limit for this solution converges to the same solution that we solve for in the psuedo-steady linear stability analysis shown below.

An even simpler version of the full linear stability analysis can be considered from the separation of timescales. Since the timescale of heat transfer in the system is significantly faster than that of mass transfer, we further assume that the energy balance is already at equilibrium

$$0 = -(\tilde{T} - 1)\tilde{h}_T - \tilde{h}\mathrm{Bi}_T\tilde{R}. \tag{76}$$

We write several useful derivatives for this phase separating system, $\frac{\partial \mu}{\partial c} = \frac{\partial \mu_h}{\partial c} + \kappa|\mathbf{k}|^2$ and $\frac{\partial \mu}{\partial \tilde{T}} = \frac{\partial \mu_h}{\partial \tilde{T}}$, where $\tilde{\kappa} = \kappa c_{max}$. Keeping only the terms that are first order in ϵ and neglecting all mechanical effects, our system of equations to solve becomes

$$\begin{bmatrix} \sigma & 0 \\ 0 & 0 \end{bmatrix} \boldsymbol{\delta} = \mathbf{J}\boldsymbol{\delta}, \tag{77}$$

where

$$\mathbf{J} = \begin{bmatrix} \frac{\partial R}{\partial c} + \frac{\partial R}{\partial \mu}\left(\frac{\partial \mu_h}{\partial c} + \kappa|\mathbf{k}|^2\right) & \frac{\partial R}{\partial T} + \frac{\partial R}{\partial \mu}\frac{\partial \mu_h}{\partial T} \\ -\mathrm{Bi}_T\left(\bar{h}\left(\frac{\partial R}{\partial c} + \frac{\partial R}{\partial \mu}\left(\frac{\partial \mu_h}{\partial c} + \kappa|\mathbf{k}|^2\right)\right) + \bar{R}\frac{\partial h}{\partial c}\right) & -\left(\bar{h}_T + \frac{\partial h_T}{\partial \bar{T}}(\bar{T} - 1)\right) - \mathrm{Bi}_T\bar{h}\left(\frac{\partial R}{\partial T} + \frac{\partial R}{\partial \mu}\frac{\partial \mu_h}{\partial T}\right) \end{bmatrix} \tag{78}$$

The growth factor σ can be found by solving the secular equation $\det|\mathbf{J} - \sigma\mathbf{e}_1| = 0$, if we again assume that the heat transfer coefficient is not affected by the temperature or concentration. This leads to

$$\sigma = \frac{-\mathrm{Bi}_T\bar{R}\frac{\partial h}{\partial c}\frac{dR}{dT} + \frac{dR}{dc}}{1 + \mathrm{Bi}_T\bar{h}\frac{dR}{dT}}. \tag{79}$$

Because of the finite size of the particle, the critical value of the perturbation is $\mathbf{k} = \frac{2\pi}{L}$, where L is the characteristic length of the nanoparticle. The critical stability value is found to be

$$\sigma = \frac{-\mathrm{Bi}_T\bar{R}\left(\frac{\partial h}{\partial c}\frac{dR}{dT} + \frac{\partial R}{\partial \mu}\frac{\partial \mu_h}{\partial T}\kappa|\mathbf{k}|^2\right) + \frac{\partial R}{\partial \mu}\kappa|\mathbf{k}|^2 + \frac{dR}{dc}}{1 + \mathrm{Bi}_T\bar{h}\frac{dR}{dT}}. \tag{80}$$

From the solution for the critical stability value, we can see that the main competition

between stability and instability is between the isothermal dependence of reaction rate on concentration $\frac{dR}{dc}$ and the dependence of reaction rate on temperature $\frac{dR}{dT}$, scaled by the Biot number which relates the ratios of mass transport to heat transport. The competition between these two terms will determine the stability of the system. At low Biot number, we expect the solution to converge to the isothermal models derived in Refs. [67, 165], while at higher Biot number, the autocatalytic effect of temperature starts to affect the stability more.

Stability depends on where positive values of the critical stability value appear. Since the stability of the system depends on $\frac{dR}{dc}$ and $\frac{dR}{dT}$, the reaction dependence on concentration and temperature, which indicates that the reaction rate used to model the system will affect the stability of the system. In our following analysis, using different reaction models, the expected magnitudes of $\frac{dR}{dc}$ and $\frac{dR}{dT}$ play important roles determining the stability of our system. The stability is highly dependent on the ratio of the Biot number to heat transfer coefficient if the temperature dependence of heat transfer coefficient is small, indicating that thermal coatings, or conductivity with system is very important to the system as well. This leads us to study the importance of material properties, especially the Biot number, on the stability of the system.

At large Biot numbers, where the denominator of the critical stability value changes sign or approaches zero, the stability of the system is significantly affected. When the Biot number is large, $\frac{dR}{dT}$ plays a much larger role in affecting the critical stability of the system, such that this value may approach zero. At high Biot number, fluctuations in the stability solutions may be induced near these values.

A.4 Results and Discussion

A.4.1 Butler-Volmer Reaction

Our open system model can be applied to an intercalation system for lithium-ion battery materials. We can perform the analysis on lithium intercalation in a phase

separating material such as lithium iron phosphate (LFP), where the LFP particle is the system and the electrolyte solution is the environment. We model the reaction as $Li^+ + e^- + M \longrightarrow LiM$, where M is LiC_6 and M_{res} is Li^+ for LFP. As mentioned earlier, the process timescale for reaction in the system is significantly larger (10^{14} if assuming a C-rate of 1) than the timescale for conductive heat transfer, indicating that at the timescales we are interested in, the temperature balance can be modeled with a pseudo-steady approximation. Thus, we see that this justifies our assumption that temperature can be approximated with the pseudo-steady state approximation.

In the equilibrium chemical potential of an intercalation material, the entropic term includes nonisothermal effects as shown in Fig. 1. A decrease in temperature causes the spinodes to become more prominent and increases the miscibility gap of the chemical potential. Thus, for a system fully in equilibrium, we expect increased phase separation and a smaller nucleation barrier to overcome for lower temperatures. However, in our intercalation systems, we never encounter systems that are fully in equilibrium. Instead, our systems are always driven by some potential or reaction, indicating that the system is rarely in equilibrium. This requires us to study the effects of temperature on these systems more carefully, coupled with the mass, energy, and momentum balances in these systems.

We can apply the regular solution model to model the chemical potential of lithium in LFP our system [241]. For this system, the regular solution model applied gives

$$\mu = \Omega(1-2c) + k_B T \ln\left(\frac{c}{1-c}\right) - \kappa \nabla c^2, \tag{81}$$

where Ω is the regular solution parameter, the second term is from the entropic contribution, and the last term is from the phase boundary energy. Applying the value of $\mathbf{k}_{crit} = \frac{2\pi}{L}$ to this system from the particle size [241], we obtain the phase diagram for stability with the above parameters applied to the system. Since the temperature effect on the heat conduction coefficient for the system is expected to be small, we simplify the critical growth rate at equilibrium above as Eq. 80.

Using the parameters $\Omega = 4.0 k_B T_b$, $\kappa = 0.684 k_B T_b L^2$ with a particle size of

$L = 100\,\text{nm}$, and $k_0 = 10\,\text{A/m}^2$ [67, 382, 383], we obtain that $\text{Bi}_T = 1 \times 10^{-5}$ in this system [384, 385]. For parameters in this system, we can assume that $h = 10 - 100\,\text{W/(m}^2\text{K)}$ since conductive heat transfer between an intercalation material and an electrolyte is taking place. [386] The activation energy is $E_A = 50\,\text{kJ/mol}$ and the exchange current density appears as $k_0(T = 298\,\text{K}) = 1.1\,\text{A/m}^2$, which gives us $k_{0,0} = 3.98 \times 10^{27}(\text{m}^2\cdot\text{s})$ for surface intercalation, giving us a Biot number of $\text{Bi}_T = 1 \times 10^{-10}$ for graphite [387, 388]. We note that the Biot number for different materials can be quite different, and thus this is a parameter whose effect should be studied carefully in intercalation systems. A study on the effect of the change of the Biot number reflects how material properties can affect the stability of an open driven system is performed. If we study the phase stability for ion intercalation of LFP using the model defined above, we separately control the current and the voltage to affect the stability of the system and consider the effects of constant current or voltage charging on the nonisothermal stability of the system, which are the two basic common modes of battery intercalation/deintercalation.

The equilibrium temperature of the system is determined by the energy balance of the system, where $T = -\text{Bi}_T hR + 1$ is true at steady state. This is generally true in our system from the large timescale difference between the energy and mass balances. In Fig. 1, we see that for a phenomological Butler-Volmer reaction rate which grows exponentially with overpotential, the temperature and the stability of the system are both highly influenced by the value of the Biot number. From a low Biot number, we see almost an exact replicate of the stability diagram under nonisothermal conditions. At a high Biot number, even in the suppressed phase separation regime [67], phase separation appears in these systems. The region of instability at higher Biot number significantly increases with respect to the lower Biot number values. This is through the increased effect of $\frac{dR}{dT}$ as the Biot number increases, which destabilizes the system from the autocatalytic properties of the Arrhenius function. For the localized and delocalized cases for the reaction kinetics, because the reaction currents are much smaller from the limiting current [347], there is a minimal effect on temperature on the stability of these reaction rates. The physical picture of limitation from electron

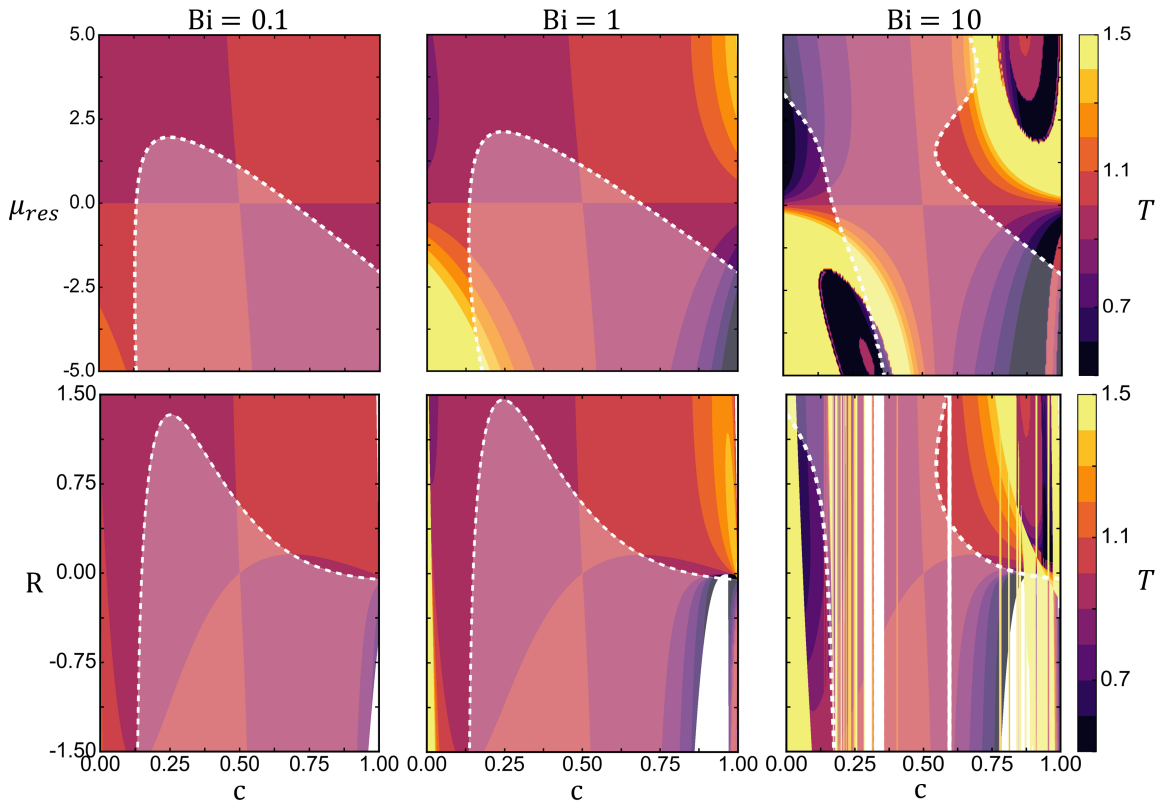

Figure 1: Stability of the system at various Biot numbers using a Butler-Volmer reaction rate, where the white shaded area surrounds the unstable region. The temperature of the solution is also plotted on the same plot using a heatmap. The solid white area is the area with no steady state energy balance solution.

availability prevents the destabilizing seen in Butler-Volmer kinetics.

Although the solutions are not trustworthy at higher overpotential values because the kinetics are not limited by electron availability at high overpotentials, we can still gain valuable insight from lower overpotentials. We expect a breakdown of the model at higher overpotentials or currents. Bi is highly dependent on material properties and system properties, and in general the system is more stable at lower Bi ratios if we use a Butler-Volmer reaction rate. For temperature stability, we should add thermal coatings or pick more thermally conductive fluids and materials. For example, the Biot number is very small, so temperature effects are much smaller, but for graphite, Bi is significantly larger, so more thermally dissipative additives or coatings should

be added to the materials. Because of our previous analysis where increased Biot number means a stronger autocatalytic effect from temperature, this destabilizes the system. However, we know that the Butler-Volmer reaction rate does not capture the effects of electron transfer, which can be rate-limiting in electrochemical reactions and thus cause current to be limiting. Thus, we turn to a first principles coupled ion-electron transfer model (CIET), which takes into account the coupled transfer of ions and electrons in the model.

A.4.2 Coupled Ion Electron Transfer

We see that the main temperature dependence in the Butler-Volmer reaction equation, other than the energy scalings of the system, is first in the Arrhenius reaction rate dependence, and second in the overpotential temperature dependence from the entropic term. For the CIET equations, the modified overpotential, specifically for a lattice model as decribed for LFP, has no temperature dependence in the overpotential since the entropic term is removed in the overpotential. There is only the Arrhenius temperature dependence on the reaction coefficient as well as a $1/\sqrt{T}$ scaling from quantum tunneling in the reaction coefficient [347, 129]. To both BV and CIET, increased temperature increases stability in both systems for voltage control. For Butler Volmer, an increase in temperature increases the reaction coefficient, but the overpotential term decreases from the increased temperature. Thus, the driving force for the reaction decreases, decreasing the overall reaction rate and driving the reaction to stability. However, for CIET, the quantum tunneling term reduces the reaction rate at increased temperature, which also drives the reaction to stability. Thus, we expect that for CIET, the temperature effects on the kinetics are weaker than the Butler-Volmer system.

Since Butler-Volmer is a phenomenological model, a first principles model will most likely capture the temperature effects of the stability of the system much better. Here we compare Butler-Volmer and couple ion-electron transfer with localized and delocalized electron densities, which can be simplified to Marcus/Marcus-Hush-Chidsey kinetics. In Fig. 2, we see that Bi has almost no effect on the stability of

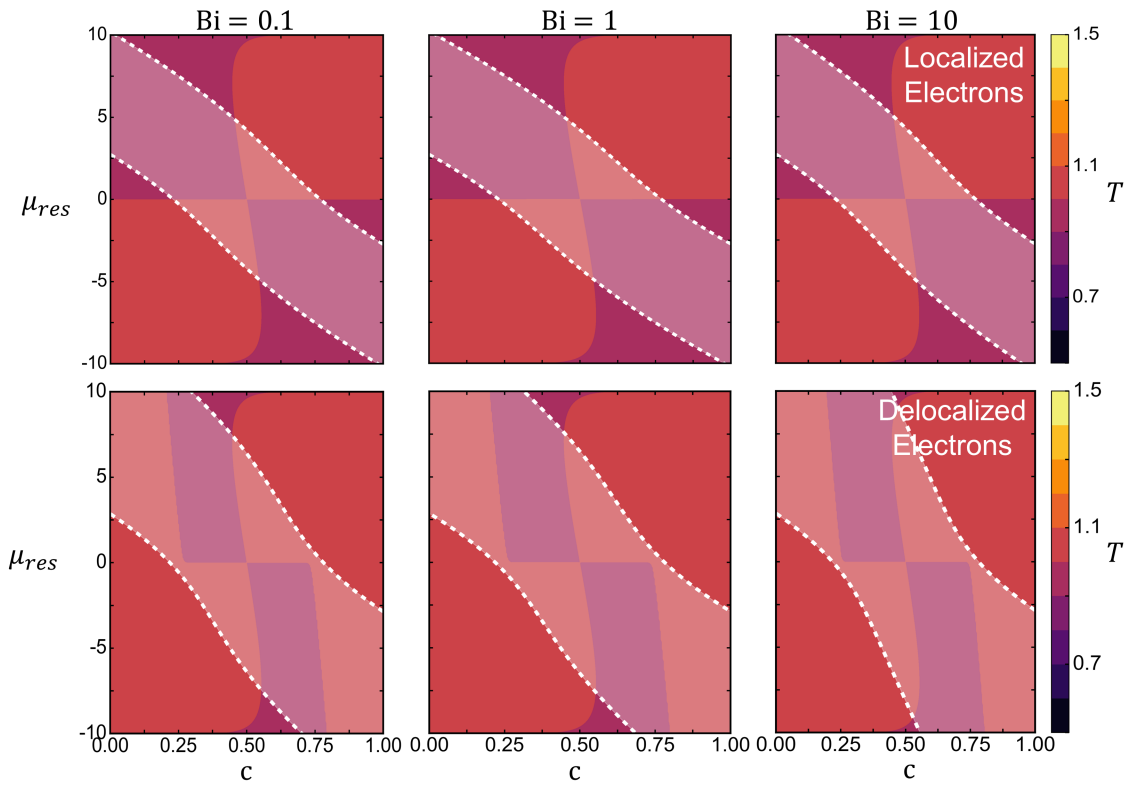

Figure 2: Stability of the system using a CIET reaction rate at various Biot numbers, where the white shaded area surrounds the unstable region. The temperature of the solution is also plotted on the same plot using a heatmap.

the system, as well as the steady state temperature solutions not changing at all with the change in Bi. Under the assumption of a single particle model, we know that because CIET has a limiting reaction rate, unlike BV, which grows exponentially at high overpotentials. Thus, the temperature in a coupled ion electron transfer system is more stable than a BV system. Especially in Eq. 80, we know that because of the limiting reaction rate for CIET, from Eq. 76, the effect of the Biot number on the stability of the system is reduced because the current is small. Because of this, there is no solution breakdown at higher overpotentials. We see why there is little effect of the Biot number on the steady state temperature or the stability of the system.

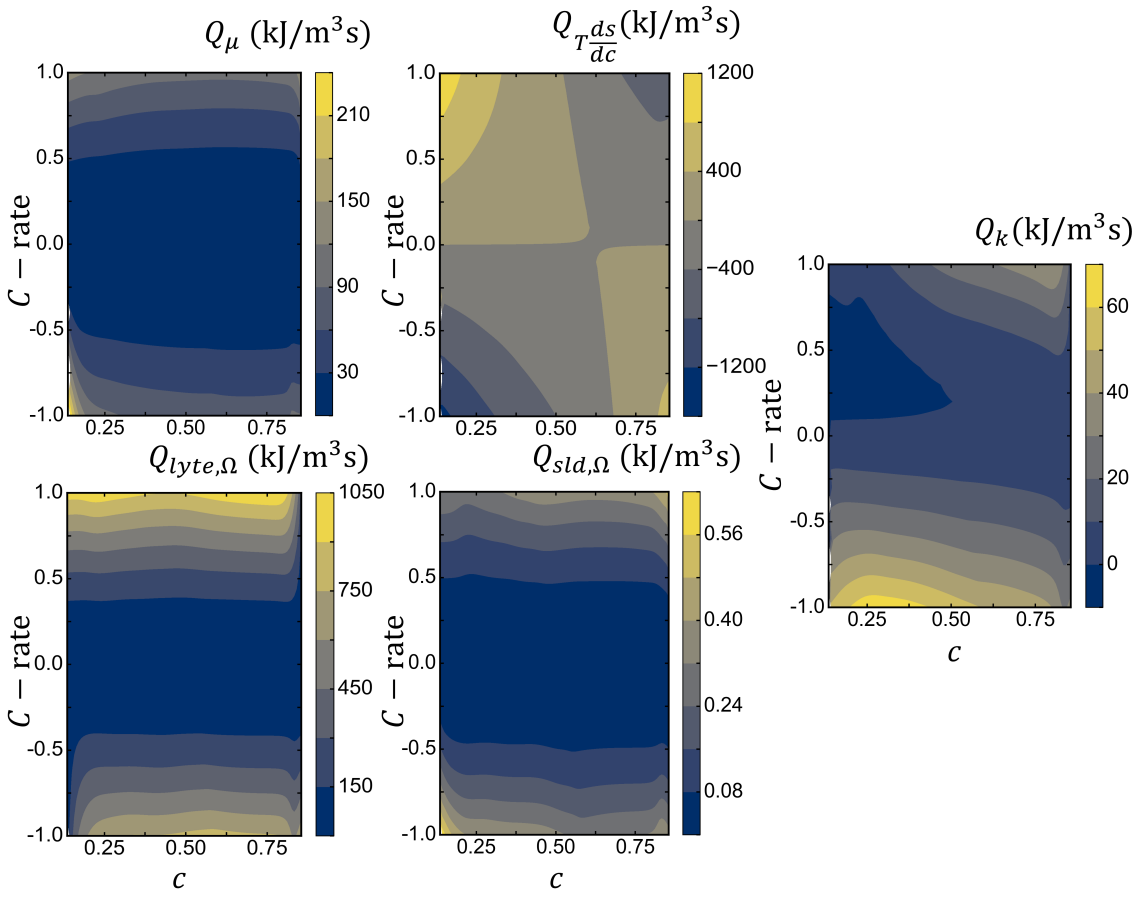

Figure 3: Heat generation terms of each of the porous electrode scale model terms relative to each other. Q_μ is from the effect of $(\mu_{res}-\mu)R$, $Q_{T\frac{ds}{dc}}$ is from the differential entropy effect, $Q_{lyte,\Omega}$ is from the Ohmic heat generation in the electrolyte, $Q_{sld,\Omega}$ is from the Ohmic heat generation in the solid, and $Q_{lyte,k}$ is from the Fourier's law heat flux in the system.

A.5 Porous Electrode Scale Model

The nonisothermal model was implemented into our in-house porous electrode theory [122, 54] software Multiphase Porous Electrode Theory (MPET) [44] for the the lithium cobalt oxide-graphite cell model in Refs. [389, 45] using the parameters from Ref. [45]. The effect of heat generation from each term is modeled below to understand what the comprehensive reasoning behind the heat generation in the systems is caused by.

From the heat generation modeled in Fig. 3, we see that the main cause of heat

generation is the reversible entropic heat generation term. However, this term is idealized and most likely is overestimated in this system. The term that generates the most heat is then most likely to be the Ohmic heat generation term from the electrolyte, especially at higher C-rates. As the temperature increases in these systems, the effect on electrolyte conductivities and diffusivities is extremely large [5, 390], and Ohmic heat generation becomes very important. The Fourier heat diffusion also increases from the heat generation increase, most likely because of increased temperature at high C-rates, which causes larger thermal gradients.

A.6 Conclusion

In this study, we derive a novel general nonisothermal modeling of coupled mass and energy balances in an open driven system. We apply this model to an intercalation reaction in battery particles with the standard Butler-Volmer reaction rate as well as the first principles-based coupled ion electron transfer to study the stability coupled with the steady state temperature solution of the system [347]. We find there is a breakdown of the model for the traditional Butler-Volmer reaction model because of the exponential growth of current at high overpotentials, which is nonphysical and can be remedied with a first-principles based reaction model [165]. In the Butler-Volmer reaction model, we see that with the increase of the material property Bi, which refers to the ratio of the reaction rate versus the external heat transfer, the stability of the system decreases while the steady state temperature increases, because the reaction rate grows exponentially with the BV model. Meanwhile, using a first principles reaction model that takes into account electron transfer limitations, reaction has little effect on the steady state temperature or the stability of the system. Temperature changes and instabilities in battery systems are a result of transport limitations and not reaction heat in the system. From our general porous electrode calculations, we see that the heat generated from reactions is much smaller than that of other sources. Though there are many factors in temperature increase such as slow diffusion, ohmic heat from resistance buildup, and reaction heat generation from the system, in our

battery temperature models, reactions are not the reason that battery systems are destabilized or temperatures increase. This important conclusion indicates that we can shift our focus in battery thermal modeling to other sources such as Ohmic heat generation, contrary to popular belief in battery models that electrode reactions can be a large heat source [348].

Our general nonisothermal model of coupled mass and energy balances in open driven systems can be generalized to other applications as well. We expect that we can also apply a similar nonisothermal modeling of open driven systems to other systems, such as photocatalysis, electrodeposition, and other systems, where the nonlinear coupling of concentration and temperature will return interesting effects on the stability of the system.

A.7 Appendix: Gibbs Fundamental Equation

To get a temperature balance from our energy balance, a local equilibrium assumption needs to be applied. Assuming local equilibrium in the system, we can start from Gibb's fundamental equation

$$du = Tds + \mathbf{T}^e : d\boldsymbol{\varepsilon} + \sum_i \mu_i dc_i \tag{82}$$

for strain $d\boldsymbol{\varepsilon}$. The definition of the unit volume in the system under deformation needs to be clarified. We can start from the local form of the combined first and second law of thermodynamics for a unit volume, where dv is the deformed unit volume and dv_0 is the unit volume. We can first derive a couple useful equalities that will be used later from the first law of thermodynamics. Within a linear approximation in a unit volume, the dilation of the system is easily found to be [391]

$$dv = ((1 + v_{xx})(1 + v_{yy})(1 + v_{zz}) - 1)\, dv_0 \approx \mathrm{tr}(\nabla \mathbf{u}) dv_0. \tag{83}$$

We separate the stress into deviatoric and dilational portions, $-P\mathbf{I} + \mathbf{T}^p = \mathbf{T}$ where $P = -\frac{1}{3}\mathrm{Tr}(\mathbf{T})$ which is defined from the negative of the average normal stress

[352, 392], and p represents the deviatoric (plastic) stress. As stated earlier, since $\boldsymbol{\varepsilon} = \frac{1}{2}\left(\nabla\mathbf{u} + (\nabla\mathbf{u})^T\right)$ and $\mathbf{T}^e = \mathbf{T} - \mathbf{T}^p \approx \mathbf{T_{RR}} - \mathbf{T}^p$ is a symmetric matrix, we know that the stress-strain term can be completely represented for such an elastic system by the Cauchy stress tensor and and strain as $\nabla\mathbf{u}\colon\ (\mathbf{T_{RR}} - \mathbf{T}^p) = \boldsymbol{\varepsilon}\colon \mathbf{T}^e$ and $d\nabla\mathbf{u}\colon \mathbf{T}^e = d\boldsymbol{\varepsilon}\colon \mathbf{T}^e$. The pressure-volume term (in the linear approximation) for an elastic system can be defined to be

$$-Pd\tilde{v} = -P\mathrm{tr}(d\nabla\mathbf{u}) = (-P\mathbf{I})\colon d\nabla\mathbf{u} = \mathbf{T}^e\colon d\boldsymbol{\varepsilon}. \tag{84}$$

Substituting the differential relations from the entropy relation [354], and by the principles of frame indifference [352], we realize that the entropy is also affected by the different control variables in the system, so that the full differential of entropy is derived as

$$ds = \left.\frac{\partial s}{\partial T}\right|_{c_i,\varepsilon_{kj}} dT + \sum_{k,j}\left.\frac{\partial s}{\partial \varepsilon_{kj}}\right|_{T,c_i,\varepsilon_{x\neq k,y\neq j}} d\varepsilon_{kj} \tag{85}$$

$$+ \sum_i \left.\frac{\partial s}{\partial c_i}\right|_{T,c_{j\neq i},\varepsilon_{kj}} dc_i. \tag{86}$$

Since we know that the stress-strain contributions can be separated in to the deviatoric and and hydrostatic terms, we can separate the full differential of entropy again into

$$ds = \left.\frac{\partial s}{\partial T}\right|_{v,c_i,\varepsilon_{kj}} dT + \sum_{k\neq j}\left.\frac{\partial s}{\partial \varepsilon_{kj}}\right|_{T,c_i,\varepsilon_{x\neq k,y\neq j},v} d\varepsilon_{kj} \tag{87}$$

$$+ \left.\frac{\partial s}{\partial v}\right|_{T,c_i,\varepsilon_{kj}} dv + \sum_i \left.\frac{\partial s}{\partial c_i}\right|_{v,T,c_{j\neq i},\varepsilon_{kj}} dc_i. \tag{88}$$

and the thermodynamic relations $\left.\frac{\partial s}{\partial T}\right|_{v,c_i} = \frac{c_v}{T}$ and $\left.\frac{\partial s}{\partial v}\right|_{T,c_i} = \frac{\alpha}{\kappa_T}$, and $\mu_i + T\left.\frac{\partial s}{\partial c_i}\right|_{v,T,c_{j\neq i}} = h_i$, we can obtain

$$du = c_v dT + \sum_i h_i dc_i + \left(\mathbf{T}^e + T\left(-\frac{\alpha}{\kappa_T}\mathbf{I} + \left.\frac{\partial s}{\partial \boldsymbol{\varepsilon}_{kj}}\right|_{k\neq j}\right)\right) : d\varepsilon, \tag{89}$$

where c_v is the isochoric heat capacity, α is the coefficient of thermal expansion under isobaric circumstances, κ_T is the isothermal compressibility, and h_i is the enthalpy of the system.

If we separate the contributions of the enthalpy effect on the strain, we see that the effects on the strain can be separated into the Gell-Mann matrices in each direction. There are two normal stress states λ_3 and λ_8 which are represented by the , while the remaining 6 matrices are all from the shear stress states. Here we see that for

$$\left.\frac{\partial s}{\partial \varepsilon_{kj}}\right|_{k\neq j} = \sum_{i=1..8, i\neq 3,8} \frac{\beta_i}{S_{T,i}} \tag{90}$$

where β_i is the coefficient of thermal shear deformation in the i direction and $S_{T,i}$ is the isothermal shear compliance [393]. We will define the sum of these terms as

$$du = c_v dT + \sum_i h_i dc_i + \left(\mathbf{T}^e + T\left(-\frac{\alpha}{\kappa_T}\mathbf{I} + \left.\frac{\beta_j}{S_{T_j}}\boldsymbol{\lambda}_j\right|_{j\neq 3,8}\right)\right) : d\varepsilon. \tag{91}$$

Bibliography

[1] Kristen A Severson, Peter M Attia, Norman Jin, Nicholas Perkins, Benben Jiang, Zi Yang, Michael H Chen, Muratahan Aykol, Patrick K Herring, Dimitrios Fraggedakis, et al. Data-driven prediction of battery cycle life before capacity degradation. *Nature Energy*, 4(5):383–391, 2019.

[2] Christoph R Birkl, Matthew R Roberts, Euan McTurk, Peter G Bruce, and David A Howey. Degradation diagnostics for lithium ion cells. *Journal of Power Sources*, 341:373–386, 2017.

[3] Dimitrios Fraggedakis, Neel Nadkarni, Tao Gao, Tingtao Zhou, Yirui Zhang, Yu Han, Ryan M Stephens, Yang Shao-Horn, and Martin Z Bazant. A scaling law to determine phase morphologies during ion intercalation. *Energy & Environmental Science*, 13(7):2142–2152, 2020.

[4] Marc D Berliner, Daniel A Cogswell, Martin Z Bazant, and Richard D Braatz. Methods—petlion: Open-source software for millisecond-scale porous electrode theory-based lithium-ion battery simulations. *Journal of The Electrochemical Society*, 168(9):090504, 2021.

[5] Andrew M Colclasure, Tanvir R Tanim, Andrew N Jansen, Stephen E Trask, Alison R Dunlop, Bryant J Polzin, Ira Bloom, Dave Robertson, LeRoy Flores, Michael Evans, et al. Electrode scale and electrolyte transport effects on extreme fast charging of lithium-ion cells. *Electrochimica Acta*, 337:135854, 2020.

[6] Roland Jung, Michael Metzger, Filippo Maglia, Christoph Stinner, and Hubert A Gasteiger. Oxygen release and its effect on the cycling stability of linixmnycozo2 (nmc) cathode materials for li-ion batteries. *Journal of The Electrochemical Society*, 164(7):A1361, 2017.

[7] Yirui Zhang, Yu Katayama, Ryoichi Tatara, Livia Giordano, Yang Yu, Dimitrios Fraggedakis, Jame Guangwen Sun, Filippo Maglia, Roland Jung, Martin Z Bazant, and Yang Shao-Horn. Revealing electrolyte oxidation via carbonate dehydrogenation on ni-based oxides in li-ion batteries by in situ fourier transform infrared spectroscopy. *Energy & Environmental Science*, 13(1):183–199, 2020.

[8] Yiyang Li, Farid El Gabaly, Todd R Ferguson, Raymond B Smith, Norman C Bartelt, Joshua D Sugar, Kyle R Fenton, Daniel A Cogswell, AL Kilcoyne, Tolek

Tyliszczak, et al. Current-induced transition from particle-by-particle to concurrent intercalation in phase-separating battery electrodes. *Nature materials*, 13(12):1149–1156, 2014.

[9] Kai Xiang, Kaiqi Yang, W Craig Carter, Ming Tang, and Yet-Ming Chiang. Mesoscopic phase transition kinetics in secondary particles of electrode-active materials in lithium-ion batteries. *Chemistry of Materials*, 30(13):4216–4225, 2018.

[10] Todd R Ferguson and Martin Z Bazant. Phase transformation dynamics in porous battery electrodes. *Electrochimica Acta*, 146:89–97, 2014.

[11] Wolfgang Dreyer, Janko Jamnik, Clemens Guhlke, Robert Huth, Jože Moškon, and Miran Gaberšček. The thermodynamic origin of hysteresis in insertion batteries. *Nature materials*, 9(5):448–453, 2010.

[12] Debbie Zhuang and Martin Z Bazant. Theory of layered-oxide cathode degradation in li-ion batteries by oxidation-induced cation disorder. *Journal of The Electrochemical Society*, 2022.

[13] Debbie Zhuang and Martin Z. Bazant. Population effects driving active material degradation in intercalation electrodes. *Phys. Rev. E*, 107:044603, Apr 2023.

[14] Debbie Zhuang and Martin Z Bazant. Scaling analysis of mosaic phase separation in li-ion batteries. *submitted*, 2024.

[15] Debbie Zhuang, Michael Lu Li, Vivek Nath Lam, Richard D Braatz, William Chueh, and Martin Z Bazant. Physics-informed design of hybrid pulse power characterization tests for rechargeable batteries. *J. Electrochem. Soc.*, 2024.

[16] Jinwook Rhyu, Debbie Zhuang, Martin Bazant, and Richard Braatz. Optimum model-based design of diagnostics experiments (doe) with hybrid pulse power characterization (hppc) for lithium-ion batteries. 2024.

[17] Daniel Weber, Đorđije Tripković, Katja Kretschmer, Matteo Bianchini, and Torsten Brezesinski. Surface modification strategies for improving the cycling performance of ni-rich cathode materials. *European Journal of Inorganic Chemistry*, 2020(33):3117–3130, 2020.

[18] Xuekun Lu, Xun Zhang, Chun Tan, Thomas MM Heenan, Marco Lagnoni, Kieran O'Regan, Sohrab Daemi, Antonio Bertei, Helen G Jones, Gareth Hinds, et al. Multi-length scale microstructural design of lithium-ion battery electrodes for improved discharge rate performance. *Energy & Environmental Science*, 14(11):5929–5946, 2021.

[19] Matthew Li, Jun Lu, Zhongwei Chen, and Khalil Amine. 30 years of lithium-ion batteries. *Advanced Materials*, 30(33):1800561, 2018.

[20] Allen J Bard, Larry R Faulkner, and Henry S White. *Electrochemical methods: fundamentals and applications*. John Wiley & Sons, 2022.

[21] Matthew B Pinson and Martin Z Bazant. Theory of sei formation in rechargeable batteries: capacity fade, accelerated aging and lifetime prediction. *Journal of the Electrochemical Society*, 160(2):A243, 2012.

[22] Qianqian Liu, Chunyu Du, Bin Shen, Pengjian Zuo, Xinqun Cheng, Yulin Ma, Geping Yin, and Yunzhi Gao. Understanding undesirable anode lithium plating issues in lithium-ion batteries. *RSC advances*, 6(91):88683–88700, 2016.

[23] William Huang, Peter M Attia, Hansen Wang, Sara E Renfrew, Norman Jin, Supratim Das, Zewen Zhang, David T Boyle, Yuzhang Li, Martin Z Bazant, et al. Evolution of the solid–electrolyte interphase on carbonaceous anodes visualized by atomic-resolution cryogenic electron microscopy. *Nano letters*, 19(8):5140–5148, 2019.

[24] Peter M Attia, Supratim Das, Stephen J Harris, Martin Z Bazant, and William C Chueh. Electrochemical kinetics of sei growth on carbon black: Part i. experiments. *Journal of the Electrochemical Society*, 166(4):E97, 2019.

[25] Supratim Das, Peter M Attia, William C Chueh, and Martin Z Bazant. Electrochemical kinetics of sei growth on carbon black: Part ii. modeling. *Journal of The Electrochemical Society*, 166(4):E107, 2019.

[26] Yunsong Li, Kevin Leung, and Yue Qi. Computational exploration of the li-electrode| electrolyte interface in the presence of a nanometer thick solid-electrolyte interphase layer. *Accounts of chemical research*, 49(10):2363–2370, 2016.

[27] Pengfei Yan, Anmin Nie, Jianming Zheng, Yungang Zhou, Dongping Lu, Xiaofeng Zhang, Rui Xu, Ilias Belharouak, Xiaotao Zu, Jie Xiao, et al. Evolution of lattice structure and chemical composition of the surface reconstruction layer in $Li_{1.2}Ni_{0.2}Mn_{0.6}O_2$ cathode material for lithium ion batteries. *Nano letters*, 15(1):514–522, 2015.

[28] Feng Lin, Isaac M Markus, Dennis Nordlund, Tsu-Chien Weng, Mark D Asta, Huolin L Xin, and Marca M Doeff. Surface reconstruction and chemical evolution of stoichiometric layered cathode materials for lithium-ion batteries. *Nature communications*, 5(1):1–9, 2014.

[29] Peter M Csernica, Samanbir S Kalirai, William E Gent, Kipil Lim, Young-Sang Yu, Yunzhi Liu, Sung-Jin Ahn, Emma Kaeli, Xin Xu, Kevin H Stone, Ann F Marshall, Robert Sinclair, David A Shapiro, Michael F Toney, and William C Chueh. Persistent and partially mobile oxygen vacancies in li-rich layered oxides. *Nature Energy*, 6(6):642–652, 2021.

[30] Chun Zhan, Tianpin Wu, Jun Lu, and Khalil Amine. Dissolution, migration, and deposition of transition metal ions in li-ion batteries exemplified by mn-based cathodes–a critical review. *Energy & Environmental Science*, 11(2):243–257, 2018.

[31] Enrico Trevisanello, Raffael Ruess, Gioele Conforto, Felix H Richter, and Jürgen Janek. Polycrystalline and single crystalline ncm cathode materials—quantifying particle cracking, active surface area, and lithium diffusion. *Advanced Energy Materials*, 11(18):2003400, 2021.

[32] Hena Das, Alexander Urban, Wenxuan Huang, and Gerbrand Ceder. First-principles simulation of the (li–ni–vacancy) o phase diagram and its relevance for the surface phases in ni-rich li-ion cathode materials. *Chemistry of Materials*, 29(18):7840–7851, 2017.

[33] Arup Chakraborty, Sooraj Kunnikuruvan, Sandeep Kumar, Boris Markovsky, Doron Aurbach, Mudit Dixit, and Dan Thomas Major. Layered cathode materials for lithium-ion batteries: Review of computational studies on lini1–x–y co x mn y o2 and lini1–x–y co x al y o2. *Chemistry of Materials*, 32(3):915–952, 2020.

[34] Abir Ghosh, Jamie M Foster, Gregory Offer, and Monica Marinescu. A shrinking-core model for the degradation of high-nickel cathodes (nmc811) in li-ion batteries: passivation layer growth and oxygen evolution. *Journal of The Electrochemical Society*, 168(2):020509, 2021.

[35] Jin-Myoung Lim, Hyungjun Kim, Kyeongjae Cho, and Maenghyo Cho. Fundamental mechanisms of fracture and its suppression in ni-rich layered cathodes: Mechanics-based multiscale approaches. *Extreme Mechanics Letters*, 22:98–105, 2018.

[36] Bo Xu, Christopher R Fell, Miaofang Chi, and Ying Shirley Meng. Identifying surface structural changes in layered li-excess nickel manganese oxides in high voltage lithium ion batteries: A joint experimental and theoretical study. *Energy & Environmental Science*, 4(6):2223–2233, 2011.

[37] Carlos Pastor-Fernández, Tung Fai Yu, W Dhammika Widanage, and James Marco. Critical review of non-invasive diagnosis techniques for quantification of degradation modes in lithium-ion batteries. *Renewable and Sustainable Energy Reviews*, 109:138–159, 2019.

[38] Jingliang Zhang and Jay Lee. A review on prognostics and health monitoring of Li-ion battery. *J. Power Sources*, 196(15):6007–6014, 2011.

[39] Juner Zhu, Ian Mathews, Dongsheng Ren, Wei Li, Daniel Cogswell, Bobin Xing, Tobias Sedlatschek, Sai Nithin R Kantareddy, Mengchao Yi, Tao Gao, et al. End-of-life or second-life options for retired electric vehicle batteries. *Cell Reports Physical Science*, 2(8):100537, 2021.

[40] Xiaowei Ma, Jessie E Harlow, Jing Li, Lin Ma, David S Hall, Samuel Buteau, Matthew Genovese, Marc Cormier, and JR Dahn. Hindering rollover failure of li [ni0. 5mn0. 3co0. 2] o2/graphite pouch cells during long-term cycling. *Journal of The Electrochemical Society*, 166(4):A711, 2019.

[41] Aravinda R Mandli, Anshul Kaushik, Rajkumar S Patil, Arunava Naha, Krishnan S Hariharan, Subramanya M Kolake, Seongho Han, and Wooin Choi. Analysis of the effect of resistance increase on the capacity fade of lithium ion batteries. *International Journal of Energy Research*, 43(6):2044–2056, 2019.

[42] Qunwei Wu, Wenquan Lu, and Jai Prakash. Characterization of a commercial size cylindrical Li-ion cell with a reference electrode. *Journal of Power Sources*, 88(2):237–242, 2000.

[43] John Newman and Nitash P Balsara. *Electrochemical Systems*. John Wiley & Sons, Hoboken, NJ, fourth edition, 2021.

[44] Raymond B Smith and Martin Z Bazant. Multiphase porous electrode theory. *Journal of The Electrochemical Society*, 164(11):E3291, 2017.

[45] Marcello Torchio, Lalo Magni, R Bhushan Gopaluni, Richard D Braatz, and Davide M Raimondo. Lionsimba: A Matlab framework based on a finite volume model suitable for Li-ion battery design, simulation, and control. *Journal of The Electrochemical Society*, 163(7):A1192, 2016.

[46] Rahul Malik, Damian Burch, Martin Bazant, and Gerbrand Ceder. Particle size dependence of the ionic diffusivity. *Nano letters*, 10(10):4123–4127, 2010.

[47] Lars Ole Valøen and Jan N Reimers. Transport properties of $LiPF_6$-based Li-ion battery electrolytes. *Journal of The Electrochemical Society*, 152(5):A882, 2005.

[48] Meng Guo, Godfrey Sikha, and Ralph E White. Single-particle model for a lithium-ion cell: Thermal behavior. *Journal of The Electrochemical Society*, 158(2):A122, 2010.

[49] Jungjin Park, Hongbo Zhao, Stephen Dongmin Kang, Kipil Lim, Chia-Chin Chen, Young-Sang Yu, Richard D Braatz, David A Shapiro, Jihyun Hong, Michael F Toney, Martin Z Bazant, and William C Chueh. Fictitious phase separation in li layered oxides driven by electro-autocatalysis. *Nature Materials*, 20(7):991–999, 2021.

[50] Hongbo Zhao, Haitao Dean Deng, Alexander E Cohen, Jongwoo Lim, Yiyang Li, Dimitrios Fraggedakis, Benben Jiang, Brian D Storey, William C Chueh, Richard D Braatz, et al. Learning heterogeneous reaction kinetics from x-ray videos pixel by pixel. *Nature*, 621(7978):289–294, 2023.

[51] Hongbo Zhao and Martin Z Bazant. Population dynamics of driven autocatalytic reactive mixtures. *Physical Review E*, 100(1):012144, 2019.

[52] Peng Bai and Guangyu Tian. Statistical kinetics of phase-transforming nanoparticles in lifepo4 porous electrodes. *Electrochimica Acta*, 89:644–651, 2013.

[53] Marc Doyle, Thomas F Fuller, and John Newman. Modeling of galvanostatic charge and discharge of the lithium/polymer/insertion cell. *Journal of the Electrochemical society*, 140(6):1526, 1993.

[54] Thomas F Fuller, Marc Doyle, and John Newman. Simulation and optimization of the dual lithium ion insertion cell. *Journal of the Electrochemical Society*, 141(1):1, 1994.

[55] Todd R Ferguson and Martin Z Bazant. Nonequilibrium thermodynamics of porous electrodes. *Journal of The Electrochemical Society*, 159(12):A1967, 2012.

[56] Seung-Taek Myung, Filippo Maglia, Kang-Joon Park, Chong Seung Yoon, Peter Lamp, Sung-Jin Kim, and Yang-Kook Sun. Nickel-rich layered cathode materials for automotive lithium-ion batteries: achievements and perspectives. *ACS Energy Letters*, 2(1):196–223, 2017.

[57] Arumugam Manthiram, James C Knight, Seung-Taek Myung, Seung-Min Oh, and Yang-Kook Sun. Nickel-rich and lithium-rich layered oxide cathodes: progress and perspectives. *Advanced Energy Materials*, 6(1):1501010, 2016.

[58] Lucia Mancini, Nicolas A Eslava, Marzia Traverso, Fabrice Mathieux, et al. Responsible and sustainable sourcing of battery raw materials. *Publications Office of the European Union: Luxembourg*, 2020.

[59] Yuwei Mao, Xuelong Wang, Sihao Xia, Kai Zhang, Chenxi Wei, Seongmin Bak, Zulipiya Shadike, Xuejun Liu, Yang Yang, Rong Xu, Piero Pianetta, Stefano Ermon, Eli Stavitski, Kejie Zhao, Zhengrui Xu, Feng Lin, Xiao-Qing Yang, Enyuan Hu, and Yijin Liu. High-voltage charging-induced strain, heterogeneity, and micro-cracks in secondary particles of a nickel-rich layered cathode material. *Advanced Functional Materials*, 29(18):1900247, 2019.

[60] Pengfei Yan, Jianming Zheng, Ji-Guang Zhang, and Chongmin Wang. Atomic resolution structural and chemical imaging revealing the sequential migration of ni, co, and mn upon the battery cycling of layered cathode. *Nano letters*, 17(6):3946–3951, 2017.

[61] Penghao Xiao, Tan Shi, Wenxuan Huang, and Gerbrand Ceder. Understanding surface densified phases in ni-rich layered compounds. *ACS Energy Letters*, 4(4):811–818, 2019.

[62] Daniel Harvey Doughty and Chris C Crafts. Freedomcar: Electrical energy storage system abuse test manual for electric and hybrid electric vehicle applications. Technical report, Sandia National Laboratories, Albuquerque, NM, and Livermore, CA, 2006.

[63] Yoshiki Kuramoto. International symposium on mathematical problems in theoretical physics. *Lecture notes in Physics*, 30:420, 1975.

[64] Michael M Desai and Daniel S Fisher. Beneficial mutation–selection balance and the effect of linkage on positive selection. *Genetics*, 176(3):1759–1798, 2007.

[65] Yang Sun, Zhenzhong Yang, Lin Gu, Yong Chen, Haoshen Zhou, et al. Electrochemical oscillation in li-ion batteries. *Joule*, 2(7):1265–1277, 2018.

[66] Hannes Risken. Fokker-planck equation. In *The Fokker-Planck Equation*, pages 63–95. Springer, 1996.

[67] Peng Bai, Daniel A Cogswell, and Martin Z Bazant. Suppression of phase separation in lifepo4 nanoparticles during battery discharge. *Nano letters*, 11(11):4890–4896, 2011.

[68] Raymond B Smith, Edwin Khoo, and Martin Z Bazant. Intercalation kinetics in multiphase-layered materials. *The Journal of Physical Chemistry C*, 121(23):12505–12523, 2017.

[69] Martin Z Bazant. Theory of chemical kinetics and charge transfer based on nonequilibrium thermodynamics. *Accounts of chemical research*, 46(5):1144–1160, 2013.

[70] Wolfgang Dreyer, Clemens Guhlke, and Robert Huth. The behavior of a many-particle electrode in a lithium-ion battery. *Physica D: Nonlinear Phenomena*, 240(12):1008–1019, 2011.

[71] A J Smith, J Chris Burns, Xuemei Zhao, Deijun Xiong, and J R Dahn. A high precision coulometry study of the SEI growth in Li/graphite cells. *Journal of The Electrochemical Society*, 158(5):A447, 2011.

[72] A J Smith, J C Burns, D Xiong, and J R Dahn. Interpreting high precision coulometry results on Li-ion cells. *Journal of The Electrochemical Society*, 158(10):A1136, 2011.

[73] J Ross Macdonald. Impedance spectroscopy. *Annals of biomedical engineering*, 20:289–305, 1992.

[74] Dennis Dees, Evren Gunen, Daniel Abraham, Andrew Jansen, and Jai Prakash. Electrochemical modeling of lithium-ion positive electrodes during hybrid pulse power characterization tests. *Journal of The Electrochemical Society*, 155(8):A603, 2008.

[75] Stephen Dongmin Kang and William C Chueh. Galvanostatic intermittent titration technique reinvented: Part I. A critical review. *Journal of The Electrochemical Society*, 168(12):120504, 2021.

[76] Stephen Dongmin Kang, Jimmy Jiahong Kuo, Nidhi Kapate, Jihyun Hong, Joonsuk Park, and William C Chueh. Galvanostatic intermittent titration technique reinvented: Part II. Experiments. *Journal of The Electrochemical Society*, 168(12):120503, 2021.

[77] Dawn M Bernardi and Joo-Young Go. Analysis of pulse and relaxation behavior in lithium-ion batteries. *Journal of Power Sources*, 196(1):412–427, 2011.

[78] B K Purushothaman and U Landau. Rapid charging of lithium-ion batteries using pulsed currents: A theoretical analysis. *Journal of The Electrochemical Society*, 153(3):A533, 2006.

[79] Jie Li, Xiaodong Wu, Min Xu, and Yonggang Liu. A real-time optimization energy management of range extended electric vehicles for battery lifetime and energy consumption. *Journal of Power Sources*, 498:229939, 2021.

[80] M Stanley Whittingham. Lithium batteries and cathode materials. *Chemical reviews*, 104(10):4271–4302, 2004.

[81] MM Kabir and Dervis Emre Demirocak. Degradation mechanisms in li-ion batteries: a state-of-the-art review. *International Journal of Energy Research*, 41(14):1963–1986, 2017.

[82] Ming Jiang, Dmitri L Danilov, Rüdiger-A Eichel, and Peter HL Notten. A review of degradation mechanisms and recent achievements for ni-rich cathode-based li-ion batteries. *Advanced Energy Materials*, page 2103005, 2021.

[83] Tianyu Li, Xiao-Zi Yuan, Lei Zhang, Datong Song, Kaiyuan Shi, and Christina Bock. Degradation mechanisms and mitigation strategies of nickel-rich nmc-based lithium-ion batteries. *Electrochemical Energy Reviews*, 3(1):43–80, 2020.

[84] Hyung-Joo Noh, Sungjune Youn, Chong Seung Yoon, and Yang-Kook Sun. Comparison of the structural and electrochemical properties of layered li [nixcoymnz] o2 (x= 1/3, 0.5, 0.6, 0.7, 0.8 and 0.85) cathode material for lithium-ion batteries. *Journal of power sources*, 233:121–130, 2013.

[85] Thomas MM Heenan, Aaron Wade, Chun Tan, Julia E Parker, Dorota Matras, Andrew S Leach, James B Robinson, Alice Llewellyn, Alexander Dimitrijevic, Rhodri Jervis, Paul D Quinn, Dan J L Brett, and Paul R Shearing. Identifying the origins of microstructural defects such as cracking within ni-rich nmc811 cathode particles for lithium-ion batteries. *Advanced Energy Materials*, 10(47):2002655, 2020.

[86] Marco Evertz, Fabian Horsthemke, Johannes Kasnatscheew, Markus Boerner, Martin Winter, and Sascha Nowak. Unraveling transition metal dissolution of li1. 04ni1/3co1/3mn1/3o2 (ncm 111) in lithium ion full cells by using the total reflection x-ray fluorescence technique. *Journal of power sources*, 329:364–371, 2016.

[87] Johannes Wandt, Anna Freiberg, Rowena Thomas, Yelena Gorlin, Armin Siebel, Roland Jung, Hubert A Gasteiger, and Moniek Tromp. Transition metal dissolution and deposition in li-ion batteries investigated by operando x-ray absorption spectroscopy. *Journal of Materials Chemistry A*, 4(47):18300–18305, 2016.

[88] Honghe Zheng, Qingna Sun, Gao Liu, Xiangyun Song, and Vincent S Battaglia. Correlation between dissolution behavior and electrochemical cycling performance for lini1/3co1/3mn1/3o2-based cells. *Journal of Power Sources*, 207:134–140, 2012.

[89] Joshua P Pender, Gaurav Jha, Duck Hyun Youn, Joshua M Ziegler, Ilektra Andoni, Eric J Choi, Adam Heller, Bruce S Dunn, Paul S Weiss, Reginald M Penner, and C Buddie Mullins. Electrode degradation in lithium-ion batteries. *ACS nano*, 14(2):1243–1295, 2020.

[90] Lars von Kolzenberg, Arnulf Latz, and Birger Horstmann. Solid–electrolyte interphase during battery cycling: Theory of growth regimes. *ChemSusChem*, 13(15):3901, 2020.

[91] Tao Gao, Yu Han, Dimitrios Fraggedakis, Supratim Das, Tingtao Zhou, Che-Ning Yeh, Shengming Xu, William C Chueh, Ju Li, and Martin Z Bazant. Interplay of lithium intercalation and plating on a single graphite particle. *Joule*, 5(2):393–414, 2021.

[92] Donal P Finegan, Alexander Quinn, David S Wragg, Andrew M Colclasure, Xuekun Lu, Chun Tan, Thomas MM Heenan, Rhodri Jervis, Dan JL Brett, Supratim Das, Tao Gao, Daniel A Cogswell, Martin Z Bazant, Marco Di Michiel, Stefano Checcia, Paul R Shearing, and Kandler Smith. Spatial dynamics of lithiation and lithium plating during high-rate operation of graphite electrodes. *Energy & Environmental Science*, 13(8):2570–2584, 2020.

[93] Pouyan Shafiei Sabet, Alexander Johannes Warnecke, Frank Meier, Heiko Witzenhausen, Egoitz Martinez-Laserna, and Dirk Uwe Sauer. Non-invasive yet separate investigation of anode/cathode degradation of lithium-ion batteries (nickel–cobalt–manganese vs. graphite) due to accelerated aging. *Journal of Power Sources*, 449:227369, 2020.

[94] Hirbod Maleki Kheimeh Sari and Xifei Li. Controllable cathode–electrolyte interface of li [ni0. 8co0. 1mn0. 1] o2 for lithium ion batteries: a review. *Advanced Energy Materials*, 9(39):1901597, 2019.

[95] Guannan Qian, Jin Zhang, Sheng-Qi Chu, Jizhou Li, Kai Zhang, Qingxi Yuan, Zi-Feng Ma, Piero Pianetta, Linsen Li, Keeyoung Jung, and Yijin Liu. Understanding the mesoscale degradation in nickel-rich cathode materials through machine-learning-revealed strain–redox decoupling. *ACS Energy Letters*, 6(2):687–693, 2021.

[96] Sanghun Lee and Sung Soo Park. Atomistic simulation study of mixed-metal oxide (lini1/3co1/3mn1/3o2) cathode material for lithium ion battery. *The Journal of Physical Chemistry C*, 116(10):6484–6489, 2012.

[97] Wu Li, JN Reimers, and JR Dahn. Crystal structure of li x ni 2- x o 2 and a lattice-gas model for the order-disorder transition. *Physical Review B*, 46(6):3236, 1992.

[98] Gerbrand Ceder and Anton Van der Ven. Phase diagrams of lithium transition metal oxides: investigations from first principles. *Electrochimica Acta*, 45(1-2):131–150, 1999.

[99] A Rougier, P Gravereau, and C Delmas. Optimization of the composition of the li1- z ni1+ z o 2 electrode materials: structural, magnetic, and electrochemical studies. *Journal of The Electrochemical Society*, 143(4):1168, 1996.

[100] Katharina Marker, Philip J Reeves, Chao Xu, Kent J Griffith, and Clare P Grey. Evolution of structure and lithium dynamics in lini0. 8mn0. 1co0. 1o2 (nmc811) cathodes during electrochemical cycling. *Chemistry of Materials*, 31(7):2545–2554, 2019.

[101] S Sallis, N Pereira, P Mukherjee, NF Quackenbush, N Faenza, C Schlueter, T-L Lee, WL Yang, F Cosandey, GG Amatucci, and Louis FJ Piper. Surface degradation of li1–x ni0. 80co0. 15al0. 05o2 cathodes: Correlating charge transfer impedance with surface phase transformations. *Applied Physics Letters*, 108(26):263902, 2016.

[102] Chao Xu, Katharina Märker, Juhan Lee, Amoghavarsha Mahadevegowda, Philip J Reeves, Sarah J Day, Matthias F Groh, Steffen P Emge, Caterina Ducati, B Layla Mehdi, Chiu C Tang, and Clare P Grey. Bulk fatigue induced by surface reconstruction in layered ni-rich cathodes for li-ion batteries. *Nature Materials*, 20(1):84–92, 2021.

[103] Mudit Dixit, Boris Markovsky, Florian Schipper, Doron Aurbach, and Dan T Major. Origin of structural degradation during cycling and low thermal stability of ni-rich layered transition metal-based electrode materials. *The journal of physical chemistry C*, 121(41):22628–22636, 2017.

[104] Jian Zhu, Soroosh Sharifi-Asl, Juan C Garcia, Hakim H Iddir, Jason R Croy, Reza Shahbazian-Yassar, and Guoying Chen. Atomic-level understanding of surface reconstruction based on li [ni x mn y co1–x–y] o2 single-crystal studies. *ACS Applied Energy Materials*, 3(5):4799–4811, 2020.

[105] Dong-Su Ko, Jun-Ho Park, Byong Yong Yu, Docheon Ahn, Kihong Kim, Heung Nam Han, Woo Sung Jeon, Changhoon Jung, and Arumugram Manthiram. Degradation of high-nickel-layered oxide cathodes from surface to bulk: A comprehensive structural, chemical, and electrical analysis. *Advanced Energy Materials*, 10(36):2001035, 2020.

[106] Jinhyuk Lee, Alexander Urban, Xin Li, Dong Su, Geoffroy Hautier, and Gerbrand Ceder. Unlocking the potential of cation-disordered oxides for rechargeable lithium batteries. *science*, 343(6170):519–522, 2014.

[107] Yukinori Koyama, Yoshinari Makimura, Isao Tanaka, Hirohiko Adachi, and Tsutomu Ohzuku. Systematic research on insertion materials based on superlattice models in a phase triangle of licoo2 linio2 limno2: I. first-principles calculation on electronic and crystal structures, phase stability and new material. *Journal of The Electrochemical Society*, 151(9):A1499, 2004.

[108] Zachary J Schiffer and Karthish Manthiram. Electrification and decarbonization of the chemical industry. *Joule*, 1(1):10–14, 2017.

[109] Ting Wang, Keliang Ren, Wei Xiao, Wenhao Dong, Huali Qiao, Anran Duan, Hongyu Pan, Yang Yang, and Hailong Wang. Tuning the li/ni disorder of the nmc811 cathode by thermally driven competition between lattice ordering and structure decomposition. *The Journal of Physical Chemistry C*, 124(10):5600–5607, 2020.

[110] Jiajun Chen and Jason Graetz. Study of antisite defects in hydrothermally prepared lifepo4 by in situ x-ray diffraction. *ACS applied materials & interfaces*, 3(5):1380–1384, 2011.

[111] Naoaki Yabuuchi, Sundeep Kumar, Hayley H Li, Yong-Tae Kim, and Yang Shao-Horn. Changes in the crystal structure and electrochemical properties of li x ni0. 5mn0. 5o2 during electrochemical cycling to high voltages. *Journal of the Electrochemical Society*, 154(6):A566, 2007.

[112] Huiwen Ji, Alexander Urban, Daniil A Kitchaev, Deok-Hwang Kwon, Nongnuch Artrith, Colin Ophus, Wenxuan Huang, Zijian Cai, Tan Shi, Jae Chul Kim, Haegyeom Kim, and Gerbrand Ceder. Hidden structural and chemical order controls lithium transport in cation-disordered oxides for rechargeable batteries. *Nature communications*, 10(1):1–9, 2019.

[113] Paul Shewmon. *Diffusion in solids*. Springer, 2016.

[114] Helmut Mehrer. *Diffusion in solids: fundamentals, methods, materials, diffusion-controlled processes*, volume 155. Springer Science & Business Media, 2007.

[115] Charles Kittel, Paul McEuen, and Paul McEuen. *Introduction to solid state physics*, volume 8. Wiley New York, 1996.

[116] John Michael Kosterlitz and David James Thouless. Ordering, metastability and phase transitions in two-dimensional systems. *Journal of Physics C: Solid State Physics*, 6(7):1181, 1973.

[117] Mehran Kardar. *Statistical physics of fields*. Cambridge University Press, 2007.

[118] Kyoungmin Min, Kihong Kim, Changhoon Jung, Seung-Woo Seo, You Young Song, Hyo Sug Lee, Jaikwang Shin, and Eunseog Cho. A comparative study of structural changes in lithium nickel cobalt manganese oxide as a function of ni content during delithiation process. *Journal of Power Sources*, 315:111–119, 2016.

[119] Donald Bashford and David A Case. Generalized born models of macromolecular solvation effects. *Annual review of physical chemistry*, 51(1):129–152, 2000.

[120] JM Zheng, ZR Zhang, XB Wu, ZX Dong, Z Zhu, and Y Yang. The effects of alf3 coating on the performance of li [li0. 2mn0. 54ni0. 13co0. 13] o2 positive electrode material for lithium-ion battery. *Journal of The Electrochemical Society*, 155(10):A775, 2008.

[121] John Reed and Gerbrand Ceder. Role of electronic structure in the susceptibility of metastable transition-metal oxide structures to transformation. *Chemical reviews*, 104(10):4513–4534, 2004.

[122] John Newman and Karen E Thomas-Alyea. *Electrochemical systems*. John Wiley & Sons, 2012.

[123] Rudolph A Marcus. On the theory of oxidation-reduction reactions involving electron transfer. i. *The Journal of chemical physics*, 24(5):966–978, 1956.

[124] Rudolph A Marcus. Chemical and electrochemical electron-transfer theory. *Annual review of physical chemistry*, 15(1):155–196, 1964.

[125] Noel Sydney Hush. Adiabatic theory of outer sphere electron-transfer reactions in solution. *Transactions of the Faraday Society*, 57:557–580, 1961.

[126] Christopher ED Chidsey. Free energy and temperature dependence of electron transfer at the metal-electrolyte interface. *Science*, 251(4996):919–922, 1991.

[127] Peng Bai and Martin Z Bazant. Charge transfer kinetics at the solid–solid interface in porous electrodes. *Nature communications*, 5(1):3585, 2014.

[128] Dimitrios Fraggedakis, Michael McEldrew, Raymond B Smith, Yamini Krishnan, Yirui Zhang, Peng Bai, William C Chueh, Yang Shao-Horn, and Martin Z Bazant. Theory of coupled ion-electron transfer kinetics. *Electrochimica Acta*, 367:137432, 2021.

[129] Yirui Zhang, Dimitrios Fraggedakis, Tao Gao, Shakul Pathak, Debbie Zhuang, Cristina Grosu, Yash Samantaray, Armando RC Neto, Sravani R Duggirala, Botao Huang, et al. Lithium-ion intercalation by coupled ion-electron transfer. *ChemRxiv*, 2024.

[130] John David Jackson. Classical electrodynamics, 1999.

[131] Chun-Chieh Chang, Jin Yong Kim, and Prashant N Kumta. Synthesis and electrochemical characterization of divalent cation-incorporated lithium nickel oxide. *Journal of the Electrochemical Society*, 147(5):1722, 2000.

[132] Arumugam Manthiram, Katharine Chemelewski, and Eun-Sung Lee. A perspective on the high-voltage limn 1.5 ni 0.5 o 4 spinel cathode for lithium-ion batteries. *Energy & Environmental Science*, 7(4):1339–1350, 2014.

[133] Michael P Mercer, Sophie Finnigan, Denis Kramer, Daniel Richards, and Harry E Hoster. The influence of point defects on the entropy profiles of lithium ion battery cathodes: a lattice-gas monte carlo study. *Electrochimica Acta*, 241:141–152, 2017.

[134] Aziz Abdellahi, Alexander Urban, Stephen Dacek, and Gerbrand Ceder. Understanding the effect of cation disorder on the voltage profile of lithium transition-metal oxides. *Chemistry of Materials*, 28(15):5373–5383, 2016.

[135] Yuan Gao, JN Reimers, and JR Dahn. Changes in the voltage profile of li/li 1+ x mn 2- x o 4 cells as a function of x. *Physical Review B*, 54(6):3878, 1996.

[136] W Li, JN Reimers, and JR Dahn. Lattice-gas-model approach to understanding the structures of lithium transition-metal oxides lim o 2. *Physical Review B*, 49(2):826, 1994.

[137] Juan C Garcia, Javier Bareño, Guoying Chen, Jason R Croy, and Hakim Iddir. Strain-driven surface reconstruction and cation segregation in layered li (ni 1-x- y mn x co y) o 2 (nmc) cathode materials. *Physical Chemistry Chemical Physics*, 22(42):24490–24497, 2020.

[138] RJ Clément, Z Lun, and G Ceder. Cation-disordered rocksalt transition metal oxides and oxyfluorides for high energy lithium-ion cathodes. *Energy & Environmental Science*, 13(2):345–373, 2020.

[139] Philippe Knauth and Harry L Tuller. Solid-state ionics: roots, status, and future prospects. *Journal of the American Ceramic Society*, 85(7):1654–1680, 2002.

[140] Colin R Groom, Ian J Bruno, Matthew P Lightfoot, and Suzanna C Ward. The cambridge structural database. *Acta Crystallographica Section B: Structural Science, Crystal Engineering and Materials*, 72(2):171–179, 2016.

[141] Clare F Macrae, Ioana Sovago, Simon J Cottrell, Peter TA Galek, Patrick McCabe, Elna Pidcock, Michael Platings, Greg P Shields, Joanna S Stevens, Matthew Towler, and Peter A Wood. Mercury 4.0: From visualization to analysis, design and prediction. *Journal of applied crystallography*, 53(1):226–235, 2020.

[142] Jacob N Israelachvili. *Intermolecular and surface forces*. Academic press, 2015.

[143] A Louis Allred and Eugene G Rochow. A scale of electronegativity based on electrostatic force. *Journal of Inorganic and Nuclear Chemistry*, 5(4):264–268, 1958.

[144] Anubhav Jain, Shyue Ping Ong, Geoffroy Hautier, Wei Chen, William Davidson Richards, Stephen Dacek, Shreyas Cholia, Dan Gunter, David Skinner, Gerbrand Ceder, and Kristin a. Persson. Commentary: The Materials Project: A materials genome approach to accelerating materials innovation. *APL Materials*, 1(1):011002, 2013.

[145] Anubhav Jain, Shyue Ping Ong, Geoffroy Hautier, Wei Chen, William Davidson Richards, Stephen Dacek, Shreyas Cholia, Dan Gunter, David Skinner, Gerbrand Ceder, and Kristin a. Persson. The Materials Project: A materials genome approach to accelerating materials innovation. *APL Materials*, 1(1):011002, 2013.

[146] So. Laubach, St. Laubach, P.C. Schmidt, D. Ensling, S. Schmid, W. Jaegermann, A. Thissen, K. Nikolowski, and H. Ehrenberg. Changes in the crystal and electronic structure of li co o2 and li ni o2 upon li intercalation and de-intercalation. *Physical Chemistry Chemical Physics*, 11:3278–3289, 2009.

[147] A. Hirano, R. Kanno, Y. Kawamoto, Y. Takeda, K. Yamaura, M. Takano, K. Ohyama, M. Ohashi, and Y. Yamaguchi. Relationship between non-stoichiometry and physical properties in li ni o2. *Solid State Ionics*, 78:123–131, 1995.

[148] Dyah S. Adipranoto, Toru Ishigaki, Akinori Hoshikawa, Kenji Iwase, Masao Yonemura, Kazuhiro Mori, Takashi Kamiyama, Yukio Morii, and Makoto Hayashi. Neutron diffraction studies on structural effect for ni-doping in lico1-xnixo2. *Solid State Ionics*, 262:92–97, 2014.

[149] Gunnar A Niklasson, Rajeev Ahuja, and Maria StrØMme. Electronic states in intercalation materials studied by electrochemical techniques. *Modern Physics Letters B*, 20(15):863–875, 2006.

[150] CJF Bottcher. Theory of electric polarization (am sterdam, 1973.

[151] Lev Davidovich Landau, JS Bell, MJ Kearsley, LP Pitaevskii, EM Lifshitz, and JB Sykes. *Electrodynamics of continuous media*, volume 8. elsevier, 2013.

[152] Masahiro Yamamoto. charge-charge, charge-dipole, dipole-charge, dipole-dipole interaction. *Dept. of Energy and Hydrocarbon Chemistry, Graduate School of Engineering, Kyoto University, Kyoto*, 2008.

[153] N Iyi, K Kitamura, F Izumi, JK Yamamoto, T Hayashi, H Asano, and S Kimura. Ceramics and inorganic crystals for optics, electro-optics, and nonlinear conversion (1988)/85. comparative study of defect structures in lithium niobate with different compositions. *J. Solid State Chem*, 101:340, 1992.

[154] MN Palatnikov, NV Sidorov, VI Skiba, DV Makarov, IV Biryukova, Yu A Serebryakov, OE Kravchenko, Yu I Balabanov, and VT Kalinnikov. Effects of nonstoichiometry and doping on the curie temperature and defect structure of lithium niobate. *Inorganic Materials*, 36(5):489–493, 2000.

[155] D Xue and K Kitamura. Dielectric characterization of the defect concentration in lithium niobate single crystals. vol. 122. *Solid State Commun*, pages 00180–1, 2002.

[156] Robert D Shannon. Dielectric polarizabilities of ions in oxides and fluorides. *Journal of Applied physics*, 73(1):348–366, 1993.

[157] Howard Coker. Empirical free-ion polarizabilities of the alkali metal, alkaline earth metal, and halide ions. *The Journal of Physical Chemistry*, 80(19):2078–2084, 1976.

[158] GJ Wilson, RK Chan, DW Davidson, and E Whalley. Dielectric properties of ices ii, iii, v, and vi. *The journal of chemical physics*, 43(7):2384–2391, 1965.

[159] GH Jonker and JH Van Santen. De dielectrische eigenschappen van titanaten van het perofskiet-type. *Chem Weekbl*, 43:672–679, 1947.

[160] Peter V Sushko, Kevin M Rosso, Ji-Guang Zhang, Jun Liu, and Maria L Sushko. Oxygen vacancies and ordering of d-levels control voltage suppression in oxide cathodes: the case of spinel lini0. 5mn1. 5o4-δ. *Advanced Functional Materials*, 23(44):5530–5535, 2013.

[161] Dilip Kondepudi and Ilya Prigogine. *Modern thermodynamics: from heat engines to dissipative structures*. John Wiley & Sons, 2014.

[162] Sybren Ruurds De Groot and Peter Mazur. *Non-equilibrium thermodynamics*. Courier Corporation, 2013.

[163] Kisuk Kang and Gerbrand Ceder. Factors that affect li mobility in layered lithium transition metal oxides. *Physical Review B*, 74(9):094105, 2006.

[164] Martin Z Bazant. Thermodynamic stability of driven open systems and control of phase separation by electro-autocatalysis. *Faraday discussions*, 199:423–463, 2017.

[165] Dimitrios Fraggedakis and Martin Z Bazant. Tuning the stability of electrochemical interfaces by electron transfer reactions. *The Journal of chemical physics*, 152(18):184703, 2020.

[166] Yi Zeng, Raymond B Smith, Peng Bai, and Martin Z Bazant. Simple formula for marcus–hush–chidsey kinetics. *Journal of Electroanalytical Chemistry*, 735:77–83, 2014.

[167] Pengfei Yan, Jianming Zheng, Zhen-Kun Tang, Arun Devaraj, Guoying Chen, Khalil Amine, Ji-Guang Zhang, Li-Min Liu, and Chongmin Wang. Injection of oxygen vacancies in the bulk lattice of layered cathodes. *Nature nanotechnology*, 14(6):602–608, 2019.

[168] Jianming Zheng, Pengfei Yan, Jiandong Zhang, Mark H Engelhard, Zihua Zhu, Bryant J Polzin, Steve Trask, Jie Xiao, Chongmin Wang, and Jiguang Zhang. Suppressed oxygen extraction and degradation of lini x mn y co z o 2 cathodes at high charge cut-off voltages. *Nano Research*, 10(12):4221–4231, 2017.

[169] Julien Bréger, Ying S Meng, Yoyo Hinuma, Sundeep Kumar, Kisuk Kang, Yang Shao-Horn, Gerbrand Ceder, and Clare P Grey. Effect of high voltage on the structure and electrochemistry of lini0. 5mn0. 5o2: A joint experimental and theoretical study. *Chemistry of materials*, 18(20):4768–4781, 2006.

[170] Debasish Mohanty, Jianlin Li, Shrikant C Nagpure, David L Wood, and Claus Daniel. Understanding the structure and structural degradation mechanisms in high-voltage, lithium-manganese–rich lithium-ion battery cathode oxides: A review of materials diagnostics. *MRS Energy & Sustainability*, 2, 2015.

[171] Roland Jung, Philipp Strobl, Filippo Maglia, Christoph Stinner, and Hubert A Gasteiger. Temperature dependence of oxygen release from lini0. 6mn0. 2co0. 2o2 (nmc622) cathode materials for li-ion batteries. *Journal of The Electrochemical Society*, 165(11):A2869, 2018.

[172] Gui-Liang Xu, Xiang Liu, Amine Daali, Rachid Amine, Zonghai Chen, and Khalil Amine. Challenges and strategies to advance high-energy nickel-rich layered lithium transition metal oxide cathodes for harsh operation. *Advanced Functional Materials*, 30(46):2004748, 2020.

[173] Fantai Kong, Chaoping Liang, Luhua Wang, Yongping Zheng, Sahila Perananthan, Roberto C Longo, John P Ferraris, Moon Kim, and Kyeongjae Cho. Kinetic stability of bulk linio2 and surface degradation by oxygen evolution in linio2-based cathode materials. *Advanced Energy Materials*, 9(2):1802586, 2019.

[174] Pinar Karayaylali, Ryoichi Tatara, Yirui Zhang, Kuei-Lin Chan, Yang Yu, Livia Giordano, Filippo Maglia, Roland Jung, Isaac Lund, and Yang Shao-Horn. Coating-dependent electrode-electrolyte interface for ni-rich positive electrodes in li-ion batteries. *Journal of The Electrochemical Society*, 166(6):A1022, 2019.

[175] A Robert Armstrong, Michael Holzapfel, Petr Novák, Christopher S Johnson, Sun-Ho Kang, Michael M Thackeray, and Peter G Bruce. Demonstrating oxygen loss and associated structural reorganization in the lithium battery cathode li [ni0. 2li0. 2mn0. 6] o2. *Journal of the American Chemical Society*, 128(26):8694–8698, 2006.

[176] Danna Qian, Bo Xu, Miaofang Chi, and Ying Shirley Meng. Uncovering the roles of oxygen vacancies in cation migration in lithium excess layered oxides. *Physical Chemistry Chemical Physics*, 16(28):14665–14668, 2014.

[177] Chaoyu Hong, Qianyi Leng, Jianping Zhu, Shiyao Zheng, Huajin He, Yixiao Li, Rui Liu, Jiajia Wan, and Yong Yang. Revealing the correlation between structural evolution and li+ diffusion kinetics of nickel-rich cathode materials in li-ion batteries. *Journal of Materials Chemistry A*, 8(17):8540–8547, 2020.

[178] Han Gao, Qiang Wu, Yixin Hu, Jim P Zheng, Khalil Amine, and Zonghai Chen. Revealing the rate-limiting li-ion diffusion pathway in ultrathick electrodes for li-ion batteries. *The journal of physical chemistry letters*, 9(17):5100–5104, 2018.

[179] Zhongfeng Tang, Sen Wang, Jiaying Liao, Shuo Wang, Xiaodong He, Bicai Pan, Haiyan He, and Chunhua Chen. Facilitating lithium-ion diffusion in layered cathode materials by introducing li+/ni2+ antisite defects for high-rate li-ion batteries. *Research*, 2019, 2019.

[180] Adam Tornheim, Soroosh Sharifi-Asl, Juan C Garcia, Javier Bareño, Hakim Iddir, Reza Shahbazian-Yassar, and Zhengcheng Zhang. Effect of electrolyte composition on rock salt surface degradation in nmc cathodes during high-voltage potentiostatic holds. *Nano Energy*, 55:216–225, 2019.

[181] A Mauger and C Julien. Surface modifications of electrode materials for lithium-ion batteries: status and trends. *Ionics*, 20(6):751–787, 2014.

[182] Binghong Han, Baris Key, Saul H Lapidus, Juan C Garcia, Hakim Iddir, John T Vaughey, and Fulya Dogan. From coating to dopant: how the transition metal composition affects alumina coatings on ni-rich cathodes. *ACS applied materials & interfaces*, 9(47):41291–41302, 2017.

[183] Heike Gabrisch, James D Wilcox, and Marca M Doeff. Carbon surface layers on a high-rate lifepo4. *Electrochemical and Solid State Letters*, 9(7):A360, 2006.

[184] Loïc Baggetto, Nancy J Dudney, and Gabriel M Veith. Surface chemistry of metal oxide coated lithium manganese nickel oxide thin film cathodes studied by xps. *Electrochimica Acta*, 90:135–147, 2013.

[185] Jiaxin Zheng, Yaokun Ye, Tongchao Liu, Yinguo Xiao, Chongmin Wang, Feng Wang, and Feng Pan. Ni/li disordering in layered transition metal oxide: electrochemical impact, origin, and control. *Accounts of chemical research*, 52(8):2201–2209, 2019.

[186] E Sarasketa-Zabala, Frederic Aguesse, Igor Villarreal, LM Rodriguez-Martinez, Carmen M López, and Pierre Kubiak. Understanding lithium inventory loss and sudden performance fade in cylindrical cells during cycling with deep-discharge steps. *The Journal of Physical Chemistry C*, 119(2):896–906, 2015.

[187] Sanjay Nanda and Arumugam Manthiram. Lithium degradation in lithium–sulfur batteries: insights into inventory depletion and interphasial evolution with cycling. *Energy & Environmental Science*, 13(8):2501–2514, 2020.

[188] Peter M Attia, Alexander Bills, Ferran Brosa Planella, Philipp Dechent, Gonçalo dos Reis, Matthieu Dubarry, Paul Gasper, Richard Gilchrist, Samuel Greenbank, David Howey, et al. " knees" in lithium-ion battery aging trajectories. *arXiv preprint arXiv:2201.02891*, 2022.

[189] Ganesan Nagasubramanian. Impedance studies on li-ion cathodes. Technical report, Sandia National Lab.(SNL-NM), Albuquerque, NM (United States); Sandia ..., 2000.

[190] Edward Ott and Thomas M Antonsen Jr. Frequency and phase synchronization in large groups: Low dimensional description of synchronized clapping, firefly flashing, and cricket chirping. *Chaos: An Interdisciplinary Journal of Nonlinear Science*, 27(5):051101, 2017.

[191] Jongwoo Lim, Yiyang Li, Daan Hein Alsem, Hongyun So, Sang Chul Lee, Peng Bai, Daniel A Cogswell, Xuzhao Liu, Norman Jin, Young-sang Yu, et al. Origin and hysteresis of lithium compositional spatiodynamics within battery primary particles. *Science*, 353(6299):566–571, 2016.

[192] Nicolas Bacaër. *A short history of mathematical population dynamics*, volume 618. Springer, 2011.

[193] Michael Herrmann, Barbara Niethammer, and Juan JL Velázquez. Kramers and non-kramers phase transitions in many-particle systems with dynamical constraint. *Multiscale Modeling & Simulation*, 10(3):818–852, 2012.

[194] Michael Herrmann, Barbara Niethammer, and Juan JL Velazquez. Rate-independent dynamics and kramers-type phase transitions in nonlocal fokker–planck equations with dynamical control. *Archive for Rational Mechanics and Analysis*, 214(3):803–866, 2014.

[195] A Kolmogorov, I Petrovskii, and N Piskunov. A study of the diffusion equation with increase in the amount of substance, and its application to a biological problem. übersetzung aus: Bulletin of the moscow state university series a 1: 1-26, 1937. *Selected Works of AN Kolmogorov*, 1.

[196] Ronald Aylmer Fisher. *The genetical theory of natural selection*. 1958.

[197] Sewall Wright. *Evolution and the Genetics of Populations, Volume 2: Theory of gene frequencies*, volume 2. University of Chicago press, 1984.

[198] Ville Mustonen and Michael Lässig. From fitness landscapes to seascapes: non-equilibrium dynamics of selection and adaptation. *Trends in genetics*, 25(3):111–119, 2009.

[199] Arijit Guha, Amit Patra, and KV Vaisakh. Remaining useful life estimation of lithium-ion batteries based on the internal resistance growth model. In *2017 Indian Control Conference (ICC)*, pages 33–38. IEEE, 2017.

[200] Stuart A Kauffman and Sonke Johnsen. Coevolution to the edge of chaos: coupled fitness landscapes, poised states, and coevolutionary avalanches. *Journal of theoretical biology*, 149(4):467–505, 1991.

[201] Doraiswami Ramkrishna. *Population balances: Theory and applications to particulate systems in engineering*. Elsevier, 2000.

[202] Doraiswami Ramkrishna and Meenesh R Singh. Population balance modeling: current status and future prospects. *Annual review of chemical and biomolecular engineering*, 5:123–146, 2014.

[203] Till Daniel Frank. *Nonlinear Fokker-Planck equations: fundamentals and applications*. Springer Science & Business Media, 2005.

[204] Yang Yang, Rong Xu, Kai Zhang, Sang-Jun Lee, Linqin Mu, Pengfei Liu, Crystal K Waters, Stephanie Spence, Zhengrui Xu, Chenxi Wei, et al. Quantification of heterogeneous degradation in li-ion batteries. *Advanced Energy Materials*, 9(25):1900674, 2019.

[205] Rong Xu, Yang Yang, Fei Yin, Pengfei Liu, Peter Cloetens, Yijin Liu, Feng Lin, and Kejie Zhao. Heterogeneous damage in li-ion batteries: Experimental analysis and theoretical modeling. *Journal of the Mechanics and Physics of Solids*, 129:160–183, 2019.

[206] Larry R Faulkner and Allen J Bard. *Electrochemical methods: fundamentals and applications*. John Wiley and Sons, 2002.

[207] John R Miller, LT Calcaterra, and GL Closs. Intramolecular long-distance electron transfer in radical anions. the effects of free energy and solvent on the reaction rates. *Journal of the American Chemical Society*, 106(10):3047–3049, 1984.

[208] Mengyun Nie, Daniel P Abraham, Daniel M Seo, Yanjing Chen, Arijit Bose, and Brett L Lucht. Role of solution structure in solid electrolyte interphase formation on graphite with lipf6 in propylene carbonate. *The Journal of Physical Chemistry C*, 117(48):25381–25389, 2013.

[209] Robert Darling and John Newman. Modeling a porous intercalation electrode with two characteristic particle sizes. *Journal of The Electrochemical Society*, 144(12):4201, 1997.

[210] Qinghao Li, Yi Wang, Xuelong Wang, Xiaorui Sun, Jie-Nan Zhang, Xiqian Yu, and Hong Li. Investigations on the fundamental process of cathode electrolyte interphase formation and evolution of high-voltage cathodes. *ACS applied materials & interfaces*, 12(2):2319–2326, 2019.

[211] Debasish Mohanty, Kevin Dahlberg, David M King, Lamuel A David, Athena S Sefat, David L Wood, Claus Daniel, Subhash Dhar, Vishal Mahajan, Myongjai Lee, et al. Modification of ni-rich fcg nmc and nca cathodes by atomic layer deposition: preventing surface phase transitions for high-voltage lithium-ion batteries. *Scientific reports*, 6(1):1–16, 2016.

[212] Shuang Li, Zhenpeng Yao, Jianming Zheng, Maosen Fu, Jiajie Cen, Sooyeon Hwang, Huile Jin, Alexander Orlov, Lin Gu, Shun Wang, et al. Direct observation of defect-aided structural evolution in a nickel-rich layered cathode. *Angewandte Chemie International Edition*, 59(49):22092–22099, 2020.

[213] Kristina Edstroem, Torbjoern Gustafsson, and John Oswald Thomas. The cathode–electrolyte interface in the li-ion battery. *Electrochimica Acta*, 50(2-3):397–403, 2004.

[214] Kristina Edström, Marie Herstedt, and Daniel P Abraham. A new look at the solid electrolyte interphase on graphite anodes in li-ion batteries. *Journal of Power Sources*, 153(2):380–384, 2006.

[215] Mohd Khari Omar and Azizah Hanom Ahmad. Electrical impedance spectroscopy and fourier transform infrared studies of new binary li2co3-lii solid electrolyte. In *Materials Science Forum*, volume 846, pages 517–522. Trans Tech Publ, 2016.

[216] Huiyuan Zheng, Li Tan, Li Zhang, Qunting Qu, Zhongming Wan, Yan Wang, Ming Shen, and Honghe Zheng. Correlation between lithium deposition on graphite electrode and the capacity loss for lifepo4/graphite cells. *Electrochimica Acta*, 173:323–330, 2015.

[217] Joel AE Andersson, Joris Gillis, Greg Horn, James B Rawlings, and Moritz Diehl. Casadi: a software framework for nonlinear optimization and optimal control. *Mathematical Programming Computation*, 11:1–36, 2019.

[218] Seong Jin An, Jianlin Li, Claus Daniel, Debasish Mohanty, Shrikant Nagpure, and David L Wood III. The state of understanding of the lithium-ion-battery graphite solid electrolyte interphase (sei) and its relationship to formation cycling. *Carbon*, 105:52–76, 2016.

[219] Seong Jin An, Jianlin Li, Zhijia Du, Claus Daniel, and David L Wood III. Fast formation cycling for lithium ion batteries. *Journal of Power Sources*, 342:846–852, 2017.

[220] Robert Zwanzig. *Nonequilibrium statistical mechanics*. Oxford university press, 2001.

[221] Yiyang Li, Hungru Chen, Kipil Lim, Haitao D Deng, Jongwoo Lim, Dimitrios Fraggedakis, Peter M Attia, Sang Chul Lee, Norman Jin, Jože Moškon, et al. Fluid-enhanced surface diffusion controls intraparticle phase transformations. *Nature materials*, 17(10):915–922, 2018.

[222] Yoshiki Kuramoto. *Chemical Oscillations, Waves, and Turbulence*. Springer, 1984.

[223] Steven H Strogatz. From kuramoto to crawford: exploring the onset of synchronization in populations of coupled oscillators. *Physica D: Nonlinear Phenomena*, 143(1-4):1–20, 2000.

[224] Mehran Kardar. *Statistical physics of particles*. Cambridge University Press, 2007.

[225] Mehran Kardar. *Statistical physics of fields*. Cambridge University Press, 2007.

[226] John G Kirkwood. Statistical mechanics of liquid solutions. *Chemical Reviews*, 19(3):275–307, 1936.

[227] Marc Mézard and Giorgio Parisi. Statistical physics of structural glasses. *Journal of Physics: Condensed Matter*, 12(29):6655, 2000.

[228] Michael M Desai, Daniel S Fisher, and Andrew W Murray. The speed of evolution and maintenance of variation in asexual populations. *Current biology*, 17(5):385–394, 2007.

[229] Joel L Lebowitz and Abner Shimony. Statistical mechanics of open systems. *Physical Review*, 128(4):1945, 1962.

[230] Alok Kumar Rai, Ly Tuan Anh, Jihyeon Gim, Vinod Mathew, Jungwon Kang, Baboo Joseph Paul, Jinju Song, and Jaekook Kim. Simple synthesis and particle size effects of tio2 nanoparticle anodes for rechargeable lithium ion batteries. *Electrochimica Acta*, 90:112–118, 2013.

[231] G Arnold, J Garche, R Hemmer, S Ströbele, C Vogler, and M Wohlfahrt-Mehrens. Fine-particle lithium iron phosphate lifepo4 synthesized by a new low-cost aqueous precipitation technique. *Journal of Power Sources*, 119:247–251, 2003.

[232] Stephen J Harris, Adam Timmons, Daniel R Baker, and Charles Monroe. Direct in situ measurements of li transport in li-ion battery negative electrodes. *Chemical Physics Letters*, 485(4-6):265–274, 2010.

[233] Stephen J Harris, Ehsan Kabiri Rahani, and Vivek B Shenoy. Direct in situ observation and numerical simulations of non-shrinking-core behavior in an mcmb graphite composite electrode. *Journal of The Electrochemical Society*, 159(9):A1501, 2012.

[234] Karen E Thomas-Alyea, Changhoon Jung, Raymond B Smith, and Martin Z Bazant. In situ observation and mathematical modeling of lithium distribution within graphite. *Journal of The Electrochemical Society*, 164(11):E3063, 2017.

[235] Michael Hess. *Kinetics and stage transitions of graphite for lithium-ion batteries*. PhD thesis, ETH Zurich, 2013.

[236] Huada Lian and Martin Z Bazant. Modeling lithium plating onset on porous graphite electrodes under fast charging with hierarchical multiphase porous electrode theory. *Journal of The Electrochemical Society*, 171(1):010526, 2024.

[237] Marion Chandesris, Damien Caliste, Didier Jamet, and Pascal Pochet. Thermodynamics and related kinetics of staging in intercalation compounds. *The Journal of Physical Chemistry C*, 123(38):23711–23720, 2019.

[238] Shubham Agrawal and Peng Bai. Dynamic interplay between phase transformation instabilities and reaction heterogeneities in particulate intercalation electrodes. *Cell Reports Physical Science*, 3(5), 2022.

[239] Akshaya K Padhi, Kirakodu S Nanjundaswamy, and John B Goodenough. Phospho-olivines as positive-electrode materials for rechargeable lithium batteries. *Journal of the electrochemical society*, 144(4):1188, 1997.

[240] Ming Tang, W Craig Carter, and Yet-Ming Chiang. Electrochemically driven phase transitions in insertion electrodes for lithium-ion batteries: examples in lithium metal phosphate olivines. *Annual Review of Materials Research*, 40(1):501–529, 2010.

[241] Daniel A Cogswell and Martin Z Bazant. Coherency strain and the kinetics of phase separation in lifepo4 nanoparticles. *ACS nano*, 6(3):2215–2225, 2012.

[242] Daniel A Cogswell and Martin Z Bazant. Theory of coherent nucleation in phase-separating nanoparticles. *Nano letters*, 13(7):3036–3041, 2013.

[243] Marnix Wagemaker, Roel van de Krol, Arno PM Kentgens, Ad A Van Well, and Fokko M Mulder. Two phase morphology limits lithium diffusion in tio2 (anatase): A 7li mas nmr study. *Journal of the American Chemical Society*, 123(46):11454–11461, 2001.

[244] Alexandros Vasileiadis, Niek JJ De Klerk, Raymond B Smith, Swapna Ganapathy, Peter Paul RML Harks, Martin Z Bazant, and Marnix Wagemaker. Toward optimal performance and in-depth understanding of spinel li4ti5o12 electrodes through phase field modeling. *Advanced Functional Materials*, 28(16):1705992, 2018.

[245] Niek JJ De Klerk, Alexandros Vasileiadis, Raymond B Smith, Martin Z Bazant, and Marnix Wagemaker. Explaining key properties of lithiation in tio 2-anatase li-ion battery electrodes using phase-field modeling. *Physical Review Materials*, 1(2):025404, 2017.

[246] Yahong Xu, Enyuan Hu, Kai Zhang, Xuelong Wang, Valery Borzenets, Zhihong Sun, Piero Pianetta, Xiqian Yu, Yijin Liu, Xiao-Qing Yang, et al. In situ visualization of state-of-charge heterogeneity within a licoo2 particle that evolves upon cycling at different rates. *ACS Energy Letters*, 2(5):1240–1245, 2017.

[247] Neel Nadkarni, Tingtao Zhou, Dimitrios Fraggedakis, Tao Gao, and Martin Z Bazant. Modeling the metal–insulator phase transition in lixcoo2 for energy and information storage. *Advanced Functional Materials*, 29(40):1902821, 2019.

[248] Bonho Koo, Jinkyu Chung, Juwon Kim, Dimitrios Fraggedakis, Sungjae Seo, Chihyun Nam, Danwon Lee, Jeongwoo Han, Sugeun Jo, Hongbo Zhao, et al. Dynamic surface phases controlling asymmetry of high-rate lithiation and delithiation in phase-separating electrodes. *Energy & Environmental Science*, 16(8):3302–3313, 2023.

[249] Martin Z Bazant. Unified quantum theory of electrochemical kinetics by coupled ion-electron transfer. *Faraday Discussions*, 246:60–124, 2023.

[250] BJ Matkowsky and Z Schuss. Eigenvalues of the fokker–planck operator and the approach to equilibrium for diffusions in potential fields. *SIAM Journal on Applied Mathematics*, 40(2):242–254, 1981.

[251] Nicolaas Godfried Van Kampen. *Stochastic processes in physics and chemistry*, volume 1. Elsevier, 1992.

[252] Abraham Nitzan. *Chemical dynamics in condensed phases: relaxation, transfer and reactions in condensed molecular systems*. Oxford university press, 2006.

[253] Nicolaas Godfried Van Kampen. Elimination of fast variables. *Physics Reports*, 124(2):69–160, 1985.

[254] Hermann Grabert. *Projection operator techniques in nonequilibrium statistical mechanics*, volume 95. Springer, 2006.

[255] NG Van Kampen and I Oppenheim. Brownian motion as a problem of eliminating fast variables. *Physica A: Statistical Mechanics and its Applications*, 138(1-2):231–248, 1986.

[256] RH413262 Terwiel. Projection operator method applied to stochastic linear differential equations. *Physica*, 74(2):248–265, 1974.

[257] Zeev Schuss and Bernard J Matkowsky. The exit problem: a new approach to diffusion across potential barriers. *SIAM Journal on Applied Mathematics*, 36(3):604–623, 1979.

[258] Richard Courant and David Hilbert. *Methods of mathematical physics: partial differential equations*. John Wiley & Sons, 2008.

[259] Hendrik Anthony Kramers. Brownian motion in a field of force and the diffusion model of chemical reactions. *Physica*, 7(4):284–304, 1940.

[260] Bernard J Matkowsky and Zeev Schuss. The exit problem for randomly perturbed dynamical systems. *SIAM Journal on Applied Mathematics*, 33(2):365–382, 1977.

[261] Aljaž Godec and Ralf Metzler. Universal proximity effect in target search kinetics in the few-encounter limit. *Physical Review X*, 6(4):041037, 2016.

[262] Arnold JF Siegert. On the first passage time probability problem. *Physical Review*, 81(4):617, 1951.

[263] Herbert B Callen. *Thermodynamics and an Introduction to Thermostatistics*. John wiley & sons, 1991.

[264] Venkat R Subramanian and Ralph E White. New separation of variables method for composite electrodes with galvanostatic boundary conditions. *Journal of power sources*, 96(2):385–395, 2001.

[265] Rouslan L Stratonovich. *Topics in the theory of random noise*, volume 2. CRC Press, 1967.

[266] Ali Eftekhari. Lithium-ion batteries with high rate capabilities. *ACS Sustainable Chemistry & Engineering*, 5(4):2799–2816, 2017.

[267] Yuxin Tang, Yanyan Zhang, Wenlong Li, Bing Ma, and Xiaodong Chen. Rational material design for ultrafast rechargeable lithium-ion batteries. *Chemical Society Reviews*, 44(17):5926–5940, 2015.

[268] Steven B Torrisi, Martin Z Bazant, Alexander E Cohen, Min Gee Cho, Jens S Hummelshøj, Linda Hung, Gaurav Kamat, Arash Khajeh, Adeesh Kolluru, Xiangyun Lei, et al. Materials cartography: A forward-looking perspective on materials representation and devising better maps. *APL Machine Learning*, 1(2):020901, 2023.

[269] Ulrike Krewer, Fridolin Röder, Eranda Harinath, Richard D Braatz, Benjamin Bedürftig, and Rolf Findeisen. Dynamic models of Li-ion batteries for diagnosis and operation: A review and perspective. *Journal of The Electrochemical Society*, 165(16):A3656, 2018.

[270] Xuebing Han, Languang Lu, Yuejiu Zheng, Xuning Feng, Zhe Li, Jianqiu Li, and Minggao Ouyang. A review on the key issues of the lithium ion battery degradation among the whole life cycle. *ETransportation*, 1:100005, 2019.

[271] Donal P Finegan, Juner Zhu, Xuning Feng, Matt Keyser, Marcus Ulmefors, Wei Li, Martin Z Bazant, and Samuel J Cooper. The application of data-driven methods and physics-based learning for improving battery safety. *Joule*, 5(2):316–329, 2021.

[272] Pallavi Verma, Pascal Maire, and Petr Novák. A review of the features and analyses of the solid electrolyte interphase in Li-ion batteries. *Electrochimica Acta*, 55(22):6332–6341, 2010.

[273] Xuekun Lu, Marco Lagnoni, Antonio Bertei, Supratim Das, Rhodri E Owen, Qi Li, Kieran O'Regan, Aaron Wade, Donal P Finegan, Emma Kendrick, et al. Multiscale dynamics of charging and plating in graphite electrodes coupling operando microscopy and phase-field modelling. *Nature Communications*, 14(1):5127, 2023.

[274] Feng Lin, Kejie Zhao, and Yijin Liu. Heterogeneous reaction activities and statistical characteristics of particle cracking in battery electrodes. *ACS Energy Letters*, 6(11):4065–4070, 2021.

[275] Rui Xiong, Yue Pan, Weixiang Shen, Hailong Li, and Fengchun Sun. Lithium-ion battery aging mechanisms and diagnosis method for automotive applications: Recent advances and perspectives. *Renewable and Sustainable Energy Reviews*, 131:110048, 2020.

[276] J C Burns, D A Stevens, and J R Dahn. In-situ detection of lithium plating using high precision coulometry. *Journal of The Electrochemical Society*, 162(6):A959, 2015.

[277] Jungsoo Kim, Huiyong Chun, Minho Kim, Jungwook Yu, Kwangrae Kim, Taegyun Kim, and Soohee Han. Data-driven state of health estimation of Li-ion batteries with RPT-reduced experimental data. *IEEE Access*, 7:106987–106997, 2019.

[278] Jessie E Harlow, Xiaowei Ma, Jing Li, Eric Logan, Yulong Liu, Ning Zhang, Lin Ma, Stephen L Glazier, Marc ME Cormier, Matthew Genovese, et al. A wide range of testing results on an excellent lithium-ion cell chemistry to be used as benchmarks for new battery technologies. *Journal of The Electrochemical Society*, 166(13):A3031, 2019.

[279] Jon P Christophersen, Chinh D Ho, Chester G Motloch, David Howell, and Herb L Hess. Effects of reference performance testing during aging using commercial lithium-ion cells. *Journal of The Electrochemical Society*, 153(7):A1406, 2006.

[280] Byoung-Yong Chang and Su-Moon Park. Electrochemical impedance spectroscopy. *Annual Review of Analytical Chemistry*, 3:207–229, 2010.

[281] Francesco Ciucci. Modeling electrochemical impedance spectroscopy. *Current Opinion in Electrochemistry*, 13:132–139, 2019.

[282] Ting Ting Lou, Wei Ge Zhang, Hong Yu Guo, and Ji Song Wang. The internal resistance characteristics of lithium-ion battery based on HPPC method. *Advanced Materials Research*, 455–456:246, 2012.

[283] Joongpyo Shim and Kathryn A Striebel. Characterization of high-power lithium-ion cells during constant current cycling: Part I. Cycle performance and electrochemical diagnostics. *Journal of Power Sources*, 122(2):188–194, 2003.

[284] Bruis van Vlijmen, Vivek Lam, Patrick A Asinger, Xiao Cui, Devi Ganapathi, Shijing Sun, Patrick K Herring, Chirranjeevi Balaji Gopal, Natalie Geise, Haitao D Deng, et al. Interpretable data-driven modeling reveals complexity of battery aging. *ChemRxiv*, 2023.

[285] Jürgen Remmlinger, Michael Buchholz, Markus Meiler, Peter Bernreuter, and Klaus Dietmayer. State-of-health monitoring of lithium-ion batteries in electric vehicles by on-board internal resistance estimation. *Journal of Power Sources*, 196(12):5357–5363, 2011.

[286] Arijit Guha and Amit Patra. State of health estimation of lithium-ion batteries using capacity fade and internal resistance growth models. *IEEE Transactions on Transportation Electrification*, 4(1):135–146, 2017.

[287] M Berecibar, I Gandiaga, I Villarreal, N Omar, J Van Mierlo, and P Van den Bossche. Critical review of state of health estimation methods of Li-ion batteries for real applications. *Renewable and Sustainable Energy Reviews*, 56:572–587, 2016.

[288] Holger Blanke, Oliver Bohlen, Stephan Buller, Rik W De Doncker, Birger Fricke, Abderrezak Hammouche, Dirk Linzen, Marc Thele, and Dirk Uwe Sauer. Impedance measurements on lead–acid batteries for state-of-charge, state-of-health and cranking capability prognosis in electric and hybrid electric vehicles. *Journal of Power Sources*, 144(2):418–425, 2005.

[289] Wenquan Lu, Andrew Jansen, Dennis Dees, Paul Nelson, Nicholas R Veselka, and Gary Henriksen. High-energy electrode investigation for plug-in hybrid electric vehicles. *Journal of Power Sources*, 196(3):1537–1540, 2011.

[290] Mahammad Abdul Hannan, MS Lipu, Aini Hussain, Pin Jern Ker, TM Indra Mahlia, Muhamad Mansor, Afida Ayob, Mohamad H Saad, and ZY Dong. Toward enhanced state of charge estimation of lithium-ion batteries using optimized machine learning techniques. *Scientific reports*, 10(1):1–15, 2020.

[291] Weihan Li, Jue Chen, Katharina Quade, Daniel Luder, Jingyu Gong, and Dirk Uwe Sauer. Battery degradation diagnosis with field data, impedance-based modeling and artificial intelligence. *Energy Storage Materials*, 53:391–403, 2022.

[292] Dennis W Dees, Shigehiro Kawauchi, Daniel P Abraham, and Jai Prakash. Analysis of the Galvanostatic Intermittent Titration Technique (GITT) as applied to a lithium-ion porous electrode. *Journal of Power Sources*, 189(1):263–268, 2009.

[293] Wiljan Vermeer, Marco Stecca, Gautham Ram Chandra Mouli, and Pavol Bauer. A critical review on the effects of pulse charging of Li-ion batteries. In *IEEE 19th International Power Electronics and Motion Control Conference (PEMC)*, pages 217–224. IEEE, 2021.

[294] Jeffrey R Belt, Dawn M Bernardi, and Vivek Utgikar. Development and use of a lithium-metal reference electrode in aging studies of lithium-ion batteries. *Journal of The Electrochemical Society*, 161(6):A1116, 2014.

[295] Brandon R Long, Steven G Rinaldo, Kevin G Gallagher, Dennis W Dees, Stephen E Trask, Bryant J Polzin, Andrew N Jansen, Daniel P Abraham, Ira Bloom, Javier Bareño, et al. Enabling high-energy, high-voltage lithium-ion cells: standardization of coin-cell assembly, electrochemical testing, and evaluation of full cells. *Journal of The Electrochemical Society*, 163(14):A2999, 2016.

[296] James A Gilbert, Javier Bareño, Timothy Spila, Stephen E Trask, Dean J Miller, Bryant J Polzin, Andrew N Jansen, and Daniel P Abraham. Cycling behavior of NCM523/graphite lithium-ion cells in the 3–4.4 V range: Diagnostic studies of full cells and harvested electrodes. *Journal of The Electrochemical Society*, 164(1):A6054, 2016.

[297] Suguna Thanagasundram, Raghavendra Arunachala, Kamyar Makinejad, Tanja Teutsch, and Andreas Jossen. A cell level model for battery simulation. In *European Electric Vehicle Congress*, pages 1–13, 2012.

[298] Jon P Christophersen. Battery test manual for electric vehicles, revision 3. Technical report, Idaho National Laboratory, Idaho Falls, ID, 2015.

[299] Yuduo Huang, Yong Li, Li Jiang, Xuebo Qiao, Yijia Cao, and Jiaqi Yu. Research on fitting strategy in HPPC test for Li-ion battery. In *IEEE Sustainable Power and Energy Conference (iSPEC)*, pages 1776–1780. IEEE, 2019.

[300] Marc D Berliner, Hongbo Zhao, Supratim Das, Michael Forsuelo, Benben Jiang, William H Chueh, Martin Z Bazant, and Richard D Braatz. Nonlinear identifiability analysis of the porous electrode theory model of lithium-ion batteries. *Journal of The Electrochemical Society*, 168(9):090546, 2021.

[301] Alan C Hindmarsh, Peter N Brown, Keith E Grant, Steven L Lee, Radu Serban, Dan E Shumaker, and Carol S Woodward. Sundials: Suite of nonlinear and differential/algebraic equation solvers. *ACM Transactions on Mathematical Software (TOMS)*, 31(3):363–396, 2005.

[302] Giacomo Galuppini, Marc D Berliner, Huada Lian, Debbie Zhuang, Martin Z Bazant, and Richard D Braatz. Efficient computation of safe, fast charging protocols for multiphase lithium-ion batteries: A lithium iron phosphate case study. *Journal of Power Sources*, 580:233272, 2023.

[303] Giacomo Galuppini, Marc D Berliner, Daniel A Cogswell, Debbie Zhuang, Martin Z Bazant, and Richard D Braatz. Nonlinear identifiability analysis of multiphase porous electrode theory-based battery models: A lithium iron phosphate case study. *Journal of Power Sources*, 573:233009, 2023.

[304] Benben Jiang, Marc D Berliner, Kun Lai, Patrick A Asinger, Hongbo Zhao, Patrick K Herring, Martin Z Bazant, and Richard D Braatz. Fast charging design for lithium-ion batteries via Bayesian optimization. *Applied Energy*, 307:118244, 2022.

[305] Peter M Attia, Aditya Grover, Norman Jin, Kristen A Severson, Todor M Markov, Yang-Hung Liao, Michael H Chen, Bryan Cheong, Nicholas Perkins, Zi Yang, et al. Closed-loop optimization of fast-charging protocols for batteries with machine learning. *Nature*, 578(7795):397–402, 2020.

[306] Kevin L Gering. Novel method for evaluation and prediction of capacity loss metrics in Li-ion electrochemical cells. *Electrochimica Acta*, 228:636–651, 2017.

[307] Shuai Wang, Lingling Zhao, Xiaohong Su, and Peijun Ma. Prognostics of lithium-ion batteries based on battery performance analysis and flexible support vector regression. *Energies*, 7(10):6492–6508, 2014.

[308] Martin Z Bazant, Katsuyo Thornton, and Armand Ajdari. Diffuse-charge dynamics in electrochemical systems. *Physical review E*, 70(2):021506, 2004.

[309] PM Biesheuvel and MZ Bazant. Nonlinear dynamics of capacitive charging and desalination by porous electrodes. *Physical review E*, 81(3):031502, 2010.

[310] PM Biesheuvel, Yeqing Fu, and Martin Z Bazant. Diffuse charge and faradaic reactions in porous electrodes. *Physical Review E*, 83(6):061507, 2011.

[311] Christopher L Campion, Wentao Li, and Brett L Lucht. Thermal decomposition of $LiPF_6$-based electrolytes for lithium-ion batteries. *Journal of The Electrochemical Society*, 152(12):A2327, 2005.

[312] Fabian Single, Birger Horstmann, and Arnulf Latz. Revealing sei morphology: in-depth analysis of a modeling approach. *Journal of The Electrochemical Society*, 164(11):E3132, 2017.

[313] Rudolph A Marcus. Electron transfer reactions in chemistry: theory and experiment (nobel lecture). *Angewandte Chemie International Edition in English*, 32(8):1111–1121, 1993.

[314] Wolfgang Schmickler and Elizabeth Santos. *Interfacial electrochemistry*. Springer Science & Business Media, 2010.

[315] Gogi K Singh, Gerbrand Ceder, and Martin Z Bazant. Intercalation dynamics in rechargeable battery materials: General theory and phase-transformation waves in lifepo4. *Electrochimica Acta*, 53(26):7599–7613, 2008.

[316] Leo Wildfeuer and Markus Lienkamp. Quantifiability of inherent cell-to-cell variations of commercial lithium-ion batteries. *ETransportation*, 9:100129, 2021.

[317] Alexis Geslin, Bruis van Vlijmen, Xiao Cui, Arjun Bhargava, Patrick A Asinger, Richard D Braatz, and William C Chueh. Selecting the appropriate features in battery lifetime predictions. *Joule*, 7(9):1956–1965, 2023.

[318] Dirk Kehrwald, Paul R Shearing, Nigel P Brandon, Puneet K Sinha, and Stephen J Harris. Local tortuosity inhomogeneities in a lithium battery composite electrode. *Journal of The Electrochemical Society*, 158(12):A1393, 2011.

[319] Muratahan Aykol, Chirranjeevi Balaji Gopal, Abraham Anapolsky, Patrick K Herring, Bruis van Vlijmen, Marc D Berliner, Martin Z Bazant, Richard D Braatz, William C Chueh, and Brian D Storey. Perspective—combining physics and machine learning to predict battery lifetime. *Journal of The Electrochemical Society*, 168(3):030525, 2021.

[320] Haijun Ruan, Jingyi Chen, Weilong Ai, and Billy Wu. Generalised diagnostic framework for rapid battery degradation quantification with deep learning. *Energy and AI*, 9:100158, 2022.

[321] Anjuli T Appapillai, Azzam N Mansour, Jaephil Cho, and Yang Shao-Horn. Microstructure of licoo2 with and without "alpo4" nanoparticle coating: combined stem and xps studies. *Chemistry of Materials*, 19(23):5748–5757, 2007.

[322] Fengxia Xin, Hui Zhou, Xiaobo Chen, Mateusz Zuba, Natasha Chernova, Guangwen Zhou, and M Stanley Whittingham. Li–nb–o coating/substitution enhances the electrochemical performance of the lini0. 8mn0. 1co0. 1o2 (nmc 811) cathode. *ACS applied materials & interfaces*, 11(38):34889–34894, 2019.

[323] Ali Akbar, Junqi Weng, Xu Zhang, Ping Li, Guanghua Ye, and Xinggui Zhou. Impact of active particle in lithium-ion battery probed by a microstructure resolved model. *Industrial & Engineering Chemistry Research*, 63(20):8971–8982, 2024.

[324] Dong-Su Ko, Jun-Ho Park, Sungjun Park, Yong Nam Ham, Sung Jin Ahn, Jin-Hwan Park, Heung Nam Han, Eunha Lee, Woo Sung Jeon, and Changhoon Jung. Microstructural visualization of compositional changes induced by transition metal dissolution in ni-rich layered cathode materials by high-resolution particle analysis. *Nano energy*, 56:434–442, 2019.

[325] Mohammad Shahjalal, Probir Kumar Roy, Tamanna Shams, Ashley Fly, Jahedul Islam Chowdhury, Md Rishad Ahmed, and Kailong Liu. A review on second-life of Li-ion batteries: Prospects, challenges, and issues. *Energy*, 241:122881, 2022.

[326] Egoitz Martinez-Laserna, Iñigo Gandiaga, Elixabet Sarasketa-Zabala, Julia Badeda, D-I Stroe, Maciej Swierczynski, and Ander Goikoetxea. Battery second

life: Hype, hope or reality? A critical review of the state of the art. *Renewable and Sustainable Energy Reviews*, 93:701–718, 2018.

[327] Yanqiu Tao, Christopher D Rahn, Lynden A Archer, and Fengqi You. Second life and recycling: Energy and environmental sustainability perspectives for high-performance lithium-ion batteries. *Science Advances*, 7(45):eabi7633, 2021.

[328] Marcio AA Cardoso and Dan Luss. Stability of catalytic wires. *Chemical Engineering Science*, 24(11):1699–1710, 1969.

[329] Samuel M Allen, Robert W Balluffi, and W Craig Carter. *Kinetics of materials*. John Wiley & Sons, 2005.

[330] Neel Nadkarni, Elisha Rejovitsky, Dimitrios Fraggedakis, Claudio V Di Leo, Raymond B Smith, Peng Bai, and Martin Z Bazant. Interplay of phase boundary anisotropy and electro-auto-catalytic surface reactions on the lithium intercalation dynamics in li x fepo 4 plateletlike nanoparticles. *Physical Review Materials*, 2(8):085406, 2018.

[331] Yiwei Tian, Jonathan Booth, Elizabeth Meehan, David S Jones, Shu Li, and Gavin P Andrews. Construction of drug–polymer thermodynamic phase diagrams using flory–huggins interaction theory: identifying the relevance of temperature and drug weight fraction to phase separation within solid dispersions. *Molecular pharmaceutics*, 10(1):236–248, 2013.

[332] Fong Liu and Nigel Goldenfeld. Dynamics of phase separation in block copolymer melts. *Physical Review A*, 39(9):4805, 1989.

[333] Joakim Stenhammar, Adriano Tiribocchi, Rosalind J Allen, Davide Marenduzzo, and Michael E Cates. Continuum theory of phase separation kinetics for active brownian particles. *Physical review letters*, 111(14):145702, 2013.

[334] Denes Hnisz, Krishna Shrinivas, Richard A Young, Arup K Chakraborty, and Phillip A Sharp. A phase separation model for transcriptional control. *Cell*, 169(1):13–23, 2017.

[335] Yayuan Liu, Yangying Zhu, and Yi Cui. Challenges and opportunities towards fast-charging battery materials. *Nature Energy*, 4(7):540–550, 2019.

[336] Gao-Long Zhu, Chen-Zi Zhao, Jia-Qi Huang, Chuanxin He, Jian Zhang, Shaohai Chen, Lei Xu, Hong Yuan, and Qiang Zhang. Fast charging lithium batteries: recent progress and future prospects. *Small*, 15(15):1805389, 2019.

[337] Xiangwen Gao, Ya-Nan Zhou, Duzhao Han, Jiangqi Zhou, Dezhong Zhou, Wei Tang, and John B Goodenough. Thermodynamic understanding of li-dendrite formation. *Joule*, 2020.

[338] Rohan Akolkar. Modeling dendrite growth during lithium electrodeposition at sub-ambient temperature. *Journal of Power Sources*, 246:84–89, 2014.

[339] HH Yan, YH Bie, XY Cui, GP Xiong, and L Chen. A computational investigation of thermal effect on lithium dendrite growth. *Energy Conversion and Management*, 161:193–204, 2018.

[340] Haakon Karlsen, Tao Dong, Zhaochu Yang, and Rui Carvalho. Temperature-dependence in battery management systems for electric vehicles: Challenges, criteria, and solutions. *IEEE Access*, 7:142203–142213, 2019.

[341] Todd M Bandhauer, Srinivas Garimella, and Thomas F Fuller. A critical review of thermal issues in lithium-ion batteries. *Journal of the Electrochemical Society*, 158(3):R1, 2011.

[342] N Boden, SA Leng, and IM Ward. Ionic conductivity and diffusivity in polyethylene oxode/electrolyte solutions as models for polymer electrolytes. *Solid State Ionics*, 45(3-4):261–270, 1991.

[343] D Bernardi, E Pawlikowski, and John Newman. A general energy balance for battery systems. *Journal of the electrochemical society*, 132(1):5, 1985.

[344] Carolyn R Pals and John Newman. Thermal modeling of the lithium/polymer battery: I. discharge behavior of a single cell. *Journal of the Electrochemical Society*, 142(10):3274, 1995.

[345] LH Saw, Yonghuang Ye, and AAO Tay. Electrochemical–thermal analysis of 18650 lithium iron phosphate cell. *Energy Conversion and Management*, 75:162–174, 2013.

[346] Christophe Forgez, Dinh Vinh Do, Guy Friedrich, Mathieu Morcrette, and Charles Delacourt. Thermal modeling of a cylindrical lifepo4/graphite lithium-ion battery. *Journal of Power Sources*, 195(9):2961–2968, 2010.

[347] Dimitrios Fraggedakis, Michael McEldrew, Raymond B Smith, Yamini Krishnan, Yirui Zhang, Peng Bai, William C Chueh, Yang Shao-Horn, and Martin Z Bazant. Theory of coupled ion-electron transfer kinetics. *arXiv preprint arXiv:2007.12980*, 2020.

[348] C Heubner, M Schneider, and A Michaelis. Detailed study of heat generation in porous licoo2 electrodes. *Journal of Power Sources*, 307:199–207, 2016.

[349] Arnulf Latz and Jochen Zausch. Thermodynamic consistent transport theory of li-ion batteries. *Journal of Power Sources*, 196(6):3296–3302, 2011.

[350] Abraham Nitzan and John Ross. Oscillations, multiple steady states, and instabilities in illuminated systems. *The Journal of Chemical Physics*, 59(1):241–250, 1973.

[351] Joel Keizer. Thermodynamics at nonequilibrium steady states. *The Journal of Chemical Physics*, 69(6):2609–2620, 1978.

[352] Morton E Gurtin, Eliot Fried, and Lallit Anand. *The mechanics and thermodynamics of continua*. Cambridge University Press, 2010.

[353] R Byron Bird, Warren E Stewart, Edwin N Lightfoot, and Robert E Meredith. Transport phenomena. *Journal of The Electrochemical Society*, 108(3):78C, 1961.

[354] John C Slattery, Leonard Sagis, and Eun-Suok Oh. *Interfacial transport phenomena*. Springer Science & Business Media, 2007.

[355] Jefferson W Tester, Michael Modell, et al. *Thermodynamics and its Applications*. Prentice Hall PTR, 1997.

[356] Leslie Colin Woods. The thermodynamics of fluid systems. *Oxford*, 1975.

[357] John W Cahn. On spinodal decomposition. *Acta metallurgica*, 9(9):795–801, 1961.

[358] R Abeyartne. Continuum mechanics volume ii of lecture notes on the mechanics of elastic solids cambridge, http. *web. mit. edu/abeyartne/lecture_ notes. html*, 11, 2012.

[359] Claudio V Di Leo, Elisha Rejovitzky, and Lallit Anand. A cahn–hilliard-type phase-field theory for species diffusion coupled with large elastic deformations: application to phase-separating li-ion electrode materials. *Journal of the Mechanics and Physics of Solids*, 70:1–29, 2014.

[360] Lallit Anand. A cahn–hilliard-type theory for species diffusion coupled with large elastic–plastic deformations. *Journal of the Mechanics and Physics of Solids*, 60(12):1983–2002, 2012.

[361] John W Cahn and John E Hilliard. Free energy of a nonuniform system. i. interfacial free energy. *The Journal of chemical physics*, 28(2):258–267, 1958.

[362] Vitaly L Ginzburg and Lev D Landau. On the theory of superconductivity. In *On Superconductivity and Superfluidity*, pages 113–137. Springer, 2009.

[363] Pierre C Hohenberg and Bertrand I Halperin. Theory of dynamic critical phenomena. *Reviews of Modern Physics*, 49(3):435, 1977.

[364] BI Halperin, PC Hohenberg, and Shang-keng Ma. Renormalization-group methods for critical dynamics: I. recursion relations and effects of energy conservation. *Physical Review B*, 10(1):139, 1974.

[365] Oliver Penrose and Paul C Fife. Thermodynamically consistent models of phase-field type for the kinetic of phase transitions. *Physica D: Nonlinear Phenomena*, 43(1):44–62, 1990.

[366] Oliver Penrose and Paul C Fife. On the relation between the standard phase-field model and a "thermodynamically consistent" phase-field model. *Physica D: Nonlinear Phenomena*, 69(1-2):107–113, 1993.

[367] Herbert B Callen. Thermodynamics and an introduction to thermostatistics, 1998.

[368] Daniel A Cogswell. Quantitative phase-field modeling of dendritic electrodeposition. *Physical Review E*, 92(1):011301, 2015.

[369] Mathis Plapp. Unified derivation of phase-field models for alloy solidification from a grand-potential functional. *Physical Review E*, 84(3):031601, 2011.

[370] Daniel M Anderson, Geoffrey B McFadden, and Adam A Wheeler. Diffuse-interface methods in fluid mechanics. *Annual review of fluid mechanics*, 30(1):139–165, 1998.

[371] J Ernest Dunn and James Serrin. On the thermomechanics of interstitial working. In *The Breadth and Depth of Continuum Mechanics*, pages 705–743. Springer, 1986.

[372] Elias C Aifantis and James B Serrin. Equilibrium solutions in the mechanical theory of fluid microstructures. *Journal of colloid and interface science*, 96(2):530–547, 1983.

[373] F Massieu. Sur les fonctions caractéristiques des divers fluides. *CR Acad. Sci. Paris*, 69:858–862, 1869.

[374] Lars Onsager. Reciprocal relations in irreversible processes. i. *Physical review*, 37(4):405, 1931.

[375] Lars Onsager. Reciprocal relations in irreversible processes. ii. *Physical review*, 38(12):2265, 1931.

[376] Herbert B Callen. The application of onsager's reciprocal relations to thermoelectric, thermomagnetic, and galvanomagnetic effects. *Physical Review*, 73(11):1349, 1948.

[377] Jasleen Kaur and Ramandeep S Johal. Irreversible thermodynamics of thermoelectric devices: From local framework to global description. *arXiv preprint arXiv:2007.04184*, 2020.

[378] Robert G Mortimer and Henry Eyring. Elementary transition state theory of the soret and dufour effects. *Proceedings of the National Academy of Sciences*, 77(4):1728–1731, 1980.

[379] Nils Ohmer, Bernhard Fenk, Dominik Samuelis, Chia-Chin Chen, Joachim Maier, Markus Weigand, Eberhard Goering, and Gisela Schütz. Phase evolution in single-crystalline lifepo 4 followed by in situ scanning x-ray microscopy of a micrometre-sized battery. *Nature communications*, 6(1):1–7, 2015.

[380] Dane Morgan, Anton Van der Ven, and Gerbrand Ceder. Li conductivity in li x mpo 4 (m= mn, fe, co, ni) olivine materials. *Electrochemical and Solid State Letters*, 7(2):A30, 2003.

[381] Karen E Thomas and John Newman. Thermal modeling of porous insertion electrodes. *Journal of the Electrochemical Society*, 150(2):A176, 2003.

[382] Masaya Takahashi, Shin-ichi Tobishima, Koji Takei, and Yoji Sakurai. Reaction behavior of lifepo4 as a cathode material for rechargeable lithium batteries. *Solid state ionics*, 148(3-4):283–289, 2002.

[383] Jan L Allen, T Richard Jow, and Jeffrey Wolfenstine. Kinetic study of the electrochemical fepo4 to lifepo4 phase transition. *Chemistry of materials*, 19(8):2108–2111, 2007.

[384] Alexei V Churikov, Alexander V Ivanishchev, Arseni V Ushakov, Irina M Gamayunova, and Ilya A Leenson. Thermodynamics of lifepo4 solid-phase synthesis using iron (ii) oxalate and ammonium dihydrophosphate as precursors. *Journal of Chemical & Engineering Data*, 58(6):1747–1759, 2013.

[385] Quan Shi, Liying Zhang, Mark E Schlesinger, Juliana Boerio-Goates, and Brian F Woodfield. Low temperature heat capacity study of fepo4 and fe3 (p2o7) 2. *The Journal of Chemical Thermodynamics*, 62:35–42, 2013.

[386] Abhay Dinker, Madhu Agarwal, and GD Agarwal. Experimental thermal performance study of natural graphite as sensible heat storage material using different heat transfer fluids. *Experimental Heat Transfer*, 31(3):219–231, 2018.

[387] YF Reynier, Rachid Yazami, and Brent Fultz. Thermodynamics of lithium intercalation into graphites and disordered carbons. *Journal of The Electrochemical Society*, 151(3):A422–A426, 2004.

[388] Marc Doyle, John Newman, Antoni S Gozdz, Caroline N Schmutz, and Jean-Marie Tarascon. Comparison of modeling predictions with experimental data from plastic lithium ion cells. *Journal of the Electrochemical Society*, 143(6):1890–1903, 1996.

[389] Karthikeyan Kumaresan, Godfrey Sikha, and Ralph E White. Thermal model for a li-ion cell. *Journal of the Electrochemical Society*, 155(2):A164, 2007.

[390] Kara D Fong, Helen K Bergstrom, Bryan D McCloskey, and Kranthi K Mandadapu. Transport phenomena in electrolyte solutions: Nonequilibrium thermodynamics and statistical mechanics. *AIChE Journal*, 66(12):e17091, 2020.

[391] Lev Davidovich Landau and Evgenii Mikhailovich Lifshitz. *Course of theoretical physics*. Elsevier, 2013.

[392] Adrian P Sutton. *Physics of Elasticity and Crystal Defects*, volume 6. Oxford University Press, USA, 2020.

[393] Amilcare Porporato, Salvatore Calabrese, and Tomasz Hueckel. Thermodynamic relations among isotropic material properties in conditions of plane shear stress. *Entropy*, 21(3):295, 2019.